5-2019

A Power Accounting Analysis of the Proto-MPEX Linear Device and Target Heat Flux Extrapolations to MPEX-based on Proto-MPEX discharges

Melissa A. Showers
University of Tennessee

A Power Accounting Analysis of the Proto-MPEX Linear Device and Target Heat Flux Extrapolations to MPEX-based on Proto-MPEX discharges

A Dissertation Presented for the
Doctor of Philosophy
Degree
The University of Tennessee, Knoxville

Melissa A. Showers
May 2019

ACKNOWLEDGEMENTS

Pursuing this PhD in Energy Science and Engineering has been an incredible journey and I am forever grateful for my amazing support team, who provided invaluable advice, encouragement, and guidance over the past few years:

I would first like to say a special thanks to my advisors, Dr. David Donovan and Dr. Ted Biewer, who were ever-present sources of information and advice, and never ran out of patience as I bombarded them with questions throughout my graduate career.

I would also like to thank the other members of my PhD committee, Dr. Arnie Lumsdaine and Dr. Steve Zinkle, for dedicating their time to helping me develop and defend this dissertation.

Thank you to my fellow graduate students who worked with me on Proto-MPEX. From arriving at o'dark-thirty to start operations before it got too hot during the summer, to climbing under the machine to install a new diagnostic, to brainstorming how to tackle the latest unexpected problem, you have all made the entire experience so much more memorable and enjoyable.

I would also like to thank Juergen Rapp, John Caughman, Rick Goulding, Cornwall Lau, and the entire Proto-MPEX team. I've learned so much over my years in the group and it has been an irreplaceable experience.

I would like to say thank you to Thomas Eich, Albrecht Herrmann, Michael Faitsch, Dirk Nille, Bernhard Sieglin and the ASDEX-U team at IPP Garching, for their invaluable help learning the THEODOR code and their hospitality for the three weeks I spent at IPP Garching.

Thank you to Dr. Lee Riedinger, Wanda Davis, Mike Simpson, Jessica Garner and all the wonderful faculty and staff at the Bredesen Center for Interdisciplinary Research and Graduate Education. Without you all, I never would have even started this PhD, much less had so much success in pursuing it.

I would also like to thank my fellow graduate students in the Bredesen Center. The student bond in our program is truly unique compared to other graduate programs. You all immediately welcomed me into the fold when I first arrived and continued to be sources of support and laughter during my graduate career.

A special thank you goes to my family, who have been incredibly supportive throughout my entire life, making sure I could be strong and independent in my life and always pushing me to reach for the stars.

Finally, THANK YOU to my fantastic fiancé, Jeff, for being a shoulder to cry on, someone I could vent to and laugh with, and my biggest fan. You're the only one who could possibly deal with all my crazy and love me anyway <3.

ABSTRACT

Plasma material interaction (PMI) studies are crucial to the successful development of future fusion reactors. Proto-MPEX is a prototype device whose primary purpose is to develop the plasma heating source concepts for the Material Plasma Exposure eXperiment (MPEX), a steady-state linear device being developed to study PMI. Multi-region power accounting studies of Proto-MPEX were performed utilizing an extensive diagnostic suite and software modeling to identify mechanisms and locations of heat loss from the main plasma. Of the 79.4 kW of input power, up to 100% of the power has been accounted for in the helicon region. Extending the analysis to the device from end plate to end plate, 62.4% of the input power was diagnostically verified. The efficiencies of the upstream and downstream regions were 9.7% and 1.9%, respectively. Regions with lower power transport efficiencies have been identified as areas requiring further diagnostic analysis, particularly the sub-region defined between the downstream edge of the helicon region (z = 1.5 m) and the central chamber (z = 2.2 m). The importance of the skimmer plate, located in this sub-region, to the operating performance of Proto-MPEX and design of MPEX has been highlighted. The data acquisition and analysis processes have been streamlined as a working model for future power balance studies of Proto-MPEX. Power-to-target plate efficiencies have been calculated for a variety of plasma production scenarios including helicon power only and helicon power supplemented with electron cyclotron heating (ECH), helicon power supplemented with ion cyclotron heating (ICH), and helicon power supplemented with combined ECH and ICH. These efficiencies are extrapolated to MPEX-level applied power sources to estimate the expected heat fluxes and powers deposited to target plate surfaces for future steady-state PMI studies. In two of the seven operating configurations analyzed, MPEX-extrapolated heat fluxes achieved or surpassed the desired 10 MW/m^2 target plate heat flux. The desired heat flux can be achieved with helicon + ICH pulses and helicon + ECH + ICH pulses, providing operational flexibility in future MPEX PMI experiments.

TABLE OF CONTENTS

LIST OF TABLES

LIST OF FIGURES

CHAPTER 0: EXECUTIVE SUMMARY

With the growing consumption of energy and finite amount of fossil fuel resources, there has been increased focus on developing new sustainable energy sources, particularly one which can provide baseload generation. Nuclear fusion has the potential to fulfill the need for that baseload generation. The successful development of future fusion reactors relies on plasma material interactions (PMI) studies. Additional information about nuclear fusion is described in chapter one of this thesis. Linear plasma devices can simulate and exceed the extreme conditions that will be experienced by plasma facing materials, allowing the long-term effects on material components to be observed in shorter periods of time. The Prototype Material Plasma Exposure eXperiment (Proto-MPEX) is a linear device with the primary purpose of developing the power source concept for MPEX, a steady-state linear device studying PMI. Proto-MPEX has four installed power sources: a (1) helicon antenna; (2) an electron cyclotron heating (ECH) launcher; (3) an ion cyclotron heating (ICH) antenna; and (4) pre-ionization heating. Additional information regarding the Proto-MPEX machine is provided in chapter two of this thesis.

There were two primary purposes of this thesis research. The first was to perform a comprehensive power accounting analysis of the Proto-MPEX machine to determine the locations and mechanisms of power loss from generated plasmas, potentially identifying areas for operational improvement. The second was to use target plate heat fluxes generated by Proto-MPEX plasma discharges to estimate the power source combinations required to achieve the desired 10 MW/m^2 target heat fluxes for future MPEX operations.

To assess the performance of the Proto-MPEX device and highlight areas of improvement with respect to machine operations, multiple power accounting[1] analyses were performed. The power accounting studies identify where and how energy is being lost from the plasma, especially in the helicon region. To perform the power balances, an extensive suite of diagnostics was employed. The diagnostic suite installed on Proto-MPEX is described in detail in chapter three. The power accounting was separated into multiple regions and sub-regions to identify areas with lower power transport efficiencies that require further diagnostic analysis. Chapter four describes the methods and components used to perform the power accounting studies and the region efficiency analyses. Chapter five encompasses all relevant previous work performed leading up to the comprehensive power accounting study and the extrapolation to MPEX-level target plate deposited heat fluxes and powers. Work includes the development and improvement of the data acquisition and analysis methods used to perform the power accounting of Proto-MPEX. Chapter six describes the comprehensive power balance performed, including the region efficiency analysis. In this power balance, up to 100% of the power has been accounted for in the helicon region, which is defined as the region from machine axial locations z = 1.0 m to 1.5 m. Extending the analysis to the device

[1] For the purposes of this thesis, the term ‘power balance’ and ‘power accounting’ are used interchangeability.

from end plate to end plate, 62.4% of the input power was diagnostically verified. The region requiring the most additional analysis is the region from z = 1.5 m to 2.2 m, specifically, from z = 1.5 m to the skimmer plate (z = 1.75 m). The pressure differential created by the skimmer plate appears to play an important role in the plasma power losses and transport along the machine. The expansion of the diagnostic suite to include additional diagnostics such as HELIOS, TALIF, and a bolometry array will improve future power balances, increasing the amount of diagnostically verified power. The data acquisition and analysis processes have been streamlined as a working model for future power balance studies of Proto-MPEX.

Extrapolations of Proto-MPEX power sources to MPEX-level installed power capacities are provided in chapter seven. The target plate heat fluxes, deposited powers, and power-to-target efficiencies are calculated for a variety of machine operating configurations and applied power combinations. Power-to-target efficiencies were analyzed early in the plasma pulse, near the time when the maximum heat flux occurred. Helicon power scans and pulse length scans are analyzed to determine the likely behavior of MPEX steady-steady plasmas. The power-to-target efficiencies over the length of the plasma pulse were compared to inject power sources to corroborate the determined power-to-target efficiencies. In two of the seven operating configurations analyzed for the extrapolation experiments, MPEX-extrapolated heat fluxes achieved or surpassed the desired 10 MW/m^2 target plate heat flux. The desired heat flux can be achieved with helicon + ICH pulses and helicon + ECH + ICH pulses, providing operational flexibility in future MPEX PMI experiments. Areas requiring further analysis have been identified. Future work includes in-depth gas scan experiments, helicon long-pulse experiments, and expansion of power balance analyses to include data from newly installed diagnostics, such as HELIOS and TALIF.

CHAPTER 1: BACKGROUND

1.1. Nuclear Fusion

By 2050, the world's population is expected to reach 10 billion. Coupled with the increased population and improved living standards, the corresponding energy demand could increase by a factor of 2-3 [1]. With the growing consumption of energy and the finite amount of available fossil fuel resources, there has been increased focus on developing new sustainable energy sources, particularly one which can provide baseload generation. One such resource is nuclear fusion energy, which releases an exorbitant amount of energy[2] from fusing two light atoms into a heavier atom [2, 3]. Specifically, fusion atoms can release approximately 4 million times more energy than burning coal or gas, and approximately four times more energy than nuclear fission reactions, for equal mass [2]. Additional benefits to nuclear fusion over fission include the absence of long-lived radioactive waste, lower risk of proliferation, and no risk of meltdown [3]. The fusion reactor system functions the same as a conventional power plant, with the exception that the thermal power is supplied by nuclear fusion rather than burning coal or nuclear fission.

Fusion reactors can achieve net energy gain; that is, the output power of the reactor is greater than the power put into the system to run it (input power). The ratio of output to input power is defined as *Q*. ITER is a multi-national effort to construct the biggest tokamak[3] to date and first fusion reactor, which intends to exceed "scientific break-even" (Q=1) and attain a Q-value of 10 [2]. If successful, the reactor will produce ten times the amount of energy that it consumes.

The leading fusion reaction is the fusion of two hydrogen isotopes, deuterium (D) and tritium (T).[4] The deuterium-tritium fusion reaction is depicted in figure 1.1 in Appendix E[5] [3].

One deuterium atom and one tritium atom fusing together produce helium and a neutron. The total energy is 17.59 MeV per fusion reaction, with 14.05 MeV attributed to neutrons, which are not confined by the magnetic field. These neutrons can carry their energy to tokamak machine walls for heat capture [3].

1.2. Tokamaks and their Divertors

In a nuclear fusion reactor system, the plasma reaches temperatures of about 100 million Kelvin, and the reactor walls will reach about 1,000 K [3].[6] Mitigating heat fluxes

[2] Per Einstein's equation, $E = mc^2$; a small amount of mass 'lost' through the fusion of two lighter atoms, multiplied by the speed of light squared, yields a large amount of energy, E [2].
[3] A tokamak is the leading machine design for producing plasmas whose ionized particles are confined by magnetic fields [i.e. 2]
[4] D-T fusion is able to produce the largest energy gain for the 'lowest' plasma temperatures [2].
[5] All figures referenced in this thesis are provided in Appendix E, with the exception of the figures provided in Appendices B and C.
[6] At high temperatures, the fuel becomes "plasma", meaning a fully ionized gas, a sea of positive ions and negative electrons. Examples of plasma include stars and lightning.

impinging on tokamak plasma facing components (PFCs), especially its divertor, is crucial to the success of future fusion reactors, such as ITER [4,5]. A divertor is a specially designed component of the tokamak whose primary purpose is to bend "the outer magnetic field lines away from the plasma" [3]. This directs the outer boundary layer of the plasma (the plasma closest to escaping confinement)[7] away from the hotter plasma core and towards the divertor plate before the plasma can hit the inner walls of the reactor [6, 7]. This reduces the heat flux on the tokamak chamber walls, whose material is generally more susceptible to high temperatures [3]. Currently, experiments and computer simulations are producing surface heat fluxes beyond the engineering limits of the plasma facing materials [6, 7]. The parallel heat fluxes[8] in the SOL region are expected to average approximately 1 GW/m^2 on the outer divertor of ITER[9] [8, 9]. However, the maximum sustainable steady-state heat load for divertor surface materials (primarily tungsten) is only about 10 MW/m^2, which corresponds to approximately a parallel heat flux of 200-300 MW/m^2 [10, 8]. If the divertor experiences a heat flux of ITER's projected magnitude, it will fail via sputtering[10] or melting. When this occurs, the divertor will not only fail to contain the heat of the plasma reaction, transferring that heat beyond the reactor container, but it will also release its material particulates into the plasma itself, causing contamination [4].

Beyond the steady-state heat load, future fusion reactors must also be concerned with transient heat loads. The base-line ITER operation scenario is the type I-ELMy H-mode. ELM stands for 'edge-localized mode', a magnetic-hydrodynamic (MHD) instability that occurs at the edge of the plasma due to a quasi-periodic relaxation of the magnetic confinement, particularly during the transition from low to high magnetic confinement (L-mode to H-mode, respectively) [i.e. 11]. The relaxation leads to a sudden expulsion of heat to the tokamak walls. Model simulations suggest that an ELM in the ITER tokamak could release up 4 MJ/m^2 of energy in less than half a millisecond, corresponding to a transient heat flux of 800 MW/m^2, several times larger than engineering material limits [i.e. 3]. A type-I ELM[11] is a 'giant' ELM with intense peaks of helium-alphas, light and high-power flux to the divertor [3]. An ELM is considered a source of *transient* heat flux, while the heat flux associated with the standard tokamak operations is considered a source of *non-transient* heat flux [i.e. 12]. Transient heat fluxes are short in duration but high in intensity (magnitude). The divertor surface must be able to withstand both.

---

[7] The outer boundary plasma region being pulled towards the divertor is called the scrape-off layer (SOL).
[8] The heat flux is often measured in terms of the *parallel* heat flux, which is the heat flux hitting perpendicular to the divertor surface divided by the (sine of) magnetic field line pitch angle (~2-3°C) [8].
[9] For fully attached plasmas [8]; divertor is considered to be *detached* when high neutral gas pressure (pumped into the divertor region) separates the plasma flowing from the separatrix from the divertor surface [3]. The separatrix is "the boundary of the last closed flux surface (LCFS) and the scrape-off layer (SOL), where open magnetic field lines intercept the limiter or the wall" [3]. Plasma within the separatrix is confined while the magnetic field lines in the SOL drive plasma towards the divertor [i.e. 3].
[10] Sputtering is the release of divertor material particles into the SOL and potentially the main plasma region [i.e. 3].
[11] Other identified types of ELMs are type II and type III ELMs. A type III ELM, also called a 'grassy' ELM, releases heat load over a longer time step. In comparison to type I ELMs, they worsen plasma confinement time, but are not catastrophic to PFCs. A type II ELM is considered the 'intermediate' ELM between the two types [3].

1.3. Linear Plasma Devices

Linear plasma devices are crucial to nuclear fusion reactor research. A primary purpose is to aid in understanding plasma-material interactions (PMI), which have been identified as among the most critical research areas to the successful development of a nuclear fusion energy reactor [13].

Linear devices have two main advantages: (1) they can currently be operated at steady state and (2) their engineering design is comparatively less complex and expensive than a tokamak (or stellarator) to operate [14, 15]. This accessibility facilitates machine adjustments, and simplifies measurements, analysis, and modeling. Further, they are capable of investigating higher particle flux and fluence operations [15], which are the extreme conditions that will be experienced by PFCs in fusion plasma environments, allowing the long-term effects on material components to be characterized in shorter periods of development time [i.e. 16].

1.4. Plasma Heating Sources and Techniques

Power inputs are the applicable plasma heating sources installed on a given linear plasma device. Plasma heating techniques include alpha heating, ohmic heating, plasma guns, plasma compression, neutral beam injection (NBI), and electromagnetic wave heating [i.e. 3]. Types of electromagnetic (EM) wave heating include microwaves, ion cyclotron waves, electron cyclotron waves, and helicon waves [3, 17]. The structural limitations of linear plasma fusion devices lead to a tendency to use electromagnetic wave heating techniques. For example, the linear plasma device, Proto-MPEX (described further in chapter two), has the capability to apply helicon waves, electron cyclotron waves[12], and ion cyclotron waves to heat its plasmas. It is important to note the coupling efficiency is a crucial parameter of each power source's operations.

1.4.1 EM waves

Electromagnetic (EM) waves are defined in terms of their angular frequency (ω) and their wave vector (or wave number) (k) [3]. The wave vector has a magnitude equivalent to $2\pi/\lambda$, where λ is the EM wavelength, a direction equal to the direction of EM wave propagation, and components parallel and perpendicular to the magnetic field [3].

The EM waves travel at the phase velocity (v_{ph}), although their associated energy and information travel at the group velocity (v_g). The v_{ph} can be greater than the speed of light (in vacuum), c, but the v_g must always be less than c [3]. Equations 1.1 and 1.2 below depict the relations for the wave phase and group velocities, respectively [3].

$$\mathrm{v_{ph}} = \frac{\omega}{\mathrm{k}} \tag{1.1}$$

$$\mathrm{v_g} = \frac{\delta\omega}{\delta\mathrm{k}} \tag{1.2}$$

[12] For this paper, the term 'microwaves' may be used interchangeably with 'electron cyclotron waves' or 'ECH'.

EM wave heating relies on the concept that under the correct conditions, “collective wavelike motion can be established in the plasma… by launching electromagnetic waves” [17]. The plasma is heated when wave particles collide and dissipate their kinetic energy, which is absorbed by the plasma [17]. The wave can also be absorbed even in the absence of collisions [18]. The wave damping occurring without particle collisions is called Landau damping, through which the plasma particles absorb energy from the EM wave itself, “like a surfer on a wave” [3]. The energy absorption is the greatest at the natural resonances of the plasma and the resonant frequencies of the plasma chamber (i.e. waveguide or antenna chamber) [3].

There are several types of electromagnetic waves used to heat plasma, including radio frequency (RF) waves, microwaves and laser beams [3, 17]. In addition to helicon wave heating, RF wave heating includes ion cyclotron heating (ICH), the excitation of ion cyclotron waves [3, 17]. The resonant frequencies are 25-100 MHz for ICH [17]. The resonant frequency for helicons typically varies between 5-30 MHz [18]. Because of the much lower rest mass of electrons compared to ions, electron resonant heating frequencies are typically 100-200 GHz, which are in the microwave range of the EM spectrum. Consequently, microwaves are often used for electron cyclotron heating (ECH).

Dispersion relations and dispersion graphs describe how the plasma characteristics affect the way the wave propagates (or disperses) through the plasma. The resonant and cutoff locations may be identified with dispersion relations. Areas of resonances, where the plasma absorbs the applied wave energy, occur as value of the wave vector, k, goes to infinity. Areas of cutoffs, where the wave cannot propagate, occur as k goes to zero [3]. Figure 1.2, provided in Appendix E, graphs the dispersion relations for common EM waves that propagate parallel to the magnetic field, with the wave frequency, ω, on the y-axis and the wave number, k, on the x-axis [3]. Helicon waves are specialized whistler waves and share the same resonance region. The speed of light, c, is depicted with a black dotted line. The electron and ion cyclotron wave resonances (ECR and ICR, respectively) are represented by the solid black lines, occurring at the electron and ion cyclotron frequencies, respectively. The whistler wave resonance range occurs between the ICR and ECR.

1.4.2 Helicon

Helicon waves are low-frequency whistler waves, which propagate in magnetized plasmas and are bounded within a cylinder [19, 18]. Whistler waves are low frequency ($v_{ph} < c$) magnetically (right) circularly polarized electromagnetic waves propagating parallel to the magnetic (B-) field. Polarization refers to the direction the electric field vector rotates in time as viewed from the B-field; a right-hand (RH) polarized wave rotates to the right (clockwise) and the left-hand (LH) wave to the left (counter-clockwise) [i.e. 20].

The helicon resonance frequency range is between the ion cyclotron and electron cyclotron frequencies [19, 21].[13] When a helicon is RH polarized, it is considered to have an azimuthal mode, m, equal to +1. When it is LH polarized, it is considered to have a mode equal to -1 [22]. When a wave is plane-polarized, it is considered to have a mode equal to zero, for which the electric (E) field changes from pure electromagnetic to pure electrostatic along the axial (z) direction [18].

The term 'helicon' is generally used to refer to a plasma-generating device designed to launch helicon waves as its plasma heating mechanism [i.e. 10]. The helicon device is often composed for a solenoid magnet, dielectric gas tube, an antenna[14], a gas feed system and a vacuum pumping system [28]. The gas tube is usually cylindrically shaped and often composed of quartz [i.e. 30, 28].

The helicon antenna wraps around the tube and is connected to an external RF power supply. When the RF power is applied, the RF current oscillates back and forth along the antenna, inducing the helicon wave that propagates into the plasma [3]. The gas tube and antenna are centered within the hollow of the solenoid magnet [21]. The entire set up is enclosed within a vacuum chamber, which is held at low pressures (~10^{-7} Torr), by the vacuum pumping system.[15] The gas to be ionized into plasma is supplied into the quartz tube by the gas feed-through system [21, 24]. The overall system will also include ports for installed diagnostics, such as Langmuir probes (LP) or interferometers, to monitor the system conditions [21]. Figure 1.3 depicts the helicon system installed on Proto-MPEX, as well as a schematic of a right-handed helicon antenna [18].

1.4.3 Ion cyclotron heating (ICH)

Ion cyclotron heating is the excitation of ion cyclotron waves [17, 3]. Ion cyclotron waves are low frequency electromagnetic waves whose resonances are equal to the ion cyclotron frequency, which is determined using equation 1.3.

$$\omega_{ci} = \frac{qB}{m_i} \tag{1.3}$$

ω_{ci} is the ion cyclotron frequency [rad/s], q is the ionic charge [C], B is the magnetic field strength [T], and m_i is the ion mass [kg] [3]. The resonance frequency varies directly with magnetic field and therefore is dependent on the machine operating conditions. The ICH resonance frequencies are on the order of tens of MHz [17].[16]

---

[13] The cyclotron frequency is the frequency at which the electrons and ions circle around magnetic field lines, defined as $\omega_c = \frac{qB}{m}$, where ω_c is the cyclotron frequency (rad/s), q is the particle charge (C), B is the magnetic field strength (T), and m is the particle mass (kg) [3, 20].

[14] In comparison, wave heating for EM waves with shorter wavelengths (higher frequencies), such as ECH, can be achieved using a waveguide. A waveguide is a long nonconductive cavity with conducting walls [17].

[15] For some system designs, like Proto-MPEX, the helicon antenna is located outside of the vacuum system to avoid sputtering from the copper in the antenna [23].

[16] The lowest resonance frequency to date [25].

The ICH power system is very similar to that of the helicon power system, consisting of the same components. The primary difference is that the antenna is designed to excite ion cyclotron waves, rather than helicon waves. Similar to a helicon antenna, when RF power is applied, the RF current oscillates back and forth along the antenna, inducing the ion cyclotron wave that propagates into the plasma [3].

Figure 1.4 provides a picture of the installed ICH antenna of Proto-MPEX. The gray boxes are the magnetic coils. The quartz tube is boxed in white. The antenna strap, which wraps around the quartz tube, is gold. The plasma path is shown in red.

1.4.4 Electron cyclotron heating (ECH)

Electron cyclotron heating is the excitation of electron cyclotron waves [3, 17]. Electron cyclotron waves are high frequency electromagnetic waves whose resonances are equal to the electron cyclotron frequency, which is determined using equation 1.4:

$$\omega_{ce} = \frac{qB}{m_e} \tag{1.4}$$

where ω_{ce} is the electron cyclotron frequency [rad/s], q is the electronic charge [C], B is the magnetic field strength [T], and m_e is the electron mass [kg] [3]. Like the ion cyclotron resonance frequency, the electron resonance frequency varies directly with magnetic field and therefore dependent on the machine operating conditions. The ECH resonance frequencies are on the order of tens to hundreds of GHz [3]. This high frequency means that only electrons can be excited by electron cyclotron waves, which reduces the overall heating efficiency of ECH [25]. However, ion heating can occur through electron-ion collisions [25]. ECH can excite ordinary (O) and extraordinary (X) wave modes, both of which propagate perpendicularly to the magnetic field. For O-mode waves, the electric field is parallel to the magnetic field. For X-mode waves, the electric field is perpendicular to the magnetic field [20].

In a high-density plasma[17], O-mode and X-mode waves do not propagate sufficiently into the plasma [3]. For these plasmas, a special type of electron cyclotron waves, called electron Bernstein waves (EBW), are employed. EBW are short wavelength, perpendicularly propagating, electrostatic waves in magnetized hot plasma [26, 27]. They do not have a density cutoff in the plasma [27]. However, EBWs cannot propagate in vacuum. O-mode or X-mode waves must be launched that mode couple to EBW [27].

The launcher for ECH is a waveguide rather than an antenna. A waveguide is a long non-conducting cavity with conducting walls [17]. Similar to an antenna, a waveguide can carry different modes and its dimensions are critical to the successful propagation of the wave [17]. In order to propagate, the wave must have a net transverse magnetic field in the middle of the waveguide that also bends to become axial along the waveguide sides. This is achieved when two plane waves with the same frequency and amplitude travel in a zigzag pattern by reflecting on the walls such that the two waves intersect precisely one wavelength in the width of the waveguide [17]. Therefore, the

[17] Which is the plasma mode used on Proto-MPEX.

width and length of waveguide must be specifically designed to successful wave propagation. A vacuum window separates the launcher from the plasma chamber. The windows are made from materials with high thermal conductivity, such as sapphire or diamond [3]. Figure 1.5 depicts the two plane waves within the waveguide creating a net horizontally propagating wave [17]. The width of the waveguide is ‘b’, the wavelength of the two waves is λ, and the angle between the zigzag path of the wave and the horizontal propagation is α [17].

Figure 1.6 provides a picture of the 28 GHz extended waveguide, tilted at a 25-degree angle in the central chamber of the Proto-MPEX machine [28]. An 18 GHz waveguide enters the far wall of the chamber. The radially launched microwaves are reflected into the axial direction by a flat plate, which can be seen in the background, highlighted by the white circle and arrow.

1.5. Summary

The successful development of future nuclear fusion reactors is important to developing a new clean baseload power source. Unlike other energy sources, fusion can achieve a net energy gain without the risk of reactor meltdown or long-lived radioactive waste. Tokamaks are the leading reactor design. Linear plasma devices are crucial to nuclear fusion reactor research, providing critical PMI studies. The main plasma heating technique applied in linear devices is EM wave heating, which encompasses helicon heating, ECH, and ICH.

CHAPTER 2: PROTO-MPEX

Understanding PMI on machine components is critical to the successful development of future fusion reactors. Linear devices can simulate and exceed the extreme conditions that will be experienced by plasma facing materials, allowing the long-term effects on material components to be observed in shorter periods of time.

The Prototype Material Plasma Exposure eXperiment (Proto-MPEX [29]) at Oak Ridge National Laboratory (ORNL) is a linear plasma device with the primary purpose of developing the plasma source concept for the Material Plasma Exposure eXperiment (MPEX [30]), which will address PMI science for future fusion reactors [31, 32]. Proto-MPEX is one of the world's highest surface flux linear plasma devices[18], having produced heat fluxes over 12 MW/m^2 to material surfaces [33]. Figure 2.1 provides a diagram of Proto-MPEX. For the purposes of this document, the machine is divided into upstream and downstream regions by the helicon power source, per figure 2.1.

2.1. Proto-MPEX Machine Components

The Proto-MPEX machine is composed of a vacuum vessel approximately 4.5 meters in length. The inner radius of the machine varies along its length. The minimum radius is approximately 4 cm, while the maximum radius surpasses 20 cm[19]. Generated plasma is contained using a set of twelve solenoid magnetic coils, which are numbered from 1-12, left to right.[20] The magnetic coils have a 21.7 cm diameter, with 40 turns of water-cooled copper conductor contained within a stainless steel or aluminum housing [34]. Each coil can achieve 9000 A, corresponding to a maximum magnetic field of 2.0 T along the machine. Figure 2.2 depicts the variation in magnetic field flux lines and on-axis magnetic field strength along the machine for a typical magnetic configuration. For this configuration, the current on coil 2 is 600 A, the current on coils 3 and 4 ('helicon' coils) is 160 A, coil 5 is off, and the current through the remaining coils (1, 6-12) is 4500 A. The minimum and maximum magnetic field strengths for this configuration are 0.05 T and 0.85 T, respectively. The minimum and maximum radii of the outermost flux lines, depicted by the red line on the top graph, are 1.5 and 10 cm, respectively. The radius of the outermost flux line (OFL) is considered the radius of the plasma within the machine.

Diagnostic ports are located on stainless steel spool pieces connecting the spaces in between magnetic coils.[21] The diagnostic ports and spool pieces are referenced according to the two magnets they connect; for example, diagnostic port "1.5" is the diagnostic port on the spool piece between magnets 1 and 2.

A stainless steel dump tank is located at the upstream end of the machine, providing a small amount of pumping and secondary containment for plasma traveling upstream. The pumping is provided by a 150 l/s turbo pump. A stainless steel ballast tank is

[18] Proto-MPEX experiments have produced heat fluxes over 12 MW/m^2 to material surfaces, interpreted using infrared (IR) thermography.
[19] At the central chamber.
[20] See figure 2.1
[21] Additional information about installed diagnostics is provided in chapter 3.

located at the downstream end of the machine, which primarily serves to provide significant pumping via a 2500 l/s turbo pump [34]. Additional pumping occurs in a stainless steel central chamber (z = 2.25 m), provided by 2800 l/s and 1000 l/s turbo pumps. The machine's base pressure is on the order of 10^{-6} torr [34].

The machine has three gas injection (fueling) locations. They are located in between magnets 1 and 2 (z = 0.6 m), just upstream of the helicon between magnets 2 and 3 (z = 1.0 m), and just downstream of the helicon between magnets 4 and 5 (z = 1.5 m)[22]. The gas may be prefilled or puffed during a plasma pulse. Puffed gas is injected via a Veeco instruments model PV-10 piezo-electric valve (at z = 0.6 m) and by MKS Instruments model 246 mass flow controllers (at z = 1.0 and 1.5 m). The max gas fueling rate is 10 standard liters per minute (SLM), while operations usually range from 5.9-7.9 SLM. Deuterium is the primary gas type for machine operations. Additional gas types include helium and argon. Plasma pulses range between 0.2 – 2.0 s, with 0.5 – 1.0 s pulses being typical for operations.

End plates are installed on either end of the machine. The 'dump' end plate is located at the upstream end of the machine, within the dump tank. The 'target' end plate is located at the downstream end of the machine, towards the ballast tank.[23] A skimmer plate is installed to constrain the plasma circumference and restrict the neutral gas traveling downstream. A RF baffle plate is installed to prevent plasma from impinging on the ICH antenna and to restrict neutral gas flowing downstream towards the target plate [35]. The skimmer and RF baffle plates are composed of 304 stainless steel and are 0.125 inches thick. The skimmer plate has an inner diameter of 5.8 inches. The RF baffle plate has an inner diameter of 8.6 inches [34].

Additional information regarding the components of the Proto-MPEX machine is provided in previously published work [34].

2.2. Proto-MPEX Power Sources

Proto-MPEX has four installed power sources[24]: (1) a helicon antenna; (2) an electron cyclotron heating (ECH) launcher; (3) an ion cyclotron heating (ICH) antenna; and (4) pre-ionization heating.[25]

The helicon system installed on Proto-MPEX[26] consists of an aluminum nitride (AlN) vacuum window and a right-handed copper helicon antenna. Fluoroptic probes (FPs) are installed under the antenna such that they are in thermal contact with the AlN window.[27] The AlN window is 30 cm long with a 13.8 cm diameter. The helicon antenna is 25 cm long and 15 cm in diameter. It operates at 13.56 MHz and provides up to 125

[22] This fueling location is shown in figure 2.1.
[23] Additional information regarding the end plates is provided in chapter 3.
[24] More detailed specifications of the power sources are described in previously presented and published documents [i.e. 34].
[25] The pre-ionization source is no longer applied during standard experimental operations.
[26] In between magnetic coils three and four (see figures 2.1 and 2.2).
[27] See section 3.3, **Fluoroptic Probes**.

kW of forward power [i.e. 36]. For standard operations, approximately 100 kW of forward power are applied.

The ICH source on Proto-MPEX is located downstream of the central chamber, at an approximate axial location of z = 2.75 m, where the magnetic field strength is at a maximum [37].[28] The ICH antenna is a 25 cm long double-helix half-turn antenna. It has an inner diameter of 9 cm. The overall antenna design is very similar to that of the helicon antenna, except the ICH antenna twists in the opposite direction [37].[29] Unlike Proto-MPEX's helicon antenna, the ICH antenna is in-vacuum, wrapping around a cylindrical quartz tube with an 85 mm outer diameter, an 80 mm inner diameter, and a length of 25 cm [38]. The ICH antenna couples power to plasma ions with a "single pass damping of the slow wave at the fundamental resonance" [37]. The antenna operates between 6-9 MHz [39]. The ICH source is currently designed to supply 30 kW of power, with the potential to be upgraded to 200 kW in the future [37]. Standard ICH pulse lengths range from 0.5 seconds at about 15-25 kW.

The full ECH system currently installed on Proto-MPEX has two different ECH power sources[30], with a third to be installed during the Proto-MPEX upgrade[31]. Two are located at the central chamber. [32] The third will be located at the cavity on spool piece 8.5. The first power source is an 18 GHz system designed to provide pre-ionization heating to 'prime' the helicon source.[33] The 18 GHz of pre-ionization heating provides approximately 5 kW of power, supplied by a Varian model VGA-934 klystron [34]. This system is only occasionally used for operations. A rectangular waveguide approximately 1.5 meters length converts to a circular convertor and tapers to an aluminum oxide window with a diameter of 63 mm and a thickness of 2.8 mm [34]. A reflector directs the launched waves upstream towards the helicon region [34]. The second power source is a 28 GHz system designed to launch O-mode waves or X-mode waves, which couple to EBWs. The 28 GHz system can provide up to 200 kW of power, supplied by a Varian model VGA-8000 gyrotron [i.e. 36, 34]. Standard ECH pulse lengths are 0.1-0.3 seconds at about 15-20 kW.[34] The waveguide is 3.2 meters long, with an 88.9 mm diameter, and is followed by two miter bends [34]. The inner surface of the waveguide is corrugated with 1.3 mm deep groves spaced equally every 1.4 mm [38]. The waveguide connects to the central chamber via a corrugated taper that intersects with a vacuum window. The vacuum window is composed of aluminum oxide. It is edge-water cooled and has a diameter of 63.5 mm [38].[35] Another length of 63.5 mm corrugated waveguide

[28] See figures 2.1 and 2.2.
[29] In this sense, it is a 'left-handed' antenna.
[30] For the purposes of this paper, 'microwaves' is used interchangeable with 'electron cyclotron waves' or 'ECH'.
[31] See section 2.4, **Proto-MPEX Upgrade and MPEX**
[32] See figure 2.1.
[33] That is, it provides a 'seed' plasma before the helicon begins ionizing supplied fuel gas [i.e. 34]. This power source is no longer used often.
[34] The voltage-to-power conversion factor for ECH is currently under review. The true launched power could be up to a factor of four greater than previously assumed. For the purposes of this thesis, the original power conversion factor is applied.
[35] Additional information regarding the ECH system has been produced previously [i.e. 28].

and miter bend with a waveguide extension directs launched microwaves in the central chamber [34]. The extension can be rotated to change the launch angle for improved O/X-mode-EBW coupling [34]. The third power source is a 104.9 GHz system. It is the newest ECH system, intended to help reduce electron trapping [40]. The 104.9 GHz system was reconfigured from a 140 GHz gyrotron, originally rated for 400 kW. However, conversion efficiencies and reconfiguring will likely limit the output power to 200 kW. Like the 28 GHz system, the 104.9 GHz system supplies power via a Varian model[36] gyrotron [41].

2.3. Proto-MPEX Operations

Proto-MPEX generates a linear column of charged particles[37] that are heated to fusion research temperatures. During operations, the plasma[38] originates in the helicon region and is preferentially launched towards the target plate, although plasma also travels upstream towards the dump plate. Additional power from ICH and ECH can be applied. During PMI experiments, a test material sample is mounted on the target plate. The sample is blasted with the incoming particles and resulting material impact can be analyzed [i.e. 13].

Proto-MPEX operations are determined during weekly group meetings on Monday morning. The group establishes what changes, if any, need to be made to the machine,[39] what days operators are available to run the machine, and what experiments should be performed during those run days. Experiments are chosen based on importance, the availability of experimentalists and diagnostics, and required machine time. Secondary experiments often 'piggy-back' off the primary experiments to maximize effective machine use. Once an experiment is selected, a shot plan is created by the lead experimentalist. The shot plan includes desired diagnostics and machine operating parameters, such as magnetic field configuration, gas puffing rates, injected power, and types of power sources.

Depending on the goals of a particular experiment, a variety of diagnostics, power sources, and machine operating parameters are applied.[40] The graduate students and scientists who are the diagnostic leads run the required diagnostics. The time between plasma pulses is ultimately determined by the temperature sensitive machine components, such as the helicon window and magnets, to ensure enough time is allotted for these components to maintain safe operating temperatures. The standard time between pulses is between 2-4 minutes. Additional time is required between pulses for longer pulse lengths and higher injected power. If diagnostics need to be adjusted in between plasma shots, such as moving a Langmuir probe further into the plasma, the time between plasma pulses can increase as well. The average number of plasma shots on a successful operating day is about 100 shots, depending on the number of

[36] Now Communications & Power Industries (CPI).
[37] Proto-MPEX has experimented with multiple ionized gases, including argon, helium, and deuterium plasmas.
[38] Primed by the pre-ionization heating source
[39] Such as installing a new diagnostic.
[40] See chapter 3, **DIAGNOSTICS**, for additional information on the diagnostic suite.

experiments scheduled. The data acquired through the experiments are analyzed by the relevant personnel and the results are presented at the next Proto-MPEX group meeting.

2.4. Proto-MPEX Upgrade and MPEX

As previously stated, the primary purpose of Proto-MPEX is do develop the power source concept for MPEX. To better achieve this goal, the Proto-MPEX machine was shutdown for a machine upgrade from May – August 2018 in order to accommodate the addition of the 104.9 GHz ECH system for improved ECH target heating. For the purposes of this thesis, the machine configuration is assumed to be the pre-shutdown configuration, unless otherwise stated.[41] During this shutdown, the ballast tank was removed. To continue providing sufficient pumping, two turbo pumps were attached to the machine 'cross', a large spool piece installed in between magnet 12 and the ballast tank.[42] A thirteenth magnetic coil was installed in between the previous magnet coils 7 and 8. To accommodate the additional coil, the spool piece lengths between the coils were reduced. Due to the decreased space between coils, diagnostic acquisition capabilities were removed from spool piece 9.5. Therefore, the setup for IR imaging of the front-side of the target plate was modified for installation at spool 12.5 from its previous location at 9.5.[43] New data acquisition capabilities were added at 8.5 and 12.5, yielding four spool pieces available for diagnostic acquistion downstream of the central chamber.[44] To provide further diagnostic access, spool piece 12.5 was constructed with sixteen diagnostic ports rather than the standard four. The ICH system was also modified. The quartz window was replaced with an AD-998 aluminum oxide window. The new window is 15 inches long, with 2.88'' and 3.25'' inner and outer diameters, respectively. The antenna is outside of vacuum and the window is a vacuum boundary.

Additional changes are planned for future installation as well. The most important change relating to MPEX and future PMI studies is the Material Analysis and Particle Probe (MAPP) system. The MAPP system is a proof-of-concept design for the in-situ material analysis system planned for MPEX, as described in later paragraphs. The MAPP system consists of a target plate with e-beam heating and an embedded thermocouple. The plate holds sample materials. The e-beam can heat the plate up to 1000°C at steady-state and up to 1200°C for two hours. The target is attached to a linear driver that can move the target plate from the Proto-MPEX vessel into a connecting chamber for analysis without breaking vacuum. The MAPP chamber has several installed diagnostics, including x-ray photoelectric spectroscopy (XPS) and Raman spectroscopy. Once in the MAPP chamber, the chamber is sealed off from the main Proto-MPEX vessel and pumps down to Ultra-High Vacuum (UVH) for analysis. First operations using the MAPP system are tentatively planned for January 2019. Figure 2.3 provides a prelimary schematic of the MAPP system installed in the upgraded version of Proto-MPEX from a bird's eye view.

[41] The majority of the data relevant to this thesis was acquired prior to the Proto-MPEX upgrade.
[42] See figure 2.1.
[43] See chapter 3, **DIAGNOSTICS**, for additional information on the pre-shutdown setup.
[44] Spool pieces 8.5, 10.5, 11.5, 12.5.

The Fusion & Materials for Nuclear Systems Divison (FMNSD) at ORNL, which manages the Proto-MPEX and MPEX projects, achieved Critical Decision (CD)-0 for MPEX in March 2018. CD-0 indicates the Department of Energy (DOE) considers there to be a need for the PMI science that the MPEX project is designed to provide that cannot be met through other material means [42].[45] The MPEX team plans to achieve CD-1 during fiscal year (FY) 2019. CD-1 indicates that the PMI science, which has demonstrated need via CD-0, will be provided the most effectively by the MPEX device.

Until the MPEX team achieves CD-3, the design of the MPEX device will not be finalized. However, the operating capabilities of the machine have been established. The MPEX machine will operate in steady-state, maintaining plasma for hours or days rather than seconds. Materials, including neutron-irradiated samples, will be exposed to tokamak divertor relavant fluxes and temperatures [43]. The design will include the capability to analyze materials after plasma exposure in vacuum. End-of-life studies of tungsten as a plasma-facing component will be performed for the first time [43]. The MPEX machine will have NbTi superconducting magnetic coils. The RF helicon power system include a liquid-cooled helicon antenna and will provide up to 200 kW of power. The ICH power source will be upgraded to 200-400 kW of installed capacity. The total installed power capacity of MPEX will be up to 800 kW [43]. Plasma conditions at the power source will include electron and ion temperatures of 25 eV, and electron densities of 6×10^{19} m^{-3}. At the target, plasma conditions will include ion temperatures of 20 eV, electron temperatures of 15 eV, electron densities of 10^{21} m^{-3}, and ion particle fluxes of 10^{24} $m^{-2}s^{-1}$ [43].

Additional information regarding the MPEX machine is provided in previously published work [43]. Figure 2.4 provides a schematic of a pre-conceptual design of MPEX [43].

2.5. Summary

Proto-MPEX at ORNL is a linear plasma device with the primary purpose of developing the plasma source concept for the MPEX, which will address plasma material interaction (PMI) science for future fusion reactors. The machine is approximately 4.5 m in length with a varying inner diameter. Twelve magnetic coils serve to confine the generated plasma and can yield a magnetic field of up to 2 T. Proto-MPEX has three main installed power sources[46]: (1) a 13.56 MHz helicon antenna; (2) a 28 GHz electron cyclotron heating (ECH) launcher; and (3) a 6-9 MHz ion cyclotron heating (ICH) antenna. Proto-MPEX experimental operations are determined and performed by research scientists and graduate students. The Proto-MPEX machine was shutdown for a machine upgrade from May – August 2018 in order to accommodate the addition of the 104.9 GHz ECH system for improved ECH target heating. FMNSD at ORNL achieved Critical Decision (CD)-0 for MPEX in March 2018. The MPEX team plans to achieve CD-1 during fiscal year (FY) 2019.

[45] At this point, the PMI science could be provided by another device.
[46] More detailed specifications of the power sources are described in previously presented and published documents [i.e. 34].

CHAPTER 3: DIAGNOSTICS

An extensive diagnostic suite is installed on Proto-MPEX. The diagnostics provide a variety of different plasma measurements and are installed along the length of the machine, with the majority of them concentrated downstream of the helicon. The suite includes ex-vessel and in-vessel diagnostics, which may be passive or active, as well as perturbative or nonperturbative.

A team of research scientists and graduate students share the responsibilities for the diagnostic suite.[47] Table 3.1 lists the diagnostics included in the suite, the relevant measurements the diagnostics provide, the individual(s) in charge of each diagnostic, and diagnostics' locations on the machine. Due to limited availability of diagnostic ports, not all the diagnostics are installed on the machine at the same time. The axial locations provided in table 3.1 list the most common installation location(s) for the diagnostic, when installed.[48]

The subsections below provide additional descriptions of the diagnostics implemented to perform the power balance, including the plasma parameter measurements acquired, their specifications, and their locations on the machine.

3.1. Infrared (IR) Cameras

The infrared cameras are critical diagnostics. The IR cameras measure the change in surface temperature of the end plates over the duration of the plasma shot.[49] The cameras additionally provide 2D thermal load distribution images of the end plates, highlighting plasma patterns like hot spots [44]. Three different IR cameras are available for use during operations. The first is a FLIR A655sc IR camera, whose parameters are described in detail in a previously published article [44]. The camera is wrapped in mu-metal to mitigate effects of the magnetic field on the camera's electronics. The A655sc camera is typically mounted horizontally at the diagnostic port between magnetic coils 9 & 10. It views the front side of the installed target plate via a periscope[50]. Additional installation locations include behind the target plate, imaging the non-plasma facing side of the plate with an in-vessel angled mirror [51] and behind the dump plate, imaging the non-plasma facing side of the dump plate.[52] The primary IR installation location depends on the installed target plate system.[53] When installed behind the target plate, due to the camera's proximity to magnetic coil 12, a soft-iron shield box is installed around the IR camera to protect the camera's electronics from the effects of the

[47] Responsibilities include maintenance, upgrades, data acquisition and data analysis.
[48] Table 3.1 and all subsequent tables in this thesis are provided in Appendix D, with the exception of the tables provided in Appendices B and C.
[49] The change in temperature (ΔT) is used to infer heat fluxes to the end plates.
[50] See subsection 3.1.5, **Periscope**, below.
[51] At approximate axial location of z ~ 4.25 m (see figure 2.1)
[52] The installation location is off the z-axis provided for the machine (see figure 2.1), but could be approximated as z ~ - 0.5 m,
[53] See subsection 3.1.4, **Installed End Plates**, below.

magnetic field.[54] The camera receives an external trigger to begin recording approximately 0.25 seconds prior to the plasma pulse. The camera records for 3-4 seconds in total, depending on the experiment. When viewing the front side of the target plate, the A655sc camera's window size is reduced from 640x480 pixels to 640x240 pixels in order to double the available frame rate from 50 Hz to 100 Hz.

The second camera is a FLIR SC4000 IR camera. This camera was inherited from Sandia National Laboratories (SNL). It has two main installation locations: horizontally behind the dump plate or horizontally at the periscope port. The SC4000 detector is a cooled indium antimonide (InSb) photoconductive detector. The camera has a spectral range of 3 – 5 microns, a detector pitch of 30 microns, and a resolution of 320 x 256 pixels [45]. The camera has two different lenses available. One has a focal length of 25 mm and a 22.0°x17.5° field of view. The second has a focal length of 50 mm and an 11.0°x8.8° field of view [45]. The camera has five temperature range settings: -10-55°C, 10-90°C, 50-150°C, 80-200°C, and 150-350°C.[55] The camera is additionally equipped with a removable neutral density (ND) filter[56], which reduces the overall intensity of light prior to it entering the IR camera lens and prevents the detector from saturating. The ND filter enables the SC4000 to image very hot temperatures, up to 1500°C. With the ND filter inserted, four additional temperature range settings are available: 150-450°C, 250-600°C, 500-1200°C, and 700-1500°C. The maximum frame rate depends on the temperature range and the window size. At the lowest temperature range setting (-10 - 55°C), the max frame rate is 298 Hz. At the highest temperature range setting (700-1500°C), the max frame rate is 432 Hz. These maximum frame rates are assuming a full window size (320 x 256). At the minimum window size (64 x 4), the camera can sample at a frame rate of 43,103 Hz. For standard operations, the -10-55°C temperature range is used with a frame rate between 50-100 Hz. Similar to the A655sc IR camera, the SC4000 is connected to the computer through a Gigabit Ethernet cable. It receives the same trigger as the A655sc camera at 0.5 second prior to the plasma pulse and also records for about 4 seconds. Unlike the A655sc camera, the SC4000 camera triggering is not fully automatic. Its record button must be enabled prior to each shot to be primed for the upcoming trigger.[57]

The third IR camera is a FLIR T250 series. This IR camera's detector is an uncooled bolometer. It has a spectral range of 7.5 – 13 μm, and a resolution of 240 x 180 pixels. The camera has a full window frame rate of 9 Hz and a maximum frame rate of 30 Hz (for a minimum window of 640 x 120). The camera has two temperature range settings: -20-120°C and 0-350°C, with an accuracy of ±2°C or ±2% of the reading [47]. The IR camera is primary used to monitor the helicon window surface temperature and corroborate fluoroptic probe measurements.[58]

---

[54] Without the soft iron shield, the camera attempts to auto-correct its focus when the magnetic coils turn on, corrupting the acquired data.

[55] The temperature range settings are programmable. These settings were created by its previous research team at SNL.

[56] The filter is a type ND2, which will reduce the light entering the lens by approximately a factor of two (i.e. 50% transmission) [46].

[57] For this reason, this camera is seldom used.

[58] See section 3.3, **Fluoroptic Probes**, in this chapter.

Figure 3.1 provides images of all three FLIR IR cameras [48, 47].

3.1.1 Camera Calibrations

The SC4000 IR camera currently operates using the calibrations from the SNL research team who previously owned the camera. The A655sc camera came directly from FLIR and uses the company's calibration. Periodically, the calibration of the camera must be rechecked. The recalibration process is performed using an Infrared Systems Development Corporation (IRDC) blackbody calibration system.[59] The system is composed of a model IR-564 Blackbody Radiation Source and a model 301 Digital Temperature Controller [49]. The blackbody source has three main components; the cavity, the resistive-heating element, and the dual thermocouples. The cavity is a "20° Recessed Conical design, manufactured from special stainless steel and processed to have a uniform, high emissivity coating" [49]. The cavity is rated with an emissivity of >0.99. The resistive-heating element is powered and controlled by the 301 Digital Temperature Controller. The dual thermocouples are Type S[60] and serve to cross calibrate the temperatures of the cavity and the controller. The blackbody source has a temperature range of 50 – 1200°C, a resolution of 0.1°C, and an accuracy of ± 0.2°C [49]. There are eight aperture sizes on the source for viewing into the cavity, ranging from 0.0125 to 1.0 inches.[61] The controller is a specially designed microprocessor based PID[62] system that regulates the blackbody source, providing capabilities such as setting the blackbody source temperature and setting deviation alarms, which sound if the temperature of the blackbody source deviates from its set temperature more than a specified amount [49]. The controller has a resolution of 0.1°C. Figure 3.2 provides images of the blackbody source and the controller [50].

The calibration process is performed through the ResearchIR software. The software program provides multiple levels of complexity in the calibration process, with each successive level increasing user control [45].[63] During the calibration process, the IR camera images the cavity inside the blackbody source, which has the known emissivity of >0.99. A successful calibration requires multiple calibration points. Calibration points have two components; (1) the blackbody temperature, and (2) the IR images of the inside of the blackbody at that temperature [i.e. 45].[64] Each calibration point is recorded in the ResearchIR software. From each point, the software creates a series of graphs[65] that provide the relations between pixel counts, radiance, and temperature. Those relations are saved in the ResearchIR software for future data acquisition and analysis, concluding the calibration process.

3.1.2 Quantifying Emissivity

In order to accurately measure changes in the temperatures of the end plates, the

[59] The calibration system was inherited from SNL.
[60] Platinum/Platinum 10% Rhodium, 0.01% error [49].
[61] The full list includes 0.0125, 0.025, 0.05, 0.1, 0.2, 0.4, 0.6, and 1.0 inches [49].
[62] PID: Proportional, Integral and Derivative [49].
[63] The exact calibration process varies between the two IR cameras.
[64] Recall the controller is used to set the blackbody source to specific temperatures [i.e. 49].
[65] Selected by the user.

emissivity of the end plates must be accurate. The dump plate is not easily removed from the machine, so both FLIR cameras are usually calibrated for the dump plate emissivity *in situ* only.[66] The target plate is more easily removed from the machine, so the A655sc camera is calibrated for the emissivity of the target plate both *in situ* and *ex situ*. The *ex situ* calibration is performed via bench testing, as described in a previously published article [44]. The *in situ* calibrations are performed throughout the day during plasma operations. For the *in situ* calibration, the IR camera measurements are compared against the TCs installed on their respective end plates.

3.1.3 Spatial Calibration

The acquired IR camera images are composed of pixels. For example, at full window size, the A655sc camera's images are 640 pixels x 480 pixels. In order to quantify the IR images in terms of length, the number of pixels per unit length must be established. For IR analysis, a pixel per centimeter ('pixel-to-cm') conversion is applied. To determine the number of pixels per centimeter, the end plate must have a fiducial with known dimensions. The type of fiducial depends on the end plate design. End plate fiducials have been etched grids or triangles, as well as washers or drilled holes a known distance apart. The known fiducial distance is measured in pixels using the IR camera and divided by the known distance in centimeters. Each time the distance between the IR camera and the end plate changes[67], the conversion must be recalculated. To improve the accuracy of the pixel-to-cm measurement, the number of pixels in the known fiducial length is measured across multiple IR acquired images using a MATLAB code. The pixel-to-cm measurements from each IR image are averaged together to establish a final pixel-to-cm conversion.

3.1.4 Installed End Plates

Multiple different target plates and two different dump plates have been designed and installed in Proto-MPEX, depending on the goal of the experiment. Table 3.2 provides a summary of the different end plates including the approximate dates and plasma shot number ranges for which they were installed in the machine.

Dump plates

The dump plate is located upstream of the first magnetic coil.[68] The current dump plate is a 304 stainless steel plate that is 0.015 inches thick. It has been water-blasted[69] to raise the emissivity to approximately 0.23. Two TCs are installed on the non-plasma facing side of the dump plate, held in good thermal contact with the plate with a screw, nut and washer. The TCs are within the field of view of the camera, allowing for cross-calibration with the IR camera temperature measurements. The TCs also help with camera focusing and provide a pixel-to-cm conversion, so the plasma diameter can be determined. The previous dump plate was also 304 stainless steel. It was 0.06 inches thick and bead-blasted to raise the emissivity to approximately 0.6. Like the new dump

[66] The dump plate is calibrated *ex situ* prior to installation.
[67] For example, if the target plate moves or a new plate is installed (see subsection '**Installed End Plates'**).
[68] Corresponding to approximate axial location z~0.25 m (see figure 2.1)
[69] The plate is too thin for bead-blasting, which is the standard procedure.

plate, the previous plate had two installed thermocouples to help with cross-calibration with the IR camera measurements. However, these thermocouples were just outside the field of view of the camera, so the comparisons were potentially inaccurate. A grid-line pattern composed of one cm and two cm squares to provide focusing and a pixel-to-cm conversion. The dump plate was redesigned to be thinner in order to improve heat transfer through the back of the plate for IR thermographic analysis. Both iterations of the plate have been 15.75 inches in diameter. Figure 3.3 provides images of the old and new dump plates.

The target plate designs have varied in level of complexity. The materials, thicknesses, emissivities, installed diagnostics, and mounts have altered with each iteration. The one constant property has been the diameter of the plates, which remained fixed at 4.5 inches.

Thick stainless steel plate

The thick stainless steel plate is 0.06'' thick. Like the thin SS plate, it is composed of 304 stainless steel. This plate was the first target plate design for Proto-MPEX that was imaged by IR cameras. Like the thin SS plate, the thick SS plate design was employed for multiple target plates. The plates were bead-blasted to raise the emissivities, which ranged from 0.23 – 0.33. The IR camera viewed the target plate from the non-plasma facing side. Fiducials were etched into the plate for IR camera focusing and pixel-to-cm conversions. The fiducials were either a grid pattern of 1cm squares or a triangle with 1 cm legs. This plate was either installed flush with the upstream plane of magnetic coil 12, supported by four aluminum rods or installed on a single aluminum rod at the diagnostic port between coils 7 & 8 (z = 2.6 m). When installed near coil 12, a TC was installed into the thick side of the plate. No TC was installed for the target plate on the single aluminum rod. Figure 3.4 depicts non-plasma facing side of the thick SS plate on the single aluminum rod (left), as well as the plasma-facing side of the plate installed on the four aluminum rods (right).

Thin stainless steel plate

The thin stainless steel (SS) target plate is composed of 304 SS and is 0.01'' in thickness. This target plate design has been employed for multiple target plates. Like the new thin dump plate, the thin SS plates were water-blasted to raise the emissivity. The emissivities of the thin plates ranged from approximately 0.26 to 0.8, depending on the extent of the surface treatment. While this plate was installed, the IR camera viewed only the non-plasma facing side of the plate. Therefore, the plate was designed to be as thin as possible to improve the thermal and time response of the plasma heat pulse through the plate. This plate is too thin for etching, so the installed thermocouple served as the fiducial to ensure the camera focus and provide a pixel-to-cm conversion. This target plate is installed flush with the leading plane of magnetic coil twelve[70] and supported by four aluminum rods. Figure 3.5 provides images of the non-plasma facing side of the target plate (left) and the plasma facing side of the plate post-plasma exposure (right).

[70] Corresponding to approximate axial location z ~ 3.75 m (see figure 2.1),

Graphite diagnostic plate

The graphite diagnostic plate is a 0.25'' thick graphite target plate with four embedded Langmuir probes and an embedded ion flux probe (IFP) that are flush with the plasma-facing side of the target. These diagnostics provided electron temperature and density measurements, as well as ion flux measurements on the target plate. A thermocouple was also installed into the width of the plate, about 0.06'' from the plasma-facing side. Graphite naturally has a high emissivity and therefore did not require surface treatment. The emissivity of this plate was approximately 0.76. The embedded probe heads were used to help focus the IR camera and the distance between the embedded probes was used to create a pixel-to-cm conversion. IR viewing of the rear-side of the target plate is blocked by the support and feedthrough systems for the diagnostics. Therefore, the IR camera viewed the target plate from the front. Figure 3.6 provides images of the graphite plate (left) after a few days of plasma exposure and a preliminary model of the target plate attached to its support structure (right). Discoloration due to plasma impingement on the graphite plate is apparent. On the target plate, five probe heads are visible. The center probe is the IFP. The two above and below the center probe are the LPs.

Self-heating SS plate with moveable mount

This target plate is a self-heating plate on a moveable mount. This plate is composed of 304 stainless steel (SS) and is 0.06'' thick, with a thermocouple installed into the width (thickness) of the plate. A Thermocoax cable sits in a groove 2 millimeters in thickness, with an inner and outer diameter of 3.01 and 3.17 inches. The Thermocoax cable is a resistively heated cable, which can heat the target plate to a uniform temperature[71], providing *in situ* camera calibrations and emissivity mapping of the entire target plate. The cable is held in place with eight equally spaced 4-40 tapped screws and No. 4 washers, plus one additional screw of the same type to direct the cable feed-out. The cable connects to in-vacuum coaxial cables, which in turn connect to a power feed-through next to the diagnostic port for the target thermocouple. Figure 3.7 provides images of the self-heating target plate (left) and its Thermocoax cable (right).

The plate is attached to a moveable mount, which moves the target along the z-axis.[72] The mount, primarily composed of aluminum, consists of a linear drive manipulator that controls two bellows, which in turn move the target plate along the z-axis [51]. The bellows provide a total range of motion of about 9 cm, from approximately 1 cm in front of the diagnostic port at 11.5 (z = 3.4 m, also the location of the Thomson scattering (TS) beam line) to about 8 cm behind the diagnostic port. During operations, the plate's location is referenced with respect to the TS beam line at z = 3.4 m. Upstream and downstream of z = 3.4 m are considered positive and negative, respectively. That is, if the plate is at -3.0 cm, then it is 3 cm downstream (behind) the z = 3.4 m location. The location of the target plate is determined via a calibrated voltage readout from a multi-meter [51]. The nuts holding the Thermocoax cable to the plate and the material sample holes are used to determine the pixel-to-cm conversion and IR camera focusing. It is important to note that the pixel-to-cm conversion must be determined for each target

[71] Corroborated by the plate's embedded thermocouple [44].
[72] In the direction of the length of the machine.

plate location. Figure 3.8 provides a picture of the fully assembled self-heating target plate on the moveable mount. The bellows, target plate, coaxial cables, and thermocouple are depicted.

Silicon carbide plate

The silicon carbide (SiC) target plate was designed specifically for PMI studies. Like the self-heating SS plate, the SiC also contained a Thermocoax cable and was installed on the moveable mount. The plate design had multiple layers and 5 total pieces. The top layer was a 310 stainless steel cover plate that is 4.5'' in diameter with a 2.0'' opening to expose the SiC disk. The SiC disk was 3.0'' in diameter and 0.125'' thick. The SiC disk nested in the stainless steel cover plate. Behind the SiC disk and 310 SS plate was a 1/64'' piece of grafoil. The next layer was composed of two 0.063'' thick 310 SS plates that were grooved to hold the Thermocoax resistively heated cable. The grafoil layer improved heat transfer between the SiC disk and the Thermocoax, which preheated the SiC disk to higher temperatures prior to plasma pulses for improved PMI studies. A TC was installed in the back plate holding the Thermocoax cable to provide temperature feedback for the Thermocoax power supply. The entire assembly was held together by ceramic spacer pieces on the rearmost 0.063'' 310 SS plate[73], which attached to the moveable mount's bellows. Finally, five 5.0'' pieces of 310 SS, each 0.01'' thick, installed on the back to reflect heat away from the bellows and back onto the target plate assembly [52]. Figure 3.9 depicts the installed SiC target plate after a few weeks of plasma exposure. The SiC disk shows appreciable blistering. The extent of material damage and mechanism of damage is being analyzed. The stainless steel cover plate shows discoloration from plasma exposure. Due to the slight misalignment of the target plate with the generated plasma column, the plasma profile was not centered on the SiC disk as intended. Instead, the upper edges of the plasma profile hit the cover plate. The center of the plasma profile is the area of the SiC disk showing the most blistering.

SS plate with inserts

This stainless steel plate has been the installed target plate since operations restarted after the Proto-MPEX upgrade. The plate serves as a 'proof-of-concept' for the future MAPP system and are able to be withdrawn from the machine through a diagnostic port on the new spool piece 12.5. Unlike other end plates, the target plate is rectangular. It is 2.250'' high and 4.5'' long, with a 0.125'' thickness and an octagonal hole (2.125'' x 2.125'') in the center. Four drilled holes in each corner allow material inserts to be secured to the target plate. The plate is attached to a 30'' aluminum rod, which exits the machine via the diagnostic port. The plate has the ability to move in the radial and axial direction, as well as rotate about its axis, providing more flexibility for experiments. Plate inserts include a 0.01'' thin stainless steel insert, a 0.06'' thick stainless steel insert, and a 0.06'' thick stainless steel insert with an array of holes along the edge to improve IR camera analysis. The target plate and its inserts are surface treated to raise their emissivities. Figure 3.10 provides an image of the target plate with the thin SS insert after plasma exposure, as well as the schematic for the 0.06'' SS insert with the gridded holes.

[73] The back 310 SS plate holding the Thermocoax cable.

MAPP target plate

A new target plate is currently being designed as part of the MAPP system.[74] While the design has not been finalized, certain features are desired. The plate must fit through a 4.5'' flange, so it can be a maximum of 2.37'' wide, rather than the standard 4.5''. The plate will be designed to hold material samples, which in turn will be analyzed using the MAPP system. As part of the MAPP system, the target plate is installed on a moveable mount. The mount will be able to completely withdraw the target plate from the main machine vacuum chamber into the MAPP chamber. Within the main machine chamber, the plate will also be able to move approximately 1 cm to the left, right, up or down. The support rod holding the plate will be composed of stainless steel. The plate holding the material samples itself will be composed of tantalum. The material samples will be approximately 15 mm x 18 mm. A e-beam heating element will be embedded in the tantalum plate to provide additional heating to the material samples, similar to the SiC target plate design. Figure 3.11 provides a preliminary concept design of the MAPP target plate installed on the target exchange system.

3.1.5 Periscope

To improve IR temperature measurements and acquisition flexibility, a periscope was designed to allow either the FLIR SC4000 or FLIR A655sc camera to view the front side of the target plate. The periscope has four main components; (1) a cylindrical tube; (2) a mirror base; (3) a window mounting flange and (4) a periscope mounting flange. The periscope was installed at the diagnostic port in between magnetic coils nine and ten (z = 3.1 m). It is held in place by the periscope mounting flange. The IR camera is mounted horizontally, looking through the window mounting flange and the inside of the tube. The mirror base changes the viewing angle to allow the imaging of the front side of the target and can be changed to allow for different installation locations. At the standard location on diagnostic port 9.5, the mirror base is angled at 46 degrees below the horizontal. A 1.5-degree shim is also inserted, for a total angle of 47.5 degrees below the horizontal. Figure 3.12 provides a schematic of the installation setup and viewing lines of the periscope design. The periscope is currently installed at the location labeled 'Option 1'. The relevant viewing lines are red. Figure 3.13 provides a picture of the periscope itself.

Each periscope component is made of stainless steel. The cylindrical tube has a diameter of 1.25 inches and a total length of just over 12 inches. The inner surface of the tube is bead-blasted to raise the emissivity to aid IR camera imaging. The mirror base is a stainless steel piece with a mirror finish, having a height of 0.75 inches and a mirror surface length of approximately one inch. The mirror base is held to the tube with two screws. To accommodate more installation locations, a second mirror base with an angle of 49 degrees below the horizontal, as well as a 1-degree shim are also available.

3.2. Thermocouples (TC)

Thermocouples are installed at seven locations on the Proto-MPEX machine. Four locations are in-vessel: the dump plate, the target plate, the skimmer plate, and the RF

[74] See section 2.4, **Proto-MPEX Upgrade and MPEX.**

baffle plate. Three locations are ex-vessel: spool piece 1.5, spool piece 2.5 and spool piece 4.5. Each thermocouple is a type K stainless steel Omega thermocouple with a temperature range of -200°C - 1250°C and an accuracy of ±2.2°C or 0.75% of the temperature reading [53].

3.2.1 In-vessel TCs

With the exception of the target plate, whose design changes, the dump, skimmer, and RF baffle plates are composed of stainless steel. The thicknesses of the SS plates are 0.015'', 0.125'' and 0.125'', respectively. The TCs installed on the end plates are primarily used to cross-check the IR camera temperature measurements, ensuring the camera is properly focused and calibrated. On the dump plate, the TC is secured to the non-plasma facing side with a screw and a nut. The installation location on the target plate depends on the target plate design. If the plate is at least 0.06'' thick, a small hole is drilled into the side of the plate into which the TC is inserted. If the plate is thinner, the TC is attached to the non-plasma facing side with a screw and a nut, like the dump plate.

The TCs installed on the skimmer and RF baffle plates provide surface temperature measurements along the machine axis and are used to infer power lost from the plasma between the helicon source and the target plate. The skimmer TC is bolted to the downstream[75] side of the skimmer plate, while the RF baffle TC is bolted to the upstream side of the plate.[76] The skimmer and RF baffle plate TCs are installed approximately 1 cm from the plates' inner diameters. Figure 3.14 provides the two plates with the locations of their installed thermocouples depicted.

3.2.2 Ex-vessel TCs

Two thermocouples are installed on each of the three spool pieces listed above (1.5, 2.5, and 4.5), for a total of six ex-vessel TCs. The spool pieces are approximately 0.2 m in length. The spool pieces are composed of stainless steel with a mass of approximately 3.6 kg.[77] The TCs are held in good thermal contact with the spool pieces using zip ties. On spool piece 1.5, the TCs are attached approximately 8 cm from the upstream end and 3 cm from the downstream end.[78] The TCs installed on spool piece 2.5 are attached approximately 8 cm from the upstream end and 1 cm from the downstream end.[79] The TCs installed on spool piece 4.5 are attached approximately 7 cm from the upstream end and 7 cm from the downstream end.[80] The TCs installed on spool pieces 2.5 and 4.5, which are on either side of the helicon, are particularly important to measuring the heat lost to the machine surfaces as the plasma leaves the helicon region and travels towards the end plates. Figure 3.15 depicts the two TC's

[75] Side of plate not facing the plasma.
[76] For the modified flat field configuration implemented for this worked power balance, the plasma circumference is small enough that the RF baffle TC is not at risk of receiving plasma directly to its surface.
[77] This mass includes the mass of their flanges connecting to either diagnostic ports or the next magnet coil.
[78] Closer to the dump plate and helicon, respectively.
[79] Closer to the dump plate and helicon, respectively.
[80] Closer to the helicon and target plate, respectively.

installed on spool 1.5.

3.3. Fluoroptic Probes (FP)

Fluoroptic probes are unique thermometric diagnostics designed by Luxtron[81]. The probe is composed of an optical fiber with a temperature sensitive phosphorescent sensor tip [54]. Immune to electromagnetic field interference, fluoroptic probes are ideal for implementation in high voltage or high radiofrequency (RF) areas.[82] A signal traveling along the fiber excites the sensor tip, causing it to fluoresce. The fluorescence decay time varies with temperature of the sensor tip [54]. Figure 3.16 depicts an example plot used to determine the sensor decay time (τ) [54].

The signal carried on the optical fiber is interpreted by the Fluoroptic thermometry instrument. The instrument has four channels, enabling data collection from four FPs simultaneously during a plasma pulse [54]. The instrument includes a power supply, 0-10 V analog outputs, and an RS-232 serial interface. It has a temperature range of -100°C - 330°C, which an accuracy of 0.5°C [54].

Surface-to-Surface (STS) fluoroptic probes are installed on Proto-MPEX, under the helicon antenna, in thermal contact with the helicon aluminum nitride (AlN) window. The STS FPs have a temperature range of -25°C - 200°C, with a temperature resolution of 0.01°C, an accuracy of ±0.5°C, and a time resolution of 25 ms [54]. Figure 3.17 shows a schematic of the fluoroptic probe diagnostic set up, depicting the probe sensor, the probe tip, the optical fiber, and the thermometry instrument. Figure 3.18 provides a picture of the FPs installed under the Proto-MPEX helicon antenna, as well as the FLIR T250 IR camera view of the helicon window. Two FPs sit under the high voltage end of the antenna and two sit under the low voltage end. A fifth FP is installed on the side of the helicon window, in the field of view of a FLIR T250-series IR camera. Since there are only four available channels, the second FP installed under the high voltage end of the helicon is not currently connected. This camera is used solely to monitor the temperature of the helicon window and cross-corroborate the FP measurements. The changes in temperature measured by the FP sensors are used to measure the helicon power lost to the AlN window, heating it rather than the plasma.

3.4. Langmuir Probes (LP)

Four double LPs are available to provide electron density and electron temperature measurements of the plasma column. These probes can be moved to multiple installation locations depending on available diagnostic ports and planned experiments. The probes may scan vertically or horizontally, depending on the installation location and available diagnostic ports. The probes may either be on motorized drives or manually scanned depending on location as well. For example, probes scan horizontally at diagnostics ports 1.5, 2.5, 4.5, 9.5 and 11.5. They will scan vertically at 10.5. The probe tips are composed of tungsten wire, with a diameter of 0.25 mm and a length of 0.9 mm. The potential difference between the probes is swept over a 2.5 ms period [44].

[81] Luxtron's FP's are now provided by LumaSense Technologies.
[82] Such as under the helicon antenna.

Figure 3.19 provides an image of the probe tip.

3.5. Mach Probes (MP)

A Mach probe is a uni-directional probe used to measure plasma flow. A MP generally consists of two directional electric probe tips separated by an insulator [55]. The plasma flow velocity is determined by the ratio between the ion saturation currents measured by each respective electric probe tip, where one tip measures the upstream ion saturation current[83] and one tip measures the downstream ion saturation current[84] [55]. There are a few different MP designs, with the parallel (or simple) MP being the most commonly used.[85] Equation 3.1 depicts the relation used to determine the Mach number for a parallel MP.

$$\frac{J_U}{J_D} = e^{kM} \tag{3.1}$$

where J_U is the upstream ion saturation current, J_D is the downstream ion saturation current, k is the calibration factor, and M is the Mach number [56]. The ratio is greater than one for directional flow [i.e. 56]. Figure 3.20 provides a schematic of an example parallel MP [55].

The Mach probe created for the Proto-MPEX device, called the 'Double Mach probe,' has a slightly different design, combining the diagnostic capabilities of a MP with those of a LP. The probe head consists of four electric probe tips in a four-bore ceramic head. Two of the bores are used as a one-directional MP and two of the bores are used as a double LP. The wire tips of the Mach probes are about 5 millimeters, while the wire tips of the LPs are about 2 millimeters. The Double Mach probe provides the Mach number, the electron temperature (kT_e) and electron density (n_e) at the plasma scanning location.[86] These plasma measurements can in turn be used to determine axial velocity and the steady-state one-dimensional particle flux [56], applying equations 3.2 – 3.4.

$$u_z = M \cdot c_s \tag{3.2}$$

$$c_s = \sqrt{\left(\frac{kT_e + kT_i}{m_i}\right)} \tag{3.3}$$

$$\frac{\partial n}{\partial t} + \nabla \cdot (n\mathbf{u}) = G \tag{3.4}$$

where u_z is the axial velocity, M is the Mach number, c_s is the plasma sound speed, k is the Boltzmann constant, T_e and T_i are the electron and ion temperatures, respectively,

[83] Ion saturation current that is parallel to the magnetic field [56].
[84] Ion saturation current that is anti-parallel to the magnetic field [56].
[85] Other designs include the rotating probe, the Gundestrup probe, the perpendicular Mach probe, and the visco-Mach probe [56].
[86] The double MP cannot provide all three measurements simultaneously. For a given plasma pulse, it can measure either T_e and n_e or M.

m_i is the ion mass, n is the particle density, and G is the particle generation rate [56].

Two MPs are currently available for installation on the machine. Like the LPs, the MPs may scan vertically or horizontally depending on their installation locations. The MPs provide vital information about the plasma flow speed, which is used to calculate convective heat transfer, as well as the electron temperature and densities, which are used to determine the conductive heat transfer. MP scans at the upstream and downstream edges of the helicon power source additionally provide information regarding the split of the launched helicon plasma; that is, what percent of the plasma travels upstream and what percent travels downstream.

3.6. B-dot Probe

The B-dot[87] probe is used to measure the amplitude and phase of RF wave fields in Proto-MPEX plasma. It most often samples the plasma at the diagnostic port between magnet coils 9 and 10 (z = 3.1 m) or the port between coils 10 and 11 (z = 3.4 m), depending on port availability. A B-dot probe is simple in design, primarily consisting of a conducting coil. Using Faraday's Law[88], the coil can measure a time varying magnetic flux. When a probe with effective coil area A is subjected to a time varying magnetic field, it generates a voltage according to equation 3.5,

$$\mathrm{V} = \omega \mathrm{BA} \tag{3.5}$$

where V is the generated voltage, ω is the operating frequency of the probe, B is the magnetic field, and A is the effective area of the coil. Since the operating frequency and effective area are both known, the time varying magnetic field can be calculated from the voltage induced by the changing magnetic field [57].

The probe installed on Proto-MPEX is more complex in design, consisting of two conducting coils perpendicular to each other in order to measure the magnetic flux in the radial, azimuthal and axial directions of the magnetic field.[89] One coil is in the radial direction and one can be rotated into the azimuthal or axial direction.[90] Figure 3.21 provides a schematic of the B-dot probe installed on Proto-MPEX [57]. Shown at the left are the conducting coil and direction of the magnetic field. A custom design coaxial cable, composed of small diameter ceramic tubing and hypodermic tubing, shields the wires carrying the conducting coil's signal from the magnetic field [57]. The electrical signals are carried outside of vacuum using a 4-pin-to-BNC conflat (CF) flange. To prevent capacitive pickup from the RF field[91], the wires are connected to a 180-degree power splitter/combiner. The resulting electromagnetic signal is then processed such that only the reference signal's amplitude and phase are digitized [57].

[87] 'B-dot' implies the time derivative of magnetic field, B. Also called an 'RF magnetic probe'.
[88] Faraday's Law states that a changing magnetic field produces an electric field.
[89] The probe can only measure the vector component of the magnetic flux that is normal to the conducting coil [57].
[90] In the direction of time-varying magnetic field, B.
[91] Via electrostatic rejection

3.7. Ion Flux Probe (IFP)

The ion flux probe is used to measure the ion fluxes in the generated plasma. The IFP is constructed similar to other probes installed on Proto-MPEX. However, the probe is negatively biased to repel plasma electrons approaching the probe tip, resulting in only ion current being collected. The ion flux is determined using equation 3.6,

$$\Gamma_i = \frac{I_i}{A} \tag{3.6}$$

where Γ_i is the ion flux, I_i is the collected ion current and A is the area of the probe tip. The IFP tip is embedded into a larger insulating surface and is flush with that surface, creating a planar collecting area and removing sheath expansion effects induced by biasing the probe tip [58]. The planar collecting area is at a 45-degree angle from the probe shaft. The probe tip consists of two wires with elliptically-shaped cross sections. The minor diameter is 1.2 mm and the major diameter is 1.7 mm. Figure 3.22 provides a schematic of a cross-section of the probe tip, as well as a side-view of the probe head. The IFP can be moved to multiple locations on the machine, but most often samples the plasma at the diagnostic port between coils 10 and 11 (z = 3.4 m).

3.8. Thomson Scattering

The TS diagnostic is an active, non-perturbative spectroscopic diagnostic[92] consisting of three components: (1) high-powered laser and laser coupling optics; (2) scattered light collection optics and routing hardware; and (3) light detection and digitization instrument [59]. The TS system design is described in more detail in previously published documents [60, 59]. The TS diagnostic provides electron temperature and electron density plasma measurements.

These plasma measurements are inferred through the scattering of the TS laser beam photons as a result of elastic plasma electron collisions, causing a Doppler shift characteristic of the electron velocity distribution [i.e. 59]. The Thomson scattering diagnostic collects the scattered light from the incident laser beam and resolves the shift spectroscopically. The Doppler shift varies with the velocity of the electrons; the distribution function width is proportional to the electron temperature. The total number of collected photons is proportional to the electron density [60, 59]. Differentiating between the small number of Thomson scattered photons and the background photons from the laser beam passing through the plasma column can be difficult. Methods used to reduce the background photons that are implemented on Proto-MPEX are described in more detail in a previously published article [60].

Two TS beam lines are currently installed on the Proto-MPEX device, produced by one laser beam. The first TS beam line is just in front of the target plate in between magnetic coils eleven and twelve.[93] That beam line is then redirected by two mirror surfaces to create the second beam line that passes through the central chamber before hitting a

[92] The non-perturbative quality of the TS diagnostic provides an advantage over LPs, which may burn under hotter plasma conditions.

[93] Corresponding to approximate axial location of z ~ 3.65 m (see figure 2.1).

dump.[94] There are twenty total lines of sight between the two beam lines, five at the target location and fifteen at the central chamber location. Both locations are critical to quantifying the plasma, especially with the addition of ICH and ECH power sources. For example, the central chamber is the region of the machine where the EBW power is absorbed [61]. Figure 3.23 depicts the current beam-line paths of the TS diagnostic on the Proto-MPEX machine.

3.9. Retarding Field Energy Analyzer (RFEA)

A retarding field energy analyzer[95] is installed at the diagnostic port on spool 10.5.[96] It measures the ion energy distribution in the Proto-MPEX plasma. An RFEA consists of an entrance, a system of grids at different voltage potentials[97], and an ion current collector [62]. Plasma particles enter through the RFEA opening, which may be a slit or larger opening. The first grid particles encounter is very negatively biased to repel incoming electrons. The second grid is positively biased to prevent ions below a desired energy level from reaching the current collector. The potential of the second grid can be varied to change the energy level of the ions collected. The third grid is negatively biased to repel any remaining electrons, especially secondary electrons resulting from ion collisions between the first and third grids [62]. This third grid is often called an 'electron suppressor'. The collector cup is also negatively biased but less biased than the electron suppressor to ensure good collection of ions. The grids must be adequately spaced to avoid space-charge effects, which occurs when charged particles selectively removed from the plasma (by the grids) creates a charge density that can change the potential. If large enough, the change in potential can yield a repulsive potential 'hill' greater that the potential imposed by the grid, reducing the current of the given charged particle [62].

The RFEA installed on Proto-MPEX has the standard three grids. The grids are spaced 130 microns apart to minimize space charge effects. The grids are composed of nickel spot-welded to stainless steel plates. The grids are insulated from one another and spaced with alumina spacers. The RFEA entrance (grid 1) consists a series of holes 100 microns in diameter. The large grid spacing allows the RFEA to withstand high heat flux. However, since the grid is larger than the plasma Debye length (~ 10 microns), some plasma might be passing through the first grid. To ameliorate this concern, the installation of a double grid is planned [57]. The first grid will be the same 100 micron grid, while the new second grid will be 12 microns. The remaining grids (ion repeller and electron suppressor) will remain 100 microns. Figures 3.24 and 3.25 provide a schematic of a typical RFEA and the RFEA design for Proto-MPEX, respectively [57].

3.10. Baratron

Baratron are installed on Proto-MPEX to measure neutral gas pressure along the machine. The baratron contains a capacitance manometer that consists of a diaphragm

[94] Corresponding to approximate axial location of z ~ 2.20 m (see figure 2.1).
[95] Also known as a retarding field analyzer (RFA), retarding potential analyzer (RPA), or gridded energy analyzer.
[96] Between magnet coils 10 and 11, at approximate axial location z = 3.4 m.
[97] Some RFEAs have only one negatively-biased grid, called single-gridded analyzers [62].

or membrane and a backplate in a metal-on-ceramic electrode structure [63]. The backside, called the 'reference' side, of the membrane is maintained at high vacuum, significantly lower than the pressure to be measured by the baratron. The pressure is calculated from the change in the capacitance induced by the change in distance between the membrane and the backplate when the membrane is exposed to pressure on the non-reference side [63]. Circuitry converts the capacitance change to an output voltage signal [64]. Figure 3.26 depicts a cross section of the baratron sensor [64, 63].

Four baratron are installed on Proto-MPEX, at axial locations z = 1.0, 1.5, 2.2, and 3.4 m. The baratron are MKS instruments model 627. To protect them from effects of the magnetic field, the baratron are wrapped in several layers of mu-metal[98] and mounted between 0.3 – 0.6 m away from the machine walls [34]. To ensure accurate measurements, the baratron are calibrated using pulses of gas only, magnetic field only and gas plus magnetic field [34].

3.11. Spectroscopy

Three spectroscopic instruments are implemented on Proto-MPEX: (1) a specially designed filterscope array; (2) a McPherson spectrometer; and (3) an ultra-violet/visible light (UV-Vis) broadband spectrometer ('Ocean Optics'). The spectroscopic instruments have multiple diagnostic ports available at nine locations along the Proto-MPEX machine: between magnetic coils (1) one and two; (2) two and three; (3) four and five; (4) five and six; (5) six and seven; (6) seven and eight; (7) nine and ten; (8) ten and eleven; and (9) eleven and twelve.[99] The three spectrometers can be interchanged at any of these ports. To collimate the field of view, a 5 mm diameter compact lens is installed in each of the collection ports that reduces the viewing angle to approximately two degrees on either side.

3.11.1 Filterscopes

The filterscope diagnostic is designed to analyze plasma light emission with rapid time response [65][100].The emitted light is collected with the compact optics described above and is transmitted to the filterscope module via optical fibers. In some instances, a beam splitter splits the light collected by the optical fiber into multiple paths that each pass through specific optical narrow bandpass filters [66, 65]. The filtered light then passes into the detector array [66, 65]. The Proto-MPEX filterscope array contains 24-channels [66]. Each channel is a photomultiplier tube (PMT) with a wavelength sensitivity range of 300 nm to 850 nm. The filterscope can sample at 100 kHz. The filterscope design components and setup are described in more detailed in previously published articles [66, 65]. Figure 3.27 provides a schematic of the filterscope diagnostic on Proto-MPEX [66]. The grey area represents the viewing cone of the Proto-MPEX plasma. The optical fibers carrying emitted light from the plasma are labeled as transfer fibers. The patch panel transitions between transfer fibers and patch fibers,

[98] Mu metal is a nickel-iron alloy used for magnetic shielding.
[99] Corresponding to approximate axial locations of z ~ 0.6, 1.0, 1.5, 1.8, 2.25, 2.6, 3.1, 3.4 and 3.65 m, respectively (see figure 2.1).
[100] Filterscope is a common term for a fast photomultiplier tube (PMT) [66], which are detectors that amplify incoming light (photon) signals [67].

which carry the collected light directly to a particular filterscope channel or to one of the beam splitters [66]. The λ's represent the different wavelength filters that could be applied. Possible filters include deuterium-alpha (D_α), deuterium-beta (D_β), and deuterium-gamma (D_γ), which have wavelengths of 656.1 nm, 486.0 nm, and 433.9 nm, respectively [i.e. 66, 68][101]. Other emission lines[102] can be monitored by choosing specific narrow-band filters, as appropriate.

More photons have sufficient energy to cross the lower-energy band gap associated with D_α emission spectrum than the higher-energy band gaps associated with D_β and D_γ. Therefore, more D_α photons are generally collected by optical fibers, increasing the overall associated emission intensity.[103] Spectroscopic data is often plotted in terms of emission intensity versus wavelength. Peaks in intensity at wavelengths associated with $D_{\alpha\text{-}\gamma}$ represent the line radiation of those photons. An example spectral plot from previous spectroscopic experiments on Proto-MPEX is provided in Figure 3.29 in the next section [66].

A total of 104 filterscope optical fibers are currently installed across eight diagnostic spool pieces along the Proto-MPEX machine.[104] Since there are 24 channels, data can be collected at 24 locations on the machine simultaneously during a single plasma shot.

3.11.2 McPherson

The McPherson spectrometer ('McPherson') installed on Proto-MPEX is a one-meter 2051 Czerny-Turner high-resolution spectrometer with a Princeton Instruments PhotonMax 512b EMCCD detector [69]. The McPherson spectrometer has a maximum wavelength range of 185 nm to 20.8 microns [70][105]. Depending on the grating installed, it has a full spectral range of 3 nm and a resolution of 0.05 nm.[106] It typically takes a data sample approximately once every 10 ms [71], but the time resolution is determined by the emission intensity of the spectral line being examined. The McPherson's high resolution functions similarly to a filter used on the filterscopes. The full spectral range for a specific wavelength setting only allows a 3 nm range of light to pass through to the detector, enabling D_α, D_β, or D_γ emission intensities measurements. In contrast to a filterscope, which integrates all the light within the pass band for high time response, the light detected through the McPherson is spectrally resolved, allowing the shape of the spectral line to be measured. However, this is at the expense of high time response. Due to the large amount of D_α photons emitted from the plasma column, the McPherson detector usually saturates when focused on the D_α wavelength range, rendering the measurements unusable. Therefore, the McPherson will often focus on the D_β wavelength range when acquiring deuterium spectra measurements. The wide range of possible wavelengths enables the McPherson spectrometer to measure photon emissions due to impurities in the machine, such as helium and argon. When searching for possible impurities within the Proto-MPEX device, the McPherson must be looking

[101] Other filters include helium and hydrogen.
[102] Impurity lines, for example.
[103] The emission intensity is directly proportional to the number of photons collected.
[104] See figure 2.1.
[105] Depending on the snap-in grating applied [69].
[106] For the 1800 g/mm grating typically used.

for a specific impurity spectroscopic signature. That is, researchers must already know what impurity to look for. To determine possible impurities, the Ocean Optics spectrometer, which is described in next subsection, is used.

Similar to the filterscopes, the McPherson uses optical fibers to collect light emitted from the plasma during pulses. The fibers feed into the same patch panel and are directed into one of the spectrometer's five available channels. Since the McPherson has five channels, despite having multiple available sampling locations across eight diagnostic spool pieces on Proto-MPEX[107], only five of those locations can sample simultaneously during a single plasma shot. Figure 3.28 provides an image of the McPherson spectrometer, as well as a schematic of the diagnostic set up. The setup is similar to that of the filterscopes [70, 66].

Figure 3.29 provides a composite spectral plot from previous McPherson experiments on Proto-MPEX [66]. The D_α and D_β lines are labeled.

3.11.3 Ocean Optics

The Ocean Optics diagnostic installed on Proto-MPEX is a model USB4000 spectrometer. It is a low resolution, wide range, survey spectrometer. It collects light across a wavelength range of 200 to 1100 nm for each plasma pulse [69], which corresponds to the ultra-violet/visible light (UV-Vis) portion of the electromagnetic (EM) spectrum. It has a resolution of 0.1 nm and can take a data sample once every 3.8 ms, though the time response is limited by the emission intensity of the spectral lines [72]. In practice, the Ocean Optics accumulates light from the entire duration of the plasma into a single exposure frame. While the Ocean Optics spectrometer has the range to measure deuterium emission spectra, the McPherson and the filterscopes are more often used for this purpose during experimental campaigns, due to their higher resolution and additional data channels. However, its wide range enables the Ocean Optics to determine emission spectra warranting further investigation, such as those of impurities. Additionally, the Ocean Optics spectrometer can be used to corroborate filterscope and McPherson emission measurements.

Similar to the filterscopes and McPherson, the Ocean Optics uses an optical fiber to collect light emitted from the plasma during pulses. The fiber feeds into the same patch panel and is directed the Ocean Optic's single channel. The Ocean Optics spectrometer can only sample at one location per plasma shot. Figure 3.30 provides an image of the Ocean Optics spectrometer, as well as a schematic of the diagnostic set up [72, 66]. The setup is similar to that of the other two spectroscopic diagnostics.

3.12. Photodiodes

Plasma radiative losses are expected to be a significant source of the power losses from the main plasma. Two photodiodes are installed on Proto-MPEX, an Absolute eXtreme Ultra-Violet (AXUV) photodiode and a Soft X-Ray (SXR) photodiode. Photodiodes are semiconducting, solid-state devices that convert incident light[108] into

[107] The McPherson has the same available sampling locations as the filterscopes (see figure 2.1).
[108] I.e. photons from plasma radiative losses

electrical current [73]. A photodiode is composed of a thin silicon dioxide protective coating, and a p-n junction, separated by a depletion region [i.e. 73]. The p-n junction consists of a p-type dopant[109] layer with electron holes and an n-type donor[110] layer with excess electrons [i.e. 74]. When the p-type layer comes into contact with the n-type layer, the excess electrons from the n-type layer flow across the junction to fill the holes of the p-type layer, creating current [i.e. 73]. The flow eventually creates a depletion region, whose electric field is equal and opposite to the induced current flow [73]. No current flows across the depletion region. Figure 3.31 provides a schematic of an example silicon photodiode, depicting the different component layers [73].

The material of the photodiode should be selected such that its bandgap energy is marginally lower than the photon energy that corresponds to the longest wavelength of the operating system [75]. This criterion enables a high absorption coefficient for good diagnostic response, while minimizing thermally generated 'dark current'[111] [75]. Silicon is the most common material used for photodiodes, due to its large bandgap[112]. When sufficient incident photon energy hits the silicon material, the photon is absorbed, creating electron-hole pairs, called carriers [i.e. 76]. The pairs drift apart through the silicon layer until they reach the p-n junction and the electrons are swept across, which induces a current proportional to the number of electron-hole pairs generated by the incident photon energy [76, 73]. The depth of the photon absorption varies based on their energy; the lower the energy, the deeper are absorbed [73]. As a result, if the photodiode's dimensions are too thick, they will not be sensitive to higher energy photons, such as those in the extreme ultra-violet (XUV)[113] [i.e. 76].

3.12.1 AXUV

AXUV photodiodes have a wide range of sensitivity through the vacuum ultraviolet, extreme ultraviolet and soft x-ray spectra [77]. AXUV photodiodes have a very thin[114] protective silicon dioxide window, which increases the possible time response [77]. The AXUV photodiode installed on Proto-MPEX is an AXUV100G model by Opto Diode Corp. It has an active area of 100 mm^2. A 6-8 nm thin SiO_2 passivating coating allows the diode to be sensitive across nearly the entire spectral range from 0.0124 nm to 1100 nm with response time of approximately 10 microseconds [78]. However, the photodiode response is not uniform across the entire spectrum, ranging from about 0.07 to 0.39 A/W.[115] For reliable measurements of incident radiated power, the responsivity of the diode should be constant. The AXUV photodiode is currently installed on the diagnostic port in the central chamber at axial location z = 2.2 m.

---

[109] The p-type semi-conductor layer has small amounts of impurities added, such as boron or gallium, creating electron 'holes' in the valence electron shell [74].
[110] The n-type semi-conductor layer has small amounts of pentavalent impurities, such as antimony or phosphorus, creating free electrons that are in excess of a full valence electron shell [74].
[111] That is, background current generated by the diode without incident photon light [i.e. 75].
[112] The bandgap of silicon is about 1.1 eV, with a corresponding wavelength of about 1100 nm [i.e. 76]. Its photodiode response is linear [i.e. 73]. Other materials for photodiodes include germanium [i.e. 75].
[113] XUV photons have energies around 3.6 eV, with an approximate absorption depth of 1 micrometer [i.e. 76]. AXUV photodiodes, which can accurately measure XUV photons, are discussed below.
[114] A few nanometers thick [77].
[115] Amperes per watt.

3.12.2 SXR

The SXR photodiode is an AXUV100AL model by Opto Diode Corp. It is an AXUV diode with a specialized filter attached to the front to narrow the detection wavelength range of the diode sensor [79]. The filter takes the form of a metallic aluminum coating that is 150 nm thick [78]. The filter narrows the passband[116] to 17-80 nm[117] [78]. The responsivity of the SXR diode ranges from 0.03 to 0.18 A/W and the response time is approximately 250 nanoseconds [79]. Like the AXUV photodiode, the active area is 100 mm^2. The SXR photodiode is currently installed on the diagnostic port at the central chamber at axial location z = 2.2 m.

3.12.3 Photodiode Set-Up

Both SXR and AXUV photodiodes have similar installation set-ups. They are mounted behind a 1.27 mm diameter pinhole and are encased within a stainless steel tube. Figure 3.32 provides a schematic of the set-up.

The photodiode detector views the plasma column through the pinhole. Using a line integral approximation, the radiated power is measured.

3.13. New Diagnostics

Newly installed diagnostics are planned for future Proto-MPEX operations. They include TALIF, HELIOS, surface eroding thermocouples, and a bolometry array.

3.13.1 TALIF

The main new diagnostic is the two-photon absorption laser induced fluorescence (TALIF). TALIF is a laser-based diagnostic recently installed on Proto-MPEX. The diagnostic was developed for Proto-MPEX in collaboration with the University of West Virginia.

The TALIF diagnostic is a modified version of the laser induced fluorescence (LIF) diagnostic. Using LIF, a photon with a specific frequency excites an electron, which emits a photon with another desired frequency as it returns to its ground state [80]. The emitted photon is collected by a high-speed photomultiplier tube (PMT).[118] A filter is applied to remove non-relevant light. The TALIF diagnostic differs from LIF by exciting the electron to the desired energy level with two photons rather than one. TALIF is used to analyze neutral deuterium because the energy required to excite the electrons is high and in the ultraviolet spectrum[119], which creates engineering difficulty in constructing the appropriate laser and optic windows [80]. In TALIF, a pulsed laser is modified to produce 205 nm light, which UV optic windows can transmit.[120] Two 205 nm photons absorbed at the same time is effectively like seeing a single photon at 102 nm [80]. When the laser is pulsed over nanosecond time scales to increase the achievable output power of the laser. The laser scans over a small range deviating from the

[116] Wavelength range over which the diode is sensitive.
[117] 15.5 - 72.9 eV.
[118] Like other spectroscopy diagnostics (see section 3.11, **Spectroscopy,** in this chapter).
[119] The required wavelength is approximately 100 nm [81].
[120] Via a series of harmonic generations and frequency mixing [82].

nominal frequency[121], causing small shifts from the rest frequency distribution. The obtained velocity distribution can be used to infer the direction of neutral particle flow and its full-width half maximum is used to infer the neutral particle temperatures. Most importantly for Proto-MPEX, the diagnostic provides absolute and direct neutral density measurements along the machine axis.

Proto-MPEX's TALIF system is installed at spool 1.5. It consists of a Nd:YAG laser operating at 532 nm at 20 Hz. The Nd:YAG laser pumps a scanning dye laser that operates at 615 nm, whose frequency is tripled in two non-linear doubling stages,[122] producing a 205 nm light at a maximum of 8 mJ over 8 ns pulses [84]. The 205 nm light is compressed by a factor of 5, passes through a 0.475'' hole in a 45-degree mirror, and passes through a focusing lens and enters the main plasma region. Two simultaneously absorbed 205 nm photons excite neutral deuterium particles, which emit 656.4 nm photons as they decay back towards a ground state [84]. The emitted photons' signal is collected along the same axis and passes back through a plano-convex lens. The collected light is reflected off the 45-degree mirror and is focused into a fast PMT, which amplifies the signal. A box car average separates the signal for the background [80]. Figure 3.33 provides a schematic of the TALIF diagnostic [84]. A straight blue line depicts the laser light, while the thicker red line depicts the photons emitted from the excited neutrals to be collected by the PMT.

3.13.2 HELIOS

Helium line spectral monitoring (HELIOS) is a diagnostic that measures plasma electron temperature and density. A less perturbative diagnostic to the plasma in comparison to probe scans, the HELIOS system on Proto-MPEX has two main components: (1) a gas injection system to puff helium gas into the Proto-MPEX plasma and (2) a filterscope with a 100 kHz sampling rate to measure the resulting light intensity of three different helium I lines. The helium I line intensities are used to determine the electron temperature and density ratios. These ratios are compared to ratios calculated using a collisional radiative model. The measured electron temperature and density of the plasma at the puffing location is determined from the comparison between the measured and calculated ratios [85].

Figure 3.34 provides a schematic of the HELIOS system in Proto-MPEX.

3.13.3 Surface-Eroding Thermocouples (STC)

Also called a 'self-renewing' or 'surface-eroding' thermocouple, an STC is unique from traditional thermocouples, engineered by NANMAC Corporation.[123] It is specifically designed to be capable of withstanding extremely high temperature environments [86, 87]. They can be directly exposed to plasma. Therefore, they have faster time

[121] On the order of picometers [81].
[122] The process is described in more detail in previously published work [83].
[123] NANMAC Corp is a Massachusetts-based company specializing in high-performance temperature sensors. The sensors were originally primarily for government research and military purposes but have been expanded into a variety of commercial applications [88].

responses and better agreement between the diagnostic measurements and actual surface temperatures.

Similar to standard thermocouples, STCs are composed of two different metal wires that form a junction where the temperature is measured. However, these wires are flattened to a thickness of about one thousandth of an inch and are thermally insulated from each other by a 10,000th of an inch thick dielectric material [86]. The thermocouple is inserted through a plasma facing component (PFC), similar to an embedded thermocouple, but it goes through to the surface of the PFC, just barely beyond flush with the surface. The initial dual-metal junction is formed when the tip of the thermocouple is filed down until it is perfectly smooth with the PFC surface [86]. The insulating layer is so thin that the process of grinding the wires to flush bends hundreds of small slivers of one metal ribbon across the dielectric material to form the thermojunction with the other ribbon[124] [87, 86]. Since the initial thermojunction is formed by friction, any subsequent corrosion/erosion from the intense plasma environment will create new junctions while old ones erode away [86]. The thermocouples are therefore 'self-renewing.' They can continue to be eroded for up to 0.5 inches [88].

Figure 3.35 provides an image of a Proto-MPEX STC to be used in future operations. The tip of the thermocouple is intended to be flush with the plasma facing side of the machine surface.

3.13.4 Bolometry array

A resistive bolometer array was recently installed on Proto-MPEX to measure absolute radiated power loss; that is, the total power loss due to light emission and neutral particles.[125] A resistive bolometer detects increases in foil temperature through a metal-resistor or a thermo-resistor, which is bonded to the back of the absorber foil[126]. The resistor, called the meander, has a known resistance. The measuring and reference resistors, corresponding to the measuring and reference bolometers, connect with wires to form a bridge circuit[127]. Incident radiated heat from the plasma raises the foil temperature, which increases the measuring meander resistance. The change in resistance yields an output voltage corresponding to the increase in temperature [i.e. 91]. The material of the meander is often the same material as the foil. These bolometers directly view plasma radiation without filters or mirrors [92].

Figure 3.36 depicts a cross-sectional diagram of an example resistive bolometer [93]. The bolometer is composed of a gold meander and absorber foil, with a thin mica insulating foil layer [93].

[124] NANMAC STCs are available in all thermocouple types, including type C, which employs two different tungsten/rhenium (W/Re) alloys [88]. Type C is the standard type for STCs [86]. The company can also engineer non-standard thermocouple junctions and their customized voltage-to-temperature calibration curves [87, 88].
[125] Photons, high-energy neutrals, charge-exchange neutrals, etc.
[126] The foil and resistor may be separated by a thin insulating film, such as mica [i.e. 89, 77].
[127] The bridge circuit is outside the vacuum chamber of the fusion device [i.e. 90].

The plasma radiation can be inferred from resistive bolometers using the following equation [77]:

$$P_{rad} = C\left(\frac{d\Delta T}{dt} + \frac{\Delta T}{\tau}\right) \quad (3.7)$$

where P_{rad} is the incident power, ΔT is the measured temperature change proportional to the measured voltage output by the bridge circuit, t is time, C is the heat capacity of material and τ is the bolometer thermal response time, which is constant [77]. Resistive bolometers have thermal response times on the order of about 10 milliseconds [i.e. 94].

The bolometer array on Proto-MPEX consists of components on loan from Princeton Plasma Physics Laboratory's (PPPL) National Spherical Torus Experiment – Upgrade (NSTX-U). Loaned components include the bolometer sensors, four-channel analyzers, air-side cables and the control board. The digitizer is provided by ORNL. Bolometer arrays can be installed on spools 2.5, 6.5, or 12.5.

The bolometer sensor has a 5-micron thick gold absorption layer with a 1.3 x 3.8 mm^2 absorption area and a gold meander. The thermal contact layer is composed aluminum and is 150 nm thick [95]. The bolometer systems used the Wheatstone bridge configuration, which consists of two measurement resistors and two reference resistors. The change in temperature is found from a measured change in resistance between the two measurement resistors. These measurements are corrected using measurements from the reference resistors [96]. Each bolometer sensor is paired with a four-channel analyzer that provides four possible lines of sight in the plasma [97]. The analyzer also amplifies the measured signal. The analyzer is controlled by the control board and is connected to the control board by the air-side cables.

Similar to the photodiode, the bolometer sensor is mounted on an internal rail system to provide flexible positioning and installation at multiple possible ports. The sensor is installed approximately 3.8'' behind a pinhole aperture to block ambient light. The radiated power incident on the bolometer sensor is measured using a line integral approximation, shown in the equation below:

$$P_{det} = P_{rad} = \frac{A_{det}A_{ap}}{4\pi l^2}\int \varepsilon \, dl \quad (3.8)$$

where P_{det} is the power measured on the detector (bolometer sensor), P_{rad} is the radiated power, A_{det} is the area of the detector, which is approximately equal to the area of the aperture, A_{ap}. l is the distance between the aperture and the detector and ε is the emissivity of the plasma.[128] Figure 3.37 provides a diagram of the bolometer diagnostic, including the field of view lines [98].

The bolometer array can be used in conjunction with the photodiodes to quantify the type of neutrals measured. Unlike bolometers, photodiodes are not sensitive to incident energy due to charge exchange neutrals [62]. If bolometers and photodiodes are

[128] The $\int \varepsilon \, dl$ term represents the line integrated brightness of the plasma [96].

employed together, comparing the measurements can quantify what incident energy is due to charge exchange and what is due to incident photons [62].

3.14. Summary

An extensive array of diagnostics is installed on Proto-MPEX. The diagnostics provide a range of different plasma measurements, including electron and ion temperatures and densities, plasma flow rates, machine surface temperatures, and neutral gas densities, all of which are used during experimental operations. Many diagnostics are designed to accommodate multiple installation locations to provide better diagnostic coverage of the machine. The diagnostic suite is constantly being improved and expanded. Each diagnostic has at least one graduate student or research scientist who is the assigned diagnostician, responsible for the maintenance and operation of that diagnostic.

CHAPTER 4: POWER BALANCE COMPONENTS & ANALYSIS METHODS

The overall ability of a linear plasma device to transport heat flux to its end plate is a measure of its ultimate effectiveness as a PMI research device, which can be established through a total power balance[129] of the machine. Power accounting helps identify areas for improvement with respect to machine operations by quantifying plasma loss locations and mechanisms. For the purposes of this thesis, the power balance is separated into three main components: input power (P_{in}), lost power (P_{loss}), and deposited power (P_{dep}).

4.1. Input Power

The input power includes the total power injected into the system. As described in previous chapters, the available power sources on Proto-MPEX are (1) a helicon antenna; (2) an electron cyclotron heating (ECH) launcher; (3) an ion cyclotron heating (ICH) antenna; and (4) pre-ionization heating. For the main power accounting study performed as part of this thesis, the helicon antenna is the sole applied power source.[130]

The input power term incorporates the power source conversion efficiencies. Power conversion efficiencies refer to the fraction of the power from a plasma generation source successfully transferred to the plasma out of the total power applied by that source. For example, for the helicon antenna, efficiency losses are due to reflected power and resistive losses. For the purposes of the power balance analysis, these losses are taken into account when determining the final input power. That is, the input power is the net power after reflected and resistive power losses are subtracted from the nominal injected ('forward') power.

4.2. Lost Power

Lost power refers to the power lost from the plasma as it travels from travels through the machine between the power source and the end plates. Leading sources of power losses for a linear plasma device include ionization, radiative transport losses and non-radiative transport losses, such as recombination, elastic collisions, and charge exchange [i.e. 11, 99].[131] Power lost from the main plasma will eventually arrive at and heat up machine surfaces. Power can also be lost from the plasma when the plasma limits on a machine surface.

4.2.1 Ionization

One of the main causes of inefficiency on Proto-MPEX, particularly for the helicon source[132], is the ionization power requirement. That is, the amount of energy required to

[129] For the purposes of this thesis 'power accounting' is used interchangeably with 'power balance'.
[130] The power accounting study is delineated in Chapter 6: **FULL POWER BALANCE**.
[131] In plasma operations, the majority of the power used in excitation, dissociation, ionization and elastic collisions results in wall heating [103].
[132] The helicon has a dual purpose of creating a high density plasma and heating the plasma itself. In comparison, ICH and ECH have the sole purpose of heating the plasma.

dissociate a neutral atom into an ion-electron pair.[133] The ionization energy required depends on the type of atom as well as the plasma temperature [i.e. 100]. For example, the dissociation energy[134] of a hydrogen molecule (H_2) is 4.52 eV [101]. The dissociation and ionization energies for D_2, the main fuel type on Proto-MPEX, are marginally greater than those of H_2 [102]. It is important to note that diatomic gases, such as H_2 and D_2, require more energy to drive the ionization process than do monoatomic gases, such as He or Ar, because they have more degrees of freedom [i.e. 100]. Further, as electron temperature increases, other molecular and dissociation processes decrease and most of the energy contributes to ionization. When the plasma temperature increases from 2 eV to 5 eV, the amount of collisional energy lost creating an electron-ion pair in ionizing H_2 gas drops by over a factor of ten [101]. For the same plasma temperature increase, the amount of collisional energy lost creating an electron-ion pair in ionizing H_2 gas is between ten to four times greater than that lost creating an electron-ion pair in ionizing Ar gas [100, 101].

The importance of plasma temperature for ionization is further demonstrated in figure 4.1, which depicts different ionization rate coefficients [m^3/s] for different hydrogen reactions [99,103]. The temperature range relevant to Proto-MPEX experiments is highlighted in green. The ionization rate coefficient[135] depends directly on the particle's cross section (σ) and velocity (v) and varies with the particle temperature (T_e, T_i) [103].

4.2.2 Radiative Transport Losses

Heat transfer from plasma is considered 'radiative' when plasma particles lose energy by means of photon emission [i.e. 104, 105].[136] Emitted photons are not confined by electromagnetic fields and escape the plasma [i.e. 17]. There are three main types of plasma radiative heat transfer: (1) Bremsstrahlung radiation; (2) line radiation; and (3) radiative recombination [i.e. 17].

Bremsstrahlung radiation is the result of electron deceleration due to Coulomb effects, such as collisions with or deflections by charged particles [17, 25]. A photon with the energy equivalent to the kinetic energy lost in the collision is emitted. Power loss through Bremsstrahlung radiation increases with the square of the effective Z, and directly with the ion density. The effective Z is determined using the formula below:

$$\mathrm{Z_{eff}} = \sum_{j \neq e} \frac{n_j z_j^2}{n_e} \tag{4.1}$$

where Z_{eff} is the effective atomic number, n_j is the density of the j[th] ion present and z_j is the atomic number of the j[th] ion present. $\mathrm{Z_{eff}}$ increases with the number of ion species present. Thus, small increases in impurities can cause significant increases in power

[133] This is in addition to the disassociation energy that is necessary to separate a diatomic molecule into individual neutral atoms.
[134] Also called the bond energy [102].
[135] Determined by integrating the particle cross-sections over the (Maxwellian) electron velocity distribution [103].
[136] The decrease in plasma temperature from radiative heat transfer is also called 'radiation cooling' [17].

radiated away from the main plasma [i.e. 25]. Bremsstrahlung radiation dominates at high temperatures, where the electron temperature is greater than 1000 eV[137] [25, 106].

Line radiation occurs when an orbital electron of a partially ionized atom is excited to a higher energy level from interactions with a plasma electron [i.e. 25, 106]. As a result, a photon will be emitted with an energy equal to that of the energy difference between the electron's ground and excited energy levels [17] as the electron returns back to its ground state or to an intermediate, lower energy state.[138] Line radiation caused by plasma impurities is called 'impurity line radiation'. Line radiation increases with the atomic number and decreases as the plasma electron temperature increases. As the plasma gets hotter, neutral or partially ionized atoms become increasingly ionized, reducing their orbital electrons and reducing their ability to lose energy through line radiation. Thus, high-Z elements are better radiators than low-Z elements [25]. They not only have higher Z values, which benefit both Bremsstrahlung and line radiative abilities, but they also have more orbital electrons, which enables them to radiate through line radiation at higher temperatures than their lower-Z counterparts [25].

Radiative recombination occurs when a free (unbound) plasma electron recombines with a (partially) ionized atom, yielding an atom with a charge state reduced by one and in an excited state [17, 25, 99]. A photon with energy equal to the energy difference between the two charge states[139] is emitted [25, 106].

Out of the three radiative heat transfer processes listed, radiative recombination has the strongest sensitivity to the atomic number. Radiative recombination occurs at much lower plasma temperatures than Bremsstrahlung and line radiation, at electron temperatures below approximately 2 eV [i.e. 107].

The combined radiative power loss[140] fluctuates with increasing plasma electron temperature [25]. Initially, radiative power losses increase as particle charge states become more ionized. As electron temperature continues increasing, the radiative power loss decreases as particles become fully ionized (i.e. losing line radiating capabilities). Finally, beyond a certain electron temperature (which varies by impurity atom), the radiative power will begin increasing and continue increasing as Bremsstrahlung radiation becomes the dominating radiative term [25].

4.2.3 Non-Radiative Transport Losses

Non-radiative transport plasma losses refer to losses as a result of particle collisions but do not result in photon emission [i.e. 103]. Types of collisions include electron-ion collisions, electron-electron collisions, ion-ion collisions, electron-neutral collisions and

[137] Beyond these temperatures, low-Z particles are completely stripped of their orbital electrons and are no longer effective radiators [i.e 106].
[138] The instantaneous photon emission creates an energy line 'spike' on relevant diagnostic instruments, such as spectrometers, hence the name 'line' emission [i.e. 105].
[139] That is, the plasma electron thermal energy [17].
[140] Here, total radiative power loss is: $P_{loss} = P_{brem} + P_L + P_R$, where P_{brem} is the power loss due to bremsstrahlung radiation, P_L is the power loss due to line radiation, and P_R is the power loss due to radiative recombination.

ion-neutral collisions [i.e. 20]. These collisions can be elastic or inelastic [i.e. 20]. In an elastic collision, the total kinetic energy of the colliding particles is the same before and after the collision [108]. In comparison, in an inelastic collision, a portion of the particles' kinetic energies is converted into internal energies, such as vibrational energies [108].[141] The particles may interact through charge exchange, recombination, or electron-ion elastic collisions. Collisions serve to cool the plasma by dissipating the momentum of the particles, reducing the heat energy held in the plasma and reducing the ionization source [109].

The effects of particle collisions depend on multiple parameters, including the cross-section of the interacting particles (σ), the angle of collision, the mass of the two particles, the charge of the two particles, the velocity of the particles, and the density and temperature of the plasma [i.e. 20, 103]. For example, as the plasma temperature increases, the particle cross-section decreases, which decreases the likelihood of two particles colliding [i.e. 20]. Further, the mean free path[142] of a collision that produces a ninety-degree deflection in the trajectories of collided particles is described by the relation

$$\lambda_{90} \propto \frac{T_P^2}{n_P} \tag{4.2}$$

where λ_{90} is the mean free path producing a 90° deflected particle trajectory, T_P is the plasma temperature, and n_P is the plasma density [99]. The overall effect of collisions is dominated by numerous small-angle deflections rather than fewer large-angle deflections [i.e. 99]. The greater the number of collisions, the greater the chance that a particle gets knocked from its current magnetic flux field line to another flux line. Eventually, the particle can make its way towards the edge of the main plasma. If it crosses the LCFS, it will escape the plasma, carrying its energy from the plasma to the PFCs.

Electron-ion[143] particle collisions give rise to more particle diffusion than like-particle[144] collisions [20]. Ion or electron collisions with neutrals will result in larger momentum losses than collisions between charged particles [20].[145] Ion-neutral collisions further create a drag on the plasma flow, enabling the plasma more time to spread across magnetic field lines or to recombine [109].

Electron-ion elastic collisions

In a plasma where particle collisions are non-negligible, conduction dominates parallel[146] heat transport in comparison to convection [i.e. 99]. The amount of energy exchanged between ion-electron collisions is an important parameter. The total energy

[141] For example, an ion-neutral collision resulting in a vibrationally-excited neutral. Ionization is also considered an inelastic collision (which is an electron-neutral collision) [i.e. 99].
[142] The average distance particles travel between collisions [i.e. 20].
[143] For the purposes of this paper, the terms 'electron-ion collisions' and 'ion-electron collisions' are used interchangeably.
[144] Electron-electron or ion-ion collisions
[145] That is, Coulomb collisions.
[146] That is, along flux field lines.

exchanged is a function of the ratio between electron and ion masses, the difference between the electron and ion temperatures, and the electron-ion collision mean free path [99]. Conductive heat transfer in the plasma occurs as the particle collisions transfer thermal energy from hotter plasma regions to colder ones [99]. That is, heat transfer via conduction can only occur if the temperature gradient across regions of the plasma is steep enough [99]. The total energy transferred through the collisions depends directly on the heat conduction coefficient. The heat conduction coefficient for the plasma charged particles is described by the relation

$$K_s \propto \frac{T_s^{5/2}}{m_s^{1/2}} \tag{4.3}$$

where K_s is the heat conduction of the charged particle (either electron or ion), T_s is the temperature of that particle, and m_s is the mass of that particle [99]. The relation highlights the fact that since heat conduction depends strongly on the plasma temperature itself, a comparatively small temperature gradient can transport a large amount of heat in the plasma SOL [99]. Further, given the relation between the particle's coefficient and its mass, electrons are better at conducting heat than ions [99].

Charge Exchange

Charge exchange is a mechanism by which hot ions are neutralized by neutral atoms, which allows the particles to escape plasma confinement [3]. During this process, a hot plasma ion collides with a neutral, exchanging an electron and producing an energetic ion and a warm[147] neutral [25]. Neutral atoms by definition have no net charge. Therefore, they are not confined by electromagnetic fields and either are re-ionized via another collision[148] or escape from plasma confinement, carrying heat away from the main plasma and ultimately to machine surfaces. The overall process results in plasma cooling.

There are multiple types of charge exchange processes, depending on the interacting species and their associated energies.

Recombination Losses

The two primary modes of recombination explored are electron-ion recombination (EIR) and molecular activated recombination (MAR) [i.e. 107, 99]. EIR occurs in cold (T_e < ~1 eV), dense plasmas [i.e. 99]. Two types of EIR exist: three-body recombination and radiative recombination (which has already been discussed). Three-body recombination is similar to radiative recombination, with two main differences. First, instead of one electron interacting with a (partially) ionized atom, there are two electrons.[149] Second, instead of a photon removing the excess energy and momentum released from the interaction, in three-body recombination an electron removes it [104]. In conditions where EIR is dominant, three-body recombination generally occurs more often, as it has

[147] Warm in terms of plasma temperature [25].
[148] The re-ionization collision also removes power from the plasma.
[149] Hence the name 'three-body' recombination. Radiative recombination is also called 'two-body' recombination [i.e. 107].

a larger cross-section [99]. However, it is more sensitive to changes in electron density [99].

In comparison to EIR, MAR involves vibrationally-excited (neutral) molecules[150], which interact with either plasma electrons or ions to become temporarily charged and then recombine [i.e. 110, 99]. MAR becomes more dominant at slightly higher plasma temperatures (1 eV < T_e < 3 eV) [i.e. 99]. The MAR process has two steps, with two different possible paths, depending on whether an ion or an electron is involved during the first interaction with the neutral gas molecule [i.e. 99]. When the first interaction involves an electron, the first step that occurs is called electron capture dissociation and the second is charge exchange recombination [99]. When the first collision involves an ion, the first step that occurs is a molecular charge exchange and the second is an electron capture dissociative recombination [99]. Figure 4.2 provides a list of the two possible two-step processes assuming the molecular involved is H_2 [99].

It is important to note that MAR does not always produce atoms in an excited state and therefore has no spectroscopic signature from photon emission, unlike EIR, which emits photons during radiative recombination processes [99].

4.2.4 Limiting surfaces

Plasma limits on the machine when the magnetic field flux lines intersect with the machine surfaces. Figure 4.3 provides a diagram of the magnetic flux tube lines on Proto-MPEX for a 'modified flat' magnetic field configuration.[151] The red and blue lines represent the outermost flux line (OFL) and flux lines, respectively. The green box highlights the area where the magnetic field lines may intersect the skimmer machine surfaces. The target and dump plate locations are also shown.

4.3. Deposited Power

The final component of the power balance is the deposited power; that is, the heat flux directly impinging on the end plates[152]. The goal of PMI studies in a linear fusion device like Proto-MPEX is to maximize the heat flux and overall power impinging on the target plate. Thus, the intended PFCs are the end plates, specifically the target plate. Depending on the layout of the fusion device, the magnitude of the heat fluxes can be directly measured from the front of the end plates or interpreted from the heat fluxes measured from the back.[153]

4.4. Region Efficiency Analysis

To perform the power balance, the Proto-MPEX machine is broken down into three main regions: (1) the helicon region, which includes the area with the helicon antenna, bounded by the nearest diagnostic ports (2.5 and 4.5, z = 1.0 and 1.5 m, respectively); (2) the upstream region, which extends from the dump plate to the upstream edge of the

[150] These molecules are generally the same species as the fuel gas [107].
[151] Magnetic coils 1, 6-12 are set to 4500 A, coils 3-4 are set to 160 A, coil 2 is set to 600 A and coil 5 is off.
[152] For the purposes of this document, particle recycling off of PFCs is ignored.
[153] These measurements are often obtained through IR thermography on Proto-MPEX.

helicon region; and (3) the downstream region, which extends from the downstream edge of the helicon region to the target plate. Each of these three regions are broken down into smaller sub-regions to better evaluate plasma transport and losses between diagnostic ports available for data acquisition. The plasma power transport efficiency can be determined in each sub-region to highlight potential areas of the machine with lower efficiency. The division sub-regions also can accommodate the application of multiple power sources with different installation locations. Figure 4.4 provides diagrams of Proto-MPEX partitioned into its three main regions and its sub-regions.

The helicon region is divided into three sub-regions: the helicon antenna, the downstream edge of the helicon window and the upstream edge of the helicon window. The upstream region is divided into two sub-regions: from diagnostic port 2.5 to diagnostic port 1.5 and from diagnostic port 1.5 to the dump plate. The downstream region is divided into five sub-regions: from diagnostic port 4.5 to 6.5, from diagnostic port 6.5 to 9.5, from diagnostic port 9.5 to 10.5, from diagnostic port 10.5 to 11.5, and from diagnostic port 11.5 to the target plate.

The amount of power entering the sub-region equals the power exiting the sub-region. The balance of power entering and exiting the sub-region can be approximated using equation 4.4.

$$\mathrm{P_{enter}} + \mathrm{P_{source}} = \mathrm{P_{exit}} + \mathrm{P_{loss}} \tag{4.4}$$

where P_{enter} is the amount of power entering the sub-region from the previous sub-region, P_{source} is the power entering the sub-region from an applied power source, such as the helicon, P_{exit} is the amount of power leaving the sub-region, continuing towards its respective end plate, and P_{loss} power lost from the main plasma due to different loss mechanisms, such as charge exchange processes.

The efficiency of each sub-region can be evaluated using the following equation:

$$\eta = \frac{\mathrm{P_{exit}}}{\mathrm{P_{enter}} + \mathrm{P_{source}}} \tag{4.5}$$

where η is the efficiency of the sub-region.

4.5. Summary

As previously stated, power accounting helps identify areas for improvement with respect to machine operations by quantifying plasma loss locations and mechanisms. The power balance is separated into three main components: input power (P_{in}), lost power (P_{loss}), and deposited power (P_{dep}). For this thesis, the helicon is the only power source. The input power is the net (helicon) power after reflected and resistive power losses are subtracted from the nominal injected power. The lost power refers to the power lost from the plasma as the plasma travels from the power source to the end plates. Sources of power losses include radiative transport losses and non-radiative transport losses, such as recombination, elastic collisions, and charge exchange [i.e.

11, 99] and limiting surfaces. Deposited power refers to the power that is deposited on the end plates. To perform the power balance, the Proto-MPEX machine is broken down into three main regions: (1) the helicon region; (2) the upstream region; and (3) the downstream region. Each of these three regions are broken down into smaller sub-regions to better evaluate plasma transport and losses between diagnostic ports available for data acquisition. The plasma power transport efficiency can be determined in each sub-region to highlight potential areas of the machine with lower efficiency.

CHAPTER 5: PREVIOUS WORK

To maximize the effectiveness and accuracy of the final power accounting study performed as part of this thesis, multiple preliminary experiments and analyses were conducted. This chapter delineates the previous work completed prior to the final power accounting study. A preliminary power balance analysis was performed twice for a given set of operating parameters to diagnostically verify input power and highlight areas requiring increased diagnostic investigation. Additionally, given the importance of the helicon antenna as a power source, fluoroptic probes and thermocouples were applied to better quantify the helicon region, identifying loss mechanisms for specific machine operating parameters.

5.1. Preliminary Power Balance

Initial power accounting studies of Proto-MPEX were performed to identify mechanisms and locations of heat loss from the plasma in the machine, especially in the helicon region. The analyses worked to account for and diagnostically verify as much of the input power as possible. They also identified areas requiring further diagnostic analysis to be implemented in future work.[154] They additionally served as an outline to determine how the data acquisition and analysis processes would be streamlined into a working model for all future power balance studies of Proto-MPEX.

The preliminary power accounting analysis was performed twice. The two analyses applied the same machine operating parameters. However, additional modeling and diagnostic capabilities not available for the first analysis were applied for the second. Data analysis techniques were also improved. As a result, more power was successfully identified and diagnostically verified through the second analysis. Both results are presented below. For the preliminary power balance analyses, power balance is separated into three main components: input power (P_{in}), lost power (P_{loss}), and deposited power (P_{dep}).[155] The input power includes the total power injected into the system. The lost power refers to the power that is lost from the plasma as it travels through the machine between the power source and the end plates. The deposited power refers to the power that is deposited on the end plates.

The power balance experiments were performed using the following machine operating parameters. The magnetic field configuration was a ‘modified flat field’, where the current in the magnet coils was 5900 A for coils 1 & 6-12, 260 A in coils 3 & 4, and 0 A for coils 2 & 5. Coils are numbered in increasing order from left (coil 1) to right (coil 12) (see figure 5.1). The plasma gas type was deuterium, with a puffed gas flow at the gas injection location between coils 4 & 5. For these experiments, the operations were performed in the high-density helicon mode with 200 ms plasma pulses. Only the helicon and pre-ionization 18 GHz ECH provided power to the system.
For the first power accounting analysis, the diagnostic suite included an IR camera, four LPs, four TCs, a filterscope array, a Thomson scattering beam line providing two

[154] Much of which is accomplished in this thesis.
[155] As described in Chapter 4: **POWER BALANCE COMPONENTS & ANALYSIS METHODS**

measurements, and two fluoroptic probes. For the second power accounting analysis, the suite was expanded to include two additional TCs, two additional FPs, two MPs with four total axial scanning locations, four baratrons, and at least three additional measurements from the Thomson scattering beam line. Further, SOLPS modeling was applied during the second analysis. Figure 5.1 provides a diagram of installation locations of the diagnostics available for the first and second power accounting analysis on Proto-MPEX.

For the first analysis, the machine was primarily considered as a whole. For the second analysis, the machine was separated into three regions: helicon, upstream and downstream. The helicon region extends axially from z = 1.0 m to 1.5 m (see figure 5.2). The upstream region extends from the dump plate (z = 0.2 m) to the upstream edge of the helicon region (z = 1.0 m). The downstream region extends from the downstream edge of the helicon region (z = 1.5 m) to the target plate (z = 3.75 m). In this analysis, a power accounting was performed for each of the three regions.

Figure 5.2 provides the magnetic flux mapping for the magnetic field configuration for these experiments. The outermost flux line is delineated by the red contour. The radius of the outermost flux line was used for the plasma radius along the machine axis. The plasma was divided into 0.005 m thick axial slices, creating incremental plasma volumetric slices.

5.1.1 Input Power (P_{IN})

The input power is the total power injected into the system. For both power accounting analyses, since the helicon was considered the main power source, the 5 kW of power from the pre-ionization source were neglected in the input power accounting. The helicon provided an average of 125 kW of forward power, 16.3 kW of which were reflected, and another 2.5 kW of which were lost due to the resistivity of the copper helicon antenna. Forward and reflected powers, together with resistive losses in the antenna and feed circuit, were measured experimentally via directional couplers, a Bird Wattmeter, and an RF magnetic field probe used to determine antenna current. Out of the total 125 kW injected, 106.3 kW were successfully coupled by the helicon antenna wrapping around the aluminum nitride (AlN) window. This is the ‘input power’.

5.1.2 Lost Power (P_L)

The lost power refers to the power that is lost from the plasma between the power source and the end plates. Several different diagnostics were employed to experimentally quantify the lost power, varying by power account analysis. The first analysis applied FPs, LPs, TCs, a TS array and filterscopes. For the second analysis, baratrons and MPs were also applied. The FPs and TCs measure temperature increases to the machine surfaces. The LPs, and TS array measure the plasma electron temperatures and densities. The MPs measure the plasma flow rate. The filterscopes measure line radiation along the length of the machine, highlighting areas of potential plasma impingement on the material surfaces. The baratrons measure the total neutral (D_0, D_2) pressure. SOLPS modeling was employed during the second analysis to quantify loss mechanisms such as charge exchange, excitation, and elastic collisions,

as well as to supplement experimental measurements.

Analysis I

Two installed fluoroptic probes measured the temperature rise of the AlN helicon window. The change in temperature was used to infer the quantity of transmitted power lost directly to the helicon window, using equation 5.1.[156] The average temperature rise measured by the FPs was 1.3°C, yielding an associated power of 17.5 ± 1.4 kW. Thus, out of the 106.3 kW of successfully transmitted power, 17.5 kW (16.4%) was lost immediately to the helicon window and not coupled to the plasma, corresponding to a 'launched' plasma power of 88.8 kW.[157]

$$\dot{Q} = \frac{mc\Delta T}{\Delta t} \tag{5.1}$$

where $\dot{Q}$ is the power [W], m is the mass of the AlN window [2.567 kg], c is the specific heat of the AlN window [780 J/kg.K], ΔT is the temperature rise measured by the FPs [K], and Δt is the plasma pulse length [0.20 s].

The thermocouples installed on the skimmer and RF baffle plates provided additional plasma measurements along Proto-MPEX's length. The average temperature rise during a plasma pulse was used to infer a power loss also using equation 5.1, which is algebraically manipulated below.

$$\dot{Q} = \frac{\rho A_c x c \Delta T}{\Delta t} \tag{5.1}$$

where ρ is the density of stainless steel [8030 kg/m^3], A_C is the cross-sectional area of the drawn disk, x is the thickness of the plate, c is the specific heat of the stainless steel [500 J/kg.K], ΔT is the temperature increase during the plasma pulse [K], and Δt is the pulse length [0.20 s]. The material density and the volume over which the temperature increase was assumed to be uniform and was approximated as a disk, with the plate's thickness. To estimate the cross-sectional area, the installed thermocouple was assumed to be approximately 0.5 cm away from the inner edge. Since the material inside the imaginary circle on which the TC sits would likely be hotter than measured by the TC, a disk with an inner radius of 2.9 cm and an outer radius of 3.9 cm was assumed to experience a uniform temperature rise measured by the installed TC.[158] The average temperature rise measured by the skimmer TC was 0.9°C, yielding a power loss to the skimmer plate of 0.16 kW. The average temperature rise measured by the RF baffle TC was 0.32°C, yielding a power loss to the skimmer plate of 0.06 kW. The lost power measured by the skimmer plate implies that the plasma could be limiting on the skimmer plate.

[156] Further details regarding the FP analysis is available in previously published work [39].
[157] For the purposes of this paper, the term 'launched power' is used to refer to the power that is transmitted to the helicon antenna ('transmitted power') and is not immediately lost to the helicon window.
[158] The installed TC sits radially in the middle of this disk.

The filterscopes were primarily used to identify possible limiting surface locations along the machine length. Suspected locations included the upstream end of the helicon window and the skimmer plate. The filterscopes sampled at eight different port locations along the machine, including two points upstream of the helicon, as shown in figure 5.1.[159] Figure 5.3 provides the emission intensities[160] of the D_α photons along Proto-MPEX's length measured by each of the installed optical fibers. Each intensity measurement represents line plasma radiation at that location.[161] For more direct reference to their locations with respect to the machine components, the emission intensities plot is aligned with the Proto-MPEX diagram.

Figure 5.3 shows that the peak emission intensity occurs at the diagnostic port in between magnetic coils two and three.[162] This port is directly behind the upstream end of the helicon window, supporting the indication in figure 5.2 that the upstream end of the helicon window is a limiting surface. There is another smaller peak in between magnetic coils five and six[163], where the skimmer plate is installed. This supports the indication that the plasma might also be limiting on the skimmer plate. Further, the decrease in line emission downstream near the target plate suggests that plasma radiation is not a significant source of plasma loss.[164] The filterscope spectroscopic signature does not preclude plasma loss through molecular activated recombination (MAR), which does not always have a spectroscopic signature [107, 99].[165] The summation of the energy carried by the D_α photons along the entire machine length is on the order of ten watts. Therefore, D_α line radiation is not considered a significant source of plasma loss for these operating parameters.

The four Langmuir probes, whose scanning locations along the Proto-MPEX device are shown in figure 5.1, provided electron temperature and density measurements. Probes A-C scanned vertically through the plasma, while Probe D scanned horizontally. The IR camera determined the approximate scanning locations of the Langmuir probes through the plasma profile shadows created during each LP scan. LP traces for each LP scan are drawn on the IR-inferred plasma profile using the ResearchIR software [44]. The approximate locations scanned by each LP through the plasma are provided in figure 5.4.[166] It is important to note that probes A-C do not scan through the same plasma location, causing an additional source of variation in their measurements. Additionally, none of the probes scan through the hottest portion of the plasma. This highlights the importance of cross-corroboration between installed diagnostics.

---

[159] There was a ninth location, but the wrong filter lens was installed during operations, causing the gap in the emission intensity plot in figure 5.3.
[160] In photons per second per centimeter squared per steradian.
[161] Each point is connected on the graph for visual purposes.
[162] At approximate axial location of z = 1.0 m
[163] At approximate axial location of z = 1.75 m
[164] Recall plasma radiative loss mechanisms includes Bremsstrahlung radiation, line radiation, and radiation recombination (electron-ion recombination, or EIR) [i.e. 107, 99].
[165] See Chapter 4 of this thesis.
[166] Due to the angled mirror involved in the IR camera set-up, although the IR camera views the back-side of the target plate, the resulting image is mirrored, creating a plasma profile image as if viewing the front side of the target plate. That is, the direction of the magnetic field lines is into the page.

The electron density was relatively constant along the machine's length downstream. It also showed primarily centrally-peaked plasma.[167] The electron temperature decreased along the machine axis. These electron temperature profiles were relatively flat. The electron density and temperature profiles are shown in figure 5.5. The electron temperatures downstream[168] were within the range associated with recombination and electron thermal conduction heat loss mechanisms.[169] However, since the electron density remained relatively constant, recombination was likely not the main cause of axial plasma losses.

Heat and particle flux measurements were inferred from those values using the following equations:

$$\Gamma_{ss} = c_s n_{se} = 0.5\, c_s n_e \tag{5.2}$$

$$\dot{q}_{ss} = \dot{\gamma} \Gamma_{ss} T_e \tag{5.3}$$

$$c_s = \sqrt{\frac{T_e}{m_i}} \tag{5.4}$$

where Γ_{ss} is the particle flux to a solid surface [#/m^2.s], c_s is the sound speed of a deuterium plasma [m/s], n_e is the electron density [#/m^3], n_{se} is the electron density at the plasma sheath edge [#/m^3], $\dot{q}_{ss}$ is the heat flux to a solid surface [W/m^2], γ is the sheath power transmission coefficient, which is assumed to have a value of 5[170], T_e is the electron temperature [J], and m_i is the mass of deuterium ions [kg].[171] The particle and heat fluxes decrease along the machine length. The LP-inferred heat flux[172] decreases from approximately 1 MW/m^2 at probe A to about 0.4 MW/m^2 at probe D. The profiles are primarily centrally peaked. The LP scan-inferred heat fluxes were used to infer power held in the plasma beam.[173]

The Thomson scattering diagnostic provided a 'two-point scan' in between magnetic coils 11 and 12. It provided that last diagnostic measurement prior to the plasma hitting the target plate. The approximate scanning location of the Thomson scattering is determined through diagnostic and machine measurements and alignments. Similar to the Langmuir probes, the TS provides electron density and temperature plasma measurements. Those measurements are used to infer particle and heat flux measurements using equations 5.2-5.4. For each scanned point, the Thompson scattering beam line sweeps over a small sample area, which can be approximated by one point within than area. Figure 5.6 provides an image of the approximate location of

[167] A centrally-peaked plasma is desired for future PMI studies on Proto-MPEX and MPEX.
[168] Shown by probe C and D scans
[169] These mechanisms become prominent at $T_e < 2$ eV [i.e. 105, 107, 111].
[170] This is the approximate value of the sheath power transmission coefficient when the ion contribution is ignored [103].
[171] See [44] for more information on the LP calculations.
[172] That is heat flux to a solid surface.
[173] This process will be describes later in the paper.

the TS profile through the plasma beam. The yellow rectangles depict the sample location, and the two white circular disks represent the associated sample points. The scanning location of probe D is also provided for reference.

The TS-inferred heat fluxes were used to infer plasma beam power in a similar manner to that used for the LP scan.

At the time of the first analysis, Proto-MPEX lacked installed diagnostics to measure the plasma flow direction and speed.[174] Data analysis of the LP and TS measurements assumed sonic flow. Due to the changing plasma radius along the machine length, the accuracy of that assumption was unknown. To adjust for the unknown plasma flow rate, a cross-diagnostic analysis was performed. The sonic flow assumption is the most accurate at the target plate. Therefore, the power deposited on the target plate is used as the 'base'. The LP and TS diagnostic power measurements are inferred by mapping back upstream from that base. To facilitate comparison between the LP, TS, and IR diagnostics, the IR-traces of the LP scans were used to create IR-inferred heat flux profiles.[175] The closest non-target diagnostic to the TS is probe D. Therefore, the heat fluxes inferred from IR camera's 'probe D' trace, from Langmuir probe D and from the TS are compared first. Their heat fluxes are plotted along their normalized scanned location[176], shown in figure 5.7. Since the two-point TS scan is created by approximating two average swept areas as a point, three identical heat fluxes are plotted at each approximate scanning location to account for the averaging.

The profiles across the diagnostics matched well. To determine the power held in the plasma inferred by the TS and probe D, their heat flux values were compared to those of the IR-trace at multiple points, created several heat flux ratios. For the two diagnostics, the heat flux ratios were averaged to create a single average ratio between the measured heat flux of probe D to the IR-trace of probe D and the TS to the IR-trace of probe D. The power held by probe D was calculated by multiplying the probe D:IR-trace ratio by the power deposited on the target plate[177], resulting in a value of 0.31 kW. The power held by the TS diagnostics was calculated by multiplying the TS:IR-trace ratio by the power deposited on the target plate, resulting in a value of 0.72 kW. Although the power measured by the TS was larger than that measured by probe D, the TS was scanning vertically and appears to be scanning through the hottest part of the plasma. The closest vertical probe scan was provided by probe C, which also scanned closer to the hottest spot.[178] The power inferred by this probe was 0.73 kW. Accounting for the fact it was slightly further upstream and not scanning through the hottest portion of the plasma, the similarity between the values increased confidence in the accuracy of the measurements.

In order to determine the power held in the plasma at the remaining LP scanning

[174] Mach probes were applied for this purpose in analysis two.
[175] Through process described in [44].
[176] The normalized scanned location is the radial location of the diagnostic measurement divided by the radius of the last closed flux surface (LCFS) at the axial location of the diagnostic.
[177] The power deposited to the target plate is discussed later in this section.
[178] See figures 5.4 and 5.6 for reference

locations, a multi-step process was applied. First, to enable comparison between the LP scans, averaged heat flux ratios between the upstream probes and probe D were determined through the same process described above.[179] Similarly, to enable comparison between the IR-traces, averaged heat flux ratios between the upstream probe IR-traces and the probe D IR-trace were determined.[180] The shapes of the traces of the LP scans and the IR-traces were similar to each other, especially for probes C and D, which were closest to the target plate. Only the probe A scan was noticeably different from the IR-trace of probe A. This probe was the furthest away from the target plate, accounting for the difference in heat flux magnitude. The peak heat flux for probe A was approximately a factor of 1.6 greater than the corresponding IR-trace. The outer peaks measured by probe A not seen on the IR-trace could be due to plasma edge effects[181] from the proximity to the helicon field. Another explanation is that probe A was the only probe scanning upstream of the skimmer plate. If the plasma was partially limiting on the skimmer, the edges could be scraping off on the skimmer, resulting in their absence from the plasma profile on the target plate. Figure 5.8 provides a comparison in heat flux profiles inferred by the IR camera and the LPs.

To enable comparison between the diagnostics, a final set of ratios was calculated; the probe to IR-trace ratios for their corresponding locations.[182] These final ratios between the LP and the IR-trace for probes A-C are multiplied by the target plate deposited power. The resulting power held in the plasma measured by probe A, probe B, and probe C were 2.23 kW, 1.02 kW, and 0.73 kW, respectively.

The method described uses the heat flux as a metric of comparison. Diagnostically measured electron temperature and density profiles are used to calculate a heat flux that would be measured on a stainless steel plate *if* it was inserted at the profile location, imaged by the IR camera. Since the profiles are one-dimensional and the plasma radius varies, the measured two-dimensional IR image was scaled to compare to the profile data.

Analysis II[183]

The helicon power system transmits 106.3 kW of power into the helicon region. A portion of this power is consumed through atomic and molecular processes such as ionization, vibration, and dissociation, estimated using SOLPS. SOLPS (B2-Eirene) solves for fluid plasma transport along magnetic field lines, which eventually hit machine surfaces or end plates, as well a neutral particle transport [112]. SOLPS modeling[184] suggests that a total of 48.9 kW of power are lost to neutrals along the entire length of the machine, with 30.6 kW, 11.5 kW and 6.7 kW of the losses occurring in the helicon,

[179] That is, there are three new ratios; (1) Probe A: Probe D, (2) Probe B: Probe D, (3) Probe C: Probe D
[180] That is, there are three additional new ratios; (4) IR-trace A: IR-trace D, (5) IR-trace B: IR-trace D, (6) IR-trace C: IR-trace D
[181] Artificial 'spikes' in LP measurement
[182] That is, there are three additional new ratios; (7) Probe A/D: IR-trace A/D, (8) Probe B/D: IR-trace B/D, (9) Probe C/D: IR-trace C/D
[183] Further details regarding the second analysis is available in previously published work [39].
[184] With a correction factor applied to adjust for SOLPS underestimation under the helicon. Correction factor is determined using baratron data.

upstream and downstream regions, respectively. Neutral losses are localized in the helicon region or the area immediately outside the helicon region. For example, the corrected SOLPS neutral losses occurring from an expanded 'helicon' analysis region of z = 0.8 m to 1.8 m total 44 kW (out of 48.9 kW of plasma power lost to neutrals over the entire machine), with only 3.2 kW and 2.2 kW occurring in the remaining upstream and downstream regions, respectively. Figure 5.9 depicts the axial variation in neutral densities inferred by SOLPS modeling and experimental baratron data [39].

To corroborate the SOLPS-estimated value of neutral losses in the helicon region, an upgraded array of four installed fluoroptic probes [54], in good thermal contact with the helicon window, were used to calculate the power loss associated with the heat deposition measured on the window. For this analysis, three FPs were located under the helicon antenna and one was located along the side, in the field of view (FOV) of a FLIR T250 series IR camera. The IR 'helicon' camera is used to corroborate the temperature measurements of the FPs. The change in temperature inferred by each of the four FPs were averaged to provide an average temperature rise on the helicon window, which is used to infer an average power deposition on the window through a 1D heat conduction analysis (see equation 5.1). The FP-inferred averaged temperature increase and power deposition on the helicon window were determined to be 2.5 ± 0.5 °C and 25.2 ± 5.0 kW, or approximately 23.7 ± 4.7 % of the input power. The helicon window extends from approximately z = 1.1 m to 1.4 m. Within this axial region, SOLPS estimates 21.5 kW of power are lost to neutrals, in good agreement with the FP-inferred deposited power.

Thermocouple and filterscope diagnostics installed at the upstream end of the helicon (near z = 1 m) suggest the plasma could be limiting on the helicon window.[185] Magnetic field flux mapping supports this prediction (see figure 5.2). The limiting plasma could account for additional heat loss not attributed to neutral processes. Thermocouples [53] were installed on stainless steel machine surfaces (outside of vacuum) at the upstream and downstream ends of the helicon region (z = 1.0 m and z = 1.5 m, see figure 5.1) The TC-inferred power depositions on the upstream edge (z = 1.0 m) and downstream edges (z =1.5 m) of the helicon region were determined to be 13.7 ± 1.0 kW (1.5 ± 0.1 °C) and 10.3 ± 0.8 kW (1.1 ± 0.1 °C), respectively. Thus, the total deposited heat inferred by TCs and FPs on the machine surfaces is 49.2 ± 6.8 kW, or 46.3 ± 6.4% of the input power. Plasma losses due to plasma limiting on the helicon window in addition to SOLPS neutral losses can account for the experimentally measured total deposited heat to machine surfaces in the helicon region.

Like the first analysis, the amount of power held in the plasma was approximated by double Langmuir probes. The downstream LPs measurements from Analysis I were supplemented by both upstream and downstream Mach probe measurements.[186] The combination of LP and MP measurements enabled parallel heat conduction and convection measurements along the machine length. The on-axis electron densities and temperatures used to determine the parallel heat transport were provided by MPs, LPs,

[185] This was expected in analysis 1.
[186] The MPs could change installed locations and scanned radially through the plasma

and a TS array. Their axial locations, electron density and temperature values, available Mach numbers and relevant diagnostic are provided in table 5.1.

The Mach probe indicated plasma flow was nearly stagnant at these two locations, with average Mach numbers of about 0.07 at both z = 1.0 m and z = 1.5 m. Thus, the plasma transport was assumed to be dominated by parallel heat conduction at the helicon region boundary.[187] For this analysis, radial heat conduction was ignored, as were ion contributions [113].

Equation 5.5 was applied to determine the parallel heat conduction [113, 20].

$$q_{cond} = -k_{||}\nabla T_e = -k_{||}\frac{dT_e}{dz} \tag{5.5}$$

where q_{cond} is the parallel conductive heat flux [W/m^2], $k_{||}$ is the parallel electron thermal conductivity [W/m^2.K], ∇T_e is the electron temperature gradient (which simplifies to $\frac{dT_e}{dz}$ [J/m]).

The electron temperature gradient, $\frac{dT_e}{dz}$, was determined by plotting on-axis electron temperatures along the length of the machine and applying a power-base equation fit. The upstream and downstream regions were assigned separate fits. The derivative of these fits estimated the axial electron temperature gradient. Since electron temperature and density values are unknown directly under the helicon, the electron temperature was fixed to the on-axis electron temperature measured at z = 1.5 m.

The heat conduction analysis was performed multiple times to create a range of possible heat conduction values (shown in brackets in table 5.2). Using the radius of the outermost flux line to determine the cross-sectional area of the plasma column, the power carried by parallel heat conduction was calculated. The results for axials locations at z = 0.6, 1.0, 1.5, and 3.4 m are summarized in table 5.2.

While the Mach numbers are nearly zero in the helicon region (M (z = 1.0, 1.5) = 0.07), the axial convective heat transport was non-negligible. For simplicity, both T_e and n_e profiles were assumed to be flat for these analyses. The power carried in the plasma via convection was determined using equation 5.6.

$$q_{conv} = 5 n_e v T_e \tag{5.6}$$

$$v = c_s M = \sqrt{\frac{2T_e}{m_i}}\, M$$

[187] Parallel heat convection analysis was still performed and is provided in the next section

where q_{conv} is the convective heat flux [W/m^2], n_e is the electron density [m^{-3}], T_e is the electron temperature [J], v is the plasma flow velocity [m/s], c_s is the ion sound speed through the plasma [m/s], M is the Mach number, and m_i is the mass of deuterium [kg]. Ion temperatures are assumed to be approximately equal to electron temperatures. This assumption was supported by spectroscopic data with argon puffing in previous experiments. A uniform plasma profile was assumed. Table 5.2 summarizes the convective power at four axial locations on Proto-MPEX.

It is important to note the sensitivity of the probe measurements at the helicon region edges (z = 1.0 m and z = 1.5 m). All probe measurements are perturbative to the plasma and are particularly perturbative near the helicon region, close to the helicon source. Two methods were applied to obtain the plasma measurements at these locations, which are described in detail in previously published work [39]. The two methods create a range of on-axis measurements. At z = 1.5 m, the on-axis measurements range from T_e = 3.8 eV and n_e = 5.3e19 m^{-3} (standard method) to T_e = 6.4 eV and n_e = 2.9e19 m^{-3} (alternative method). The increase in T_e at z = 1.5 m in the alternative method drastically increases the parallel electron temperature gradient. Since the downstream heat conduction is strongly dependent on the parallel electron temperature gradient, the increase changes the power balance analysis, both upstream and downstream of the helicon region.

Using the alternative T_e and n_e values at z = 1.5 m, the power carried in the plasma by parallel heat conduction and convection at z = 1.5 m increase to 28.5 kW and 2.7 kW, respectively. At the upstream edge (z = 1.0 m), the heat conduction and convection become 12.0 kW and 3.8 kW. Using the alternative method, of the 106.3 kW of power entering the helicon region, 49.2 kW of power are measured on the machine surfaces and 47.0 kW are transported out of the helicon region, accounting for 96.2 kW of power. The total power being carried into the upstream and downstream regions of the plasma ranges from 7.2 to 15.8 kW and from 4.4 kW to 31.2 kW, respectively, depending on the measurement method applied at z = 1.5 m. Recall the total power loss according to SOLPS modeling in the upstream and downstream regions are 11.5 and 6.7 kW, respectively, creating a range for the total parallel heat transported out the helicon region. For example, if 11.5 kW of power are lost by neutrals upstream of z = 1.0 m, then it is logical that more than 7.2 kW of power should be measured as carried into the upstream region. Literature reviews of previous helicon experiments support the idea that more power is carried out of the helicon region than the first measurement method suggests, increasing the confidence in the higher heat transport values of the measured range for Proto-MPEX. The analysis is described in more detail in [39]. Analysis II proved accurate plasma measurements at z = 1.5 m were pivotal, in particular with respect to where to apply future efforts to identify power loss mechanisms. If the plasma values are closer to T_e = 3.8 eV and n_e = 5.3e19 m^{-3}, then efforts to increase efficiency should be focused in the helicon region. If closer to T_e = 6.4 eV and n_e = 2.9e19 m^{-3}, then the power balance of the helicon region is effectively complete and efforts should be focused in the downstream region. The degree of uncertainty in combination with the strong influence the z = 1.5 m measurements have on the overall power balance highlighted the need for better, non-perturbative measurements. A new HELIOS diagnostic, currently installed at z = 1.5 m, puffs gas into the plasma to obtain electron

temperature and density measurements in a much less perturbative manner [114]. The diagnostic is still being developed and will provide further constraints to this power balance, at z = 1.5 m and perhaps at z = 1.0 m as well, when fully commissioned.

5.1.3 Deposited Power (P_{DEP})

The deposited power refers to the power that is deposited on the end plates. Thermocouples installed on the dump and target plates serve to ensure the camera is properly calibrated to permit accurate data analysis. The A655sc camera was used to acquire plasma heat profiles of both the dump and target plates, viewing from the non-plasma facing side of the two plates. Figure 5.10 depicts the profiles of plasma deposited on the dump and target plates acquired by the IR camera. The machine operating conditions result in a centrally-peaked plasma with a lower outer 'lobe'.

The two profiles on the end plates are very similar to each other. Differences in the expansion of the magnetic flux field lines at each end plate result in the radius of the 'lobe-less' dump plate profile being about four times as large as that of the target plate profile, which are 6.3 cm and 1.5 cm, respectively. The radius of the 'lobey' target plate profile is about 2.0 cm. The lobe is suspected to be scraped off from the plasma in the upstream region prior to the arriving at the dump plate, perhaps near z = 1.0 m as suggested by TCs and filterscopes. The maximum temperature rise (ΔT) measured on the target plate was 90.8°C and the maximum ΔT measured on dump plate was about 2.6°C. The analysis method to determine the deposited power differed slightly between the first and second analyses. During the first analysis, the ResearchIR program was the primary analysis program used to determine measured temperature increases. For the second analysis, the data analysis suite included a Matlab script to improve accuracy. The two analysis methods yielded similar results. In analysis one, the resulting maximum heat fluxes were approximately 0.6 MW/m^2 and 0.13 MW/m^2 for the target and dump plate, respectively.[188] The difference in the heat flux is the result of the magnetic flux line expansion at the dump end. The corresponding total deposited power on the target and dump plates were 0.34 kW and 0.73 kW, respectively. In analysis two, the maximum heat fluxes were approximately 0.9 MW/m^2 and 0.15 MW/m^2 for the target and dump plate, respectively. The total deposited power on the target and dump plates are 0.6 kW and 0.8 kW, respectively. The values from both analyses one and two were comparable to the initial SOLPS modeling of the power deposited on the target and dump plates, which are 0.94 kW and 2.1 kW, respectively. Moreover, these measured IR values were consistent with the total conductive and convective power calculated near the end plates in analysis two, which total 0.6 kW in front of the target plate (z = 3.4 m) and 1.6 kW in front of the dump plate (z = 0.6 m), for either measurement method used.

5.1.4 Summary

Upon the completion of the power balance using the first analysis method, 18.8 kW of the 106.3 kW of the input power were diagnostically verified. Approximately 17.7 kW of power were categorized as 'lost' power, with about 17.5 kW of power measured on the helicon window by fluoroptic probes and 0.2 kW of power measured on the skimmer

[188] Using the analysis method described in [44].

and RF baffle plates by installed thermocouples. Approximately 1.1 kW of power were measured on the end plates by the IR camera, with about 0.75 kW of power on the dump plate and 0.35 kW of power on the target plate.

Upon completion of the power balance using the second analysis method, 52.3 kW of power were diagnostically verified, where 50.9 kW of power have been lost to machine surfaces (P_L) and 1.4 kW have been deposited on the end plates (P_{DEP}). The power lost as heat on the helicon window, 25.2 ± 5.0 kW, was measured by fluoroptic probes. Thermocouples installed at the upstream and downstream edges of the helicon region suggest an additional 24.0 ± 1.8 kW of power is lost to the machine walls as heat, resulting in a total of 49.2 ± 6.8 kW of deposited power, close to the SOLPS estimated power loss due to neutral processes in this region of the machine. Out of the 106.3 kW of input power, up to 96.2 kW, or 90.5%, have been accounted for within the bounds of the helicon region, if the upper range of the values measured at z = 1.5 m are used.

Future work highlighted by both analyses include two main foci. The first was to investigate radial transport effects, which had previously been excluded. The second was to apply a series of new diagnostics to improve experimental measurements along the machine axis. Diagnostics include the HELIOS puffer diagnostic to provide non-perturbative electron temperature and density measurements in the helicon region, AXUV and SXR photodiodes to measure radiative losses in the downstream region and two resistive bolometers to also measure total radiative losses in the downstream region. The addition of these diagnostics was intended to allow better quantification of the overall Proto-MPEX power accounting. They are applied to the main power accounting analysis delineated in this thesis.[189]

5.2. Helicon Power Source Analysis of the Prototype Material Exposure eXperiment (Proto-MPEX) using Fluoroptic Probes

Recall the primary purpose of Proto-MPEX is to develop plasma heating source concepts for MPEX, which include a helicon antenna surrounding an aluminum nitride window, whose strong electromagnetic (EM) fields inhibit reliable data collection of the helicon region from most installed diagnostics. The helicon antenna, as the primary source of power for this thesis' power accounting study, is of particular importance. Five fluoroptic probes installed under the antenna in thermal contact with the helicon window estimate heat loss from the plasma under the helicon antenna via observed temperature increases on the helicon window. Analyzed in conjunction with installed thermocouples (TCs), the FPs quantify the helicon plasma, identifying loss mechanisms for specific machine operating parameters.

5.2.1 Experiment

The FPs and supplementary TCs were applied to quantify the plasma in the helicon region, defined as the region containing the helicon bounded by its two nearest diagnostic ports (z = 1.0 m and z = 1.5 m, see figure 5.1), for different input powers, pulse lengths, magnetic field configurations and gas flow rates. Table 5.3 summarizes the magnetic field

[189] See Chapter 6: **FULL POWER BALANCE**

configuration variations included in this paper. Table 5.4 summarizes the gas puff rate variations. Table 5.5 summarizes the gas puffing locations.

The resulting magnetic flux lines for each configuration are shown in figure 5.11. The field lines are constructed based on the machine geometry and magnetic field strength on each magnet coil.

5.2.2 Data & Analysis

The analysis methods implemented to infer the power deposited on the helicon window and spool pieces 2.5 and 4.5 using the FPs and TCs, respectively, are provided in previously published work [39].

To determine the effect of large variations in magnetic field configurations on the power deposited to the helicon window and nearby machine surfaces, configuration 3 and 4 were compared using gas puff type 2 (see tables 5.3 and 5.4). The plasma pulses were 300 ms and the input power was approximately 100 kW. For configuration 3, the FP-inferred shot-averaged power deposition on the helicon window was determined to be 34.8 ± 3.3 kW. One-dimensional heat conduction analyses using equation 5.1 were performed at each TC location (z = 1.0 m, 1.5 m) for the same plasma pulses, where m is 3.6 kg, c is 500 J/kg.K, ΔT is the temperature rise measured by the TC [K], and Δt is 0.3 s. The TC-inferred shot-averaged power depositions on the upstream edge (z = 1.0 m) and downstream edges (z =1.5 m) of the helicon region were determined to be 4.4 ± 0.3 kW and 5.0 ± 1.0 kW, yielding a total deposited power in the helicon region of 44.7 ± 4.6 kW. For configuration 4, with the same gas puff rate at configuration 3, the FP-inferred shot-averaged power deposition on the helicon window was determined to be 18.3 ± 3.3 kW, or approximately 18.3% of the input power. Since these machine parameters are close to those used for an FEA-1D heat conduction comparison[190] (same gas puff type and similar configuration), it is reasonable that the percent power lost to the helicon window for the two experiments would be close in value (18.3% vs. 16.3%). The TC-inferred shot-averaged power depositions at z = 1.0 m and 1.5 m were 11.7 ± 0.8 kW and 9.3 ± 0.7 kW, respectively. The total deposited power in the helicon region was 39.3 ± 4.8 kW. When the gas flow rate was increased to gas puff type 3 for configuration 4, the FP-inferred deposited power increased to 25.9 ± 3.3 kW, while the TC-inferred deposited power increased to 12.8 ± 1.0 kW (z = 1.0 m) and 10.2 ± 0.8 kW (z = 1.5 m), yielding the most total deposited power in the helicon region, at 48.9 ± 5.1 kW.

Trends observed in this analysis reflect expectations. Based on the magnetic field configuration (see figure 5.9), it is reasonable that the power deposited to the machine surface at z = 1.0 m would be much higher for configuration 4 than for configuration 3, since the outermost flux line in configuration 4 appears to contact with the machine surface at that axial location. It also is reasonable that the overall power measured on the helicon window would decrease as the magnetic field strength around the helicon window increases, going from configuration 3 to 4. The stronger field reduces the plasma radius, pulling the plasma away from the helicon surface.

[190] See analysis in [39].

Further, when the gas puff is increased for configuration 4, it is reasonable that the additional particles would increase the number of particle collisions, which would increase the number of particles escaping from the main plasma, thereby increasing the power deposited to the helicon window and machine surfaces. The effect is strongest under the helicon, where the deposited power increases from 18.3 kW to 25.9 kW. A similar effect is observed in the power deposited to machine surfaces at z = 1.5. The power deposited at z = 1.5 m is a factor of two greater for configuration 4 in comparison to configuration 3. While the gas flow rates are the same, the gas fueling locations are different (see table 5.5). The gas fueling is located at z = 1.0 m and 1.5 m for configurations 3 and 4, respectively. Therefore, the gas pressure at z = 1.5 m is greater for configuration 4 than for configuration 3, thereby increasing the number of particle collisions. This would increase the total particles escaping from the plasma and increase the power deposited to the machine surface.

5.2.3 Summary & Future Work

Fluoroptic probe diagnostics in conjunction with installed TCs and an IR camera provide information about the plasma under the helicon for the first time. Two magnetic field configurations and two gas puff rates were directly compared, highlighting differences in plasma behavior in the region near the helicon. Results suggest higher puffed gas increases power deposition to the helicon window, while higher magnetic fields around the helicon decrease it. Further experiments are required to confirm these correlations.

5.3. Overall Summary

A considerable amount of data acquisition and analysis has been completed leading up to the final power balance provided in the next chapter in order to maximize its effectiveness and accuracy. A preliminary power accounting analysis was performed twice. The two analyses applied the same machine operating parameters. Additional modeling and diagnostic capabilities, as well as improved data analysis techniques, were employed for the second analysis (Analysis II). In Analysis I, 18.8 kW of the 106.3 kW of input power were diagnostically verified, with 17.7 kW of power lost to heating machine surfaces and 1.1 kW deposited to the end plates. In the improved Analysis II, 52.3 kW of the 106.3 kW of input power were diagnostically verified, where 50.9 kW of power were lost to the machine surfaces (P_{loss}) and 1.4 kW were deposited on the end plates. Up to 90.5% of the input power was accounted for in the helicon region. The two power balance analyses highlighted areas for future work, which included investigating radial transport effects and installing new diagnostics to improve experimental measurements along the machine axis.

The helicon region was further analyzed using installed fluoroptic probes and thermocouples to identify loss mechanisms for specific machine operating parameters. Results suggest higher puffed gas increases power deposited to the helicon window, while higher magnetic fields around the helicon decrease it.

CHAPTER 6: FULL POWER BALANCE

To estimate a full power balance of Proto-MPEX, a set of boundaries were applied. The boundaries included a specific set of machine parameters, a set of assumptions about the plasma and power conversions, and a set of fully calibrated installed diagnostics for plasma measurements.

6.1. Configuration Boundaries

The full power balance performed is defined by the following machine operating parameters listed in figure 6.1. PS1 refers to magnet coils 1 and 6-9. PS2 refers to coils 10-12.

Figure 6.2 provides the magnetic field flux field lines[191] ('flux tube' lines) and the magnetic field strength along the machine axis for the magnetic field configuration used in the power balance.

Figure 6.2(a) depicts the magnetic field line mapping along the machine length. The blue lines represent the various flux tube lines and the red line represents the outermost flux line (OFL). The radius of the plasma at any given *z*-location is defined by the radius of the OFL. The field line mapping depicts how the plasma expands and contracts as it travels along the machine. The expansion and contraction provide insight not only into locations where the plasma may be impinging on machine surfaces, but also the plasma flow rate. The more condensed the field lines, the faster the plasma should be flowing, if the plasma behaves as an incompressible fluid.[192] Figure 6.2(b) depicts the variation in the on-axis[193] magnetic field strength along the Proto-MPEX machine. The coils are numbered 1-12. Notice the field dips in between the magnet coils, corresponding to expansions in the magnetic field lines in figure 6.2(a). Coils 2-4 have significantly lower currents applied as compared to coils 1 and 6-12 (see figure 6.1). The lower currents result in lower magnetic fields, which is apparent in the drop in the magnetic field strength at coils 2-5.

6.2. Diagnostics

The power balance used many but not all the diagnostics installed on Proto-MPEX. Table 6.1 lists the diagnostic suite used to acquire data for the power balance analysis, the relevant measurements, relevant installation locations, and assigned diagnosticians. Figure 6.3 provides a visual representation of the installation locations of the diagnostics of the Proto-MPEX device.

6.3. Modeling

A combination of the MATLAB and Python programming languages, the THEODOR programming code, and the COMSOL simulation software program was applied over the course of the power balance analysis, with an emphasis on MATLAB and

[191] Also referred to as 'flux tube lines'.
[192] Experimental analysis suggests this may behave as a compressible fluid. Further analysis is required.
[193] That is, at plasma radius, *r*, equal to zero.

THEODOR[194]. This subsection describes their relevant applications in the power balance analysis.

6.3.1 MATLAB

MATLAB is the primary programming language and numerical computing environment used for all diagnostic analyses, especially those of the IR camera. While the IR camera acquires images through the FLIR-provided ResearchIR program[195], the plasma shot is also processed into MATLAB, through which the majority of the IR data analyses occur. Calculations of deposited heat and power to machine surfaces measured by thermocouples and fluoroptic probe are conducted in MATLAB. Neutral gas pressures acquired through the baratrons are processed in MATLAB. The conductive and convective powers along the machine length are calculated via MATLAB. It is also the program used to produce all figures and plots in this thesis, including those of COMSOL and THEODOR. It is used to map plasma heat traveling along magnetic field lines, to facilitate inter-shot analysis, and determine error propagation. Nearly all the modeling and calculations employed over the course of the analyses in this thesis have interfaced with the MATLAB program.

6.3.2 THEODOR

On Proto-MPEX, the THEODOR code is used to determine the heat fluxes and powers deposited to the end plates, based on data acquired from the IR cameras.[196] The THEODOR code was developed by scientists at the Max Planck Institute for Plasma Physics (IPP) in Garching, Germany and is the standard analysis program used to determine heat fluxes from IR thermography data across multiple fusion research programs globally. Using the material and physical properties of the end plate, the code calculates a 2D heat flux profile (1D along the target surface and 1D into the target thickness) on the end plate from IR-measured surface temperatures, $T(s,t)$, where T is the temperature measured by the IR camera, s is the y location along the target surface at a selected x value[197], and t is the time of the measurement. The two-dimensional temperature distribution (and corresponding heat flux) is calculated along the surface of the target and into the end plate; that is, along the plate thickness [115]. Additional information regarding the THEODOR program can be found in previously published works [115].

After a vertical slice through the center of the temperature profile is made, THEODOR determines the corresponding heat flux from the selected line temperature profile. The line slice heat flux is plotted along surface location, s. Assuming radial symmetry, the center peak and outer edge of the profile are used to determine the plasma profile area. The heat flux is integrated from the edge to the center to calculate the corresponding power deposited on the target from the heat flux profile. To ensure any asymmetries in the heat flux profile are accounted for, the heat flux integration is performed twice, from

[194] THermal Energy Onto DivertOR (THEODOR)
[195] See Chapter 3.
[196] MATLAB codes are additionally employed during this process.
[197] This is for a vertical sample of the target surface temperature. For a horizontal sample, s would represent the x location along the target surface with a fixed y value.

the right side of the profile (s ~ 0 m) to the center (s ~ 0.03 m) and from the left side of the profile (s ~ 0.06 m) to the center. The resulting two calculated powers are averaged together for the final deposited power value. Figure 6.4 depicts the plasma temperature profile for a helicon-only pulse obtained from the IR camera and the heat flux profile corresponding to the line trace through the temperature profile.

6.3.3 PYTHON

The Python programming language is applied only as an intermediary program between the THEODOR analysis and additional MATLAB analyses. The IR data is initially acquired and analyzed via MATLAB. That data is then processed into Python so the THEODOR code can interpret it and perform the heat flux calculations. MATLAB extracts the analyzed data back out of Python afterward.

6.3.4 COMSOL

COMSOL Multiphysics is a simulation software program that provides multiphysics and general engineering modeling. The COMSOL program is used to create 3D heat flux profiles of the target plate, using MATLAB-processed IR data. The specific COMSOL code applied in this thesis uses the same material property inputs for the target plate as the THEODOR program. The main differences between the two programs are the dimensionality and the analysis method. The THEODOR program is only one-dimensional along the surface of the target plate, while the COMSOL code is two-dimensional. The THEODOR program assumes no heat flows through the sides of the target plate and uses a forward-time center spaces (FTCS) finite difference analysis method [115]. The COMSOL code assumes the back of the plate is adiabatic and the plate sides are radiative [116]. Additional assumptions and process techniques are further described in previously published work [116].

6.4. Input Power

As previously stated in chapter 4, the input power is the total power injected into the system. The main power source was the helicon antenna. The 5 kW of power provided by the pre-ionization power source were neglected from the total source input power. The helicon supplied an average of 101.3 $\pm$ 3.4 kW of forward ('injected') power, with an average of 19.3 $\pm$ 2.3 kW of that power reflected and another 2.6 $\pm$ 0.3 kW of power lost to the resistivity of the helicon antenna. The method of calculating the forward, reflected and resistive powers is described in previously published work [39]. Out of the 101.3 kW of forward power applied to the helicon system, approximately **79.4 $\pm$ 4.2 kW** of power were successfully coupled by the antenna wrapping around the helicon window. This is the 'input power' for the power accounting. The total input power efficiency was **78.4 $\pm$ 1.5 %.** Figure 6.5 provides a diagram of Proto-MPEX, highlighting the input power component of the power balance on the device. The machine is separated into the sub-regions used for the region efficiency analysis in section 6.7. The green arrows depict the power in the plasma going into each sub-region of the machine. The red arrows depict the power leaving the plasma in each sub-region. The locations of the end plates and skimmer and RF baffle plates are also provided

6.5. Lost Power

The lost power is the power lost from the plasma between the power source and the end plates. The diagnostic suite used to experimentally quantify the power lost includes FPs, LPs, MPs, two TS arrays, in-vessel and ex-vessel TCs, baratrons, filterscopes and an AXUV photodiode (see table 6.1). The thermocouples and fluoroptic probes measure machine surface temperature increases. The Langmuir probes and TS arrays measured the electron densities and temperatures. The Mach probes measured the plasma flow rate. The baratrons measure the total neutral deuterium (D_0, D_2) pressure. The filterscopes measure the line radiation along the machine length, highlighting areas of possible plasma contact with machine surfaces (see table 6.1). The photodiode measures photon radiation.

To predict the power lost from the plasma, the radial and axial electron densities and temperatures along the machine were inferred through MATLAB based on the on-axis electron density, electron temperature and plasma flow measurements provided by the LPs, MPs, and TS array. Table 6.2 summarizes those measurements.

Based on the radial probe scans at each axial location, the electron temperature profiles are considered to be radially flat and the electron density profiles radially symmetric and centrally-peaked. For each z location, the electron temperature in the radial direction is set equal to the measured on-axis (r = 0) electron temperature values. Figure 6.6 depicts the on-axis electron temperature measurements along the machine length and the axial data fit. It is important to note that there are no available diagnostics sampling the actual plasma under the helicon window. Since the electron densities and temperatures are unknown directly under the helicon, the on-axis electron temperatures and densities are set to the on-axis measurements estimated at axial location z = 1.5 m. It is also important to note that a probe scan was not available at the downstream end of the helicon region (z = 1.5 m). The on-axis electron temperatures and densities were estimated based on trends in the downstream electron temperature and density measurements, as well as those in previous power accounting analyses. The best-approximation for the electron density and temperature at z = 1.5 m are 3e19 m^{-3} and 9.0 eV, respectively.

Figure 6.7 provides the contour plot of the electron temperature in the radial and axial directions based on the electron temperature fits shown in figure 6.6. Since the electron temperature profile is considered to be radially flat, there is no variation in the radial direction. Beyond the plasma radius, the electron temperature was assumed to be zero.

The on-axis electron density along the machine length is determined using the probe measurements. The radial variation is defined as a function of plasma radius, r, and azimuthal magnetic vector potential, A_ϕ, at each axial location, to ensure the electron density follows the magnetic field lines. The contours of rA_ϕ correspond to the magnetic flux field lines [117]. Equation set 6.1 describes the relationship for the radial variation in electron density [117].

$$n_e = \begin{cases} n_{e,peak}(1-\chi^a)^b + n_{edge} & \chi \le 1 \\ n_{edge} & \chi > 1 \end{cases}$$
$$\chi = \frac{A_\phi r}{A_{\phi,LF} R} \tag{6.1}$$

where n_e is the radial component of the electron density at a given axial location, z, $n_{e,peak}$ is the peak electron density, defined as the on-axis electron density whose axial profile is shown in figure 6.8, n_{edge} is the electron density at the edge of the radial plasma profile, R, and is held at a constant value of 1e16 m^{-3}. Constants a and b are set to 2 and 6, respectively. A_ϕ is the magnetic vector potential, r is the given radial location, and $A_{\phi,LF}R$ is the limiting magnetic flux line; that is, the flux line that first intersects the machine surface in the helicon region. χ is the ratio of the radially local magnetic flux line, $A_\phi r$ and the limiting flux line, $A_{\phi,LF}R$ [117].

Figure 6.8 depicts the on-axis electron density measurements along the machine length and the axial data fit.[198] The electron density under the helicon (from z = 1.0 to 1.5 m) is set to the on-axis electron density estimate at z = 1.5 m.

Figure 6.9 provides the contour plot of the electron density in the radial and axial directions based on the electron density fits shown in figure 6.8. The radial variation follows similar trends as the plasma radius variations along the machine length.

6.5.1 Parallel heat transport

The parallel heat transport in the plasma was determined from the on-axis electron temperature and density measurements acquired by the LPs, MPs, and TS diagnostics (see table 6.2) and their curve fits. Recall that the electron density and temperature values at the downstream edge of the helicon region (z = 1.5 m) are best-approximations equal to 3e19 m^{-3} and 9.0 eV, respectively. Similarly, Mach values were not obtained at the downstream edge of the helicon region and the central chamber (z = 2.2 m). Therefore, these values were given a best approximation based on trends in the available plasma Mach number measurements, as well as those in previous power accounting analyses, and the magnetic flux field lines. The best-approximation of the Mach number at z = 1.5 m was assumed almost equal to the Mach number at the upstream edge of the helicon region (z = 1.0 m), with a value of 0.08. Previous analyses have suggested that the flow is effectively stagnant at the edges of the helicon region and the Mach numbers on either end are approximately equal to each other. The best-approximation for the Mach number in the central chamber was based on the Mach number at z = 0.6 m, since the radius of the plasma at this location is close to the plasma radius in the central chamber, as well as the closest downstream Mach number measurement, which was sampled at z = 3.1 m. Taking axial locations and plasma

[198] The best reasonable assigned fit was a linear interpolation between data points. Based on experimental data, the electron density is assumed to remain constant from the most upstream and downstream locations to their respective dump and target plates.

radii[199] into account, the best-approximation in the central chamber was given a value of 0.2.

Conduction

Since Mach probe measurements show the plasma is nearly stagnant on the edges of the helicon region, the plasma transport was assumed to be dominated by parallel heat conduction at the helicon region boundary. Previous work on helicon linear devices has demonstrated that the electron temperature (and therefore the heat transport) is mainly determined by heat conduction [113, 39]. For this analysis, as well as for this thesis power balance, radial heat conduction and ion contributions were ignored [113]. A similar set of equations to those used in previously performed power accounting studies on Proto-MPEX [39] was applied to determine the parallel heat conduction [113, 20].

$$q_{cond} = -k_{||} \nabla T_e = -k_{||} \frac{dT_e}{dz} \tag{6.2}$$

with the defining equation set 6.3 [39]:

$$k_{||} = \frac{3.2 \tau_T n_e T_e}{m_e}$$

$$\tau_T = \left[\frac{1}{\tau_e} + \nu_{D,tot} \right]^{-1}$$

$$\tau_e = \frac{16 \pi \varepsilon_0^2 \sqrt{m_e} T_e^{1.5}}{n_e e^4 \ln(\Lambda)}$$

$$\Lambda = 12\pi \sqrt{\frac{\varepsilon_0^3 T_e^3}{n_e e^6}}$$

$$\nu_{D,tot} = \nu_{D2} = \sum_j (q E_j K_{v,j})_{D2} \tag{6.3}$$

where q_{cond} is the parallel conductive heat flux [W/m^2], $k_{||}$ is the parallel electron thermal conductivity [W/m^2.K], ∇T_e is the electron temperature gradient (which simplifies to $\frac{dT_e}{dz}$ [J/m]), n_e is the electron density [m^{-3}], T_e is the electron temperature [J], m_e is the electron mass [kg], τ_T is the total collisional time for both electron and neutral collisions [s], τ_e is the electron collisional time [s], e is the electron charge [C], ε_0 is the permittivity of free space [F/m], Λ is the Coulomb logarithm [dimensionless], $\nu_{D,tot}$ is the total neutral

[199] Which is defined by the outermost magnetic field flux line.

collisional frequency, which is defined as the molecular collisional frequency, ν_{D2} [s^{-1}], n_{D2} is the molecular deuterium density [m^{-3}], and $\sum_j (qE_j K_{\nu,j})_{D2}$ [$W.m^3$] is the summation of the molecular deuterium collision loss densities estimated from baratron data.

As with previous Proto-MPEX power balance analyses, the electron temperature gradient, $\frac{dT_e}{dz}$, was determined by plotting on-axis electron temperatures along the length of the machine and applying a MATLAB fit (see figure 6.6). The derivative of these fits estimated the axial electron temperature gradient. To calculate the conductive power from the conductive heat flux (see equation 6.2) along the machine length, the heat flux is integrated from the plasma radial edge to the center. Figure 6.10 depicts the resulting parallel power conduction. The power being transported out of the helicon region and downstream towards the target is **25.4 ± 3.6 kW**.[200] The power transported by conduction upstream towards the dump plate is **7.2 ± 1.2 kW**.[201] The conductive power contribution to the parallel heat transport drops off dramatically downstream of the helicon. Near the target plate, the contribution is nearly zero. The plasma appears to remain conductive upstream as the plasma approaches the dump plate, potentially because the gas fueling location is upstream. Recall the dump plate is located at z = 0.2 m, delineated by the solid black line in figure 6.10. Any modeled losses due to deuterium processes after this point are artificial.

The heat conduction analysis was performed multiple times to create a range of possible heat conduction values.

Convection

The percent contribution of the convective power to the parallel heat transport follows the general complementary trend to the conductive power contribution. Downstream of the helicon region, the heat transport goes from being nearly completely conductive to completely convective. Upstream of the helicon region, the heat transport also goes from being conductively dominant to convectively dominant, but the ratio of conductive to convective transport is more balanced than it is in the downstream region.

Although the Mach numbers are nearly zero at the edges of the helicon region (M (z = 1.0, 1.5) = 0.1), the axial convective heat transport at these locations was measurable. The convective power was calculated using equation set 6.4:[202]

$$\mathrm{q_{conv}} = 5\mathrm{n_e v T_e} \tag{6.4}$$

$$\mathrm{v} = \mathrm{c_s M} = \sqrt{\frac{2\mathrm{T_e}}{\mathrm{m_i}}}\,\mathrm{M}$$

where q_{conv} is the convective heat flux [W/m^2], n_e is the electron density [m^{-3}], T_e is the electron temperature [J], v is the plasma flow velocity [m/s], c_s is the ion sound speed

[200] Calculated at z = 1.5 m.
[201] Calculated at z = 1.0 m.
[202] Equation 6.8 is a reproduction of equation 5.6

through the plasma [m/s], M is the Mach number, and m_i is the mass of deuterium [kg]. Ion temperatures are assumed to be approximately equal to electron temperatures. This assumption was supported by spectroscopic data with argon puffing in previous experiments. As previously stated, the temperature radial profile was assumed to be flat and the density radial profile is centrally peaked and defined by equation 6.1. To calculate the convective power from the convective heat flux (see equation 6.4) along the machine length, the heat flux is integrated from the plasma radial edge to the center. Despite being nearly stagnant, the high electron density at the upstream edge of the helicon region and high electron temperature at the downstream edge of the helicon region resulted in convective powers of 3.1 ± 0.7 kW and 3.0 ± 0.5 kW at z = 1.0 m and 1.5 m, respectively. Figure 6.11 depicts the variation in the parallel convective power along the machine. The convective power fit does not include the data point at z = 3.1 m. The probe sampling the plasma at this location was found to be drooping near the end of the scan.[203] This results in the probe sampling closer to the plasma edge, where the plasma density and flow are lower, and therefore yields an artificially low convective power measurement.

Table 6.3 summarizes the conductive and convective powers held in the plasma at along Proto-MPEX. The power being transported through the plasma at z = 3.1 m is highlighted in light red since the probe measurements yield as suspiciously low convected power.

Figure 6.12 provides a diagram of Proto-MPEX, building off of figure 6.5, highlighting the parallel power transport through the sub-regions of the machine, as well as the input power component of the power balance. The green arrows depict the power in the plasma traveling into each sub-region of the machine. The red arrows depict the power leaving the plasma in each sub-region.

6.5.2 Collisional losses

The helicon system injects 79.4 kW of net input power into the helicon region (z = 1.0 to 1.5 m). A portion of this power is lost due to ionization, excitation, dissociation and elastic collisional processes of atomic and molecular deuterium. However, since previous analysis demonstrates the neutral density due to atomic deuterium is significantly less than that of molecular deuterium, the contribution of atomic deuterium to collisional power losses is neglected. A portion of the power is also lost due to photon radiation. This sub-section analyzes the losses due to D_2 processes and photon radiation.

Molecular Deuterium Losses

The cross sections and energy values for the interactions for molecular deuterium were obtained from the LXCat website database [118]. Table 6.4 summarizes the processes for molecular deuterium. For the purposes of this table, dissociation is considered a subgroup of excitation.

The resulting collisional energy loss rate coefficients grouping each main collision type (ionization, excitation, and elastic) for a given electron temperature are provided in

[203] This is discussed further in section 6.7: **Region Efficiency Analysis**

figure 6.13. The rate coefficients associated with each process were determined assuming a Maxwellian energy distribution function.

To determine the power lost due to molecular deuterium processes along the machine, the MATLAB-inferred electron temperatures and densities in the axial and radial directions[204], as well as the baratron-inferred neutral density measurements were used. The baratrons measure neutral gas pressures at the wall. The neutral gas density is calculated from the pressure measurements using the ideal gas law, assuming room temperature (300 K), as shown in equation 6.5.

$$n_0 = \frac{N}{V} = \frac{P}{RT} \tag{6.5}$$

where n_0 is the neutral gas density, N is the number of gas particles (moles), V is the gas volume, P is the pressure, R is gas constant, and T is temperature.

Only four baratron-inferred neutral density measurements along the machine axis were available, at axial locations z = 1.0, 1.5, 2.2, and 3.4 m. The baratron pressure measurements were made at each location over several pulses with the operating configuration applied for this power accounting. A linear fit between points was applied to estimate the axial variation of the neutral densities. The neutral density profile was assumed to be radially flat, although the neutral densities are likely greater at the edge, which implies that the neutral densities are an overestimation in the plasma. Figure 6.14 provides the neutral density measurements and the estimated fit along the Proto-MPEX machine.

To calculate the losses associated with the molecular processes, the following general equation was applied:

$$P = qEK_v n_e n_N V \tag{6.6}$$

where P is the lost power [W], q is the electron charge [1.602e-19 J/eV], E is the energy associated with the process [eV], K_v is the averaged collisional rate coefficient (<vσ>) [m^3/s], n_e is the electron density [m^{-3}], n_N is the neutral particle density [m^{-3}], and V is the volume of the plasma [m^3]. The power loss associated with each individual molecular process (provided in table 6.4) were summed to determine the total power loss. To integrate over the volume, a similar process to that used in the THEODOR-inferred power analysis was applied. That is, assuming radial symmetry, the plasma profile area was determining using the plasma radius, defined as the radius at the outermost flux line (see figure 6.2). The power density (kW/m^3) is integrated from the plasma radial edge to the center to calculate the corresponding power per unit length (kW/m) for each axial location. Figure 6.15 depicts the resulting total power loss due to molecular deuterium processes, as well as the individual ionization, dissociation, excitation, and elastic contributions, along the length of Proto-MPEX. The majority of these losses occur in the helicon region, as expected, since the plasma is formed under the helicon.

[204] See figures 6.6-6.9.

In comparison, a very small percent (4.4%) of the power lost due to D_2 processes occurs downstream of the skimmer plate (see figure 6.15). The increase in the power losses near z = 0 m is due to expansion of the magnetic flux lines, which flares out significantly near the dump plate. The dump plate is located at z = 0.2 m, delineated by the solid black line in figure 6.15. Any modeled losses due to deuterium processes after this point are artificial.

Table 6.5 summarizes the power lost in each main region and sub-region of Proto-MPEX, for each of the molecular processes, as well as the total power lost. Since the power loss due to elastic collisions is so small in comparison to the other three processes, its contribution is only provided for the three main regions of the machine.

The total calculated power lost due to the molecular deuterium processes is 183.8 $\pm$ 123.4 kW, with 122.0 $\pm$ 81.9 kW, 27.0 $\pm$ 18.0 kW, and 35.6 $\pm$ 24.2 kW of power lost in the helicon, upstream and downstream regions, respectively. Of the 183.8 kW of lost power, ionization losses accounted for 57.2 $\pm$ 38.6 kW, dissociation losses accounted for 40.4 $\pm$ 26.9 kW, excitation losses accounted for 86.2 $\pm$ 57.9 kW and elastic losses were effectively negligible. The total power lost over the entire machine due to molecular deuterium is about a factor of two higher than the total input power (79.4 kW). The difference between the input power and the lost power due to the D_2 molecular process is expected. The D_2 lost power is directly dependent on the baratron-inferred neutral deuterium gas density, which, as previously stated, only had four points of measurement and sampled the plasma near the machine surface, where the neutral pressures are likely to be higher, resulting in an overestimate of the neutral gas pressure.[205] Additionally, about two-thirds of the losses occur in the helicon region. Recall, very little is known about the plasma conditions under the helicon. The electron density and temperature values under the helicon are set to the on-axis electron temperature and density at the downstream end of the helicon region (z = 1.5 m), which are estimated values themselves. The combination of the estimation at z = 1.5 m being slightly off and the overestimation of the neutral densities could easily result in a factor of two difference between the calculated total input power and the D_2 power loss. The error associated with the power losses due to D_2 processes are approximately two-thirds of the calculated power losses.

It is possible the approximate *ratio* of the power losses in the helicon region of the machine aligns with the diagnostically-determined power losses in the helicon region. Using the ratio of the estimated total lost power to the input power (183.8:79.4), the 're-scaled' total power lost in the helicon region would be 52.7 kW of lost power, which is relatively close to the measured 45.8 kW of power lost to machine surfaces. This value is also within the error calculated for the total power lost in the helicon region, whose lower bound is 40.1 kW, increasing the confidence in the reasonableness of the 're-scaling' factor. A similar 're-scaling' method has been applied to compare SOLPS modeling and baratron data in previous Proto-MPEX power accounting analyses [39]. To better compare the input and lost power components of the power balance, the

[205] Preliminary filterscope analysis of the neutral plasma density suggests the baratron-inferred neutral densities are approximately a factor of two greater than the filterscope-inferred neutral densities.

power losses due to D_2 processes were adjusted using the re-scaling factor for the analyses performed in the rest of this chapter's power balance.

Photon Radiation

One AXUV photodiode, installed in the central chamber at axial location z = 2.2 m, sampled the plasma to infer power lost from the plasma due to photon radiation. The radiant intensity measured by the AXUV photodiode was 46.8 ± 2.4 kW/m^2.[206] Equation 6.7 is used to infer the power lost due to photon radiation from the AXUV data [96].

$$P_{rad} = 0.5\pi r_p z_{tot} \int \varepsilon dl \tag{6.7}$$

where P_{rad} is the total power lost due to photon radiation, r_p is the local plasma radius, z_{tot} is the length of the Proto-MPEX device, and $\int \varepsilon dl$ is the brightness density. Since the plasma radius varies along the machine length, the plasma radiation is calculated for incremental plasma slices and summed over the length of the machine. Figure 6.16 provides the variation in radiated power along the length of the machine. Table 6.6 summarizes the photon radiation power loss in the main regions and sub-regions of Proto-MPEX.

The total power lost due to radiation along the machine length was **7.3 ± 0.4 kW**, with **2.2 ± 0.1 kW** of that power lost in the helicon region, **1.8 ± 0.1 kW** lost in the upstream region, and **3.3 ± 0.2 kW** lost in the downstream region.

Figure 6.17 provides the diagram of the Proto-MPEX power balance, updated to include the locations of the collisional power losses due to D_2 processes and photon radiation. It is important to note that the D_2 power losses drop off dramatically immediately after the skimmer plate. This phenomenon will be discussed in greater detail in section 6.7, **Region Efficiency Analysis.**

6.5.3 Machine surface losses

The power lost to machine surfaces were primarily determined through fluoroptic probe and thermocouple measurements. The filterscopes were consulted as well. As described in a previously published work on Proto-MPEX power accounting [39], a 1D heat conduction analysis is a reasonable method to calculate the total power deposited to machine surfaces. The 1D heat conduction analysis to determine the power deposited to the helicon window, measured by the FPs, was performed using equation 6.8:[207]

$$\dot{Q} = \frac{mc\Delta T}{\Delta t} \tag{6.8}$$

where $\dot{Q}$ is the power [W], m is the mass of the AlN window [2.567 kg], c is the specific heat of the helicon window [780 J/kg.K], ΔT is the temperature rise measured by the

[206] Averaged from time, t, equals 4.2 – 4.35 seconds.
[207] Equation 6.7 is a reproduction of equation 5.1.

FPs [K], and Δt is the plasma pulse length [0.50 s]. Approximately fifteen pulses were analyzed to ensure reliability. The total average power deposited to the helicon window was calculated to be **37.2 ± 2.0 kW**, or 46.9 ± 2.0 % of the input power.

Recall thermocouples are installed ex-vessel on spool pieces 1.5, 2.5 and 4.5.[208] Two thermocouples are installed on each spool piece, totaling 6 ex-vessel thermocouples. To determine the power lost to the spool pieces, the same 1D conduction analysis was applied using equation 6.8. where m is 2.2 kg, c is 500 J kg^{-1} K^{-1}, ΔT is the temperature rise measured by the TC (K), and Δt is 0.5 s. Approximately fifteen pulses were analyzed to ensure reliability. The total power lost on spool 4.5 was calculated to be **5.8 ± 0.5 kW**. The total power lost on spool 2.5 was **2.8 ± 0.2 kW** and the total power lost on spool 1.5 was **1.9 ± 0.1 kW**.

Two in-vessel thermocouples are installed downstream on the skimmer and RF baffle plates, located at z = 1.75 m and z = 2.35 m, respectively, providing additional power loss measurements along the length of the machine. As described in Chapter 5, both plates are 0.125'' thick and composed of stainless steel. The inner diameter of the skimmer is 5.8 cm and the inner diameter of the RF baffle plate is 8.6 cm. The TC on the skimmer plate is installed on the non-plasma facing side of the plate. The TC on the RF baffle plate is installed on the plasma facing side, which is generally avoided to protect the diagnostic. However, the plasma radius at z = 2.35 m for this configuration is just under 2 cm. The inner radius of the RF plate is 4.3 cm. The TC is installed another centimeter away from the inner edge. Therefore, even if the plasma radius at the RF baffle plate is larger for a different configuration, the TC is considered far enough away to avoid direct contact with the plasma.

The average temperature rise during a plasma pulse was used to infer a power loss also using equation 6.8, which is algebraically manipulated below.

$$\dot{Q} = \frac{\rho A_c x c \Delta T}{\Delta t} \tag{6.8}$$

where ρ is the density [kg/m^3], A_C is the cross-sectional area of the drawn disk, x is the thickness of the plate, c is the specific heat of the stainless steel [J/kg.K], ΔT is the temperature increase during the plasma pulse [K], and Δt is the pulse length [s]. The material density and the volume over which the temperature increase could be assumed to be uniform was approximated as a disk, with the plate's thickness. To estimate the cross-sectional area, the installed thermocouple was assumed to be approximately 1 cm away from the inner edge. Since the material inside the imaginary circle on which the TC sits would likely be hotter than measured by the TC, a disk with an inner radius of 2.9 cm and an outer radius of 4.9 cm was assumed to experience a uniform temperature rise measured by the installed TC.[209] The average temperature rise measured by the skimmer TC was 1.77± 0.01°C, yielding a power loss to the skimmer plate of **0.22 ± 0.01 kW**. The average temperature rise measured by the RF baffle TC

[208] Axial locations z = 0.6 m, 1.0 m, and 1.5 m.
[209] The installed TC sits radially in the middle of this disk.

was 0.68± 0.01°C, yielding a power loss to the RF baffle plate of **0.11 ± 0.01 kW**.

The filterscopes were primarily used to identify possible limiting surfaces locations along the machine length. The filterscopes sampled at nine different port locations along the machine.[210] Figure 6.18 provides the emission intensities[211] of the D_α photons along Proto-MPEX's length measured by each of the installed optical fibers for a plasma pulse with the operating configuration provided in figure 6.1. The emission intensities are plotted on a $\log_{10}$ scale. Each intensity measurement represents line plasma radiation at that location. For more direct reference to their locations with respect to the machine components, the emission intensities plot is aligned with the Proto-MPEX diagram.

The emission intensity depends on the neutral density, the electron density and the deuterium excitation rate coefficient, which itself is a function of the electron temperature. The behavior of the emission intensities at each axial location follow the general trends suggested by the electron density, electron temperature and neutral density behaviors along the length of the machine (see figures 6.6, 6.8 and 6.14). The peak intensities occur in the upstream region at z = 0.6 m and z = 1.0 m. Since the gas fueling occurs at z = 0.6 m and the magnetic field lines bring the plasma close to the upstream edge of the helicon window near z = 1.0 m, this behavior is reasonable. Downstream of the helicon, with the exception of the drops at z = 3.1 m and 3.65 m, the emission intensity is relatively constant, varying within reason of the electron density, electron temperature and neutral density measurements at each axial location. The decrease in intensity at z = 3.65 m, the last diagnostic port before the target plate, is reasonable since the electron density and temperature have decreased and the neutral density remained roughly constant in comparison to the plasma measurements made at z = 3.4 m, the nearest diagnostic port upstream of z = 3.65 m (see figures 6.6, 6.8, and 6.14). The unexpected decrease in intensity at z = 3.1 m requires further analysis. The decrease in intensity at this location is reflective of the unexpected drop in the convective power at this location, shown in figure 6.11. While the general consensus is the low convective power is due to probe drooping during the scan that obtained the electron density, electron temperature and Mach number, the decrease in D_{alpha} emission intensity observed by the filterscope suggests that the calculated convective power drop could be reflecting a real plasma behavior. Another explanation is the diagnostics[212] were not able to properly sample the plasma at this location, perhaps due to obstructed line of sight, probe drooping or improper installation. Additional analysis of this plasma region is required to definitively quantify the local plasma behavior, such as a repeated probe scan, once the drooping issue has been resolved.

Figure 6.19 provides the diagram of the Proto-MPEX power balance, updated to include the locations of the power loss measured on machine surfaces by the fluoroptic probes and thermocouples.

[210] See table 6.1.
[211] In photons per second per centimeter squared per steradian.
[212] The MP/LP and the filterscope.

6.5.4 Discussion

The total power being transported out of the helicon region towards the dump plate was 10.3 kW. The total power being transported out of the downstream end of the helicon region was 28.4 kW. The two values imply about 73.4% of the helicon power is preferentially launched downstream and 26.6% is launched upstream. The total power leaving the helicon region was 38.7 kW, or 48.7% of the input power. Recall approximately 79.4 kW of input power entered the helicon region and approximately 37.2 kW were lost to the helicon window.[213] Additionally, the thermocouples installed on spool pieces 2.5 and 4.5 inferred 2.8 kW and 5.8 kW of power deposited to spool pieces 2.5 and 4.5, respectively. The total power lost to machine surfaces in the helicon region is 45.8 kW, or 57.7% of the input power, which results in 33.6 kW of power remaining in the plasma. This value is extremely close to the calculated total power being transported out of the helicon region (38.7 kW).

Recall, the estimated total power lost due to molecular deuterium processes along the machine was 183.8 kW, with 122.0 kW of that power being lost in the helicon region. As previously stated, the total power lost is approximately a factor of two greater than the input power, likely due to an overestimation of the neutral density from the assumption that the neutral density profile is radially flat. Using the ratio of the estimated total lost power to the input power (183.8:79.4), the 're-scaled' total power lost in the helicon region would be 52.7 kW of lost power, which is relatively close to the measured 45.8 kW of power lost to machine surfaces.

From table 6.5, the majority of the power appears to be lost from the plasma between the downstream end of the helicon region (z = 1.5 m) and the central chamber (z = 2.2 m). According to the D_2 loss analysis, the majority of those losses occur before the plasma even reaches the skimmer plate (z = 1.75 m), which is also highlighted in figure 6.15. Recall the skimmer plate serves to restrict neutral gas flowing downstream towards the target plate. Therefore, it effectively divides the machine into a "high pressure" and "low pressure" region, where the "high pressure" region extends from the dump plate to the skimmer plate and the "low pressure" region extends from the skimmer plate to the target plate. It is reasonable that the higher pressure would result in larger power losses due to collisional processes, such as those included in the D_2 processes. The total (re-scaled) power lost due to D_2 processes from z = 1.5 m to 2.2 m is 13.3 kW, 11.5 of which are lost prior to the skimmer (see figure 6.19). In comparison, the power lost in this region due to photon radiation is small and more evenly distributed on either side of the skimmer, with 1.5 kW lost over the entire region from z = 1.5 to 2.2 m and 0.8 kW of lost prior to the skimmer. Recall, the total power loss along the machine axis due to photon radiation, which was inferred by one AXUV photodiode, was 7.3 ± 0.4 kW. Therefore, approximately 20% of the power loss measured by the AXUV photodiode occurred from the downstream end of the helicon region to the central chamber. Additional analysis of this region, and other regions is provided in sub-section 6.7, **Region Efficiency Analysis**.

[213] Measured by the fluoroptic probes.

It is important to note there was a general lack of diagnostic coverage in the downstream region of the machine capable of measuring power lost through photon radiation, charge exchange, etc. For this power balance analysis, only one AXUV photodiode was available for data collection at axial location in the central chamber. The SXR photodiode and bolometer array were not available. It is also important to note that the plasma measurements at z = 1.5 m, which were pivotal to the data fits used to determine the parallel heat transport, especially in the helicon and downstream region, were based on a best-approximation, rather than experimental data. Previous power accounting studies on Proto-MPEX highlighted not only the importance of the measurements at z = 1.5 m, but also the difficulty in obtaining reliable measurements with LPs at that location, since they are too perturbative to the plasma so close proximity to the helicon source [39]. Efforts were made to analyze the plasma at this location using the HELIOS diagnostic, which would provide less perturbative electron density and temperature measurements, but it has not been fully commissioned. Future power balance analyses will include HELIOS, AXUV and SXR photodiodes, bolometers, and TALIF, which will provide much desired supplementary data to better understand the plasma behavior in the downstream region of Proto-MPEX. To further diagnostically verify the power lost due to D_2 processes, additional diagnostics to measure machine surface temperatures, such as (S)TCs, are recommended, particularly in the region between z = 1.5 m and the skimmer plate (z = 1.75 m).

6.6. Deposited Power

The deposited power refers to the power deposited to the target and dump plates. The FLIR A655sc IR camera was the main diagnostic used to measure the deposited power on both end plates [44, 39]. The thermocouples installed on the end plates serve to corroborate the IR measurements to ensure accurate data analysis. The IR camera viewed the target plate from the plasma-facing side and the dump plate from the non-plasma facing side. For the power balance in this chapter, the target plate was the 0.25'' thick graphite target plate.[214] The dump plate was the 0.015'' stainless steel plate.

To determine the power and heat fluxes arriving at each plate, the IR camera acquires the plasma temperature profiles over the course of the plasma pulse at a frame acquisition rate of 100 Hz. The images are analyzed using a series of MATLAB codes and the THEODOR code. Figure 6.20 depicts the plasma profiles of the helicon pulse on the end plates.

The target plate plasma profile shown in figure 6.20 is centrally peaked with decent radial symmetry. The profile radius is approximately 2 cm. The dump plate plasma profile is slightly less radially symmetric and shows more heat along the edge. The plasma radius on the dump plate is approximately 6 cm, about three times larger than that of the target plate, due to the expansion of the magnetic field flux lines at the dump in comparison to the target. Prior to the start of the plasma pulse, the gas is injected into the machine at axial location z = 0.6 m through a port at the bottom of the machine. The dump plate is located at z = 0.2 m, close to the gas injection location. The proximity to

[214] See Chapter 3.

the gas injection location results in additional heat along the bottom left of the dump plate plasma profile, as shown in figure 6.20. The heat from the generated plasma has not had time to move radially inward prior to the plasma impinging on the dump plate, resulting in a more edge-peaked profile.

The target plate profile created by the operating configurations is close to ideal for future PMI studies. For comparison, the target plate plasma profile from the previous power accounting study[215] is reproduced in figure 6.21 alongside the target plate plasma profile shown in figure 6.20. The plasma profile from the new power accounting study, which is being described in this chapter, has a preferable profile as compared to the plasma profile of the previous power accounting study. The profile is much more even and lacks the lower lobe that exists in the plasma profile of the previous study.

The target plate heat flux profiles resulting from the THEODOR analysis are provided in figure 6.22.

The start of the plasma pulse is apparent in the left image of figure 6.22. Prior to time approximately equal to 4.16 seconds, the heat flux profile is zero. The heat flux hits its maximum shortly after the start of the plasma pulse, near time equal to 4.25 seconds, shown in the right image of figure 6.22. The heat flux decreases over the course of the pulse as the neutral pressure increases in front of the target plate. The maximum heat flux and total power deposited to the plate at t = 4.25 s are **1.22 ± 0.02 MW/m^2** and **0.55 ± 0.05 kW**. The input power to target plate efficiency is **0.69 ± 0.07%.**

To increase the confidence in the THEODOR-inferred heat fluxes and powers the, the target plate heat flux was also modeled in COMSOL. Figure 6.23 shows the COMSOL-inferred 2D heat flux plasma profile of the target plate. For comparison, the 2D temperature profile is also shown.

Similar to the temperature profile, the COMSOL-inferred 2D heat flux profile is approximately radial symmetry and centrally-peaked. The heat flux corresponding to the hot center of the temperature profile is approximately 1.18 MW/m^2. To better compare the two analysis methods, a vertical 1D slice of the COMSOL heat flux profile was analyzed at the same x location as that of the temperature profile used for the THEODOR code (delineated by the white lines in figure 6.23). The resulting heat flux profiles are provided in figure 6.24. The heat flux line trace is analyzed at the same time in the pulse as the THEODOR analysis, t = 4.25 seconds. Comparing the THEDOR heat flux profiles of figure 6.22 to the COMSOL heat flux profiles of figure 6.24 shows the similarities in the results and increases the confidence in the accuracy of both analysis processes.

The dump plate was analyzed using the THEODOR code in the same method as that used for the target plate. The resulting heat flux profiles are shown in figure 6.25.

[215] Described in Chapter 5

In comparison to the target plate heat flux profiles, the dump plate profiles are much flatter in shape. No distinct shape is apparent. The maximum heat flux occurs along the profile edge, with a value of **0.25 ± 0.02 MW/m^2**. The lower maximum heat flux is due to the field expansion at the dump plate. Recall the plasma radius at the dump plate is three times that of the radius at the target plate, spreading out the heat flux. The resulting power deposited on the dump plate is **1.0 ± 0.1 kW**, corresponding to an input power-to-dump plate efficiency of **1.12 ± 0.17%.**

It is important to note that unlike the target plate heat flux line traces, the dump plate heat flux line trace is noisy. Prior analysis of noisy target plate profiles using the THEODOR code typically results in an artificially high calculated target power. To ensure the accuracy of the inferred power, the curve was smoothed and reanalyzed. The inferred power varied by approximately 0.2%. Therefore, the noisier heat flux line trace was considered accurate.

Figure 6.26 provides the diagram of the Proto-MPEX power balance, updated to include the power deposited to the end plates.

6.7. Region Efficiency Analysis

To gain a better understanding of where and how power is being lost from the plasma, efficiencies are calculated for the three main regions of Proto-MPEX (helicon, upstream and downstream) and their sub-regions. Sub-regions with low efficiencies highlight areas where more power is being lost from the plasma and therefore should be the focus of future experiments. The efficiency in each (sub-)region is calculated using equations 6.9 and 6.10:[216]

$$\mathrm{P_{enter}} + \mathrm{P_{source}} = \mathrm{P_{exit}} + \mathrm{P_{loss}} \tag{6.9}$$

where P_{enter} is the amount of power entering the sub-region from the previous sub-region, P_{source} is the power entering the sub-region from an applied power source, such as the helicon, P_{exit} is the amount of power leaving the sub-region, continuing towards its respective end plate, and P_{loss} is the power lost from the plasma within the region. The analysis considers two different types of P_{loss} to avoid double counting lost power. $P_{loss,surf}$ are the plasma losses measured on machine surfaces by the TCs and FPs. $P_{loss,coll}$ are the plasma losses due to collisional mechanisms, which include the losses due to D_2 processes and photon radiation losses inferred by the AXUV photodiode. Recall, the power losses due to D_2 processes are the ‘re-scaled’ power loss values (see figure 6.26). Since the power lost through D_2 processes and photon radiation eventually is deposited on the machine surfaces, the $P_{loss,surf}$ and $P_{loss,coll}$ would approximately equal each other if all power was accounted for along the machine.

The efficiency of each sub-region can be evaluated using the following equation:

[216] Equations 6.9 and 6.10 are reproductions of 4.4 and 4.5, respectively

$$\eta = \frac{P_{exit}}{P_{enter}+P_{source}} \quad (6.10)$$

where η is the efficiency of the sub-region.

Since the power accounting was performed for helicon-only plasmas, P_{source} is equal to zero outside of the helicon region. Table 6.7 summarizes the input powers, output powers, and resulting efficiencies for each main region and sub-region. The table includes columns summarizing power lost from the plasma due to collisional losses ($P_{loss,coll}$)[217] and plasma losses measured on machine surfaces ($P_{loss,surf}$). The table also includes a calculation of the missing power, $P_{missing}$, defined as the power that has not been accounted for via parallel heat transport (exiting the region) or machine surface power losses. If the sum of the $P_{missing}$ and the $P_{loss,surf}$ is approximately equal to $P_{loss,coll}$, then the power in the sub-region is considered to be accounted, because extended diagnostic coverage to further measure power lost to the machine surfaces (i.e. additional TCs) should diagnostically verify more of the $P_{loss,coll}$. This would increase the amount of $P_{loss,surf}$ and reduce the amount of $P_{missing}$. Again, in theory, $P_{loss,surf}$ should approximately equal $P_{loss,coll}$. The efficiency analyses including measurements at z = 3.1 m are highlighted in light red since the convective power measured at z = 3.1 m is suspiciously low, which affects the resulting efficiencies that include plasma measurements at z = 3.1 m.

6.7.1 Helicon System & Region

As previously stated in the *Input Power* section of this chapter, 79.4 kW of the 101.3 kW of power injected into the helicon system reached the plasma region under the helicon window. The resulting efficiency of the helicon system is 78.4%.

Based on the calculated power being transported from the helicon region into the upstream and downstream region, the helicon preferentially launches about 26.8% of the input power into the upstream region and 73.4% into the downstream region. Therefore, 26.6% of the input power (21.1 kW) was assumed to be the power entering the sub-region defined as the middle of the helicon to the upstream edge of the helicon (z = 1.0 to 1.25 m). Similarly, the power entering the sub-region defined as the middle of the helicon to the downstream edge of the helicon (z = 1.25 to 1.5 m) was assumed to be 58.3 kW. A similar ratio split was given to the power deposited to the helicon window.[218] The resulting efficiencies are both 48.7%. The power lost in the overall helicon region includes the power lost to the helicon window (37.2 kW) and the power lost to spool pieces 2.5 and 4.5 (8.6 kW) totaling 45.8 kW out of the 79.4 kW of input power. The power loss inferred by the AXUV photodiode (2.2 kW) along with the (re-scaled) power loss due to D_2 processes (52.7 kW), totaling 54.9 kW, should approximately equal the measured deposited power on the machine surfaces in the helicon region (45.8 kW).[219] The total power lost to the machine surface in the helicon

[217] No error bars are provided for $P_{loss,coll}$ because its main component are the power losses due to D_2, which have been re-scaled and are within the error bar of the original D_2 power losses.
[218] Measured by the FPs.
[219] Power lost through the D_2 processes and photon radiation eventually ends up on machine surfaces.

region may be slightly lower, since power lost the spool pieces is all included in the helicon region, although the spool pieces extend slightly past the diagnostic ports at z = 1.0 m and 1.5 m. Some of the inferred lost power measured by the TCs on these spool pieces may technically belong in the upstream and downstream sections. However, it was difficult to reasonably estimate what portion of the power to include in each region, so it was considered sufficiently accurate to include all the power lost to the 2.5 and 4.5 spool pieces in the helicon region analysis.

The inferred power being carried out of the helicon region was 38.7 kW, with 10.3 kW traveling upstream towards the dump plate and 28.4 kW traveling downstream towards the target plate. Recall approximately 58.3 kW of power were assumed to be launched downstream towards the target plate. The total collisional losses from the mid-line of the helicon to the downstream edge of the helicon region were 26.5 kW (see figure 6.26 and table 6.7). Subtracting these losses from the power assumed to be launched in this region, the available power to exit the downstream end of the helicon region is 31.8 kW, which is very close to the 28.4 kW inferred to be transported out of the helicon region via power convection and conduction. The comparison for the upstream edge of the helicon region is not as precise. Of the 21.1 kW available from the mid-line of the helicon to the upstream edge, 10.3 kW were transported upstream to the target and 28.4 kW were calculated to be lost due to collisional processes. Approximately twice the amount of power was accounted for on the machine surface and transported upstream (38.7 kW) as was assumed to be available (21.1 kW). However, accounting for the error range on the inferred values, the difference between the two values is not unreasonable.

The sum of the total lost power and the power carried out of the helicon region was 84.6 kW, only 5.2 kW (6.5%) greater than the calculated input power. Based on this analysis, all the power in the helicon region is considered accounted for.

6.7.2 Upstream Region

Out of the 10.3 kW of power entering the upstream region, 1.0 kW reaches the target plate, resulting in a 9.7% efficiency. The total power being carried into the sub-region from spool 2.5 to spool 1.5 was 10.3 kW. The total power being carried out of the region was 4.1 kW, resulting in a 39.8% efficiency. In this sub-region, 1.9 kW of power were lost to spool piece 1.5. Collisional loss calculations imply that about 8.6 kW of power were lost (7.6 kW due to D_2 processes and 1.0 kW due to photon radiation). Improved diagnostic coverage of this region (i.e. additional TCs) could result in a larger portion of the calculated collisional power losses being measured on the machine surfaces. Since only 4.3 kW of power are diagnostically unverified, with a possible 6.7 kW lost through collisions[220], the power in this sub-region is considered effectively accounted for. The total power entering the sub-region defined from spool piece 1.5 to the dump plate was 4.1 kW, 1.0 kW of which arrived at the dump plate, yielding a 24.4% region efficiency. According to the AXUV photodiode, 0.8 kW of power were lost due to photon radiation in this region. Another 4.1 kW were potentially lost due to D_2 processes. While 3.1 kW of power were not verified by the TCs, the photodiode-inferred and ‘re-scaled’ D_2-inferred

[220] 8.6 kW minus 1.9 kW measured by the TC.

losses in this region suggest that additional TCs or calorimeters may reveal additional power lost to the machine surfaces. Overall, the upstream region may benefit from some more diagnostic coverage and analysis, but it is considered relatively efficient.

6.7.3 Downstream Region

Of the 28.4 kW of power entering the downstream region, only 0.55 kW of that power reached the target plate, yielding an overall downstream region efficiency of 1.9%. Analysis of the downstream sub-regions shows that the sub-regions from z =1.5 m to 2.2 m and from z = 2.2 m to 3.1 m have the lowest efficiencies, equaling 15.5% and 15.9%, respectively. The sub-region with the largest amount of missing plasma is the sub-region from z = 1.5 m to 2.2 m. In this sub-region, 23.8 kW of the 28.4 kW entering the region were not diagnostically verified.[221] There are a few factors that could affect the amount of missing power. First, as previously stated, the plasma values at z = 1.5 m (electron density and temperature and Mach number) are based on best-approximations. The amount of power being transported into the downstream region could be smaller than calculated. Second, the Mach number value at z = 2.2 m is also a best-approximation. If the Mach number is larger than estimated, the total power in the plasma at z = 2.2 m would be larger, which would also serve to reduce the amount of missing power. However, the most likely contributor to the missing power are the collisional power losses inferred by calculated D_2 processes and AXUV photodiode measurements. In the region from z = 1.5 to 2.2 m, the total inferred collisional power loss was 14.8 kW, with 12.3 kW being lost by the time the plasma reached the skimmer plate (see figure 6.26). Assuming the 14.8 kW of power are really lost from the plasma due to the collisional processes, the missing power in the region between the downstream end of the helicon region and the central chamber drops to 9.0 kW. This implies that 68.3% of the power in this region has been quantified, which is a reasonable value.

In theory, all the lost power due to collisional processes should go to the machine surfaces. However, there is currently not sufficient diagnostic coverage in this region to confirm the inferred power losses due to these processes are correct. Therefore, the region between z = 1.5 and 2.2 m is an area of the machine where additional diagnostic coverage and analysis is highly recommended. Additional modeling of heat transport to machine surfaces would be greatly beneficial as well. Since the machine radius is so large in the central chamber, machine surface temperature rises are likely very small, but when summed over the entirety of the central chamber could result in an appreciable amount of power deposited to the machine surface. Additional diagnostics recommended include AXUV and SXR photodiodes, the bolometer array, the HELIOS diagnostic, Mach probe, and TALIF system, sampling at both z = 1.5 and z = 2.2 m.

The sub-region from z = 2.2 m to 3.1 m has the second lowest efficiency along the machine. The power held in the plasma at z = 2.2 m is 4.4 kW and the power held in the plasma at z = 3.1 m is 0.7 kW, which is less than the power measured in the plasma at z = 3.4 m (1.4 kW). The amount of power lost due to collisional processes from z = 2.2 to 3.1 m is approximately 2.6 kW. This implies a more reasonable value for the power

[221] I.e. measured on the machine surfaces.

held in the plasma at z = 3.1 would be 1.8 kW, about twice was is currently being calculated from probes scans. As previously stated, the main expected reason for the difference is the MP sampling the plasma at z = 3.1 m was drooping slightly as it scanned horizontally through the plasma. While there were attempts to correct the droop, the Mach probe value measured at z = 3.1 m is likely too low. The electron density measurement may have been affected as well.[222] If this is the case, then the calculated power in the plasma, particularly the convective contribution, is too low (see figure 6.11). Increasing this value would increase the efficiency of the sub-region from spool 6.5 to 9.5 and decrease the efficiency of the sub-region from spool 9.5 to 10.5 to a reasonable value. Currently, it is approximately 200% efficient, which is not realistic. If the power held in the plasma at z = 3.1 m were 1.8 kW[223], the region efficiency would be 77.8%, which is more realistic. A repeat of the probe scan after the drooping issue has been fixed at 9.5 is recommended to clarify the plasma conditions at z = 3.1 m. Additional analysis using the filterscopes is recommended as well, since the filterscopes also observed a decrease in the D_{alpha} emission intensity at z = 3.1 m.

The sub-region from z = 3.4 m to z = 3.65 has an efficiency of 38.5%. About 0.9 kW of power are unaccounted for in this region. Additional bolometric and photodiode coverage is recommended at z = 3.65 m to attempt to account for this power. As the closest diagnostic port to the target plate, acquired data in this region is important. The sub-region from z = 3.65 m to the target plate (z = 3.75 m) has an efficiency of 110%. The power measured on the plate is 0.05 kW larger than the power measured in the plasma at z = 3.65 m. The most likely source of the difference is the fact that two different diagnostics acquired the data at each location. The power in this sub-region is considered accounted for.

Before concluding this sub-section, it is important to note the large fraction of the power being lost prior to the skimmer in the region from z = 1.5 to 2.2 m highlights the important role the skimmer plays in the plasma and its implications for Proto-MPEX operations. As previously stated, the skimmer plate restricts neutral gas flowing downstream towards the target plate. It effectively divides the machine into a “high pressure” and “low pressure” region, where the “high pressure” region extends from the dump plate to the skimmer plate and the “low pressure” region extends form the skimmer plate to the target plate. Although the “high pressure” region leads to more collisional plasma losses, the “high pressure” region is necessary for the helicon to successfully create high density plasmas. The “low pressure” region is necessary to maintain the plasma as it travels downstream and ensure heat fluxes are deposited on the target plate. Otherwise, the high pressures in the downstream region would lead to plasma detachment from the target, undermining the ability to perform PMI studies on the target plate. Thus, the skimmer plate is a crucial component to Proto-MPEX and its operations. Since the skimmer plate is required, the high collisional losses in the high-pressure region, especially from the upstream edge of the helicon region to the skimmer plate, may have to be considered acceptable and unavoidable losses to standard Proto-

[222] The electron temperature is likely still reasonably accurate since the electron temperature is radially flat, so the electron temperature on the edge of the plasma profile can corroborate the value.
[223] 4.4 kW (power in plasma at z = 2.2 m) – 2.6 kW (collisional losses in region from z = 2.2 m to 3.1 m).

MPEX operations. For this power balance, of the 79.4 kW of power injected, only about 15.9 kW, or 20.0%, made it past the skimmer plate, assuming the 12.3 kW of inferred collisional losses from z = 1.5 to 1.75 m were correct. The plasma then has to travel another 2 m before reaching the target plate. Thus, a power-to-target helicon efficiency of about 0.5-2.0%[224] may not be able to be greatly improved and should be considered a reasonable value. Any efforts to increase the power-to-target efficiency and target heat fluxes should be focused in the region downstream of the skimmer plate, such as increasing pumping near the target plate.[225]

The large portion of power lost upstream of the skimmer plate due to the higher neutral pressure has important implications for MPEX operations, specifically with respect to machine surface cooling. Recall, there are 37.2 kW, or 46.9% of the input power, are lost to the helicon window. Scaling up to MPEX level helicon power capacity (180 kW of input power), the deposited power to the helicon window could reach 84.3 kW. While cooling of the helicon system is already planned, additional machine surface cooling may be necessary outside the helicon region. For example, collisional loss calculations imply that 12.3 kW (15.5%) of power are lost in the region between the downstream end of the helicon region and the skimmer plate. This would increase to 27.9 kW at MPEX-level helicon capacity. Understanding the scale of power lost to the machine surfaces is important information for MPEX engineers as the MPEX machine design, especially the cooling system, is further developed.

6.8. Summary

As a result of the data analysis described in the above sections, a new power accounting study of the Proto-MPEX device was completed using the set of operating parameters described in figure 6.1. The three main regions of the machine were analyzed, as well as their sub-regions. The power in the helicon region is considered completely accounting for. The efficiencies of the upstream and downstream regions were 9.7% and 1.9%, respectively, with the sub-region from z = 1.5 m to z = 2.2 m identified as the area of the device most in need of additional analysis. Of the 79.4 kW of input power, 49.6 kW were diagnostically verified, meaning 62.4% of the power in the machine has been located. This is an improvement over previous power accounting studies, where the largest percentage of accounted power was 49.2%. Of the 49.6 kW of diagnostically verified power, 48.05 kW were lost to machine surfaces (P_{loss}) and 1.55 kW of power were deposited to the end plates (P_{dep}). The remaining power that has not been diagnostically verified is characterized as the missing power (P_{miss}).[226] Figure 6.27 summarizes the power balance in terms of input power, lost power, deposited power and missing power.

6.9. Working Model

One of the main goals of the thesis work was to develop a working model to recreate power balances for various machine operating conditions. The following subsection lists

[224] The helicon power-to-target efficiency for this power balance is 0.7%

[225] Recall improving pumping near the target plate was one of the goals of the Proto-MPEX upgrade, described in chapter 2.

[226] The power inferred by the AXUV is not considered ‘verified’ power to avoid lost power double counting.

the critical steps, including the diagnostics and experiments required to amass the data necessary, to perform a new power balance.

I. Identify a set of operating parameters and hold constant for all experiments. Operating parameters that must be fixed include:
    a. Input power
    b. Magnetic field configuration
    c. Gas flow rate and gas injection location
    d. Gas type
    e. Pulse length
II. Acquire data using diagnostic suite[227] at as many diagnostic ports as possible
    a. Electron temperatures, electron densities and Mach numbers to calculate the parallel heat transport throughout the device (HELIOS, LPs, MPs)
    b. Power deposited to machine surfaces to infer lost power (IR camera, FPs, (S)TCs)
    c. Power losses due to neutral deuterium processes and radiative processes (TALIF, baratrons, photodiodes, bolometer array, spectroscopy).
III. Use software modeling to determine power generation, transport, loss and deposition along the machine
    a. MATLAB for all general analyses, including error calculations and parallel heat transport along the machine
    b. THEODOR for power and heat flux deposition to the end plates
    c. COMSOL to measure and corroborate heat deposited to end plate other machine surfaces
    d. SOLPS to verify measurements of plasma transport and losses, if available.
IV. Compare diagnostic data and modeling data
V. Analyze Proto-MPEX, dividing machine into three main regions (helicon, upstream, and downstream), as well as sub-regions.
    a. Use region analysis to highlight areas with low inefficiencies or larger quantities of missing power for future analysis.

[227] See Chapter 3.

CHAPTER 7: POWER SOURCE CONCEPT EXTRAPOLATION

To increase the opportunity of success of MPEX PMI research, it is crucial to have an understanding of how MPEX plasmas might behave. To gain this understanding, experiments performed on Proto-MPEX are analyzed and extrapolated to MPEX operating conditions, particularly its increased power source capacity. In this chapter, the power and heat flux deposited on the target plate were calculated for multiple machine operating configurations and for a variety of plasma production scenarios: helicon power only, helicon power supplemented with electron cyclotron heating (ECH), helicon power supplemented with ion cyclotron heating (ICH), and helicon power supplemented with combined ECH and ICH. Figure 7.1[228] provides a diagram of the Proto-MPEX machine, highlighting the locations of the power sources and end plates. The power-to-target efficiencies[229] for each scenario were also determined. For each machine configuration, the power sources efficiencies were used to predict the power and heat fluxes to the target plate when MPEX-scale power sources were applied. The analyses identify machine operating parameters that estimate power and heat fluxes to the target plate for future PMI studies. They additionally suggest power source combinations required to achieve MPEX heat flux requirements.

Five main operating conditions were varied across the various experiments on Proto-MPEX: magnetic field configuration, gas flow rates[230], plasma pulse length, total injected power, and type of applied power (i.e. helicon + ECH or helicon + ICH). Table 7.1 lists the variety of the magnetic field operating conditions used in this chapter's analyses. Table 7.2 lists the variety of gas flow rates applied. The primary diagnostic applied for these experiments was an infrared (IR) camera [44].

It is important to note a potential error was discovered in the ECH voltage-to-power calibration process shortly before the defense of this dissertation. The possible error could result in the calculated ECH power being a up to a four greater than previously thought. However, the issue was not fully resolved prior the completion of this thesis. Therefore, an ECH voltage-to-power calibration that was the average of the possible calibration range was used for the detailed extrapolation analysis, using the following equation set.

$$\mathrm{P_{ECH}} = \bar{\mathrm{C}}\,\mathrm{V} \tag{7.1}$$

$$\bar{\mathrm{C}} = \mathrm{C_{min}} + \mathrm{C_{max}}$$

where P_{ECH} is the ECH power that corresponds to the ECH voltage signal, V, $\bar{C}$ is the average voltage-to-power calibration factor, C_{min} is the minimum (and original) calibration factor, $\frac{100}{9}$, and C_{max} is the maximum calibration factor, $\frac{400}{9}$. Appendix B provides example analyses of the extrapolation using the minimum and maximum of the ECH power calibration range.

[228] Figure 7.1 is slightly edited reproduction of figure 2.1.
[229] The total power arriving at the target plate compared to the total input power.
[230] For this thesis, the terms 'gas flow rate' and 'gas puff rate' are used interchangeably.

7.1. Efficiency and Extrapolation Method

The efficiency of the power-to-target is described using the following equation,

$$\eta = \frac{P_{target}}{P_{in}} \tag{7.2}$$

where η is the efficiency, P_{target} is the power measured on the target plate, and P_{in} is the net input (forward minus reflected) power. The power deposited to the target plate was determined via images acquired from the IR camera that were analyzed using a combination of MATLAB and THEODOR[231] codes. The efficiencies of the additional power sources are determined by comparing pulses using just the helicon and the helicon with an additional power source. The following set of equations is used to determine the ECH efficiency as an example,

$$\eta_H = \frac{P_{target,H}}{P_H}$$

$$\eta_{H+E} = \frac{P_{target,H+E}}{P_{H+E}} \tag{7.3}$$

$$\eta_H P_H + \eta_E P_E = \eta_{H+E}(P_H + P_E)$$

where η_H is the helicon efficiency, $P_{target,H}$ is the power to the target from the applied helicon power alone, P_H is the net input helicon power, η_{H+E} is the combined helicon + ECH efficiency, $P_{target,H+E}$ is the power to the target from the applied helicon and ECH power, P_{H+E} is the net input helicon and ECH power, P_E is the net input ECH power, and η_E is the ECH efficiency, for which the equations are solved. A similar process can be applied for determining the ICH power, if applied, or if all three power sources are applied. It is important to note that this process assumes that there is no destructive or constructive interference between the power sources. For example, the helicon efficiency is assumed to remain constant when ICH or ECH is applied. When all three power sources are applied, their efficiencies are assumed to remain constant as well. To justify this assumption in the instance of applying all three power sources, the ECH efficiency derived from the helicon + ECH pulse is used to back-calculate the ICH efficiency. The ICH efficiency derived from the helicon + ICH pulse is used to back-calculated the ECH efficiency. The two ECH efficiencies and ICH efficiencies are compared to ensure the assumption of constant efficiencies is valid.

To extrapolate the deposited power expected on MPEX with increased capacity for the three power sources, the efficiencies are held constant while the applied net input power is increased, using equation 7.4.

$$\eta_H P_H + \eta_E P_E + \eta_I P_I = P_{target} \tag{7.4}$$

[231]Recall the description of THEODOR is provided in Chapter 6.

To extrapolate the heat flux expected on MPEX, the heat flux profile at a given time, *t*, for the helicon + ECH pulse (for example) is plotted along with the helicon only pulse. The heat flux profile of the helicon pulse is subtracted from the helicon + ECH pulse. The resulting heat flux profile represents the change in heat flux solely due to the application of the ECH. The helicon heat flux profile and ECH heat flux profiles are scaled-up by the ratio of the MPEX-capacity of the power source to the Proto-MPEX input power of the power source. This process ensures the integrity of the heat flux profile is maintained as the applied power is extrapolated. That is, if the ECH application tends to cause increases in the heat flux at the edge in Proto-MPEX, then the MPEX-level ECH application should also increase the heat flux at the edge of the profile. Assuming 10 MW/m^2 heat fluxes desired on the target plate, the required power from each source can be back-calculated based on the heat fluxes measured during experiments. Combinations of required power from each power source can be determined to achieve the 10 MW/m^2 benchmark heat flux.

7.2. Power Scan Analysis

One of the main differences between Proto-MPEX and MPEX is the increased power capacity. In order to be better prepared for MPEX operations and plasmas, power scan analyses of the helicon antenna and the target plate were performed.

7.2.1 Effect on helicon window

As demonstrated previously, the helicon antenna generates high density plasma that can be further heated with ICH and ECH; hence, the helicon is an important power source to obtaining the desired target plate heat fluxes. It is crucial that the measurements of the deposited power and heat expected on the MPEX helicon window be available for the design of the MPEX helicon system and MPEX experimental operations.

To determine the effect of varying the input power on the power deposited to the helicon window, a power scan was performed for 500 ms pulses using the configuration 1 and gas puff type 1 listed in tables 5.3 and 5.4; note, these are different machine parameters than those used for the FEA-1D heat conduction comparison, a process described in detail in previously a published work [39]. The input powers included 50 kW, 60 kW, 70 kW, and 100 kW. For an input power of roughly 50 kW, the FP inferred 18.9 ± 2.0 kW of power deposited to the helicon window, or approximately 37.8% of the input power. For 60 kW of input power, the FP inferred 24.1 ± 2.0 kW of deposited power, approximately 40.2 % of the input power. For 70 kW of input power, the FP inferred 28.5 ± 2.0 kW of deposited power, or 40.7% of the input power. For 100 kW of input power, the FP inferred 37.3 ± 2.0 kW, or 37.3% of input power. Based on these results, in can be concluded that the percent of power lost to the helicon window is approximately constant for varying input power, for a given set of magnetic field configuration, pulse length, and gas puff rate, held constant. This correlation is useful for future MPEX operations. MPEX planned helicon capacity is 200 kW. Assuming the percent power deposited to the helicon window remains approximately constant, the total power predicted to be deposited on the helicon window for MPEX is about 75-80 kW for this

specific operating configuration. Understanding the expected power deposition is necessary to the design of the MPEX helicon cooling system.

7.2.2 Effect on target plate

To understand how the power-to-target efficiencies would behave as the injected power increased to MPEX-level capacity, a multi-shot analysis was performed for multiple different machine configurations where the injected power ranged from 20-95 kW of net helicon power. The primary concern was the power-to-target efficiencies would degrade as the injected power increased for MPEX operations. Fortunately, analysis of the helicon power scans implies the opposite - as the injected power increases, the efficiency to target either remains constant or slightly increases. The apparent effect varies with different machine parameters, such as gas flow rate and magnetic field configuration. Table 7.3 summarizes the operating configurations for each power scan experiment. Assuming the trend is valid beyond approximately 100 kW of net helicon power, the helicon power-to-target efficiencies on MPEX should be equal to or slightly greater than those observed on Proto-MPEX, for a given operating configuration. This implies that the MPEX-scaled powers and heat fluxes deposited to the target will be at least as large as those listed in tables 7.5, 7.7, and 7.9 later in this chapter. The resulting efficiencies of the power scan experiments are plotted versus net injected helicon power in figure 7.2 to further demonstrate the correlation.

The plasma pulses in experiment D of the power scan analysis (see table 7.3) used a similar operating configuration to the pulses used in experiment 3 of the MPEX extrapolation analysis (see tables 7.1 and 7.2), which is described later in this chapter. Experiment D also included helicon + ECH pulses. However, the efficiencies of experiment D provided in figure 7.2 were evaluated prior to the ECH power was applied. For experimental set D, the ECH power applied was approximately 8 kW.[232] An analysis of the same pulses was performed approximately 50 ms after the ECH was applied to determine the effect of the net helicon power (and therefore the plasma density) on the ECH coupling to the helicon plasma (see figure 7.3). This analysis supplements experiment 3 of the MPEX extrapolation analysis (see *ECH Extrapolation* section).

The operating configuration of experiment D was implemented to allow the current 28 GHz ECH system to mimic a 104.9 GHz ECH system, which has recently been installed on Proto-MPEX. Helicon generated plasmas on Proto-MPEX achieve densities on the order of 5e19 m^{-3}. The cutoff density of the 28 GHz system is only 1e19 m^{-3}, preventing effective heating of the helicon plasma. In comparison, the 104.9 GHz system would be able to directly heat helicon plasmas with densities of up to 6.8e19 m^{-3}. To enable to 28 GHz system to mimic a 104.9 GHz system, the density and B-field needed to be reduced to maintain the same values for two dimensionless ratios: the electron plasma frequency ratio and the gyrofrequency ratio, according to equation set 7.5.

$$ratio_{ce} = \frac{\omega}{\omega_{ce}}$$

[232] Recall, the power calibration used to determine the applied ECH power is under review.

$$ratio_{pe} = \frac{\omega}{\omega_{pe}}$$

$$\omega_{pe}^2 = \frac{n_e e^2}{\varepsilon_0 m} \tag{7.5}$$

$$\omega_{ce}^2 = \frac{qB}{m}$$

where $ratio_{ce}$ is the gyrofrequency ratio, $ratio_{pe}$ is the electron plasma ratio, ω is the frequency of the ECH system, ω_{pe} is the electron plasma frequency, ω_{ce} is the electron gyrofrequency, n_e is the electron density, e is the electron charge, ε_0 is the vacuum permittivity, m is the electron mass, q is the electron charge, and B is the magnetic field strength. Keeping these ratios constant will enable similar physics from the Stix cold plasma dielectric tensor [119], ECH resonance, and UH resonance [120].

To reduce the density, the power and gas flow rates were reduced from standard operating levels (see tables 7.1 and 7.2). Unfortunately, Langmuir probe data for this experiment was not available to provide specific measurements of the electron density reduction. Figure 7.3 depicts the total power-to-target efficiency as a function of the injected power for experiment D. For the operating conditions, the ECH efficiency maximizes around 55 kW of net helicon power. There is a marked increase in the ECH efficiency around 40 kW of net helicon power. This implies that the plasma density is close to the necessary value required for the 28 GHz system to achieve the electron plasma/gyrofrequency ratio of the 104.9 GHz system. This power scan additionally increased confidence that operating the 104.9 GHz system will allow the ECH to better heat the helicon plasma and achieve increased heat fluxes and power on the target plate. This notion is further supported in the *ECH Extrapolation* section.

During the power scan, analysis demonstrated that for a given set of operating parameters, a certain level of helicon power was required to produce a smooth plasma. Below this level, the plasma profile is noisy and difficult to properly analyze. For plasmas with operating conditions like experiments A-C, the required net helicon power is approximately 70 kW. Figure 7.4 provides the heat flux profiles of two plasma shots from the experiment A power scan. Between the two shots, the net helicon power increased from about 65 kW to 75 kW. The plasma at approximately 75 kW net helicon power is considerably smoother.

7.3. Pulse Length Analysis

For Proto-MPEX operations, plasma pulse lengths range between 300 ms and 2000 ms. Since MPEX is intended to be a steady-state device, it is important to have an understanding of how the increased pulse lengths will affect machine surfaces, especially the helicon window and the target plate. In this subsection, analyses of the helicon window and the target plate are performed to determine what effect, if any, the pulse length has on the power deposition to their surfaces.

7.3.1 Helicon pulse length scan

To determine the effect of varying the pulse length on the power deposited to the helicon window, a plasma pulse length scan was performed for approximately 100 kW of input power using configuration 2 and gas puff type 1 listed in tables 5.3 and 5.4. In theory, since power is equal to energy over time, the power should not be dependent on the pulse length. The helicon pulse length scan served to confirm that concept. The pulse lengths included 500 ms, 750 ms, and 1000 ms. For a 500 ms pulse, the deposited power inferred by the FPs was 34.5 ± 2.0 kW. For a 750 ms pulse, the deposited power was 34.2 ± 2.0 kW. For a 1000 ms pulse, the deposited power was 34.2 ± 2.0 kW. Therefore, it can be concluded that the pulse length does not change the power deposited to the helicon window, for a constant input power, magnetic configuration and gas puff rate. This correlation has positive implications for future MPEX operations. In theory, for a given operating configuration, the power deposited to the helicon window should remain constant for longer pulses as MPEX works towards steady-state operations.

7.3.2 Effect on target plate

To determine the effect of varying the pulse length on the power and heat fluxes hitting the target plate, analyses were performed for 500 ms, 750 ms, and 1000 ms plasma pulses. For a given fixed set of operating conditions, other than increasing the pulse length, the greatest overall heat flux profiles occurred shortly after the application of a given power source.[233] Figure 7.5 provides the 2D heat flux profiles over time for a 500 ms pulse and a 1000 ms pulse with the same operating conditions with the exception of pulse lengths. These two shots were helicon-only, using magnetic configuration 5 and gas puff rate 2 (see tables 7.1 and 7.2). Their power-to-target efficiencies at time, *t*, approximately equals 4.65 seconds, where their heat fluxes were close to their highest, were both about 0.6%. Small variations in their profiles is typical of sequential plasma pulses during operations.

Comparing their two profiles, it is evident the maximum heat flux occurs towards the beginning of the plasma pulse. Therefore, it is reasonable to assume the actual pulse length will not greatly affect the maximum power-to-target plate efficiencies. The efficiencies calculated should be applicable to MPEX steady-state operations.

It is important to note that the target plate heat flux is continuing to fall over the course of the 1000 ms pulse length in figure 7.5 (right). It appears to drop approximately 30% in one second. If this trend continues, no heat flux will be arriving at the target plate within 10 seconds of plasma operations; that is, the plasma will have detached from the target. This has serious implications for steady-state PMI operations on MPEX. Further experiments where the pulse lengths are longer than 1000 ms are required to explore this phenomenon. It is possible the heat flux fall-off rate plateaus rather than reaching zero. Regardless, additional experimentation is necessary in the near future.

[233] Unless the operating conditions are changing within the pulse, such as the application of additional power sources, the most heat flux and thereby power, impinges on the plate towards the beginning of the pulse, well within the standard pulse length of 500 ms.

7.4. Power-to-Target Efficiency Time Analysis

To compare the power-to-target efficiency to other machine operating parameters, the efficiency can be plotted along the time length of the plasma pulse. In this subsection, the overall power-to-target efficiencies are compared to the injected power source for different applied power combinations. An effort was also made to compared to the neutral gas pressure for different gas flow rates and for different applied power sources, since the neutral gas pressure was expected to affect the target plate heat fluxes and power-to-target efficiencies. Unfortunately, the initial analysis of the relationship between the baratron-inferred neutral pressures and the resulting target plate heat fluxes revealed no reliable trend and the analysis was instead included as appendix C.

7.4.1 Efficiency vs. Applied Power

In this subsection, the overall power-to-target efficiency is compared to the net applied power for a helicon + ECH pulse, a helicon + ICH pulse, and a helicon + ECH + ICH pulse. By plotting the efficiency with the inject power sources, the effect of the application of additional power becomes more apparent. The efficiency plotted is the total power-to-target efficiency – that is, the total power to the target over the total power being applied, at a given point in time. Figure 7.6 compares the efficiency to the injected power over time for shot 19240 in experiment 2 (see table 7.4 in next section, *ECH Extrapolation*). The light green box highlights the approximate time range where the helicon efficiency and ECH efficiency were calculated. For this shot, helicon and ECH were applied. The ECH was applied approximately 120 ms after the pulse began. The power-to-target efficiency trace decreases initially with the application of the ECH, perhaps as the power source starts to couple with the helicon plasma, at a time, *t*, approximately 4.32 seconds and then increases again as the ECH application continues. When the ECH power drops at time, *t*, approximately equal to 4.41 s, the overall efficiency appears to increase again, surpassing the efficiency during the helicon-only portion of the pulse. Figure 7.6 demonstrates that the ECH slightly increases the power-to-target efficiency, indicating that the ECH efficiency is greater than the helicon efficiency for this shot. Table 7.5 reiterates this correlation, with a helicon efficiency of 0.75% and a 1.0% ECH efficiency.

Figure 7.7 compares the efficiency to the inject power over time for shot 19721 in experiment 4, which is a helicon + ICH pulse (see *ICH Extrapolation* section later in this chapter). The ICH was applied approximately 2-3 ms after the start of the pulse, rendering it difficult to determine the effect of the ICH application when it is first injected. However, the ICH power steps down from approximately 30 kW to approximately 10 kW at time, *t*, equals 4.47 seconds. When the ICH power steps down, there appears to be a slight increase in the total power-to-target efficiency. This indicates that the helicon efficiency is slightly higher than the ICH efficiency. Table 7.7 reiterates this correlation for experiment 4, with a helicon efficiency of 1.0% and an ICH efficiency of 0.7%.

Figure 7.8 compares the target efficiency to the total injected power over time for a helicon + ECH + ICH pulse from experiment 7. Like shot 19721, the ICH was applied a few milliseconds after the start of the pulse, as defined by the application of helicon power. The ECH was applied approximately 5 ms after the pulse start. The helicon trace

experiences a brief power drop of about 20 kW shortly after the ECH is applied before recovering to normal power. The unexpected loss of power is demonstrated in the slight dip in the target efficiency trace around time, *t*, equal to 4.21 s. The helicon power drop obscures the ability to determine the effect of adding the ECH at the beginning of the pulse. The effect of the application of ECH and ICH, as compared to only the helicon, is apparent when the two power sources turn off. The ECH and ICH turn off at approximately the same time, around t = 4.45 seconds, although the ECH turns off shortly before the ICH. The efficiency trace begins dropping at the same time as the end of the ECH pulse. The efficiency does not seem to react to the end of the ICH pulse. The trends in the efficiency trace imply that the helicon and ICH efficiencies are approximately the same and the ECH efficiency is greater. Referring to the efficiencies listed in table 7.9 the helicon, ECH, and ICH efficiencies are 0.7%, 1.0%, and 0.6%, respectively, confirming the trend observed in figure 7.8.

7.5. ECH Extrapolation

In this subsection, power and heat flux deposited on the target plate was calculated for helicon-only and helicon + ECH plasma pulses for three different operating conditions. For the three configurations, the deuterium gas is injected into the machine at z = 0.6 m (see figure 7.1). The plasma pulse lengths, defined by the length of the helicon pulse, were either 500 ms or 1000 ms. The pulse starts when time, *t,* is approximately equal to 4.16 seconds. When applied, the ECH pulse lengths ranged from 230-350 ms.[234]

7.5.1 Experimental Results & Analysis

The plasma shots that were analyzed for the three ECH extrapolation experiments are listed in table 7.4, which provides a summary of the conditions for each set of experiments and for each shot within an experimental set. Multiple shots were analyzed for each set condition to ensure reliability and repeatability. Table 7.5 summarizes the resulting efficiencies for each applied power source, the total power and heat flux deposited on the target when both power sources were applied, and the power and heat flux predicted to reach the target on MPEX.

As previously stated, MPEX will have the following power source capabilities: 200 kW of helicon power and 200 kW of ECH power [32]. The nominal helicon power for Proto-MPEX is 100 kW. However, on average, about 90 kW of helicon power reaches the plasma. Therefore, when determining the scale-up power for MPEX, 90% of the available helicon power, or 180 kW, was assumed. The ECH was assumed to be 200 kW. Comparing the power-to-target efficiencies across each experiment provides insight regarding which machine operating configurations would enable the best plasma-power source coupling and therefore, be the best for future MPEX PMI operations.

To determine the effect of adding the ECH to the helicon plasma, the plasma shot was analyzed right before the ECH was applied to determine the helicon efficiency and approximately 50 ms after to determine the ECH efficiency. Initially, helicon-only pulses were used to determine the helicon efficiency and helicon + ECH pulses were used to

[234] Recall that the power applied during the ECH pulses is under review to a potential error in the ECH power calibration.

determine the ECH efficiency. However, it is difficult to recreate the same exact plasma across different operating days. The helicon-only and helicon + ECH pulse for experiment 2 were performed on different days. Therefore, to avoid variations attributed to different operating days and to ensure the same analysis method was applied across all three experiments, the same shot was used to determine both efficiencies for each experiment. The helicon pulse length was 500 ms for these two experiments.

The main difference between experiments 1 and 2 was the gas puff type. Both gas puffs started at t = 3.985 s. The gas flow rate for experiment 1 started at 7910 sccm and decreased to 6910 sccm at t = 4.22 s, while the gas flow rate for experiment 2 started at 7510 sccm and remained at 7510 sccm after t = 4.22 s (see table 7.2). All the plasma analyses were performed during the second puff, after t = 4.22 s; thus, differences in the power-to-target efficiencies and heat fluxes between experiments 1 and 2 are likely due to the differences in the second gas puff, though further experiments are required to confirm the relation.

The higher gas rate during the second puff in experiment 2 had little effect on the overall helicon efficiency and the power arriving on the target. (It is important to note that the target power listed in table 7.4 is the power measured on the target for the helicon + ECH cases). However, the higher second gas puff reduced the ECH efficiency by about 65%. The increase in the gas flow rate also likely resulted in more heat being localized on the edge of the plasma profile, rather than the desired center. Figure 7.9 compares the Proto-MPEX plasma profiles for experiments 1 and 2, as well as their heat flux profiles extrapolated to MPEX-level power capacities.

Figure 7.9 demonstrates that the greater secondary gas rate results in more plasma heat remaining on the outside of the generated plasma. The profiles show that the ECH for experiments 1 and 2 tends to deposit power on the edges of the plasma profile as well. The center heat flux with and without the ECH applied for both experiments appears to be approximately the same. The additional power arriving on the target plate is due to additional heat on the edges of the plasma profiles, implying the ECH power is not coupling to the helicon plasma as well as desired. The green dotted lines in the left column of figure 7.9 shows the ECH contribution to the target heat flux.[235] For both experiments 1 & 2, the ECH heat flux profile is edge peaked. Between the two experiments, shot 17791 prior to ECH application (blue line in upper left of figure 7.9) has the most desirable profile for PMI experiments, with the majority of the plasma in the center of the profile. Although the maximum center heat flux with ECH applied is nominally the same for both experiments, the higher secondary gas rate appears to cause a more uneven plasma profile of the edges, implying the ECH gets ‘stuck’ on the outer plasma flux lines near the injection location and does not couple to the plasma quite as well as it does in experiment 1. This behavior was predicted by previous EBW modeling performed in previously published works [121, 122]. According to the EBW modeling, the ECH should be absorbed at the plasma edge for plasmas generated by the machine operating parameters of experiments 1 and 2. When scaling up to MPEX-

[235] Determined by subtracting the heat flux profile of the helicon only pulse from the heat flux profile of the helicon + ECH pulse.

level applied power in the right column of figure 7.9, the tendency of the ECH to deposited heat to the edge of the plasma profile becomes more apparent. The solid orange line represents the sum of the MPEX-level expected helicon (dotted blue line) and ECH heat flux profiles (dotted green line). The maximum heat fluxes occur on the edges of the profiles for both experiments 1 and 2. The maximum heat flux for experiment 1 and 2 were 3.3 MW/m^2 and 4.1 MW/m^2, respectively.

Experiment 3 is the outlier from experiments 1 and 2, which applied standard machine operating conditions with the current 28 GHz ECH system. Like experiment D in *Power Scan Analysis,* experiment 3's conditions were selected to best mimic an upgraded 104.9 GHz ECH system. Again, to reduce the density, the power and gas flow rates were reduced from standard operating levels (see tables 7.1 and 7.2). The plasma pulses were 1000 ms. The low injected helicon power and the low gas rate result in an edge-peaked plasma profile, as depicted in figure 7.10. Unlike in experiments 1 and 2, the application of ECH resulted in a considerable increase in heating in the plasma core, rather than the edge. The center heat flux increased by over a factor of three with the addition of ECH. There also appears to be a slight reduction in the edge heat flux, supporting the notion that the 104.9 GHz will provide better core plasma heating. The resulting maximum heat flux expected on MPEX is 8.0 MW/m^2.

The amount of power required from each power source to achieve a desired heat flux can be determined using the calculated target power and heat flux. The helicon contributions to the heat flux profiles with both helicon and ECH applied are known from the helicon-only pulses. The contributions of the ECH were calculated by subtracting the helicon heat flux contribution from the helicon + ECH heat flux. The helicon heat flux was scaled up by the ratio between the MPEX helicon capacity and the input helicon power for the pulse. The same process is applied to scale up the ECH heat flux. The two heat flux profiles are then added together to determine the total heat flux profile expected on the target plate for MPEX-scale plasmas. The necessary input power can be obtained by varying those ratios and seeing the resulting effect on the total heat flux profile. For example, using the conditions from experiment 3, the ratio of MPEX helicon power capacity to the input helicon power was 180:34.6. The ratio of MPEX ECH power capacity to the input ECH power was 200:17.7, yielding a maximum heat flux of 8.0 MW/m^2, well above the desired 10 MW/m^2. The targeted 10 MW/m^2 heat flux cannot be achieved for experiment 3, unless the installed helicon and ECH power capacities increase on MPEX or the final ECH power calibration factor is determined to be closer to the minimum (see equation 7.1).

The comparison between experiments 1-3 highlights the importance of the neutral gas, particularly the flow rate, in the target heat flux and power-to-target efficiencies. As the secondary gas puff (after t = 4.22 s) decreased in experiments 1-3, the ECH efficiency increased, from 0.95% (experiment 2) to 1.5% (experiment 1) to 2.0% (experiment 3). Decreasing the gas puff lowered the neutral gas pressure. The observed trend is supported by previous EBW modeling, which suggests that at low neutral pressure, ECH collisional damping at the plasma edge is reduced and the 28 GHz ECH power should be absorbed closer to the plasma core [121, 122]. The dramatically lower gas

flow rate in experiment 3 yields a significant improvement in core heating by the ECH. However, additional experimentation is recommended to confirm this trend.

Using the conditions from experiments 1 and 2, a center heat flux of 10 MW/m^2 cannot be achieved and the maximum heat fluxes occur on the edges of the plasma profile. In comparison, although experiment 3 also cannot achieve 10 MW/m^2, the maximum heat flux is approximately a factor of two higher than those of experiments 1 and 2 and that maximum heat flux occurs in the center of the plasma profile. The results highlight the importance of installing the 104.9 GHz system. The conditions of experiment 3 significantly improve the performance of the plasma in comparison to those of experiments 1 and 2.

7.6. ICH Extraplation

Given the fact that the ICH is intended to have the largest installed capacity out of the three power sources, the machine operating conditions chosen for MPEX should maximize the ICH efficiency. Therefore, the extrapolation analysis was also applied to plasma pulses with helicon and ICH applied, as well as with all power sources applied. Unfortunately, for a fixed operating configuration, there were not as many repeated plasma pulses as were available for the ECH extrapolation, reducing the level of confidence in the resulting extrapolations. However, due to the importance of ICH operations to future MPEX experiments, the extrapolations were included in this thesis.

In this section, helicon-only and helicon + ICH pulses were analyzed using two different machine operating conditions. The analysis process applied is the same as that explained in the previous subsection, *ECH Extrapolation*. All pulse lengths analyzed were 500 ms, with a pulse start time at time, *t*, approximately equal to 4.16 s. When applied, the ICH pulses were approximately 500 ms. ICH power was applied approximately 2-3 ms after the helicon power was applied. The pulses were analyzed during the second gas puff, after t = 4.22 s.

The analyzed plasma shots are listed in table 7.6, which, like the analysis in *ECH Extrapolation*, provides a summary of the conditions for each set of experiments and for each shot within an experimental set. As previously stated, the experiments in this subsection did not have as many repeated pulses available for analysis for each set of experiments. Experiment 4 did not have repeated helicon-only pulses but had eight repeated helicon + ICH pulses. Experiment 5 had nine repeated helicon-only pulses but only had four repeated helicon + ICH pulses. However, for both experiments, the resulting combined helicon + ICH efficiencies were relatively constant and in experiment 5, the helicon-only efficiencies were relatively constant for the available repeated pulses.

Table 7.7 summarizes the resulting efficiencies for each applied power source, the total power and heat flux deposited on the target when both power sources were applied, and the power and heat flux predicted to reach the target on MPEX. Like the analysis in *ECH Extrapolation*, when determining the scale-up power for MPEX, 90% of the available helicon power, or 180 kW, was assumed to be coupled to the plasma. The ICH was assumed to couple 400 kW.

Experiments 4 and 5 compare helicon-only shots to helicon + ICH shots. No ECH power was applied. Therefore, only the helicon and ICH efficiencies were determined. Thus, the power and heat fluxes scaled up to MPEX capabilities do not include ECH.

To determine the effect of adding the ICH to the helicon plasma, a helicon-only plasma shot was analyzed at the same time, *t*, as a helicon + ICH plasma pulse, approximately 100 ms after the ICH pulse started for experiments 4 and 5. Since the ICH is applied effectively at the same time as the helicon, the analysis method used in the *ECH Extrapolation* subsection is not applicable. Nominally, the machine operating conditions in experiments 4 and 5 were the same, with the exception of a small change in the machine field configuration. The current on coils 3 and 4 were 200 A and 180 A for experiments 4 and 5, respectively.

Since the ICH is the largest power source available on MPEX, any increase in ICH efficiency is magnified when scaling to MPEX. Increasing the efficiency from about 0.7% to 1.6% increased the expected target plate heat flux from 9.6 MW/m^2 to 11.1 MW/m^2, surpassing the 10 MW/m^2 required for PMI studies. Figure 7.11 depicts the differences between the plasma profiles for the two experiments, as well as their heat flux profiles extrapolated to MPEX-level power capacities.

Figure 7.11 clearly demonstrates that the addition of the ICH power increases the central heat flux. Both experiments 4 and 5 demonstrated approximately a 30% increase in their central heat fluxes. It makes more of a contribution to the central heat flux than the additional of the ECH. The application of the ICH also appears to create a narrower plasma profile in the center. Both experiments applied a lower gas rate similar to that of experiment 2, which is demonstrated in the secondary peak in the right of the heat flux profile. The slight decrease in the helicon coil currents appears to yield a narrower core plasma profile as well, comparing the helicon-only shot from experiment 4 with that of experiment 5.

The purpose of experiments 4 and 5 was the explore the effect changing the helicon would have on the ICH coupling. The belief was that the closer that plasma was to the ICH antenna, the better the ICH coupling would be. Reducing the helicon current in experiment 5 marginally decreased the diameter of the plasma downstream under the ICH antenna and in theory, should have slightly reduced the ICH coupling to the plasma core. However, in experiment 5, the helicon efficiency remained approximately the same as that in experiment 4, the ICH efficiency doubled, and the central heat flux increased, contradicting the notion that increasing the proximity of the plasma to the ICH antenna improved the ability of the ICH antenna to couple to the plasma and provide plasma core heating. However, further analysis revealed that during experiment 4, the plasmas were experiencing mid-pulse ‘mode jumping’. The term ‘mode-jumping’ refers to the plasma going from a lower electron density mode to a higher electron density mode. Prior experimentation has shown the higher density mode to improve plasma performance, such as better centrally peaked plasma profiles. Figure 7.12 provides the electron density profiles provided by probe scans at diagnostic port 10.5 (z = 3.4 m) for experiments 4 and 5. The heat flux analysis and extrapolations were performed at approximately t = 4.3 s for both experiments. Figure 7.12 clearly

demonstrates that the electron density in experiment 4 had not entered the higher density phase experienced by experiment 5. The electron density at t = 4.3 s was approximate 50% less for experiment 4 in comparison to experiment 5. As a result, experiments 4 and 5 cannot be used to affirm whether or not a larger plasma radius under the ICH antenna improves the ICH coupling. The differences between the target heat fluxes in experiments 4 and 5 is likely due to the lower electron density mode in experiment 4.

Of the two experiments analyzed in this subsection, experiment 5 can provide 10 MW/m^2 heat fluxes to the installed target plate assuming 180 kW and 400 kW of coupled helicon and ICH power, respectively, although experiment 4 gets close. It is unclear if the conditions of experiment 4 would yield 10 MW/m^2 at the target if the plasma were in the higher density mode for the entirety of the pulse. Given the similarity of its configuration to experiment 5, it would be reasonable for experiment 4 to also reach 10 MW/m^2 assuming 180 kW of coupled helicon power and 400 kW of coupled ICH power, but further experimentation is required.

In experiment 5, if 180 kW of helicon power are applied, 340 kW of ICH power are required to achieve a target heat flux of 10 MW/m^2. If 120 kW of helicon power are applied, then 400 kW of ICH power are required. If 160 kW of helicon power are applied, then 365 kW of ICH power are required. Therefore, using the operating conditions applied in experiment 5, the desired heat flux can not only be achieved without the application of ECH, but with the helicon and ICH sources operating at about 90% of their installed capacities.

7.7. All Power Source Extrapolation

In this section, helicon-only, helicon + ECH, and helicon + ECH + ICH pulses are analyzed and extrapolated using four different machine operating conditions. The analysis process applied is the same as that explained in *ECH Extrapolation*. All pulse lengths analyzed were 500 ms, with a pulse start time at time, t, approximately equal to 4.16 s. When applied, the ICH pulses were 500 ms and ECH pulses were 230-350 ms. ICH power was applied approximately 2-3 ms after the helicon power was applied. The ECH power was applied approximately 5-6 ms after the helicon power was applied.

As previously mentioned, a potential error was discovered in the ECH power calibration process shortly before the defense of this dissertation. Like in the *ECH Extrapolation* sub-section, the original ECH voltage-to-power calibration was used for the detailed extrapolation analysis, using equation 7.1.

Like in previous analyses, the pulses were analyzed during the second gas puff, after t = 4.22 s. Further, like to the ICH extrapolations, there were not as many repeated plasma pulses as were available for the ECH extrapolation, reducing the level of confidence in the resulting extrapolations. Experiment 6 did not have any repeated pulses available, making it the least verified experiment analyzed. Experiment 7 did not have repeated pulses available for the helicon-only and helicon + ECH pulses, but two repeated pulses were available for helicon + ICH pulses and six repeated pulses were

available for the pulses with all three power sources applied. To increase the confidence in the efficiencies derived from analyses in experiments 6 and 7, the ICH efficiency derived from the helicon + ICH pulse(s) was used to infer the ECH efficiency from the helicon + ECH + ICH pulse(s) and compared to the ECH efficiency derived from the helicon + ECH pulse. Similarly, the ECH efficiency derived from the helicon + ECH pulse was used to infer the ICH efficiency from the helicon + ECH + ICH pulse(s) and compared to the ICH efficiency derived from the helicon + ICH pulse(s). The ECH and ICH efficiencies determined from either method were within 5-10% of each other.

The analyzed plasma shots are listed in table 7.8, which, like the previous extrapolation analyses, provides a summary of the conditions for each set of experiments and for each shot within an experimental set.

Table 7.9 summarizes the resulting efficiencies for each applied power source, the total power and heat flux deposited on the target when all power sources were applied, and the power and heat flux predicted to reach the target on MPEX. When determining the scale-up power for MPEX, 90% of the available helicon power, or 180 kW, was assumed to be coupled to the plasma. The ECH assumed 200 kW of coupled power and the ICH assumed 400 kW of coupled power.

Experiments 6 and 7 compared helicon-only, helicon + ECH, helicon + ICH, and helicon + ECH + ICH pulses. Like experiments 4 and 5, they had the same operating conditions except for the magnetic field configuration. The magnetic field configuration of experiment 7 is very similar to that of experiments 4 and 5. Experiment 6 has a different configuration (see tables 7.1 and 7.8). The main purpose of experiments 6 and 7 was to demonstrate the combined effect of the application of all three power sources on the target plate heat fluxes and powers. The effect of changing the magnetic field configuration was also of interest. Figure 7.13 compares the Proto-MPEX plasma profiles for experiments 6 and 7, as well as their heat flux profiles extrapolated to MPEX-level power capacities.

Figure 7.13 demonstrates that the application of ECH increases the central peak heat flux in experiment 6, while the ICH barely effects the central heat flux. The operating conditions yield more evenly distributed power across the plasma profile, which means a larger portion of the ECH and ICH power is deposited closer to the edges of the plasma profile. The ECH (green dotted line) and ICH (purple dotted line) heat flux profiles demonstrate this behavior. In comparison, the operating conditions yield more power to the plasma profile center in experiment 7. As previously stated, the magnetic field configuration in experiment 7 is similar to that of experiments 4 and 5 (see tables 7.1, 7.6 and 7.8). The resulting plasma profiles in experiment 7 demonstrate the similarity, with the peak center heat flux increasing approximately by 25% from the helicon-only shot to the helicon + ECH and helicon + ICH shot and the profile narrowing with the application of additional power sources. Both experiments have the same gas flow rate as experiment 1 (see tables 7.2, 7.4 and 7.8). Like experiment 1, the plasma profiles of experiments 6 and 7 are centrally peaked, lacking the secondary peak on the right side of the plasma profile shown in experiments 2, 4 and 5.

While the helicon and ECH efficiencies are approximately the same across both experiments and the ICH efficiency for experiment 6 is a factor of three greater than the ICH efficiency for experiment 7, the target plate heat fluxes observed in experiment 7 are higher than those observed in experiment 6. It is important to note the power-to-target efficiency is dependent on the total power deposited on the plate, but not necessarily *where* the power is deposited on the plate. On the other hand, the heat flux is dependent on where and how concentrated the power is at a specific location on the plate; that is, the plasma density. The distinction is important for future MPEX PMI studies. While each source's power-to-target efficiency is a good indicator of the power source's performance and important for the MPEX extrapolation, it must be considered in conjunction with the target plate heat flux. For experiments 6 and 7, the target plate heat fluxes become the more important factor for extrapolation. As stated above, in experiment 6, the application of ECH slightly increases the central heat flux. The ICH application contributes effectively no additional heat flux to the center of the plasma. In comparison, the application of ECH and ICH in experiment 7 increased the central heat flux by about 25%. Additionally, the heat flux of the helicon-only shot in experiment 7 is about 35-40% greater than that of experiment 6. Thus, it is reasonable to conclude that the magnetic field configuration of experiment 7 leads to improved coupling to the center of the plasma across all three power sources, especially the helicon and ICH. Therefore, the comparison between experiments 6 and 7 also supports the notion that the closer the plasma is to the ICH antenna, the better the ICH couples power to the plasma core. The average radius of the plasma under the ICH antenna for experiment 6 is about 1.5 cm. The average radius of the plasma under the ICH antenna for experiment 7 is 1.7 cm, which is about a 13% increase over that of experiment 6.

When scaled to MPEX-level installed power capacities, the operating conditions of experiments 7 is capable of achieving 10 MW/m^2 heat fluxes on the target plate, although experiment 6 gets very close. The major difference between the two cases is that since the addition of the ICH and ECH sources distributes heat more evenly across the plasma profile and not specifically in the center for experiment 6, when scaled to MPEX-level power capacities, the plasma profile becomes more edge-peaked. The maximum heat fluxes are found at the edges of the plasma profile, with values of 8.2 and 9.6 MW/m^2 at approximately s = 0.012 m and s = 0.038 m, respectively (see figure 7.13). In comparison, the addition of the ECH and ICH power sources deposit more heat directly in the center of the plasma profile for experiment 7. Therefore, when scaling to MPEX-level power capacities, the heat flux profile is distinctly centrally peaked. The maximum heat flux for MPEX-scale power applications is 12.8 MW/m^2. Interestingly, the total power arriving at the target plate in experiment 6 is actually greater than in experiment 7 (10.4 kW and 5.8 kW, respectively). However, the power is more spread out across the target plate for experiment 6, as previously mentioned. For the purposes of PMI experiments, the conditions for experiment 7 are preferable to those of experiment 6. Experiment 7 appears to have better power coupling to the center of the plasma, which is ideal for PMI experiments.
Of the two experiments analyzed in this subsection, only experiment 7 can provide 10 MW/m^2 heat fluxes to the installed target plate, although experiment 6 gets very close. In experiment 7, the targeted heat flux can also be using 180 kW of helicon power, 200

kW of ECH power, and 200 kW of ICH power. It can also be achieved with 180 kW of helicon power, 8 kW of ECH power, and 400 kW of ICH power. Another option is 120 kW of helicon power, 150 kW of ECH power and 345 kW of ICH power, or 65-85% of their installed capacities.

7.8. Summary

This chapter focused on calculating the power and heat flux deposited on the target plate for multiple machine operating conditions and a variety of plasma production scenarios. The power-to-target efficiencies for each scenario were also determined. The power source efficiencies were used to predict the power and heat fluxes to the target plate when MPEX-scale power sources were applied. Power scan analyses were performed to the MPEX extrapolations to ensure the determined efficiencies would not decrease with increase applied power. Pulse length analyses were also performed to determine the effect of increasing the pulse length on the target plate heat fluxes and power-to-target efficiencies. The pulse length analyses suggested additional long pulse (1000+ ms) experiments are necessary to gain a better idea of plasma behavior near the target for future steady-state operations. Power-to-target efficiency time analyses were also performed to corroborate the extrapolations performed. The need for additional neutral gas experiments were also highlighted through the extrapolation analyses and the power-to-target time analyses.

The extrapolation experiments provide significant flexibility for future PMI experiments on MPEX. Trends in gas puff types and magnetic field configurations have been highlighted, which lead to reduced auxiliary power requirements that achieve a 10 MW/m^2 benchmark. Alternatively, the power systems can be tailored to provide more than 10 MW/m^2 at specific radial locations. For example, the targeted 10 MW/m^2 heat fluxes can be achieved with ECH power or without ECH power, assuming the helicon and ICH are operating at 90% installed capacity. The heat flux cannot be achieved without the application of ICH power unless the MPEX installed power capacity of the helicon and ECH is increased or the final ECH power calibration is closer to the minimum value (see equation 7.1). Finally, the desired heat flux can also be achieved in each power source is operating at 65-85% installed capacity, using the conditions of experiment 7. Therefore, PMI-required target heat fluxes are readily achievable on MPEX for at least two different operating conditions that have been analyzed in this subsection.

CHAPTER 8: CONCLUSION AND FUTURE WORK

8.1. Summary of Work

The successful development of future nuclear fusion reactors is important to developing a new clean baseload power source. Unlike other energy sources, fusion can achieve a net energy gain without the risk of reactor meltdown or long-lived radioactive waste. Tokamaks are the leading reactor design. Linear plasma devices are crucial to nuclear fusion reactor research, providing critical PMI studies. The main plasma heating technique applied in linear devices is EM wave heating, which encompasses helicon heating, ECH, and ICH.

Proto-MPEX at ORNL is a linear plasma device with the primary purpose of developing the plasma source concept for the MPEX, which will address plasma material interaction (PMI) science for future fusion reactors. Proto-MPEX has three main installed power sources[236]: (1) a 13.56 MHz helicon antenna; (2) a 28 GHz electron cyclotron heating (ECH) launcher; and (3) a 6-9 MHz ion cyclotron heating (ICH) antenna. An extensive array of diagnostics is installed on Proto-MPEX. The diagnostics provide a range of different plasma measurements, including electron and ion temperatures and densities, plasma flow rates, machine surface temperatures, and neutral gas densities, all of which are used during experimental operations. Many diagnostics are designed to accommodate multiple installation locations to provide better diagnostic coverage of the machine. The diagnostic suite is constantly being improved and expanded. The Proto-MPEX machine was shutdown for a machine upgrade from May – August 2018 in order to accommodate the addition of the 104.9 GHz ECH system for improved ECH target heating. FMNSD at ORNL achieved Critical Decision (CD)-0 for MPEX in March 2018. The MPEX team plans to achieve CD-1 during fiscal year (FY) 2019.

Multiple power accounting analysis were performed on Proto-MPEX to quantifying plasma loss locations and mechanisms. With each successive analysis, the power accounting method improved, revealing more information about the Proto-MPEX plasma behavior. The power balance was separated into three main components: input power (P_{in}), lost power (P_{loss}), and deposited power (P_{dep}). For this thesis, the helicon was the only power source. The input power was the net (helicon) power after reflected and resistive power losses are subtracted from the nominal injected power. The lost power referred to the power lost from the plasma as the plasma travels from the power source to the end plates. Sources of power losses included radiative transport losses and non-radiative transport losses, such as recombination, elastic collisions, and charge exchange [i.e. 11, 99] and limiting surfaces. Deposited power referred to the power that is deposited on the end plates. To perform the power balance, the Proto-MPEX machine is broken down into three main regions: (1) the helicon region; (2) the upstream region; and (3) the downstream region. Each of these three regions are broken down into smaller sub-regions to better evaluate plasma transport and losses

[236] More detailed specifications of the power sources are described in previously presented and published documents [i.e. 34].

between diagnostic ports available for data acquisition. The plasma power transport efficiency can be determined in each sub-region to highlight potential areas of the machine with lower efficiency.

The helicon region was further analyzed using installed fluoroptic probes and thermocouples to identify loss mechanisms for specific machine operating parameters. Results suggest higher puffed gas increases power deposited to the helicon window, likely due to increased particle collisions. Higher magnetic fields around the helicon decrease it, since a higher field reduces the plasma radius and pulls it away from the helicon window.

Finally, the power and heat flux deposited on the target plate were calculated for multiple machine operating conditions and a variety of plasma production scenarios. The power-to-target efficiencies for each scenario were also determined. The power sources efficiencies were used to predict the power and heat fluxes to the target plate when MPEX-scale power sources were applied. Power scan analyses were performed to the MPEX extrapolations to confirm the determined efficiencies would not decrease with increase applied power. Pulse length analyses were also performed to determine the effect of increasing the pulse length on the target plate heat fluxes and power-to-target efficiencies. The pulse length analyses suggested additional long pulse (1000+ ms) experiments are necessary to gain a better idea of plasma behavior near the target for future steady-state operations. Power-to-target efficiency time analyses were also performed to corroborate the extrapolations performed. The need for additional neutral gas experiments were also highlighted through the extrapolation analyses and the power-to-target time analyses.

8.2. Key Conclusions

8.2.1 Power Accounting Analysis

The full power accounting analysis provided in chapter 6 yielded several important conclusions regarding the Proto-MPEX plasma during experimental operations. Upon the conclusion on the power accounting analysis, 51.65 kW (62.4%) of the input power was diagnostically verified. That is, it was measured on the machine surfaces and end plates by installed diagnostics. The majority of these losses occurred in the helicon region. Analysis of collisional losses suggest that more power is lost to the machine surfaces, particularly in the region from z = 1.5 m to the skimmer plate (z = 1.75 m). Increased diagnostic coverage of the machine surface temperatures should increase the amount of diagnostically verified power.

The skimmer plate plays an extremely important role in Proto-MPEX operations. It effectively divides the machine into a “high-pressure” region from the dump plate to the skimmer plate, and a “low-pressure” region from the skimmer plate to the target plate. The higher pressures upstream of the skimmer plate are required to create high-density helicon plasmas. However, the higher pressures also resulted in increased collisional losses. Only 20% of the injected power passes into the “low-pressure” region downstream of the skimmer plate. Research efforts should focus on maximizing the

plasma transport from the downstream side of the skimmer plate to the target plate to maximize heat fluxes to the target. The high collisionality of the region upstream on the skimmer plate additionally has important implications for the MPEX design and operations. For the machine operating conditions of the full power balance in chapter 6, 37.2 kW of power were deposited to the helicon window. Scaling the input power to expected MPEX-level coupled helicon power, approximately 84.3 kW of power will be deposited to the helicon window. The helicon cooling system must be designed accordingly. Further, in the machine region between the helicon region and the skimmer plate (z = 1.5 to 1.75 m), an additional 12.3 kW (15.5%) of power was lost to the machine surface through collisional processes. While not all of this power lost was diagnostically verified, if it the calculations are reliable, approximately 27.2 kW of power will be deposited to machine surfaces in this region on MPEX. Additional cooling may be required.

In the downstream, “low-pressure” region of the machine, few collisional losses are observed. Additional diagnostics such as bolometers and photodiodes should be applied in this region to confirm the behavior. However, according to the power accounting study of this thesis, the downstream region of the machine will not require significant cooling on MPEX. The only area where cooling may be a concern is immediately in front of the target plate. Analyses suggest the MPEX steady-state pulses could result in a build-up of neutral gas pressure in front of the target plate, which will result in machine surface heating near the target.

8.2.2 Power Source Concept Extrapolations

The extrapolation experiments provide significant flexibility for future PMI experiments on MPEX. Trends in gas puff types and magnetic field configurations have been highlighted, which lead to reduced auxiliary power requirements that achieve a 10 MW/m^2 benchmark. Alternatively, the power systems can be tailored to provide more than 10 MW/m^2 at specific radial locations on the target plate. For example, the targeted 10 MW/m^2 heat fluxes can be achieved with ECH power or without ECH power, assuming the helicon and ICH are operating at 90% installed capacity. The heat flux cannot be achieved without the application of ICH power unless the MPEX installed power capacity of the helicon and ECH is increased or the final ECH power calibration is closer to the minimum value (see equation 7.1). Finally, the desired heat flux can also be achieved in each power source is operating at 65-85% installed capacity, using the conditions of experiment 7. Therefore, PMI-required target heat fluxes are readily achievable on MPEX for two different operating conditions that have been analyzed in this subsection, with another two operating conditions within 5% of the 10 MW/m^2 target.

8.3. Future Work

The power accounting analyses and extrapolation analyses highlighted several areas of interest for future work. Future power accounting studies must pay particular attention to the plasma at the downstream edge of the helicon region (z = 1. 5 m) and the sub-region defined between z = 1.5 m and 2.2 m. The (sub-)region analysis demonstrated the largest portion of missing power occurs in this area of the machine. A suite of newer

diagnostics is necessary to provide the necessary analysis. The suite includes: HELIOS, TALIF, photodiodes, and bolometers. Since probes are too perturbative to provide reliable data at z = 1.5 m, the HELIOS diagnostic will provide much needed electron density and temperature data. Further, the TALIF diagnostic will be critical to acquire neutral gas densities along the machine axis, supplementing the baratron data and providing a better idea of the neutral gas behavior within the machine, which was a large source of uncertainty in the power accounting analyses. Finally, the addition of AXUV and SXR photodiode data, along with bolometric data will provide improved power radiation measurements. The addition of these diagnostics should be able to increase the amount of diagnostically-verified accounted power.

For the MPEX extrapolation analyses, the main source of future work includes the analysis of additional operating configurations to better identify the parameters that will yield the best plasma at the target for PMI studies. Thus far, seven configurations were studied in depth. Proto-MPEX experiments have encompassed dozens of different operating configurations, which may be of interest.

REFERENCES

1. Culham Centre for Fusion Energy (2012). Why fusion is needed. Retrieved 2018, from http://www.ccfe.ac.uk/Why_fusion.aspx.
2. ITER Organization. (2016). Retrieved March 2016, from http://www.iter.org/.
3. Dolan, T. (2013). *Magnetic Fusion Technology*. Springer-Verlag London.
4. Brunner, D., et al. (2016). Feedback system for divertor impurity seeding based on real-time measurements of surface heat flux in the Alcator C-Mod tokamak, *Review of Scientific Instruments, 87*.
5. Makowski, M. A., et al. (2013). The scaling of the heat flux width in DIII-D. *Journal of Nuclear Materials, 438*, S208-S211.
6. Power of fusion power. Lecture 12: tokomak - continued (powerpoint).
7. Max-Planck-Institut für Plasmaphysik. ASDEX Upgrade fusion experiment, https://www.ipp.mpg.de/987491/AUG_engl.pdf.
8. Makowski, M. A., et al. (2012). Analysis of a multi-machine database on divertor heat fluxes a). *Physics of Plasma, 19,* 056122.
9. LaBombard, B., et al. (2010). *Boundary Layer Heat Transport Experiments in Alcator C-Mod in Support of the FY2010 US DoE Joint Research Target*. Cambridge: Massachusetts Institute of Technology Plasma Science and Fusion Center. Retrieved from http://www.psfc.mit.edu/library1/catalog/reports/2010/10rr/10rr014/10rr014_full.pdf
10. Brunner, D., et al. (2011). Comparison of heat flux measurements by IR thermography and probes in the Alcator C-Mod divertor. *Journal of Nuclear Materials, 415* (1), S375-S378.
11. Lipshultz, B., et al. (1995). Dissipative divertor operation in the Alcator C-Mod tokamak. *Journal of Nuclear Materials, 220-222*, 50-61.
12. Petrie, T.W., et al. (2011). Results from radiating divertor experiments with RMP ELM suppression and mitigation. *Nuclear Fusion, 51.*
13. T.M. Biewer, e-mail attachment to M. Showers, “Plasma-Material Interaction Studies for Fusion Energy Relevant Conditions on the ORNL Proto-MPEX Device.” October 8, 2014.
14. EUROfusion. *Linear plasma device*. (2016). Retrieved March 2016, from https://www.euro-fusion.org/glossary/linear-plasma-device/.
15. PMTS2010: International Workshop on Requirements for Next Generation PSI Facilities for Fusion Research. (2010). Oak Ridge, TN. Retrieved from http://web.ornl.gov/sci/fed/PMTS10/pmts_summary.pdf.
16. Biewer, T.M, et al., “Status of the Prototype Material Plasma Exposure Experiment (Proto-MPEX) at ORNL,” (abstract, Oak Ridge National Laboratory, 2014). http://www.iccworkshops.org/epr2014/abstract.php?view=333.
17. Stacey, W. M. (2010). *Fusion*. John Wiley & Sons.
18. Chen, F.F. (1994). Helicon Plasma Sources. In O. A. Popov (Ed.), *High Density Plasma Sources*.
19. Guittienne, P., Chevalier, E., and Hollenstein, C. (2005). Towards an optimal antenna for helicon waves excitation. *Journal of Applied Physics, 98*.
20. Chen, F. F. (2013). *Introduction to Plasma Physics and Controlled Fusion*. Springer.

21. Carter, M. D., et al. (2002). Comparing experiments with modeling for light ion helicon plasma sources. *Plasma of Physics, 9* (12), 5097-5110.
22. Chen, F. F. and Boswell, R.W. (1997). Helicons – The Past Decade. *IEEE Transactions of Plasma Science, 25* (6), 1245-1257.
23. R. Goulding, e-mail to M. Showers, April 25, 2016.
24. Pucci, J. M. (2007). *An Analysis of Energy Balance in a Helicon Plasma Source for Space Propulsion*. Massachusetts Institute of Technology, Cambridge, MA.
25. Stacey, W. M. (2012). *Fusion Plasma Physics*. John Wiley & Sons.
26. Laqua, H. P. (2007). Electron Bernstein wave heating and diagnostic. *Plasma Physics and Controlled Fusion, 49,* R1-R42.
27. Diem, S. J., et al. (2017). *Progress on electron heating with 28 GHz ECH/EBW.* Presentation, Oak Ridge, Tennessee.
28. Bigelow, T., et al. (2016). ECH/EBW Plasma Coupling and Heating Experiments on Proto-MPEX*. 58th Annual Meeting of the APS Division of Plasma Physics, San Jose, CA, October 31 – November 4, 2016.
29. Rapp, J. et al. (2016). The development of the Material Plasma Exposure eXperiment MPEX. *IEEE Transactions on Plasma Science, 44.*
30. Rapp, J. et al. (2013). The Development of Plasma-Material Interaction Facilities for the Future of Fusion Technology. *Fusion Science and Technology*, *64*, 237-244.
31. Rapp, J. et al. (2015). Transport simulations of linear plasma generators with the B2.5-Eirene and EMC3-Eirene Codes. *Journal of Nuclear Materials*, *463*, 510-514.
32. Caughman, J.B.O, et al. (2016). High Heat Flux Operation of the Prototype Materials Plasma eXperiment, 22nd International Conference on Plasma Surface Interactions, Rome, Italy, May 30-June 4, 2016.
33. Biewer, T. M., et al. (2016). First results from the Thomson scattering diagnostic on proto-MPEX. *Review of Scientific Instruments,* 87 (**11)**.
34. Caughman, J. B. O., et al. (2017). Plasma Source Development for Fusion Relevant Material Testing. *Journal of Vacuum Science and Technology A: Vacuum, Surfaces, and Films*, 35.
35. T.M. Biewer, e-mail to M. Showers, February 16, 2017.
36. Goulding, R. H., et al. (submitted). Production of High Density Deuterium Plasmas in the Prototype Material Plasma Exposure eXperiment (Proto-MPEX)*. *Applied Physics Letters.*
37. Goulding, R. H. (2016). Ion Cyclotron Heating on Proto-MPEX. 58th Annual Meeting of the APS Division of Plasma Physics, San Jose, CA, October 31 – November 4, 2016.
38. J.B.O. Caughman, e-mail to M. Showers, February 17, 2017.
39. Showers, M., et al. (2018). Power accounting in the helicon region of plasma discharges in the linear device Proto-MPEX. *Plasma Physics and Controlled Fusion*, *60* (**6**).
40. T. Bigelow, e-mail to M. Showers, May 3, 2018.
41. T. Bigelow, e-mail to M. Showers, May 9, 2018.
42. Howard, L. (2011). Subject Area: Critical Decision (CD) Management. Retrieved 2018, from https://www.emcbc.doe.gov/pmo/critical_decision_management.htm.

43. Rapp, J. et al. (2017). Developing the science and technology for the Material Plasma Exposure eXperiment. *Nuclear Fusion*, *57* (**11**).
44. Showers, M. et al., (2016). Heat flux estimates of power balance on Proto-MPEX with IR imaging. *Review of Scientific Instruments*.
45. FLIR Systems, Inc. *ThermoVision® SC4000 Science-Grade Infrared Camera,* Retrieved from https://www.testequipmentconnection.com/specs/FLIR_SC4000.PDF
46. Martin Bailey Photography, K.K. (2016). *All About Neutral Density Filters (Podcast 391).* Retrieved February 2017, from https://www.martinbaileyphotography.com/2013/10/14/all-about-neutral-density-filters-podcast-391/
47. FLIR Systems, Inc. (2018). *FLIR T-Series specifications.* Retrieved 2018, from http://www.flir.co.uk.
48. FLIR Systems, Inc. (2017). Retrieved January 2017, from www.flir.com.
49. Infrared Systems Development Corporation. *Operators Manual – Blackbody Reference Source Model: IR-564/301.*
50. Infrared Systems Corporation (2017). Retrieved February 2017, from www.infraredsystems.com.
51. C.J. Beers, e-mail to M. Showers, May 15, 2018.
52. C.J. Beers, e-mail to M. Showers, May 16, 2018.
53. Omega Engineering, Inc. (2016). *Thermocouples*. Retrieved 2016, from www.omega.com.
54. LUXTRON Corporation. (2005). *FOT Lab Kit Fluoroptic Thermometer.* LUXTRON Corporation.
55. Chung, K. S. (2012). Mach probes. *Plasma Sources Science and Technology*, 21(**6**).
56. N. Kafle, e-mail attachment to M. Showers, “Mach Probe.” February 1, 2017.
57. Piotrowicz, P.A. (2018). *Physics of RF Heating Systems on Proto-MPEX* (dissertation proposal). University of Illinois at Urbana-Champaign, Urbana-Champaign, IL, USA.
58. J. Caneses and P.A. Piotrowicz, e-mail to M. Showers, May 18, 2018.
59. Biewer, T. M., and Shaw, G. (2014). Initial implementation of a Thomson scattering diagnostic for Proto-MPEX. *Review of Scientific Instruments,* 85 (**11**).
60. Biewer, T. M., et al. (2016). First results from the Thomson scattering diagnostic on proto-MPEX. *Review of Scientific Instruments,* 87 (**11)**.
61. T.M. Biewer, e-mail to M. Showers, February 9, 2017.
62. Hutchinson, I.H. (2002). *Principles of Plasma Diagnostics* (2nd e). Cambridge, MA: Cambridge University Press.
63. MKS Instruments. How an MKS Baratron Capacitance Manometer Works. Retrieved 2018, from https://www.mksinst.com/docs/ur/barainfo2b.aspx.
64. Rahman, M., Abbas, S., and Chowdhury, S. (2009). *A simple capacitance calculation formula for MEMS capacitive type sensors with square membranes,* 2009 Joint IEEE North-East Workshop on Circuits and Systems and TAISA Conference, Toulouse, France, June 28 – July 1, 2009. DOI: 10.1109/NEWCAS.2009.5290456

65. Colchin, R. J., et al. (2003). The Filterscope. *Review of Scientific Instruments,* 74 (**3**).
66. Ray, Holly, et al. (2016). Spectral survey of helium lines in a linear plasma device for use in HELIOS imaging. *Review of Scientific Instruments,* 87 (**11**).
67. Olympus America Inc. (2012). *Photomultiplier Tubes*. Retrieved February 2017, from http://www.olympusmicro.com/primer/digitalimaging/concepts/photomultipliers.html.
68. Rogers, J., & Turcotte-Tremblay, P. (2006, October 10). Physics 439 – Lab in Modern Physics Atomic Spectra Experiment [Scholarly project]. Retrieved February, 2017, from http://www.ugrad.physics.mcgill.ca/Library/Atomic_Spectra-Rogers-Turcotte-Tremblay.pdf
69. Biewer, T. M., et al. (2015). *Overview of Diagnostic Implementation on Proto-MPEX at ORNL.* 57th Annual Meeting of the APS Division of Plasma Physics, Savannah, GA, November 16-20, 2015.
70. McPherson, Inc. *Model 2061 High Throughput High Resolution Spectrometer – General Features*.
71. Ted Biewer, in-person conversation with Missy Showers, February 15, 2017.
72. Ocean Optics, Inc. *USB4000 Data Sheet.*
73. AP Technologies. *Photodiode Theory of Operation*. Retrieved December 2016 from https://www.aptechnologies.co.uk/support/photodiodes/photodiode-theory-of-operation.
74. HyperPhysics. *The Doping of Semiconductors*. Retrieved December 2016 from http://hyperphysics.phy-astr.gsu.edu/hbase/Solids/dope.html#c4.
75. Lecture 12: Photodiode detectors. Retrieved December 2016 from http://course.ee.ust.hk/elec509/notes/Lect12-photodiode%20detectors.pdf.
76. IRD UV Photodiodes. Retrieved December 2016 from http://optodiode.com/pdf-library/1.%20IRD%20Photodiodes%20-%20AXUV%20Operating%20Principles%20and%20Apps.pdf
77. Ingesson, L.C, et al. (2008). Chapter 7: Tomography diagnostics: bolometry and soft-x-ray detection. *Fusion Science and Technology, 53,* 528-576.
78. OPTO DIODE CORP. AXUV/SXUV/UVG Salient Applications (brochure).
79. OPTO DIODE CORP. (2017). PHOTODIOE 100mm^2 With Integrated Thin Film Filter. Retrieved 2018, from https://optodiode.com/pdf/AXUV100Al.pdf.
80. T. Steinberger, e-mail to M. Showers, June 21, 2018.
81. T. Steinberger, e-mail to M. Showers, June 25, 2018.
82. Elliott, D., et al. (2016). Two photo LIF on the HIT-SI3 experiment: Absolute density and temperature measurements of deuterium neutrals. *Review of Scientific Instruments*, *87*. https://doi.org/10.1063/1.4955494.
83. Magee, R.M., et al (2012). A two photon absorption laser induced fluorescence diagnostic for fusion plasmas. *Review of Scientific Instruments*, *83* **(10)**. https://doi.org/10.1063/1.4728092.
84. Galante, M.E., Magee, R.M, and Scime, E.E. (2014). Two photo absorption laser induced fluorescence measurements of neutral density in a helicon plasma. *Physics of Plasma*, *21* **(5)**. https://doi.org/10.1063/1.4873900.
85. H. Ray, e-mail attachment to M. Showers, “HELIOS blurb”, October 1, 2018.

86. Nanigian, J., & Nanigian, D. *A Unique Thermocouple to Measure Temperatures of Squibs, Ingniters, Propellants, and Rocket Nozzles.* Holliston, MA: NANMAC Corporation. Retrieved from http://www.nanmac.com/documents/eroding-thermocouple.pdf.
87. Brunner, D., & LaBombard, B. (2012). Surface thermocouples for measurement of pulsed heat flux in the divertor of the Alcator C-Mod tokamak. *Review of Scientific Instruments, 83,* 033501.
88. NANMAC Corporation, *NANMAC is QUALITY PERFORMANCE SOLUTIONS*. Presentation.
89. Wurden, G. A. *A Rad-Hard, Steady-State, Digital Imaging Bolometer System for ITER.* Los Alamos: Los Alamos National Laboratory. Retrieved December 2016 from http://wsx.lanl.gov/Publications/ITER_Diagnostics_Varenna_Paper.pdf.
90. Peterson, B. J., et al. (2001). Infrared imaging video bolometer for the large helical device. *Review of Scientific Instruments, 72* **(1)***,* 923-926.
91. Konoshima, S., et al. (2001). Tomographic reconstruction of bolometry for JT-60U diverted tokamak characterization. *Plasma Physics and Controlled Fusion, 43,* 959-983.
92. Reinke, M.L. and Hutchinson, I.H. (2008). Two dimensional radiated power diagnostics on Alcator C-Mod. *Review of Scientific Instruments, 79*.
93. Huber, A., et al. (2007). Upgraded bolometer system on JET for improved radiation measurements. *Fusion Engineering and Design, 82* **(5-14)**, 1327-1334.
94. Wurden, G.A. and Peterson, B. J. (1997). Imaging Bolometry Development for Large Fusion Devices, ITER Diagnostic Workshop, Varenna, Italy.
95. M. Reinke, e-mail to M. Showers, June 29, 2018.
96. van Eden, G.G., et al. (2018). Plasma radiation studies in Magnum-PSI using resistive bolometry, *Nuclear Fusion*, *58* **(10)**.
97. S.S. Lee, e-mail attachment to M. Showers, “Resistive Bolometer Calibration”, July 2, 2018.
98. M. Reinke, e-mail attachment to M. Showers, “Design of a Resistive Bolometer Capability for proto-MPEX”, June 29, 2018.
99. Trojan, L. (2010). *Radial Transport and Detachment in the University of Manchester Linear System.* University of Manchester, Manchester, United Kingdom.
100. Caneses, J. F. (2015). *Helicon wave propagation and plasma equilibrium in high density plasma in converging magnetic fields*. Australian National University, Canberra, Australia.
101. Hjartarson, A. T., Thorsteinsson, E. G., and Gudmundsson, J. T. (2010). Low pressure hydrogen discharge diluted with argon explored using a global model. *Plasma Sources Science and Technology, 19.*
102. Millsian, Inc. *Summary Tables of Calculated and Experimental Parameters of Diatomic, Triatomic, Organic, Silicon, Boron, Aluminum and Organometallic Molecules, Exemplary Results on Condensed Matter Physics, One-Through Twenty-Electron Atoms, Excited States of Helium, g Factor, and Fundamental Particle Masses.* Retrieved from http://www.millsian.com/summarytables/SummaryTables022709S.pdf.

103. Stangeby, P. C. (2000). *The plasma boundary of magnetic fusion devices.* Institute of Physics Publishing.
104. Physics Stack Exchange. *Recombination rate/time calculation for plasma vs. solid state semiconductors.* Retrieved October 2016 from http://physics.stackexchange.com/questions/242251/recombination-rate-time-calculation-for-plasma-vs-solid-state-semiconductors.
105. Wenzel, U., et al (2005). A Plasma Beam Passing From the Ionizing to the Recombining State. *IEEE Transactions of Plasma Science, 33* (**2**), 366-367.
106. Ding, Y. (2008). *Modelling of the radiative power loss from the plasma of the Tore Supra tokamak – Comparisons of predictions from onion-skin-collisional-radiative modeling with experimental data.* Royal Institute of Technology, Stockholm, Sweden.
107. Lumma, D., Terry, J.L. and Lipshultz, B. (1997). Radiative and three-body recombination in Alcator C-Mod divertor. *Physics of Plasmas, 4* **(7)**, 2555-2566.
108. Baragiola, R. A. (2003). *Introduction & Collision Kinematics,* Retrieved February 2017, from http://www.virginia.edu/ep/Interactions/1__introduction_&_collision_kinematics.htm.
109. Hollmann, E. M., et al. (2001). Evidence for the importance of radial transport in plasma detachment in the Nagoya University Divertor Simulator (NAGDIS-II). *Physics of Plasma, 8* **(7)**, 3314-3320.
110. Browning, P.K., et al. (2005). Spatial structure of detached plasmas in the ULS divertor simulator. *Journal of Nuclear Materials, 337-339*, 232-236.
111. Rosenau, P. and Degani, D. (1980). Thermal and radiation losses in a linear device. *Physics of Fluids, 23,* 2318-2325.
112. Rapp, J., et al (submitted 2017). Radial transport modeling of high density deuterium plasmas in Proto-MPEX with the B2.5-Eirene code. *Plasma Physics and Controlled Fusion.*
113. Sudit, I. D. and Chen, F.F. (1996). Discharge equilibrium of a helicon plasma. *Plasma Sources Science and Technology,* 5.
114. Unterberg, E. A., et al. (2012). HELIOS: A helium line-ratio spectral-monitoring diagnostic used to generate high resolution profiles near the ion cyclotron resonant heating antenna on TEXTOR. *Review of Scientific Instruments*, 83 (**10**).
115. Sieglin, B. (2014). *Divertor Power Load Studies in All Metal ASDEX Upgrade and JET* (thesis). Technische Universität München, Garching, Germany.
116. Jin-Ming, G., et al (2012). Reconstruction of heat flux profile on the HL-2A divertor plate with a three-dimensional analysis model*, *Chinese Physics B, 22*. DOI: 10.1088/1674-1056/22/1/015202.
117. Piotrowicz, P.A., et al (2018). Helicon normal modes in Proto-MPEX. *Plasma Sources Science and Technology*, *27* **(5)**.
118. LXCat. *DATA CENTER*. Retrieved August 2017, from https://fr.lxcat.net/data/set_type.php.
119. Stix, T. H. (1992). *Waves in Plasma*. New York, NY: AIP-Press.
120. Lau, C., et al (submitted 2018). Evidence of upper-hybrid electron heating on Proto-MPEX, *Plasma Sources Science and Technology*.
121. Diem, S. J., et al (2018). An electron Bernstein wave heating scheme for the

Proto-MPEX linear device. *Physics of Plasma*, *25*.
122. Biewer, T. M., et al (2018). Observations of electron heating during 28 GHz microwave power application in proto-MEPX. *Physics of Plasma*, *25*.

APPENDICES

a.

a.

Appendix A. Error Analysis Method

To determine the accuracy of the heat fluxes and powers calculated across the power balance and extrapolation analyses, two main error analysis methods were applied: a simple analysis relying on the accuracy of the diagnostic instrument and an error propagation analysis.

A.1. Simple Diagnostic Analysis

Recall the fluoroptic probes and thermocouples infer the power deposited from measured temperature increases on the helicon window and some machine components, respectively. In the 1D heat conduction analysis process [39], the only variable is the temperature change, which is determined by the FP and TC diagnostics. Therefore, the error calculated for these inferred powers is primarily due to the accuracy of the diagnostics used. As mentioned in the chapter on diagnostics, the accuracy of the TCs is ± 2.2°C or 0.75% of the temperature measurement. The accuracy of the FPs is 0.5°C. When calculating the deposited power, these accuracy ranges were applied to determine the respective error.

A.2. Error Propagation Analysis

The error propagation analysis was applied to determine the error associated with power and heat flux deposited in the end plates, as well as the convective power, conductive power, and power lost due to D_2 processes.

Heat Flux and Deposited Power Error

The analysis used to determine the heat flux and power deposited on the end plates using MATLAB and THEODOR is a multi-step process requiring researcher inputs over which error can propagate. Researcher inputs are required at several points, rather than employing a fully automated analysis, to better account for inter-shot plasma variations. Therefore, a more complex error propagation analysis method was applied to determine the accuracy of the Proto-MPEX deposited heat fluxes and powers, and the MPEX efficiency extrapolations. The basic formula applied is provided in equation A.1

$$\sigma_f^2 = \left(\frac{\partial f}{\partial x}\sigma_x\right)^2 + \left(\frac{\partial f}{\partial y}\sigma_y\right)^2 \quad \text{(A.1)}$$

where σ_f is the error of a two-variable function, $f(x,y)$, $\frac{\partial f}{\partial x}$ is the partial derivative with respect to variable x, σ_x is the error due to x, $\frac{\partial f}{\partial y}$ is the partial derivative with respect to variable y, and σ_y is the error due to y.

There were two sources of error considered when determining the total error attributed to the temperature measurements on the end plates, which is propagated through THEODOR to the heat flux values. The first is the error due to the accuracy of the IR camera, which is 2% of the temperature measurement. The second is the error due to the researcher input required by the plasma shot MATLAB analysis code used to prepared IR data for THEODOR analysis. As previously stated, the THEODOR code

takes a line slice through the plasma profile acquired through the IR camera and analyzed in a MATLAB program. A researcher must select the x-coordinate pixel[237] that allows the line slice to go through the approximate the hot center of the plasma profile. To account for selecting one or two x-coordinate pixels away from the hot center, the temperature difference between the desired center and two x-coordinate pixels away is added to the 2% error from the IR camera measurement. The sum of the two errors is the total error in temperature measurements, σ_{deltaT}.

To calculate heat fluxes from the 1D temperature line trace, the THEODOR code uses a forward time centered space (FTCS) discretization of the heat flux potential equation [115]. Since it is extremely difficult to determine error propagation through a discretization method, the standard 1D heat conduction equation (reproduced below) was used. The resulting error is assumed to be greater than or equal to the true error associated with the THEODOR analysis.

$$\dot{Q} = \frac{\rho V c \Delta T}{\Delta t} \tag{A.2}$$

where $\dot{Q}$ is the power [W], ρ is the density of the end plate material [kg/m^{-3}], V is the volume of the end plate [m^{-3}], c is the specific heat capacity of the end plate material [J/kg.K], ΔT is the temperature rise measured by the IR camera [K], and Δt is the time between IR camera frames [s]. Since different sources provide slight variations in the material properties of the end plates, an error factor for the specific heat capacity, (σ_{cp}) and density (σ_{ρ}) values were included. Also included was possible researcher error in measuring the volume of the plate from its diameter and thickness (σ_V). Since the time between frames is held fixed, the Δt is assumed to be accurate enough such that its error (σ_{deltat}) is negligible. The resulting equation to determine the total heat flux error is

$$\sigma_q^2 = \left(\frac{\partial q}{\partial \rho}\sigma_\rho\right)^2 + \left(\frac{\partial q}{\partial c_p}\sigma_{c_p}\right)^2 + \left(\frac{\partial q}{\partial V}\sigma_V\right)^2 + \left(\frac{\partial q}{\partial \Delta T}\sigma_{\Delta T}\right)^2 \tag{A.3}$$

where σ_q is the error in the heat flux, q, $\frac{\partial q}{\partial \rho}$ is the partial derivative of the heat flux with respect to the density, σ_ρ is the error in the density, $\frac{\partial q}{\partial c_p}$ is the partial derivative with respect to the specific heat capacity, σ_{cp} is the error in the specific heat capacity, $\frac{\partial q}{\partial V}$ is the partial derivative with respect to the plate volume, σ_V is the error in the plate volume, $\frac{\partial q}{\partial \Delta T}$ is the partial derivative with respect to the measured temperature, and $\sigma_{\Delta T}$ is the error in the temperature measured.

Recall the power is calculated from the THEODOR-derived heat flux line trace by integrating from the edge to the center of the heat flux profile, assuming radial symmetry. Therefore, the power deposited on the plate is a function of the calculated

[237] This is for a vertical line slice. The y-coordinate pixel would need to be specified for a horizontal line slice.

heat flux and the radius. The same process was applied to determine the error in power. The error in heat flux, σ_q, was determined in equation A.3. The radius of the heat flux profile is the difference between the *s* location of the center and edges of the profile, with a standard value of 0.0305 m. The *s* location of the center and edges of the heat flux profile are selected by the researcher and are accurate within 0.01 cm of the selected value. Therefore, the error in the radius, σ_r, is assumed to be 0.01 cm. Additional researcher errors were included in the total power error. To account for additional error when selecting the center and edge *s* location values, the heat flux integration analysis was performed for *s* locations slightly to the left and right of the ideal *s* locations. The resulting difference in the calculated deposited power using different *s* locations is approximately 1.5%, $\sigma_{p,click}$. Another source of researcher error occurs when selecting the time in the pulse when the heat flux is calculated. The heat flux integration was performed for one frame (0.01 seconds) prior to and after the intended evaluation time. The greater of the differences between the resulting power one frame away from the intended evaluation time and at the intended time is considered the error in time selection for power, $\sigma_{p,time}$. The total power error is summarized in equation A.4.

$$\sigma_{P_T}^2 = \left(\frac{\partial P_T}{\partial \mathrm{q}}\sigma_\mathrm{q}\right)^2 + \left(\frac{\partial P_T}{\partial \mathrm{r}}\sigma_\mathrm{r}\right)^2 + \sigma_{\mathrm{p,click}}{}^2 + \sigma_{\mathrm{p,time}}{}^2 \qquad \text{(A.4)}$$

where $\sigma_{P,T}$ is the total error in the power-to-target calculation, *P*, $\frac{\partial P}{\partial q}$ is the partial derivative of the power with respect to the heat flux, σ_q is the error in the heat flux, $\frac{\partial P}{\partial r}$ is the partial derivative with respect to the radius of the plasma, $\sigma_{p,click}$ is the error associated with selecting a center and edge *s* location used to calculate the power, and $\sigma_{p,time}$ is the error associated with selecting an intended evaluation time at which to evaluate the heat flux.

To determine the error in the power-to-target efficiency, the error in the input power sources were determined. 200-300 ms samples of the power traces of several plasma pulses with the same operating conditions as the pulse being analyzed were averaged to determine the average and standard deviation of the power traces. The standard deviations were considered the errors associated with the given power source. The power-to-target efficiency is a function of the power arriving at the target plate and the input power, and their respective errors.

$$\sigma_\eta^2 = \left(\frac{\partial \eta}{\partial \mathrm{P}_T}\sigma_{P_T}\right)^2 + \left(\frac{\partial \eta}{\partial P_s}\sigma_{P_s}\right)^2 \qquad \text{(A.5)}$$

where σ_η is the error in the power-to-target efficiency calculation, η, $\frac{\partial \eta}{\partial P_T}$ is the partial derivative of the efficiency with respect to the power-to-target, $\sigma_{P,T}$ is the error in the power-to-target, $\frac{\partial \eta}{\partial P_s}$ is the partial derivative with respect to the total input (source) power, which may include a combination of helicon, ECH and ICH, and $\sigma_{P,S}$ is the error in the total source power.

To determine the error associated with the ECH or ICH efficiency derived from the total efficiency and helicon efficiencies, the following equations were used. A helicon + ECH analysis is used as an example.

$$\eta_E = \frac{\eta_{H+E}(P_H+P_E)-\eta_H P_H}{P_E} \quad (A.6)$$

$$\sigma_{\eta_E}^2 = \left(\frac{\partial \eta_E}{\partial \eta_{H+E}}\sigma_{\eta_{H+E}}\right)^2 + \left(\frac{\partial \eta_E}{\partial \eta_H}\sigma_{\eta_H}\right)^2 + \left(\frac{\partial \eta_E}{\partial P_E}\sigma_{P_E}\right)^2 + \left(\frac{\partial \eta_E}{\partial P_H}\sigma_{P_H}\right)^2 \quad (A.7)$$

where $\sigma_{\eta,E}$ is the ECH efficiency error, η_E, $\frac{\partial \eta_E}{\partial \eta_{H+E}}$ is the partial derivative of the ECH efficiency with respect to the combined helicon + ECH efficiency, $\sigma_{\eta,H+E}$ is the error in the combined helicon + ECH efficiency, $\frac{\partial \eta_E}{\partial \eta_H}$ is the partial derivative with respect to the helicon efficiency, $\sigma_{\eta,H}$ is the error in the helicon efficiency, $\frac{\partial \eta_E}{\partial P_E}$ is the partial derivative with respect to the ECH input power, $\sigma_{P,E}$ is the error in the input ECH power, $\frac{\partial \eta_E}{\partial P_H}$ is the partial derivative with respect to the helicon input power, and $\sigma_{P,H}$ is the error in the input helicon power. The $\sigma_{\eta,H+E}$ and the $\sigma_{\eta,H}$ are determined using equation A.5 for a helicon + ECH pulse and a helicon-only pulse, respectively.

The extrapolation to MPEX employed the following equations, assuming a helicon + ECH pulse.

$$P_{target,MPEX} = \eta_H P_{H,MPEX} + \eta_E P_{E,MPEX} \quad (A.8)$$

$$\sigma_{P_{T,MPEX}}^2 = \left(\frac{\partial P_{T,MPEX}}{\partial \eta_H}\sigma_{\eta_H}\right)^2 + \left(\frac{\partial P_{T,MPEX}}{\partial P_{H,MPEX}}\sigma_{P_{H,MPEX}}\right)^2 + \left(\frac{\partial P_{T,MPEX}}{\partial \eta_E}\sigma_{\eta_E}\right)^2 + \left(\frac{\partial P_{T,MPEX}}{\partial P_{E,MPEX}}\sigma_{P_{E,MPEX}}\right)^2 \quad (A.9)$$

where $\sigma_{PT,MPEX}$ is the error of the MPEX-scale power to the target plate, $P_{target,MPEX}$, $\frac{\partial P_{T,MPEX}}{\partial \eta_H}$ is the partial derivative of the MPEX-scale power to the target plate with respect to the helicon efficiency, $\sigma_{\eta,H}$ is the error in the helicon efficiency, $\frac{\partial P_{T,MPEX}}{\partial P_{H,MPEX}}$ is the partial derivative with respect to the MPEX-level helicon power, $\sigma_{PH,MPEX}$ is the error in the MPEX-level helicon power, $\frac{\partial P_{T,MPEX}}{\partial \eta_E}$ is the partial derivative with respect to the ECH efficiency, $\sigma_{\eta,E}$ is the error in the ECH efficiency, $\frac{\partial P_{T,MPEX}}{\partial P_{E,MPEX}}$ is the partial derivative with respect to the MPEX-level ECH power, and $\sigma_{PE,MPEX}$ is the error in the MPEX-level ECH power.

Parallel Power Transport & D_2 Lost Power Error

The error associated with the parallel power transport and the power lost due to D_2 processes relied on the electron density, electron temperature and plasma flow

measurements provided by the LPs and MPs. The $n_e \pm dn_e$ and $T_e \pm dT_e$ values measured at each sample location were used to in the analysis. dn_e and dT_e were considered the errors associated with the electron temperatures and densities, which were applied in the error propagation analysis used to calculate the convected and conducted plasma power, using the same method listed in sub-section Heat Flux and Deposited Power Error provided above (see equation A.1). The relevant equations for which the error propagation was applied include 6.6, 6.2, 6.3, 6.4, reproduced below as equations A.10, A.11, A.12 and A.13, respectively. Equation A.10 calculates the power lost due to D_2 molecular processes.

$$P = qEK_v n_e n_N V \tag{A.10}$$

where *P* is the lost power [W], *q* is the electron charge [1.602e-19 J/eV], *E* is the energy associated with the process [eV], K_v is the averaged collisional rate coefficient (<vσ>) [m^3/s], n_e is the electron density [m^{-3}], n_N is the neutral particle density [m^{-3}], and *V* is the volume of the plasma [m^3]. The values of *q* and *V* are assumed to have no error. The error associated with EK_v is assumed to be about 5%. The error associated with n_e is the probe-measured dn_e value.[238] As described in Chapter 6, the value of n_N based on four baratron measurements, which sample the plasma at the edge, where the neutral gas density is higher. Using electron density radial profiles to estimate the relationship between the edge and on-axis densities, the error assigned to the neutral density was 50%. And additional error of 10% was assigned to the total power loss calculation, *P*, to account for the fact that the atomic deuterium processes were neglected.

Equations A.11 and A.12 are used to calculate the conducted power in the plasma.

$$q_{cond} = -k_{||} \nabla T_e = -k_{||} \frac{dT_e}{dz} \tag{A.11}$$

with the defining equation set A.12 [39]

$$k_{||} = \frac{3.2 \tau_T n_e T_e}{m_e} \qquad \tau_e = \frac{6\sqrt{2}\pi^{1.5}\varepsilon_0^2 \sqrt{m_e} T_e^{1.5}}{n_e e^4 \ln(\Lambda)}$$

$$\tau_T = \left[\frac{1}{\tau_e} + \nu_{D,tot}\right]^{-1} \qquad \Lambda = 4\pi \sqrt{\frac{\varepsilon_0^3 T_e^3}{n_e e^6}}$$

$$\nu_{D,tot} = \nu_{D2} = \sum_j (qE_j K_{v,j})_{D2} \tag{A.12}$$

[238] Since the electron temperature and density at *z* = 1.5 was a best estimate, the dn_e and dT_e was assumed to be twice the dn_e and dT_e measured at *z* = 1.0 m.

where q_{cond} is the parallel conductive heat flux [W/m^2], $k_{||}$ is the parallel electron thermal conductivity [W/m^2.K], ∇T_e is the electron temperature gradient (which simplifies to $\frac{dT_e}{dz}$ [J/m]), n_e is the electron density [m^{-3}], T_e is the electron temperature [J], m_e is the electron mass [kg], τ_T is the total collisional time for both electron and neutral collisions [s], τ_e is the electron collisional time [s], e is the electron charge [C], ε_0 is the permittivity of free space [F/m], Λ is the Coulomb logarithm [dimensionless], $\nu_{D,tot}$ is the total neutral collisional frequency, which is defined as the molecular collisional frequency, ν_{D2} [s^{-1}], n_{D2} is the molecular deuterium density [m^{-3}], and $\sum_j (qE_j K_{\nu,j})_{D2}$ [W.m^3] is the summation of the molecular deuterium collision loss densities estimated from baratron data. The error associated with q and EK_ν are the same as those used for equation A.10. No error was assigned to constants ε_0, m_e, and e. The error associated with T_e and n_e was calculated using the multi-fit error analysis.

Equations A.13 is used to calculated the convective power in the plasma.

$$q_{conv} = 5 n_e v T_e \tag{A.13}$$

$$v = c_s M = \sqrt{\frac{2T_e}{m_i}}\, M$$

where q_{conv} is the convective heat flux [W/m^2], n_e is the electron density [m^{-3}], T_e is the electron temperature [J], v is the plasma flow velocity [m/s], c_s is the ion sound speed through the plasma [m/s], M is the Mach number, and m_i is the mass of deuterium [kg]. Ion temperatures are assumed to be approximately equal to electron temperatures. The error associated with T_e and n_e was calculated using the multi-fit error analysis. No error was assigned to constant m_i. The calculated Mach numbers were assigned an error of 5%. The Mach number estimated at z = 1.5 m was also assigned an error of 5%, since confidence is fairly high that the Mach number at z = 1.5 m is effectively equal to the Mach number at z = 1.0 m. The Mach number estimated at z = 2.2 m was assigned an error of 50%, since a Mach number of 0.3 at z = 2.2 m was deemed reasonable, which is 50% greater than the assigned value of 0.

Appendix B. ECH Power Calibration Adjustment

As previously mentioned in chapter 7, a potential error was discovered in the ECH power calibration process shortly before the defense of this dissertation. The possible error could result in the calculated ECH power being a up to a four greater than previously thought. However, the issue was not fully resolved prior the completion of this thesis. Therefore, the average of the minimum and maximum ECH voltage-to-power calibration was used for the detailed extrapolation analysis provided in chapter 7, using the following equation.

$$P_{ECH} = \bar{C}\, V \tag{B.1}$$

$$\bar{C} = C_{min} + C_{max}$$

where P_{ECH} is the ECH power that corresponds to the ECH voltage signal, V, $\bar{C}$ is the average voltage-to-power calibration factor, C_{min} is the minimum (and original) calibration factor, $\frac{100}{9}$, and C_{max} is the maximum calibration factor, $\frac{400}{9}$.
where P_{ECH} is the ECH power that corresponds to the ECH voltage signal, V.

Regardless of the correct applied ECH power, the extrapolation method remains the same. Therefore, the extrapolations included applied ECH power can be modified accommodate a different ECH power calibration. In this appendix, the ECH extrapolation performed in experiment 3 was repeated for the minimum and maximum ECH power calibrations to estimate how the a different ECH power calibration factor might affect the experiments that included ECH extrapolations (1-3, 6-7).

Table B.1 compares ECH extrapolations for experiment 3 using the minimum (original) ECH power calibration and the maximum ECH power calibration. The applied helicon power, helicon efficiency, and target heat flux and power are unaffected by a change in the ECH power calibration.

Figure B.1 provides a comparison of the Proto-MPEX-acquired and MPEX-scale heat flux profiles from experiment 3 using the minimum and maximum ECH power calibrations. Note the Proto-MPEX-acquired heat flux profile remains the same.

Table B.1. Comparison of experiment 3 ECH extrapolation with original and adjusted ECH power calibration.

	Minimum ECH Power Calibration	Maximum ECH Power Calibration
Applied ECH [kW]	7.0 ± 1.9	28.0 ± 7.2
ECH Efficiency [%]	5.0 ± 2.2	1.25 ± 0.25
MPEX Power [kW]	13.1 ± 4.2	5.5 ± 1.1
MPEX Heat Flux [MW/m^2]	19.0 ± 1.2	6.8 (8.2) ± 0.6

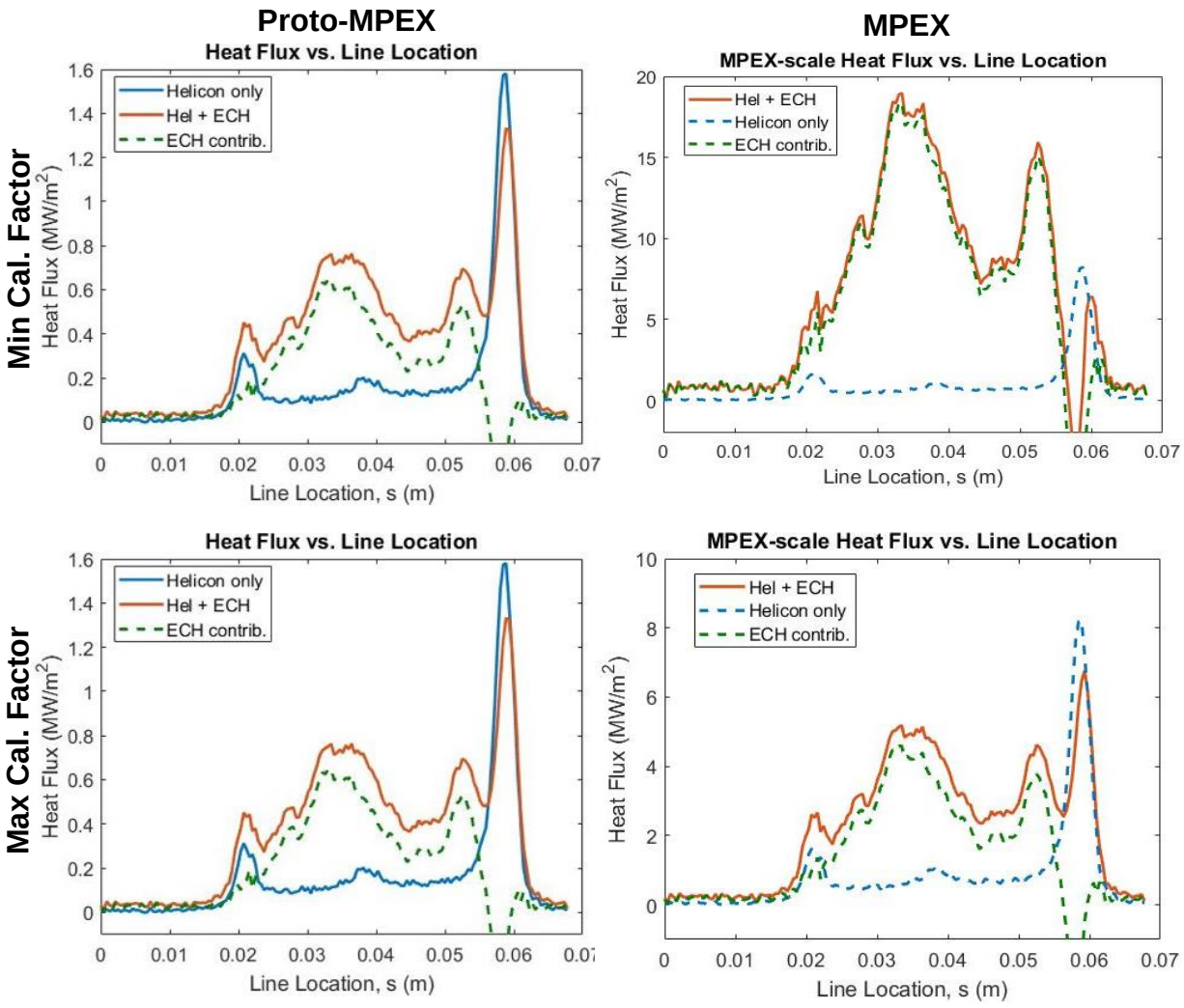

Figure B.1. Comparison of heat flux profiles from experiments 3, taken at time ~ 50 ms after the application of ECH. The top and bottom row shows the analysis performed using the minimum and maximum ECH power calibration factor, respectively. The left column shows the Proto-MPEX-acquired heat flux profiles. The right column shows the expected MPEX-scale heat flux profiles.

Note that the change in the applied ECH power based on the different calibration factors does not change the general shape of the MPEX-scale helicon + ECH heat flux profile. Using the minimum ECH power calibration factor, the maximum heat flux occurs in the center, reaching a value of 19.0 MW/m^2. The maximum ECH power calibration factor yields a central maximum heat flux profile of 5.1 MW/m^2 and a maximum edge heat flux of 6.8 MW/m^2. However, the helicon-only pulse profile for the maximum calibration factor demonstrates that 180 kW of coupled helicon power using this configuration would yield 8.2 MW/m^2 on the profile edge, which is higher than the maximum heat flux achievable by the helicon + ECH pulse (6.8 MW/m^2). For both the helicon-only and

helicon + ECH pulses using the maximum ECH power calibration factor, the maximum heat flux occurs on the edge of the profile. With additional ECH power applied, the heat flux profile will become increasingly centrally peaked, as demonstrated by the MPEX-scale helicon + ECH pulse using the minimum ECH power calibration factor (upper right of figure B.1). The magnitude of the center of the heat flux profile changes by approximately the same factor of four that exists between the minimum and maximum ECH power calibration factors (5.1 MW/m^2 vs. 19.0 MW/m^2). Using the maximum power calibration, experiment 3 cannot achieve the desired target plate heat flux of 10 MW/m^2. In comparison to the extrapolation using the minimum ECH power calibration, which requires 105 kW of coupled ECH power in addition to 180 kW of coupled helicon power, approximately 420 kW of coupled ECH power (in addition to 180 kW of coupled helicon power) would be required to achieve 10 MW/m^2 on the target using the maximum ECH power calibration.

It is important to note that this extrapolation method is equally as useful even if the exact ECH applied power has not been determined. The analysis can provide the factor increase in the applied power required by each power source in order to achieve the 10 MW/m^2 desired for PMI studies. The required power 'scale-up' factor does not change even if the power calibrations were initially incorrect. Once the power calibrations are corrected and confirmed, the exact power requirement can be calculated. For example, in experiment 3, the power 'scale-up' factor required for the applied ECH, holding the coupled helicon power at a constant 180 kW, to achieve 10 MW/m^2 is 15. If the original (minimum) power calibration holds, then only 105 kW of coupled ECH power are required. If the final power calibration yields a factor of four increase, then 420 kW of coupled ECH power are required. Similarly, if the power calibration yields a factor of two increase, then only 210 kW of coupled ECH power is required. The other extrapolation experiments that included ECH[239] can be analyzed using this method to determine the adjusted ECH power required to achieve the targeted 10 MW/m^2.

[239] Experiments 1, 2, 6 and 7.

Appendix C. Efficiency vs. Pressure

As previously mentioned in chapter 7, the neutral gas pressure was expected to affect the target plate heat fluxes and power-to-target efficiencies. Recall the baratrons provide neutral gas density measurements at four axial locations along the machine (z = 1.0, 1.5, 2.2, and 3.4 m, see figure 7.1) and infer the corresponding neutral gas pressures via the ideal gas law. Since previous gas scan experiments[240] demonstrated that the IR-inferred target heat flux is highly dependent on the gas puffing scheme, researchers working on Proto-MPEX anticipate that finding the appropriate gas puffing and pumping rates will yield improved target heat fluxes. In this appendix, the total power-to-target efficiency is compared to the neutral gas pressure near the target for different applied powers and for different gas flow rates over the length of the plasma pulse. Unfortunately, the initial analysis of the relationship between the baratron-inferred neutral pressures and the resulting target plate heat fluxes revealed no reliable trend. Additional in-depth gas puff scan experiments focusing solely on one baratron location at a time are likely to determine definite trends between the neutral pressure and the plasma impinging on the target plate. Once fully commissioned, the TALIF diagnostic will provide much additional needed insight.

While no firm trend was identified in the initial analysis comparing the neutral gas pressure and the power-to-target efficiency, the ability to compare multiple gas configurations[241] to the target heat flux and power is valuable to future Proto-MPEX and MPEX operations. That ability was therefore developed and included in this appendix.

Figure C.1 depicts comparisons between the power-to-target efficiencies for a helicon-only pulse (shot 19352) and a helicon + ECH pulse (shot 19433) and the neutral gas pressure at four axial locations along the Proto-MPEX machine. These pulses used magnetic configuration listed in table C.1 and gas puff type C1.[242] These are the same conditions as those used in experiment 2. Tables C.1 and C.2 reproduce the magnetic field configuration and gas puff types relevant for appendix C for reference.

Table C.1. Magnetic field configuration used for appendix C analysis.

Magnetic Field Configuration	Coils 1, 6-9	Coil 2	Coils 3-4	Coil 5	Coils 10-12
	4500 A	600 A	160 A	0 A	4500 A

[240] Not included in this thesis.
[241] As well as other changes in machine configurations
[242] These are the same conditions as those used for experiment 2.

Table C.2. Gas puff types used for appendix C analysis.

Gas Puff Type	Puff 1		Puff 2		Puff Off
	t [s]	Puff [sccm]	t [s]	Puff [sccm]	t [s]
C1	3.985	7510	4.22	7510	4.70
C2	3.985	8910	4.22	6910	5.50

Like the power-to-target efficiencies shown in figures 7.6 and 7.8, the effect of applying the ECH pulse is apparent in the helicon + ECH power-to-target efficiency trace (dotted blue line in figure C.1). The ECH is applied at time, *t*, approximately equal to 4.32 seconds. The goal of the comparison was to determine the effect, if any, the addition of ECH had on the neutral gas pressure. Figure C.1 implies that the neutral gas pressures for the two pulses remain nominally the same at axial locations *z* = 1.0 and 1.5 m. The gas pressures differ at the downstream *z* locations. The ECH is launched in the central chamber, located at *z* = 2.20 m (figure C.1 (c)). The addition of the ECH appears to reduce the neutral gas pressure in the central chamber. The lower neutral gas pressure due to the ECH application is also apparent at the baratron closest to the target at *z* = 3.4 m (figure C.1 (d)), which is the only other baratron location downstream of the ECH injection location.

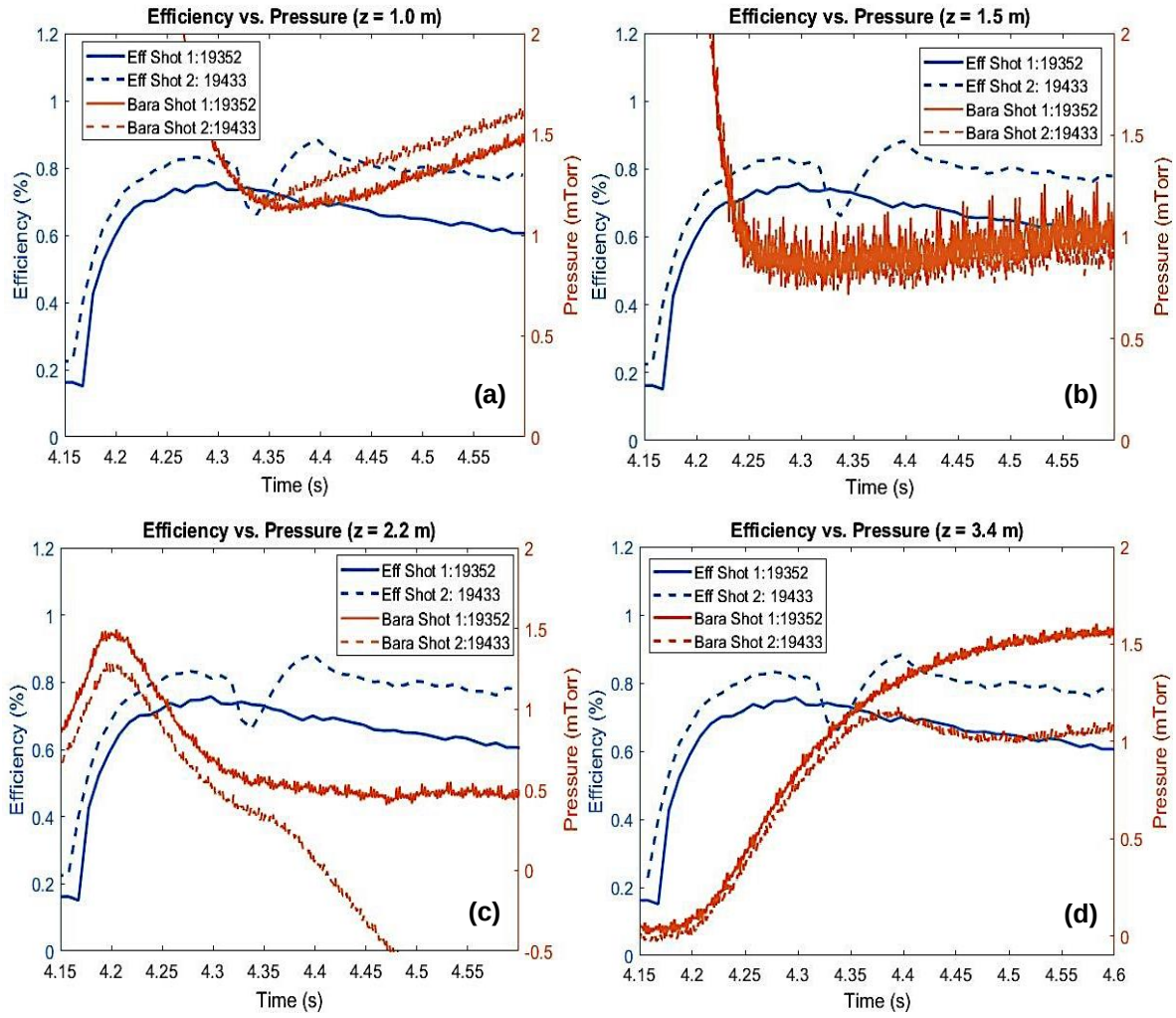

Figure C.1: Power-to-target efficiencies versus neutral gas pressures measured by baratrons at axial locations z = 1.0 m, 1.5 m, 2.25 m, and 3.4 m for helicon only and helicon + ECH pulses using the machine operating conditions of experiment 2.

Figure C.2 depicts comparisons between the power-to-target efficiencies for two helicon-only pulses at two different gas puff rates and the neutral gas pressure at four axial locations along the Proto-MPEX machine. These pulses were 1000 ms in length and used the magnetic configuration listed in table C.1. The gas flow rates used were gas configurations C1 (shot 19877[243]) and C2 (shot 20111) (see table C2). The neutral pressures are measured by four baratrons installed at axial locations z = 1.0 m, 1.5 m, 2.25 m, and 3.4 m (see figure 7.1). The goal of the comparison was to determine the effect, if any, a higher initial gas flow rate would have on the power-to-target efficiencies and neutral gas pressures. From time, t, equal to 3.985 – 4.22 seconds, the gas flow rate was 7510 sccm for shot 19877 and 8910 sccm for shot 20111. After time, t, equals 4.22 seconds, both shots had gas flow rates of 7510 sccm. Since the gas is injected at z = 0.6 m, all four baratrons, especially those at z = 1.0 m and 1.5 m, should show

[243] The sudden drop in the power-to-target efficiency for shot 19877 at about t = 4.75 seconds is due to an unexpected noise spike in the helicon power.

differences, if any, in neutral gas pressure prior to t = 4.22 seconds. After t = 4.22 seconds, any differences might equilibrate over the rest of the pulse. Figure C.2 implies that the neutral gas pressures for the two pulses remain effectively the same at axial locations z = 1.0, 1.5 and 3.4 m over the entire pulse. There appears to be a slight difference at z = 2.25 m (figure C.2 (c)). The pulse with the higher initial gas flow rate (shot 20111) appears to have a slightly higher neutral gas pressure prior to t = 4.22 seconds and a lower neutral gas pressure after t = 4.22 seconds, while the power-to-target efficiency are effectively equal for the two shots over the length of the pulse.

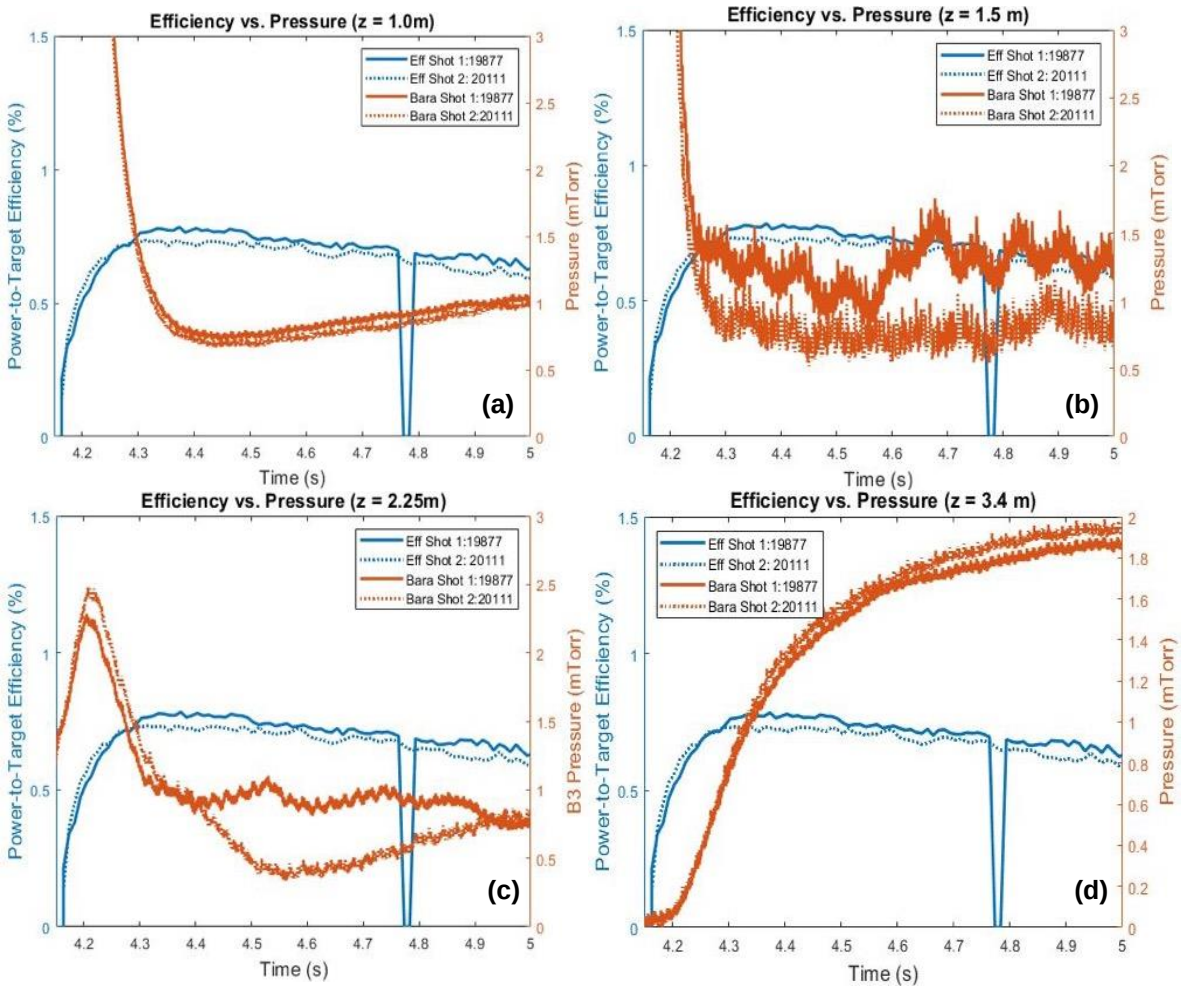

Figure C.2: Power-to-target efficiencies versus neutral gas pressures measured by baratrons at axial locations z = 1.0 m, 1.5 m, 2.25 m, and 3.4 m for helicon only pulses using the machine operating conditions of experiment.

Additional analysis is required to determine if the behavior for this shot comparison demonstrates a reliable pattern. As previously mentioned, in-depth gas puff scan experiments focusing solely on one baratron location at a time are should be performed to determine definite trends between the neutral pressure and the plasma impinging on the target plate. However, the value of being able to compare the power-to-target efficiencies to other machine operating conditions has been demonstrated.

Appendix D. Tables

D.1. Chapter 3 Tables

Table 3.1 Summary of Proto-MPEX diagnostic suite

Diagnostic	Measurement	Axial Location (m)	Diagnostician
IR Cameras	End plate & helicon window surface temperatures 2-D thermal load distribution profiles	z ~ -0.5 z ~ 1.25 z ~ 3.1 z ~ 4.25	Missy Showers
In-Vessel Thermocouples (TCs)	Surface temperatures of end plates, skimmer plate and RF baffle plate	z ~ 0.2 z ~ 1.75 z ~ 2.35 z ~ 3.75	Missy Showers
Ex-Vessel Thermocouples (TCs)	Surface temperatures of spool pieces outside of vacuum	z ~ 0.6 z ~ 1.0 z ~ 1.5	Missy Showers
Fluoroptic Probes (FPs)	Helicon window surface temperature	z ~ 1.25	Missy Showers
Langmuir Probes (LPs)	Electron temperature Electron density	z ~ 0.6 z ~ 1.0 z ~ 1.5 z ~ 3.1 z ~ 3.4 z ~ 3.65	Nischal Kafle Juan Caneses
Mach Probes (MPs)	Electron temperature Electron density Mach number	Same as LPs	Nischal Kafle Juan Caneses
B-dot probe	RF magnetic field strength RF magnetic field phase	z ~ 3.1 z ~ 3.4	Juan Caneses Pawel Piotrowicz
Ion flux probe	Ion fluence	z ~ 3.4	Juan Caneses
Thomson Scattering (TS)	Electron temperature Electron density	z ~ 2.2 z ~ 3.65	Nischal Kafle Ted Biewer
Retarding Field (Energy) Analyzer (RF(E)A)	Ion energy distribution	z ~ 3.4	John Caughman Pawel Piotrowicz
Baratrons	Neutral pressure	z ~ 1.0 z ~ 1.5 z ~ 2.2 z ~ 3.4	Ted Biewer

Table 3.1. Continued.

Diagnostic	Measurement	Axial Location (m)	Diagnostician
Filterscopes	Photon emission intensity	z ~ 0.6 z ~ 1.0 z ~ 1.5 z ~ 1.8 z ~ 2.2 z ~ 2.6 z ~ 3.1 z ~ 3.4 z ~ 3.65	Holly Ray
McPherson Spectrometer	Photon emission intensity Ion temperature Ion concentration Ion flow velocity	Same as filterscopes	Josh Beers Elizabeth Lindquist
Ocean Optics Spectrometer	Photon emission intensity	Same as filterscopes	Josh Beers Holly Ray
SXR Photodiodes	Soft x-ray emission intensity	z ~ 1.0 z ~ 2.20	Seungsup Lee Ted Biewer Matt Reinke
AXUV Photodiodes	Radiative power loss	z ~ 1.0 z ~ 2.2	Seungsup Lee Ted Biewer Matt Reinke

Table 3.2. Summary of end plates installed on Proto-MPEX.

End Plate Name	End Plate Type	Date	Shot numbers
Gridded dump plate	Dump	6/15/15 – 5/15/2018	3920 - 21876
Thin dump plate	Dump	5/15/18 - current	21191 - current
Thick SS plate	Target	7/21/15- 9/23/16	4232 - 10600
Thin SS plate	Target	9/29/16 – 7/7/17	10601-15706
Graphite plate	Target	7/18/17 – 1/9/18	15707 - 18989
Self-heated SS plate	Target	1/16/18 – 4/13/18	18990 - 21275
SiC plate	Target	4/13/18 – 5/2/18	21276 - 21876
SS plate with inserts	Target	8/8/18 - current	21191 - current
MAPP plate	Target	TBD	---

D.2. Chapter 5 Tables

Table 5.1. Summary of on-axis electron temperatures and densities and available Mach numbers along machine length

Axial Location (z [m])	T_e (r = 0, z) [eV]	n_e (r = 0, z) [m^{-3}]	|Mach number|	Diagnostic
0.6	1.91 ± 0.06	9.47e19 ± 2.71e18	0.5	Mach Probe
1.0	3.09 ± 0.5	8.14e19 ± 1.26e18	0.07	Mach Probe
1.5	3.78 ± 0.89	5.28e19 ± 3.13e18	0.07	Langmuir Probe, Mach Probe
2.2	2.44 ± 0.27	6.41e19 ± 5.30e18	---	Langmuir Probe
3.1	1.71 ± 0.04	5.85e19 ± 1.01e19	---	Langmuir Probe
3.4	1.29 ± 0.09	5.03e19 ± 9.20e18	1.0	Langmuir Probe, Mach Probe
3.65	0.96	2.33e19	----	TS array

Table 5.2. Summary of conductive and convective power held in the plasma along machine length.

Axial Location (z [m])	P_{cond} [kw]	P_{conv} [kw]
0.6	0.1	1.5 ± 0.1
1.0	3.4 [1.2, 7.3]	3.8 ± 1.0
1.5	2.2 [0.7, 5.2]	2.2 ± 1.0
3.4	~ 0	0.6 ± 0.2

Table 5.3. Magnetic field configurations for helicon power source analysis.

Magnetic Field Configuration	Coils 1, 6-9	Coil 2	Coils 3-4	Coil 5	Coils 10-12
1	5800 A	600 A	120 A	0 A	6000 A
2	5800 A	600 A	180 A	0 A	6000 A
3	4000 A	600 A	160 A	0 A	4000 A
4	5900 A	0 A	260 A	0 A	5900 A
5	3650 A	0 A	80 A	0 A	3330 A

Table 5.4. Gas puff rates for helicon power source analysis.

Gas Puff Type	Puff 1 t [s]	Puff 1 Puff [sscm]	Puff 2 t [s]	Puff 2 Puff [sccm]	Puff Off t [s]
1	3.985	8910	4.22	6910	4.70 -5.50
2	3.850	2330	4.10	770	4.55
3	3.850	2370	4.10	1710	4.55

Table 5.5. Gas puff locations for helicon power source analysis.

Magnetic Field Configuration	Gas puff location, z (m)
1	0.6
2	0.6
3	1.0
4	1.5
5	1.5

D.3. Chapter 6 Tables

Table 6.1. Diagnostic suite applied for power balance.

Diagnostic	Measurement	Axial Location (m)	Diagnostician
IR Cameras	End plate & helicon window surface temperatures 2-D thermal load distribution profiles	z ~ -0.5 z ~ 1.25 z ~ 3.1	Missy Showers
In-Vessel Thermocouples (TCs)	Surface temperatures of end plates, skimmer plate and RF baffle plate	z ~ 0.2 z ~ 1.75 z ~ 2.35 z ~ 3.75	Missy Showers
Ex-Vessel Thermocouples (TCs)	Surface temperatures of spool pieces outside of vacuum	z ~ 0.6 z ~ 1.0 z ~ 1.5	Missy Showers
Fluoroptic Probes (FPs)	Helicon window surface temperature	z ~ 1.25	Missy Showers
Langmuir Probes (LPs)	Electron temperature Electron density	z ~ 0.6 z ~ 1.0 z ~ 3.1 z ~ 3.4 z ~ 3.65	Nischal Kafle Juan Caneses
Mach Probes (MPs)	Electron temperature Electron density Mach number	Same as LPs	Nischal Kafle Juan Caneses
Thomson Scattering (TS)	Electron temperature Electron density	z ~ 2.2 z ~ 3.65	Nischal Kafle Ted Biewer
Baratrons	Neutral pressure	z ~ 1.0 z ~ 1.5 z ~ 2.2 z ~ 3.4	Ted Biewer
Filterscopes	Photon emission intensity	z ~ 0.6 z ~ 1.0 z ~ 1.5 z ~ 1.8 z ~ 2.2 z ~ 2.6 z ~ 3.1 z ~ 3.4 z ~ 3.65	Holly Ray

Table 6.1. Continued.

Diagnostic	Measurement	Axial Location (m)	Diagnostician
AXUV Photodiodes	Radiative power loss	z ~ 2.2	Seungsup Lee Ted Biewer Matt Reinke

Table 6.2. Summary of on-axis electron temperatures, electron densities and flow along machine length.

Axial Location (z [m])	T_e (r = 0, z) [eV]	n_e (r = 0, z) [m^{-3}]	|Mach Number|	Diagnostic
0.6	3.4 ± 0.29	7.99e19 ± 2.62e18	0.50	DLP/MP
1.0	3.88 ± 0.36	6.01e19 ± 9.59e17	0.10	DLP/MP
2.2	6.18	2.23e19	--	TS array
3.1	2.75 ± 0.61	5.41e19 ± 6.86e18	0.21	DLP/MP
3.4	2.53 ± 0.22	6.98e19 ± 4.68e18	0.69	DLP/MP
3.65	1.93 ± 0.13	5.86e19 ± 8.89e17	0.43	DLP/MP

Table 6.3. Summary of parallel conductive, convective and total transport power held in the plasma along machine length.

Axial Location (z [m])	P_{cond} [kw]	P_{conv} [kw]	$P_{ll,ror}$ [kW]
0.6	1.4 ± 0.2	2.7 ± 0.55	4.1 ± 0.75
1.0	7.2 ± 1.2	3.1 ± 0.7	10.3 ± 1.9
1.5	25.4 ± 3.6	3.0 ± 0.5	28.4 ± 4.1
2.2	2.9 ± 0.5	1.5 ± 0.3	4.4 ± 0.8
3.1	0.2 ± 0.07	0.5 ± 0.2	0.7 ± 0.27
3.4	0.1 ± 0.02	1.3 ± 0.3	1.4 ± 0.32
3.65	0.04 ± 0.005	0.45 ± 0.1	0.5 ± 0.105

Table 6.4. Summary of molecular deuterium collision processes.

Process	Particle Energy Loss (eV)	Collision Type
E + D2 -> E + D2	---	Elastic
E + D2 -> E + D2 (V1)	0.371	Excitation (vibrational)
E + D2 -> E + D2 (V2)	0.391	Excitation (vibrational)
E + D2 -> E + D2 (V3)	0.735	Excitation (vibrational)
E + D2 -> E + D2 (V4)	1.085	Excitation (vibrational)
E + D2 -> E + D2 (R0)	0.0226	Excitation (rotational)
E + D2 -> E + D2 (R1)	0.0377	Excitation (rotational)
E + D2 -> E + D2 (R2)	0.0528	Excitation (rotational)
E + D2 -> E + D2 (R3)	0.0679	Excitation (rotational)
E + D2 -> E + D2 (R4)	0.083	Excitation (rotational)
E + D2 -> E + D2 (R5)	0.0981	Excitation (rotational)
E + D2 -> E + D2*	8.85	Excitation (dissociation)
E + D2 -> E + D2*	12	Excitation (dissociation)
E + D2 -> E + E + $D2^+$	15.427	Ionization

Table 6.5. Summary of power losses due to D2 processes.

Machine Main Region	Machine Sub-region	Z range (m)	Total P_{loss} (kW)	$P_{loss,\ ion}$ (kW)	$P_{loss,\ diss}$ (kW)	$P_{loss,\ ex}$ (kW)	$P_{loss,\ elas}$ (kW)
Total		**0.2 – 3.75**	**183.8 ± 123.4**	**57.2 ± 38.6**	**40.4 ± 26.9**	**86.2 ± 57.9**	**0.05 ± 0.03**
Helicon		**1.0 – 1.5**	**122.0 ± 81.9**	**42.6 ± 28.6**	**22.4 ± 15.0**	**57.0 ± 38.2**	**0.01 ± 0.005**
	Spool 2.5 – Mid Hel.	1.0 – 1.25	63.3 ± 42.1	21.8 ± 14.5	11.9 ± 7.9	29.6 ± 19.7	-
	Mid Hel. – Spool 4.5	1.25 – 1.5	58.8 ± 39.9	20.8 ± 14.1	10.5 ± 7.1	27.5 ± 18.7	-
Upstream		**0.2 – 1.0**	**27.0 ± 18.0**	**3.7 ± 2.5**	**10.6 ± 7.1**	**12.7 ± 8.5**	**0.03 ± 0.02**
	Dump – Spool 1.5	0.2 – 0.6	9.6 ± 6.3	1.2 ± 0.8	3.8 ± 2.5	4.5 ± 2.9	-
	Spool 1.5 - 2.5	0.6 – 1.0	17.5 ± 11.8	2.5 ± 1.7	6.8 ± 4.6	8.1 ± 5.5	-
Downstream		**1.5 – 3.75**	**35.6 ± 24.2**	**11.0 ± 7.6**	**7.7 ± 5.1**	**16.8 ± 11.4**	**0.01 ± 0.005**
	Spool 4.5 - 6.5	1.5 – 2.2	30.5 ± 21.4	10.3 ± 7.3	6.0 ± 4.1	14.2 ± 10.0	-
	Spool 4.5 – skimmer	*1.5 – 1.75*	26.6 ± 19.4	*9.1 ± 6.6*	*5.0 ± 3.6*	*12.4 ± 9.0*	-
	Spool 6.5 – 9.5	2.2 – 3.1	3.5 ± 1.9	0.7 ± 0.3	1.2 ± 0.7	1.6 ± 0.8	-
	Spool 9.5 – 10.5	3.1 -3.4	1.0 ± 0.6	0.07 ± 0.04	0.4 ± 0.025	0.6 ± 0.4	-
	Spool 10.5 – 11.5	3.4 – 3.65	0.5 ± 0.3	0.01 ± 0.006	0.1 ± 0.05	0.3 ± 0.175	-
	Spool 11.5 - Target	3.65 – 3.75	0.2 ± 0.1	0	0.02 ± 0.013	0.1 ± 0.05	-

Table 6.6. Summary of power losses due to photon radiation.

Machine Main Region	Machine Sub-region	Z range (m)	Total $P_{loss,\ rad}$ (kW)
Total		**0.2 – 3.75**	**7.28 ± 0.38**
Helicon		**0.2 – 1.0**	**2.16 ± 0.11**
	Spool 2.5 – Mid Hel.	1.0 – 1.25	1.08 ± 0.06
	Mid Hel. – Spool 4.5	1.25 – 1.5	1.07 ± 0.06
Upstream		**1.0 – 1.5**	**1.82 ± 0.09**
	Dump – Spool 1.5	0.2 – 0.6	0.75 ± 0.04
	Spool 1.5 - 2.5	0.6 – 1.0	1.03 ± 0.05
Downstream		**1.5 – 3.75**	**3.34 ± 0.17**
	Spool 4.5- 6.5	1.5 – 2.2	1.48 ± 0.08
	Spool 4.5 – skimmer	*1.5 – 1.75*	*0.75 ± 0.04*
	Spool 6.5 – 9.5	2.2 – 3.1	1.09 ± 0.06
	Spool 9.5 – 10.5	3.1 -3.4	0.35 ± 0.02
	Spool 10.5 – 11.5	3.4 – 3.65	0.28 ± 0.02
	Spool 11.5 - Target	3.65 – 3.75	0.14 ± 0.01

Table 6.7. Summary of (sub-)region efficiency analysis.

Machine Main Region	Machine Sub-region	Z range (m)	P_{enter} (kW)	P_{exit} (kW)	$P_{loss,surf}$ (kW)	$P_{loss,coll}$ (kW)	$P_{missing}$ (kW)	η_{region} (%)
Helicon System		**1.1-1.4**	**101.3± 3.4**	**79.4 ± 4.2**	**21.8 ± 2.6**	**-**	**0**	**78.4 ± 1.5**
Helicon		**0.2 – 1.0**	**79.4 ± 4.2**	**38.7± 6.0**	**45.8 ± 2.7**	**54.9**	**0**	**48.7 ± 4.8**
	Spool 2.5 – Mid Hel.	1.0 – 1.25	21.1 ± 1.1	10.3 ± 1.9	12.2 ± 0.7	28.4	0	48.7 ± 6.2
	Mid Hel. – Spool 4.5	1.25 – 1.5	58.3 ± 3.1	28.4± 4.1	33.6 ± 2.0	26.5	0	48.7 ± 4.2
Upstream		**1.0 – 1.5**	**10.3 ± 1.9**	**1.0 ± 0.1**	**1.9 ± 0.1**	**13.7**	**7.4 ± 2.1**	**9.7 ± 0.7**
	Dump – Spool 1.5	0.2 – 0.6	4.1 ± 0.75	1.0 ± 0.1	0	4.9	3.1 ± 0.85	24.4 ± 1.7
	Spool 1.5 - 2.5	0.6 – 1.0	10.3 ± 1.9	4.1 ± 0.75	1.9 ± 0.1	8.6	4.3 ± 2.75	39.8 ± 0.05
Downstream		**1.5 – 3.75**	**28.4 ± 4.1**	**0.55 ± 0.05**	**0.33 ± 0.02**	**15.4**	**27.5 ± 4.17**	**1.9 ± 0.05**
	Spool 4.5- 6.5	1.5 – 2.2	28.4 ± 4.1	4.4 ± 0.8	0.22 ± 0.01	14.8	23.8 ± 4.9	15.5 ± 0.5
	Spool 6.5 – 9.5	2.2 – 3.1	4.4 ± 0.8	0.7 ± 0.27	0.11 ± 0.01	2.6	3.6 ± 1.08	15.9 ± 2.8
	Spool 9.5 – 10.5	3.1 -3.4	0.7 ± 0.27	1.4 ± 0.32	0	0.8	-	200 ± 22.7
	Spool 10.5 – 11.5	3.4 – 3.65	1.4 ± 0.32	0.5± 0.105	0	0.5	0.9 ± 0.425	35.7 ± 1.8
	Spool 11.5 - Target	3.65 – 3.75	0.5 ± 0.105	0.55 ± 0.05	0	0.21	0 ± 0.155	110 ± 10.8

D.4. Chapter 7 Tables

Table 7.1. Magnetic field configurations for extrapolation analysis.

Magnetic Field Configuration	Coils 1, 6-9	Coil 2	Coils 3-4	Coil 5	Coils 10-12
1	4500 A	600 A	160 A	0 A	4500 A
2	5800 A	600 A	120 A	0 A	6000 A
3	4000 A	600 A	160 A	0 A	4000 A
4	2000 A	600 A	60 A	0 A	2500 A
5	5800 A	600 A	200 A	0 A	6000 A
6	2500 A	600 A	80 A	0 A	2500 A
7	5800 A	600 A	180 A	0 A	6000 A
8	5200 A	600 A	160 A	0 A	6000 A
9	5800 A	600 A	220 A	0 A	6000 A

Table 7.2. Gas puff rates for extrapolation analysis.

Gas Puff	Puff 1		Puff 2		Puff Off
Type	t [s]	Puff [sccm]	t [s]	Puff [sccm]	t [s]
1	3.985	7910	4.22	6910	4.70
2	3.985	8910	4.22	6910	4.70
3	3.985	8510	4.22	6910	4.70
4	3.985	5910	4.22	3910	5.50
5	3.985	7510	4.22	7510	4.70
6	3.985	6910	4.22	6910	4.70

Table 7.3. Summary of operating configurations for each power scan experiment.

Experiment	Magnetic Field Configuration	Gas Puff Type
A	1	1
B	2	2
C	3	3
D	4	4

Table 7.4.Summary of applied powers and operating configurations for experiments 1-3.

Experiment	Shot	Applied Power		Magnetic Field Configuration	Gas Puff Type
		Helicon [kW]	ECH [kW]		
1	17791	82.8 ± 4.5	36.6 ± 22.7	1	1
2	19240	89.5 ± 2.9	32.6 ± 22.2	1	5
3	20836	34.6 ± 0.4	17.7 ± 11.6	4	4

Table 7.5. Summary of resulting power source efficiencies, target plate powers and heat fluxes, and MPEX scaled powers and heat fluxes for experiments 1-3.

Experiment	Helicon Efficiency [%]	ECH Efficiency [%]	Target Power [kW]	Target Heat Flux [MW/m^2]	MPEX Power [kW]	MPEX Heat Flux [MW/m^2]
1	0.7 ± 0.1	1.5 ± 1.0	1.1 ± 0.05	1.25 ± 0.02	4.1 ± 2.0	3.7 ± 0.2
2	0.75 ± 0.1	0.95 ± 0.7	1.0 ± 0.1	1.2 ± 0.02	3.3 ± 1.4	4.1 ± 0.3
3	1.7 ± 0.15	2.0 ± 1.5	0.9 ± 0.1	0.75 ± .03	7.0 ± 3.0	8.0 ± 0.8

Table 7.6. Summary of applied powers and operating configurations for experiments 4-5.

Experiment	Shot	Applied Power			Magnetic Field Configuration	Gas Puff Type
		Helicon [kW]	ECH [kW]	ICH [kW]		
4	19722	86.2 ± 2.0	x	x	5	6
	19721	86.1 ± 2.1	x	29.7 ± 3.9		
5	19789	73.8 ± 2.1	x	x	7	6
	19804	75.2 ± 2.2	x	30.6 ± 8.3		

Table 7.7. Summary of resulting power source efficiencies, target plate powers and heat fluxes, and MPEX scaled powers and heat fluxes for experiments 4-5.

Experiment	Helicon Efficiency [%]	ECH Efficiency [%]	ICH Efficiency [%]	Target Power [kW]	Target Heat Flux [MW/ m^2]	MPEX Power [kW]	MPEX Heat Flux [MW/ m^2]
4	1.0 ± 0.1	x	0.7 ± 0.1	1.1 ± 0.1	1.9 ± 0.05	4.7 ± 1.9	9.6 ± 0.8
5	1.1 ± 0.1	x	1.6 ± 0.15	1.3 ± 0.1	2.2 ± 0.05	8.2 ± 2.6	11.1 ± 1.3

Table 7.8. Summary of applied powers and operating configurations for experiments 6-7.

Experiment	Shot	Applied Power			Magnetic Field Configuration	Gas Puff Type
		Helicon [kW]	ECH [kW]	ICH [kW]		
6	17917	80.7 ± 1.9	x	x	8	1
	17915	76.9 ± 1.8	39.8 ± 24.3	x		
	17916	77.8 ± 1.8	x	15.9 ± 1.1		
	17913	78.9 ± 1.8	41.0 ± 25.1	15.1 ± 1.1		
7	18630	96.5 ± 3.2	x	x	9	1
	18632	95.7 ± 3.2	35.3 ± 22.6	x		
	18626	98.2 ± 3.2	x	23.5 ± 1.7		
	18634	89.5 ± 3.0	36.0 ± 23.1	20.8 ± 1.5		

Table 7.9. Summary of resulting power source efficiencies, target plate powers and heat fluxes, and MPEX scaled powers and heat fluxes for experiments 6-7.

Experiment	Helicon Efficiency [%]	ECH Efficiency [%]	ICH Efficiency [%]	Target Power [kW]	Target Heat Flux [MW/ m^2]	MPEX Power [kW]	MPEX Heat Flux [MW/ m^2]
6	0.6 ± 0.1	0.95 ± 0.6	1.9 ± 0.1	1.1 ± 0.1	1.4 ± 0.02	10.4 ± 1.3	9.6 ± 1.5
7	0.7 ± 0.05	1.0 ± 0.7	0.6 ± 0.1	1.1 ± 0.1	2.3 ± 0.02	5.8 ± 1.5	12.8 ± 0.8

Appendix E. Figures

E.1. Chapter 1 Figures

Name	Abbreviation	Reaction (energy, MeV)	Total (MeV)	Energy (10^{-12} J)
DT	$T(d,n)^4He$	$D + T \rightarrow {}^4He(3.54) + n(14.05)$	17.59	2.818

Figure 1.1. Tabulated information regarding the D-T fusion reaction.

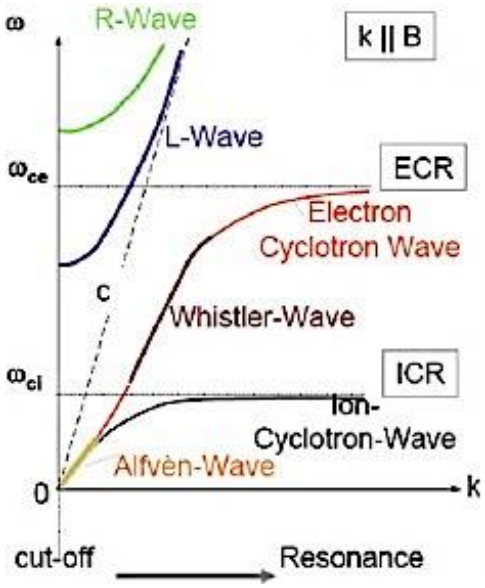

Figure 1.2. Dispersion relation for EM waves propagating parallel to the magnetic field (B) in cold plasmas (where ion motion is neglected).

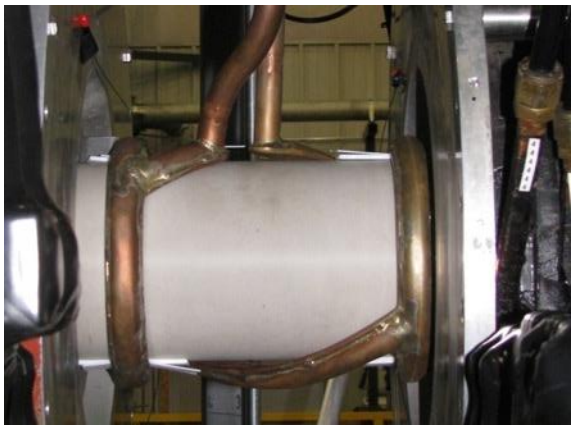

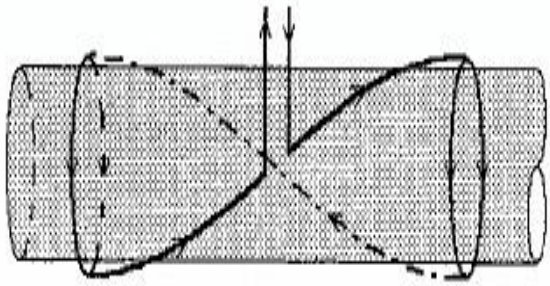

Figure 1.3. Picture of the Proto-MPEX's helicon system (left). Supplementary diagram of right-handed helicon antenna provided (right) [18].

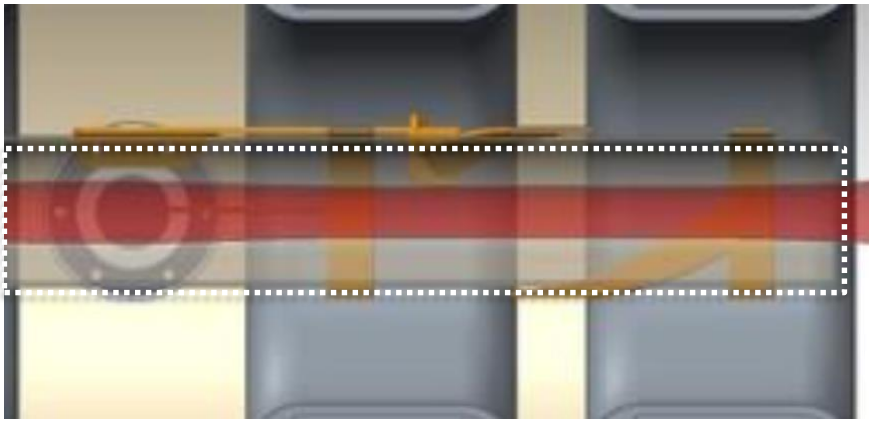

Figure 1.4. Picture of the Proto-MPEX's ICH antenna. The quartz tube is highlighted by the dotted white box. The plasma path along the machine axis is also shown.

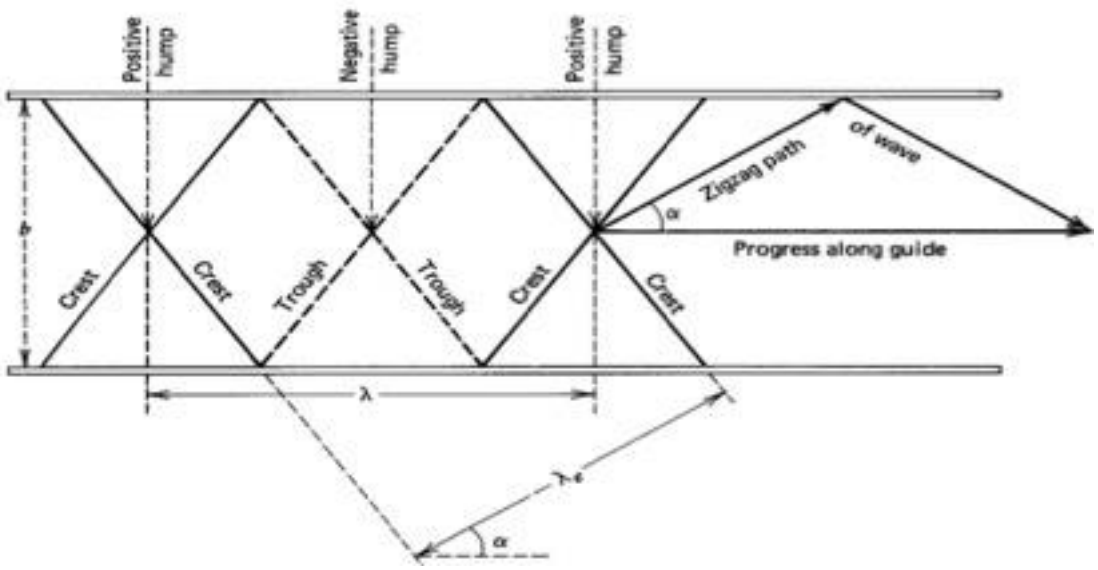

Figure 1.5. Schematic of plane waves creating a net horizontally propagating wave within a waveguide [17].

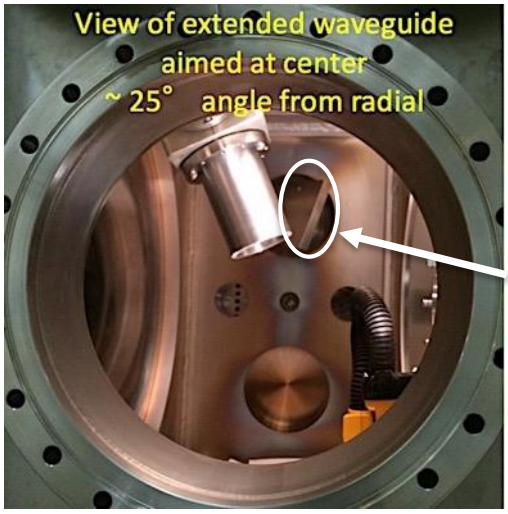

Figure 1.6. Picture of installed 28 GHz waveguide extension from view of central chamber on Proto-MPEX. The waveguide is tilted at 25 degrees from vertical. The 18 GHz waveguide location is highlighted by a white circle and arrow.

E.2. Chapter 2 Figures

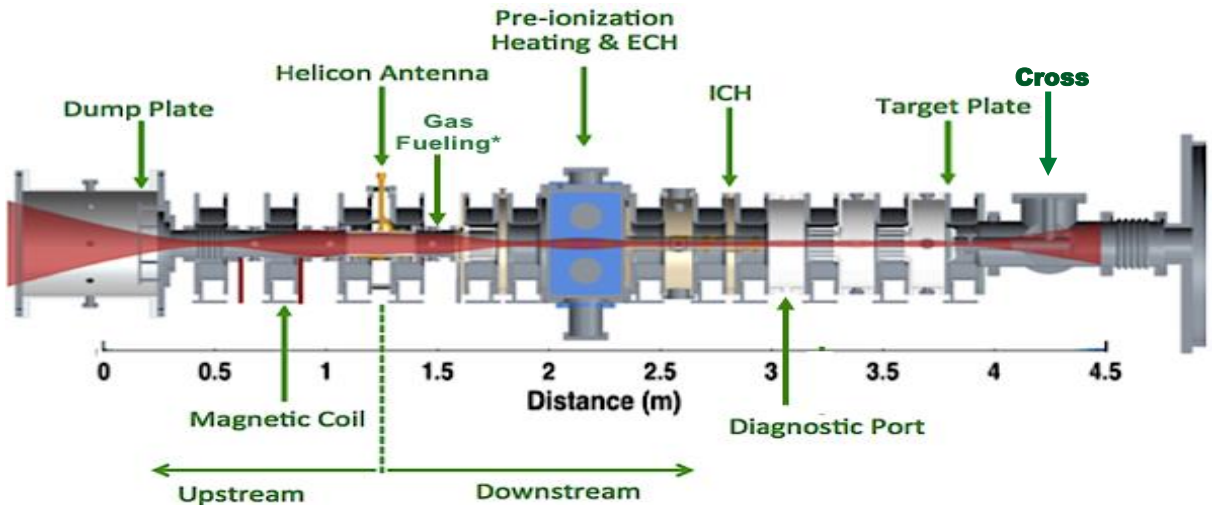

Figure 2.1. Diagram of Proto-MPEX. Magnetic coils, diagnostic ports, installed power sources and end plates are depicted. One possible gas fueling location is shown. Machine length is approximately 4.5 m.

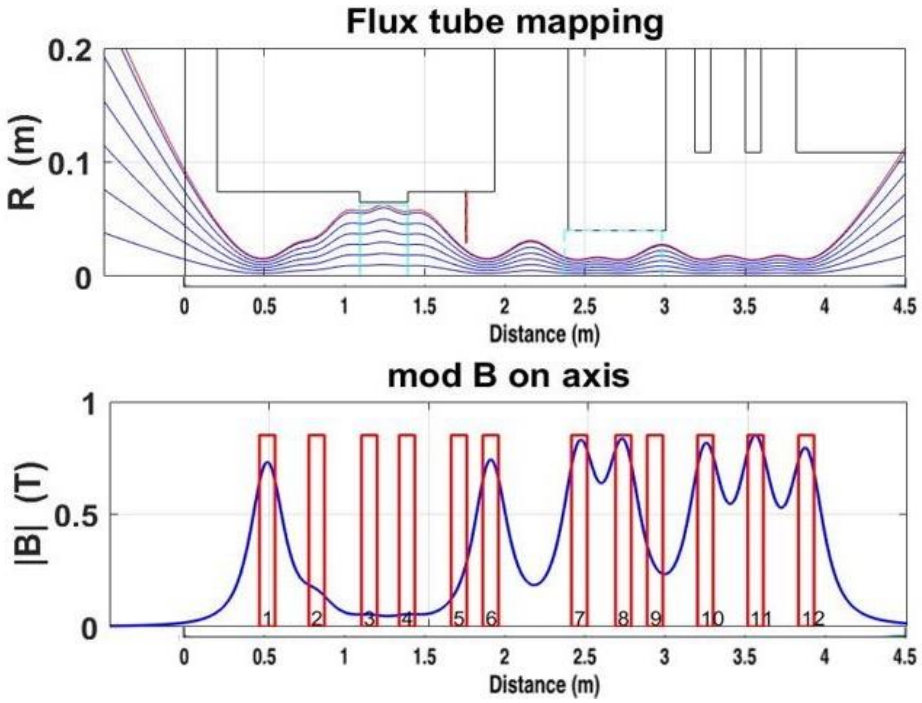

Figure 2.2. Top: diagram of magnetic field flux lines, mapped along the length of Proto-MPEX, for a standard magnetic field configuration. Blue lines represent flux lines and red line represents the outermost flux line. Bottom: diagram of on-axis magnetic field strength mapped along the length of Proto-MPEX, for a standard magnetic field configuration.

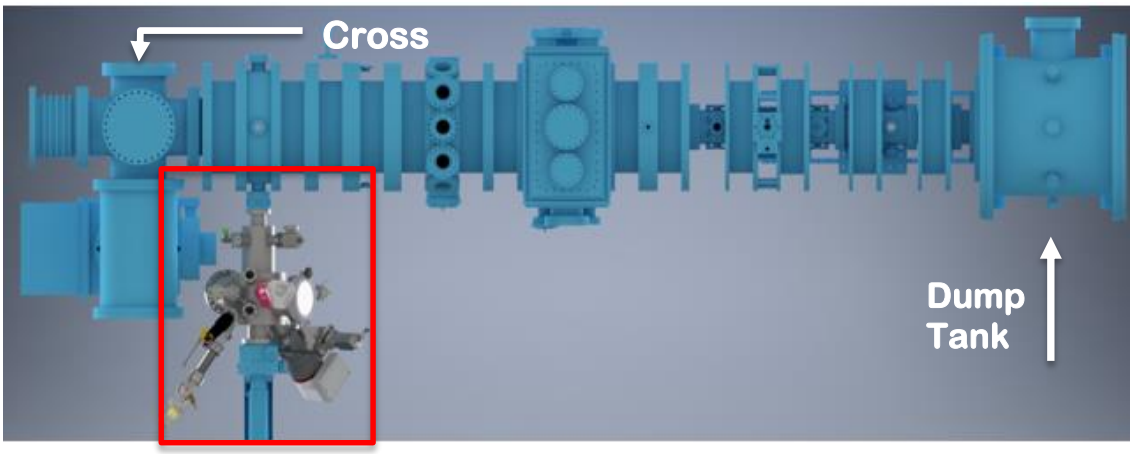

Figure 2.3. Diagram of the MAPP system installed on the upgraded Proto-MPEX machine from a bird's eye view. The MAPP system is highlighted by the red box. The upstream dump tank and the downstream cross are labeled for reference.

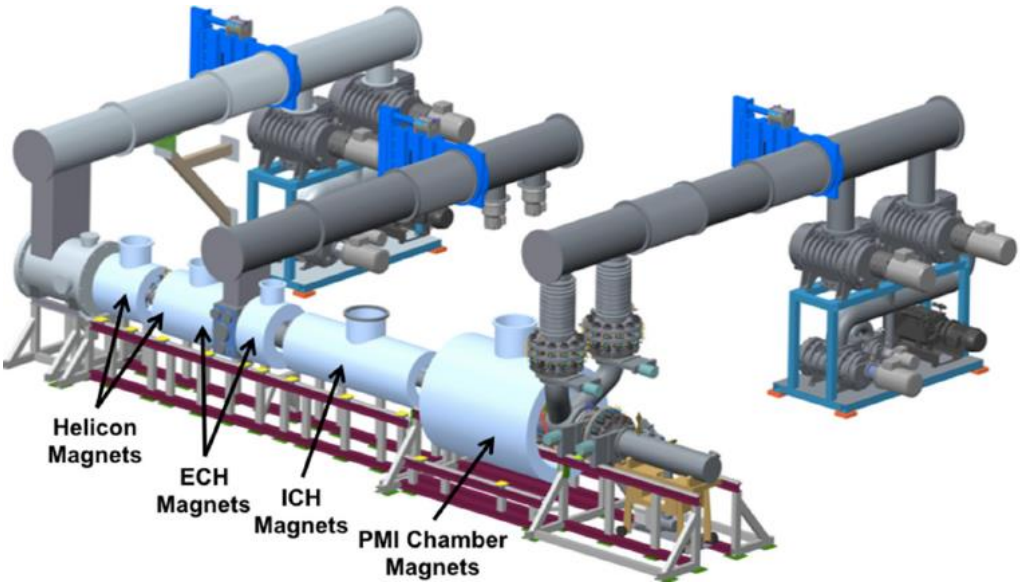

Figure 2.4. Diagram of pre-conceptual design of the MPEX linear plasma device.

E.3. Chapter 3 Figures

Figure 3.1. Images of FLIR A655sc (left) and SC4000 (center) and T250 (left) IR cameras.

Figure 3.2. Images of IR-564 Black Body Radiation Source (left) and 301 Digital Temperature Controller (right).

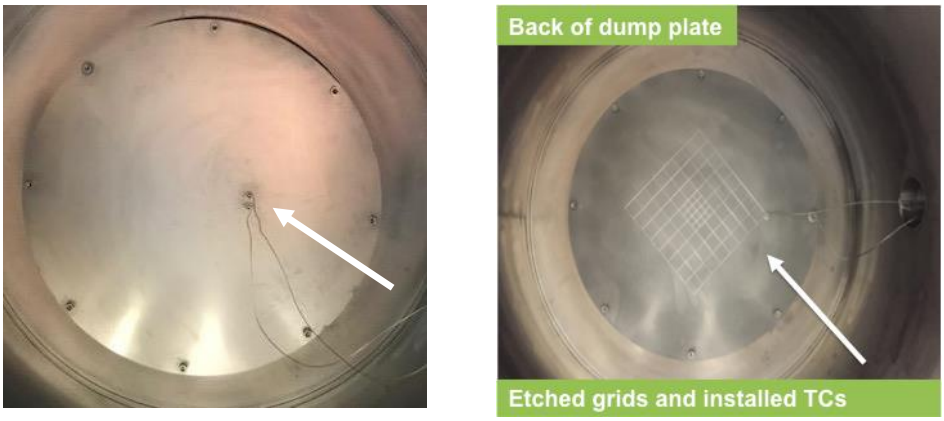

Figure 3.3. Non-plasma facing sides of the currently installed (left) and previously installed (right) dump plates. White arrows point out installed thermocouple locations. Etched gridlines visible on old dump plate.

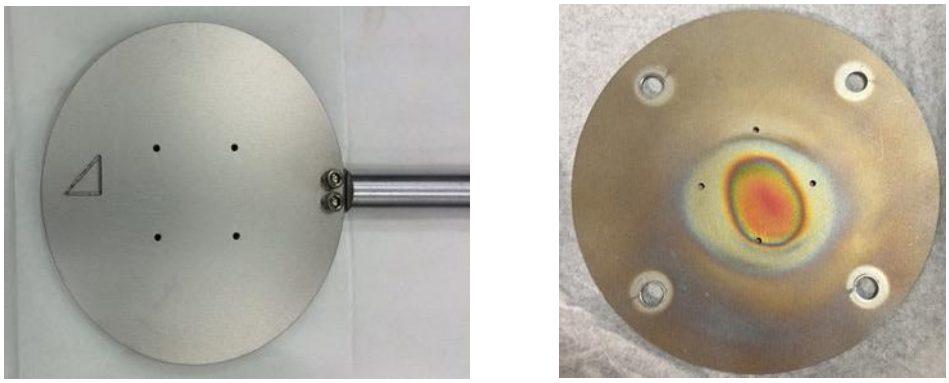

Figure 3.4. Non-plasma facing (left) and plasma facing (right) sides of the thick SS target plates. Surface damage due to plasma exposure is apparent on plasma-facing side (right).

Figure 3.5. Non-plasma facing (left) and plasma facing (right) sides of the thin SS target plates. White arrows point out installed thermocouple locations. Surface damage due to plasma exposure is apparent on plasma-facing side (right).

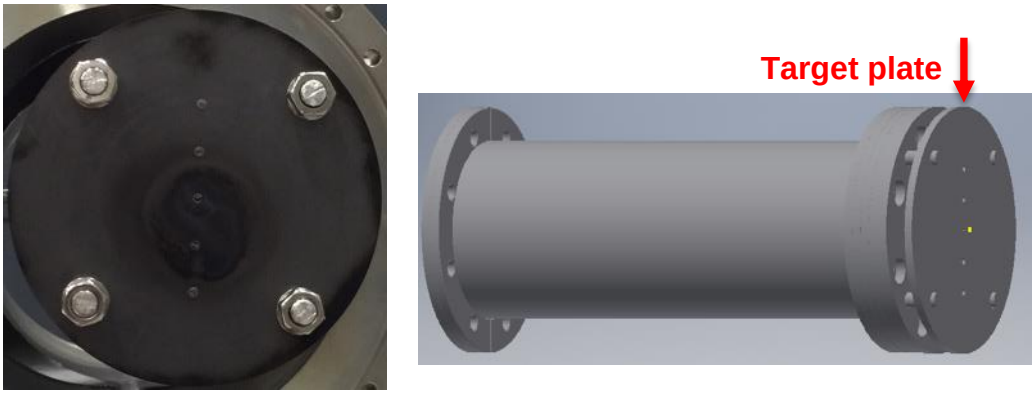

Figure 3.6. Images of graphite target plate (left) and preliminary model of target plate attached to support structure (right). The red arrow delineates the location of the target plate in the model.

Figure 3.7. Images of self-heating target plate (left) and example of Thermocoax resistive heating cable (right).

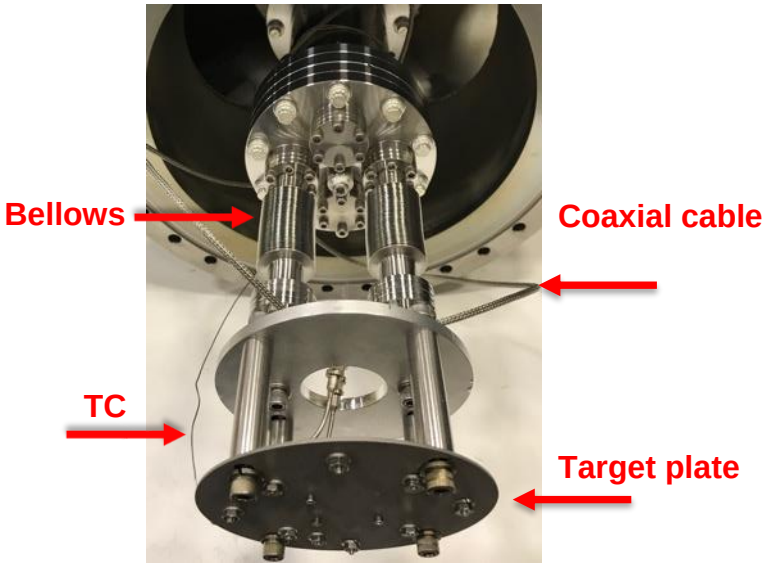

Figure 3.8. Image of the self-heating target plate fully assembled on moveable mount. The target plate, coaxial cables, bellows, and thermocouple are highlighted by red arrows and labeled.

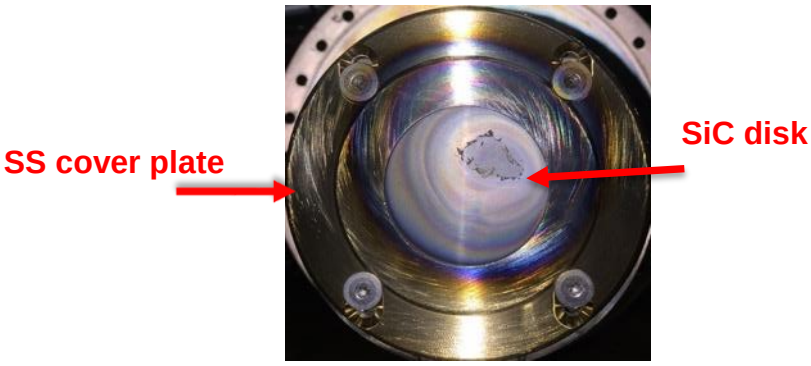

Figure 3.9. Plasma facing side of the SiC target plate. Blistering on SiC disk is apparent. The stainless steel cover plate and SiC disk are highlighted by red arrows and labeled.

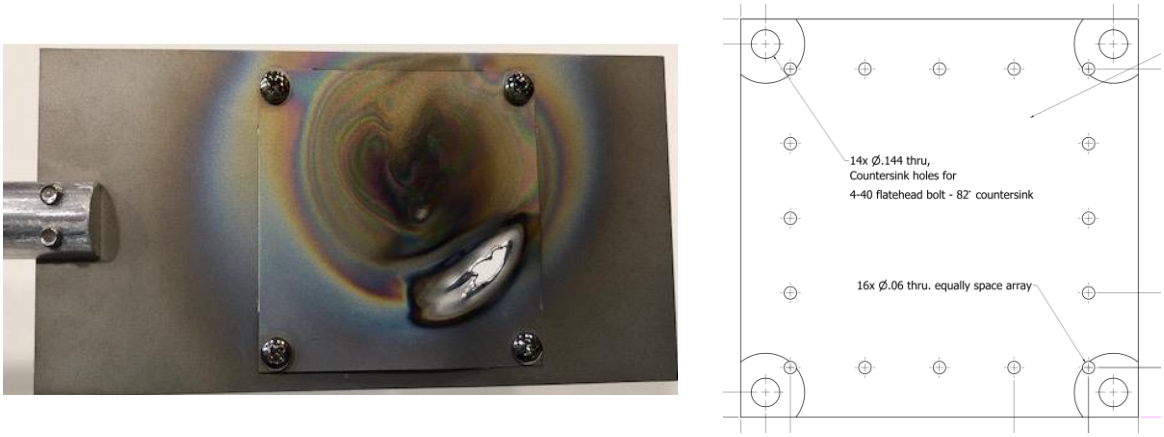

Figure 3.10. Picture of new SS target plate with thin SS insert plate after plasma exposure (left). Significant damage and discoloration are apparent. Schematic of thick SS insert plate with gridded holes also shown (right).

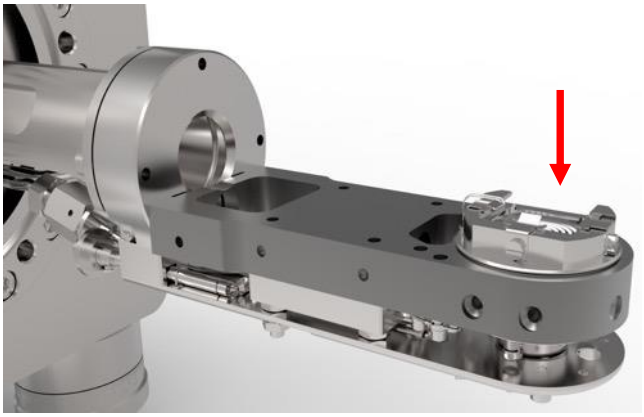

Figure 3.11. Preliminary design of the MAPP target plate and exchange system. The location of the target plate is delineated by the red arrow.

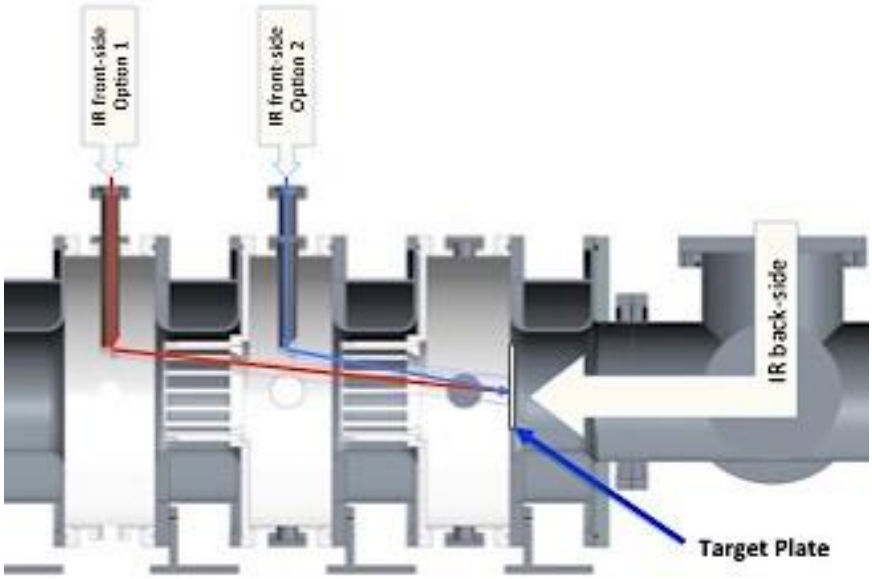

Figure 3.12. Schematic of periscope installation location and viewing lines. Red lines represent the line of sight between the IR camera and the target plate through the periscope if installed at Option 1 location (z = 3.1 m, current installation location). Target plate and its back-side IR imaging are also depicted.

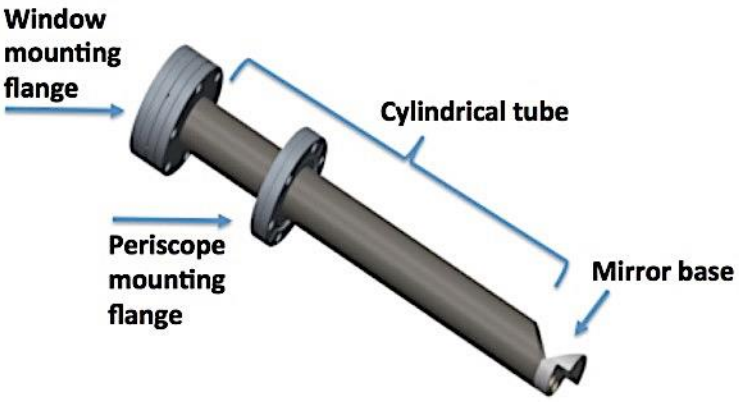

.

Figure 3.13. Picture of periscope.

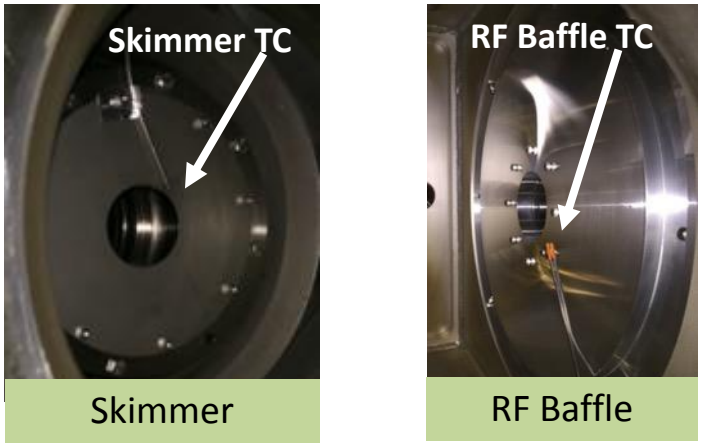

Figure 3.14. Installed skimmer (left) and RF baffle (right) plates. White arrows point out installed thermocouple locations.

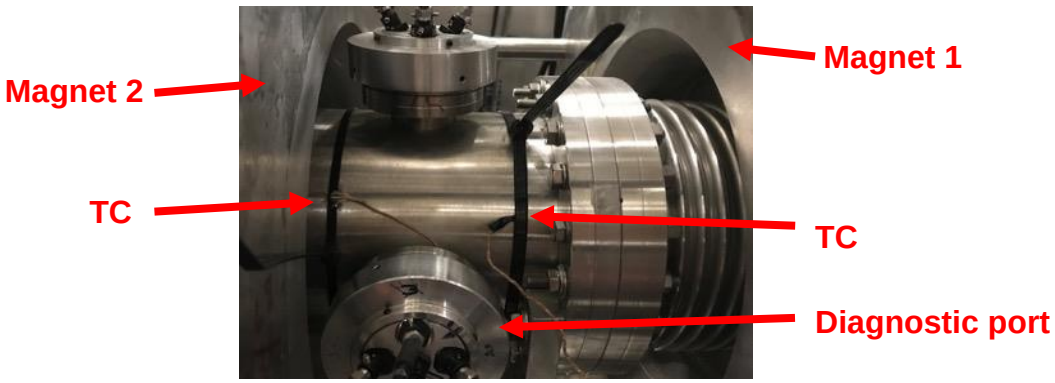

Figure 3.15. Installed TCs on spool piece 1.5. Red arrows point out installed thermocouples. Diagnostic ports and magnet coils 1 and 2 are visible.

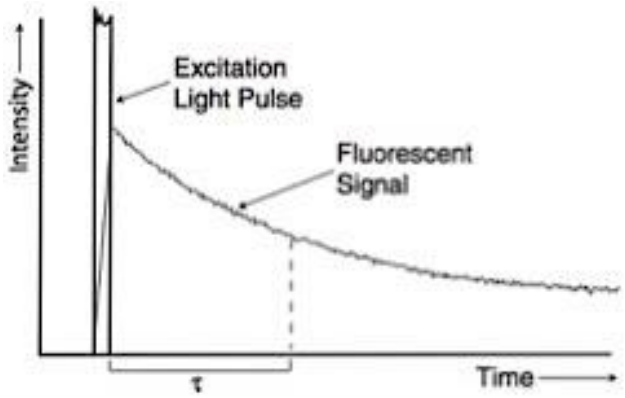

Figure 3.16. Diagram of example fluoroptic probe fluorescence decay time.

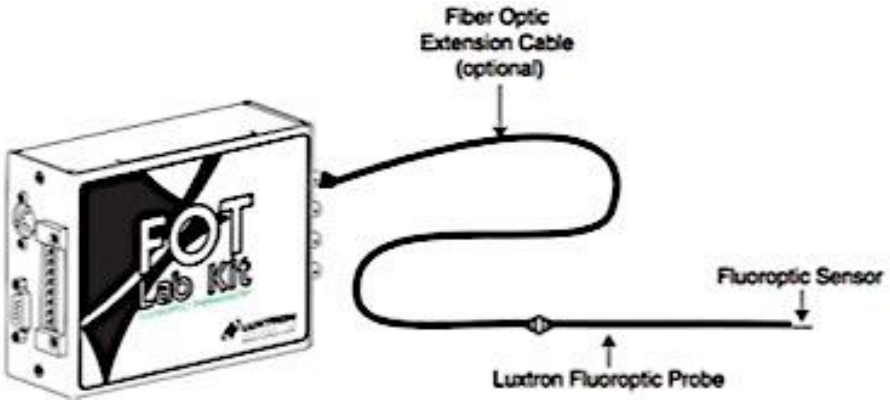

Figure 3.17. Diagram of fluoroptic probe diagnostic set up [54].

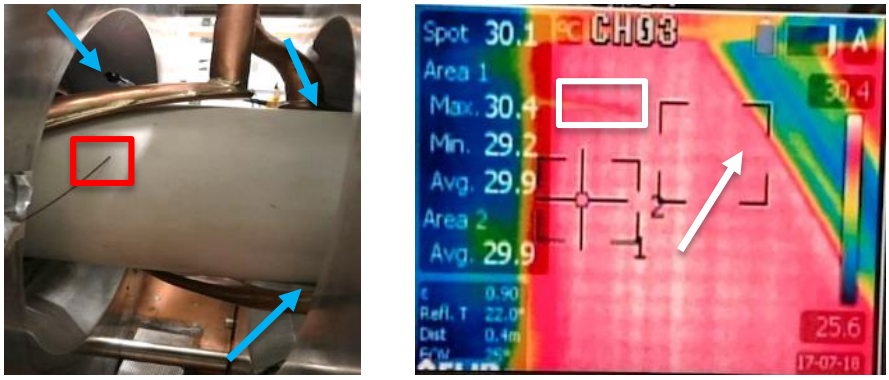

Figure 3.18. Images of the helicon window and antenna with visible connected FPs. The left image shows locations of the FPs under the helicon antenna and the FP in the field of view (FOV) of the IR camera are delineated by the blue arrows and the red rectangle, respectively. The right image shows IR camera view of the helicon window (appears red), with the FP in its FOV highlighted by the white rectangle. The top helicon antenna strap (appears blue) is delineated by the white arrow.

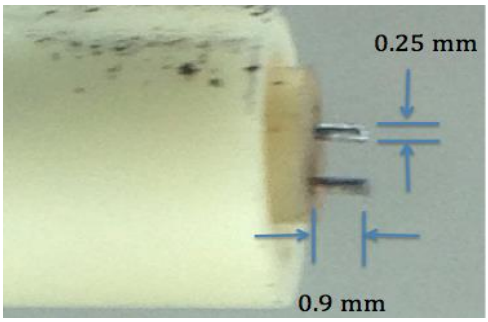

Figure 3.19. Picture of LP used during operations. Tungsten wires and their dimensions are depicted.

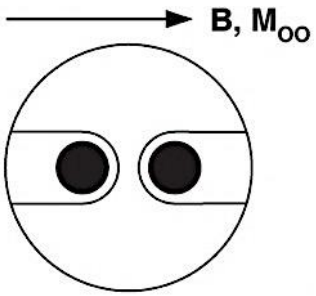

Figure 3.20. Schematic of parallel MP. The direction of the magnetic field (B) and plasma flow (Moo) are depicted.

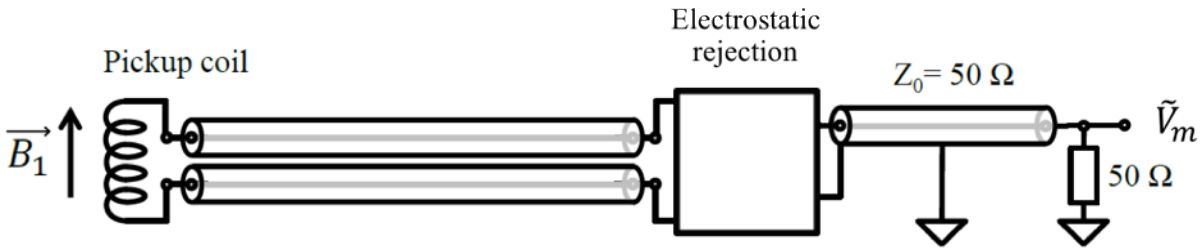

Figure 3.21. Schematic of B-dot probe installed on Proto-MPEX. The conducting coil and direction of the magnetic field, B, are shown.

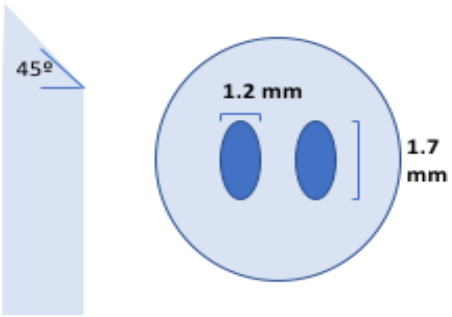

Figure 3.22. Schematic of IFP installed on Proto-MPEX. The side-view of the probe head is shown on the left and a cross-section of the probe tip is shown on the right, with the dimensions of the tip wires.

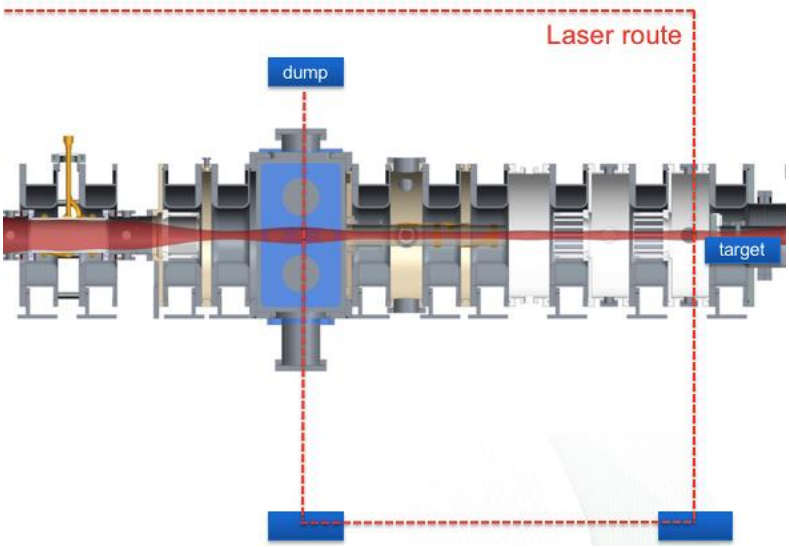

Figure 3.23. Schematic of TS laser beam path with respect to the Proto-MPEX machine. The red dotted line represents the current TS laser path. The dump location is depicted, as well as the location of the target plate.

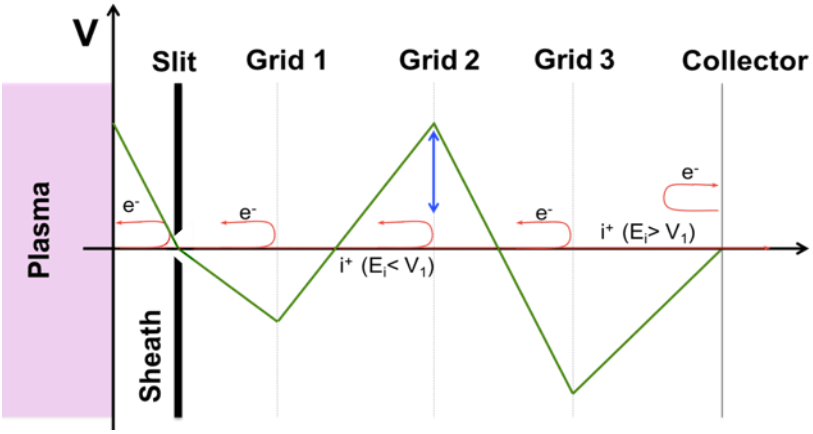

Figure 3.24. Schematic of standard RFEA. Entrance slit, electron repelling grid, ion repelling grid, electron suppressing grid, and collector are shown.

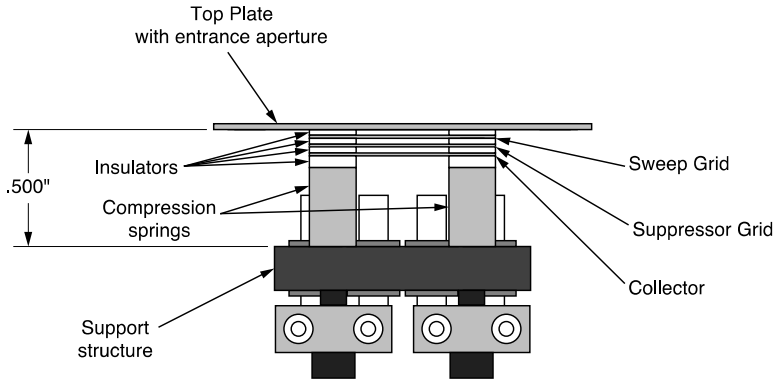

Figure 3.25. Diagram of RFEA installed on Proto-MPEX. Grids, insulators, and support structure are depicted.

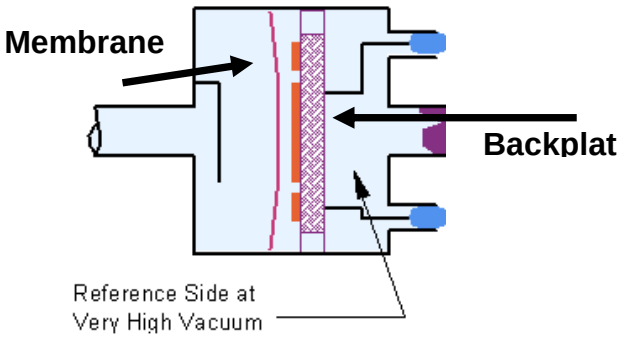

Figure 3.26. Diagram of baratron sensor. Reference (high-vacuum) side of membrane, membrane, and backplate are labeled.

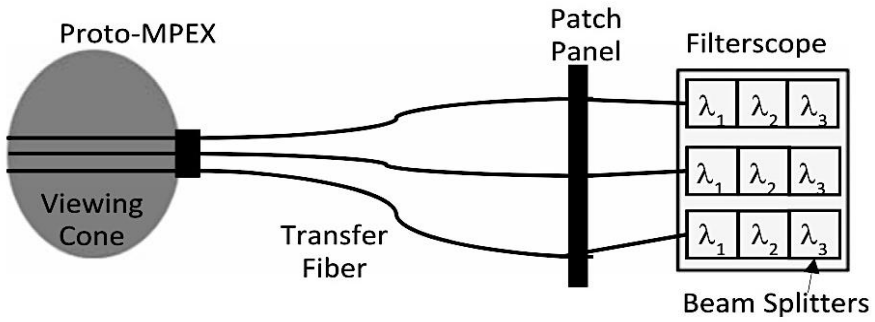

Figure 3.27. Schematic of Proto-MPEX filterscope diagnostic. The viewing cone of the Proto-MPEX plasma, the transfer optical fibers, patch panel, filterscope array and beam splitters are labeled.

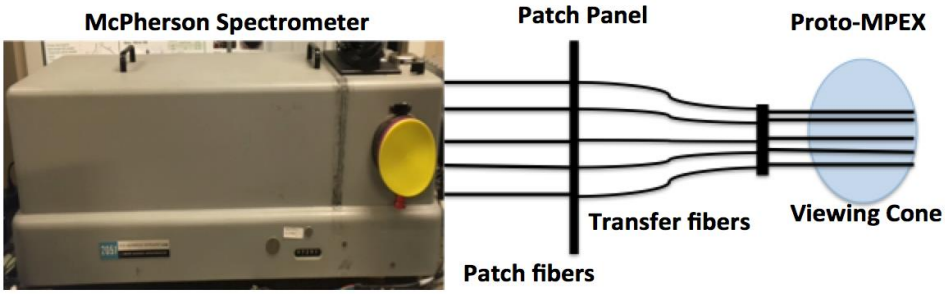

Figure 3.28. Schematic of Proto-MPEX McPherson diagnostic. The viewing cone of the Proto-MPEX plasma, the transfer optical fibers, patch panel, and McPherson spectrometer are labeled.

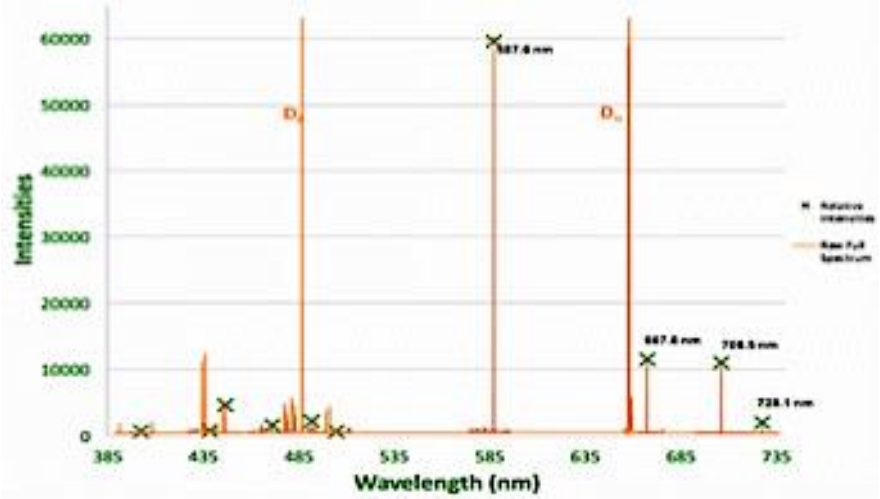

Figure 3.29. Photon emission intensity plot using McPherson data gathered from previous Proto-MPEX experiment. The y-axis represents the intensity in counts. The x-axis represents the wavelength in nanometers. The D_α and D_β emission spectra are labeled and represented by oranges line peaks.

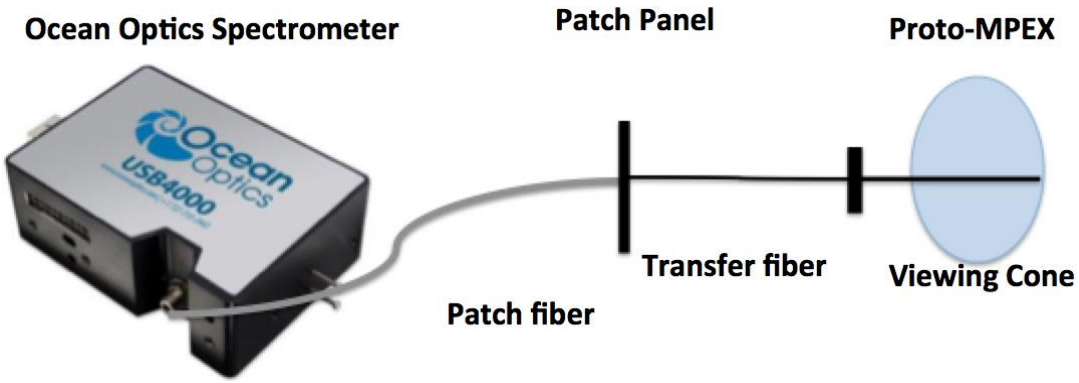

Figure 3.30. Schematic of Proto-MPEX Ocean Optics diagnostic. The viewing cone of the Proto-MPEX plasma, the transfer optical fiber, patch panel, and Ocean Optics spectrometer are labeled.

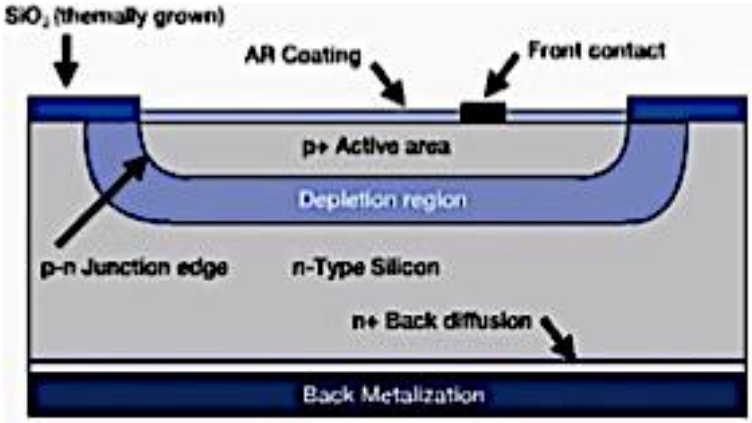

Figure 3.31. Schematic of example silicon photodiode.

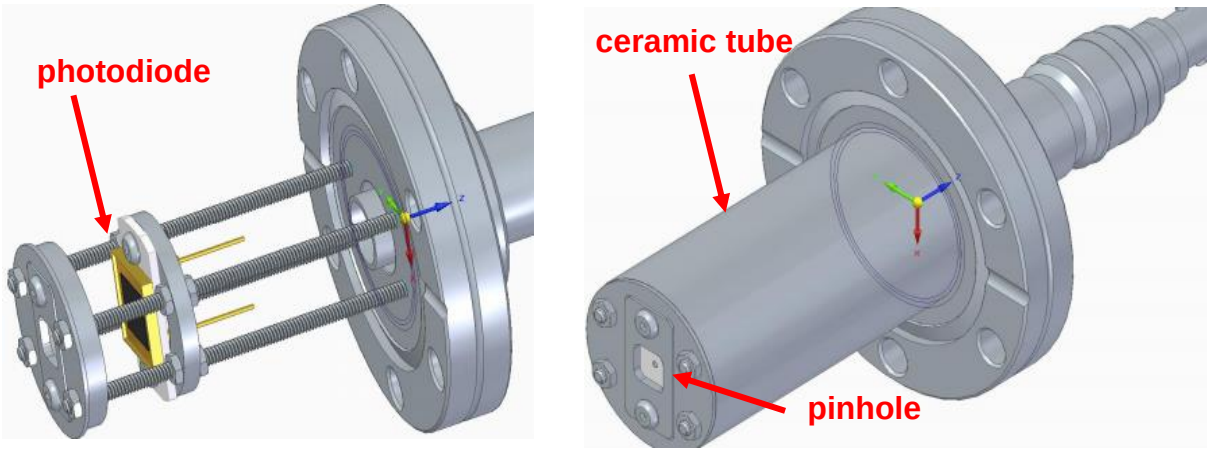

Figure 3.32. Schematics of the photodiode installation set-up, with (right) and without (left) the stainless steel tube. The pinhole, photodiode, and stainless steel tube are labeled.

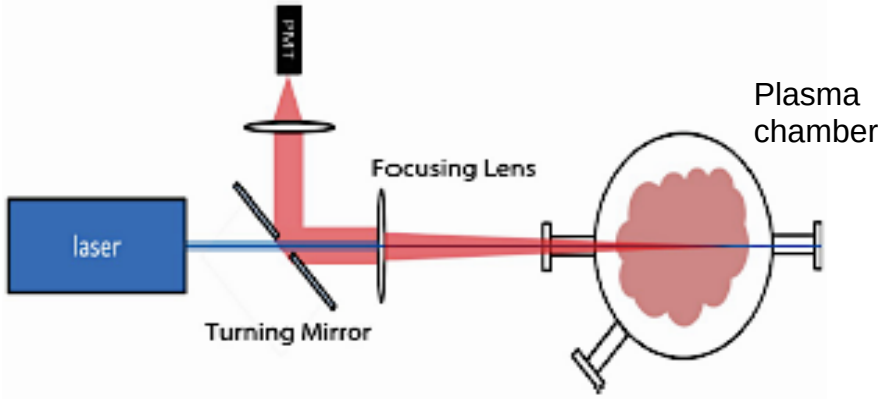

Figure 3.33. Schematic of TALIF system. Blue box and line depict laser system and laser line. Red line path depicts collected photons emitted by excited neutrals. Plasma chamber, focusing lenses, turning mirror and PMT are also labeled.

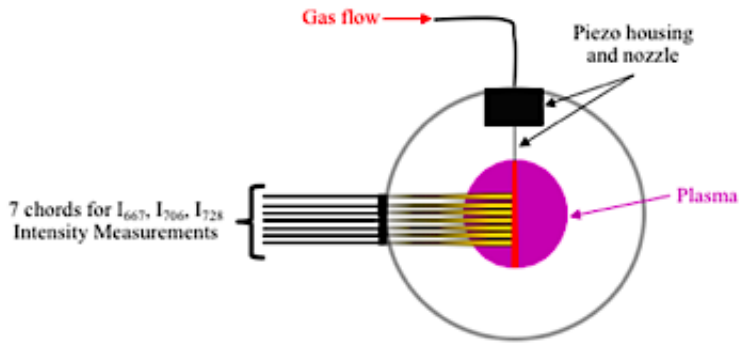

Figure 3.34. Schematic of HELIOS system.

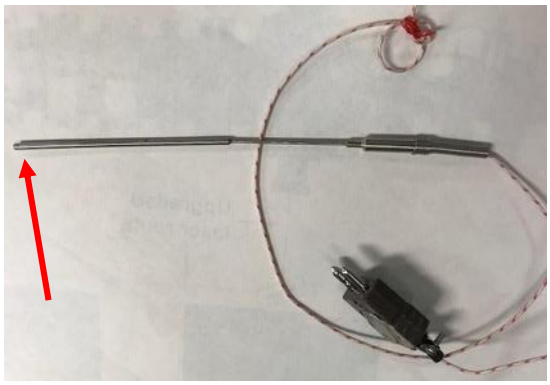

Figure 3.35. Image of STC. The red arrow highlights the surface eroding tip of the thermocouple.

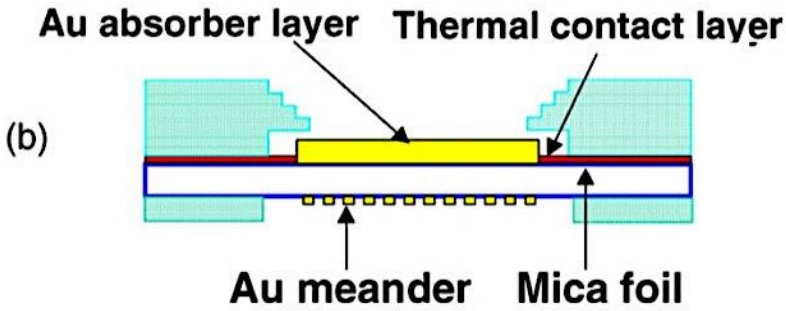

Figure 3.36. Cross-sectional diagram of gold resistor bolometer.

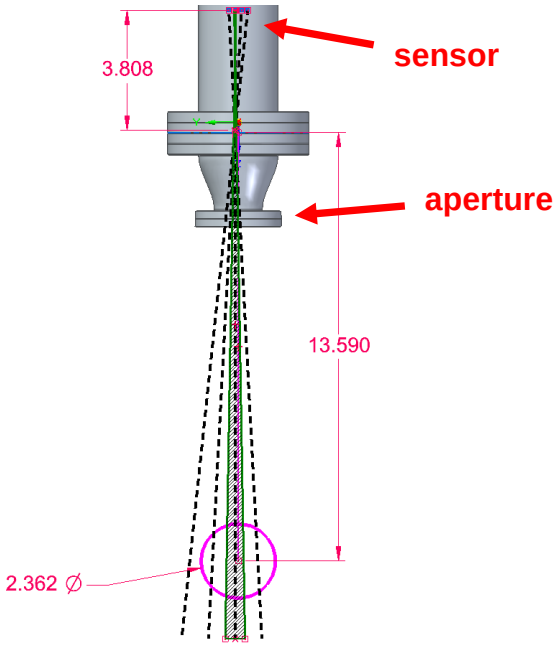

Figure 3.37. Diagram of bolometer system, including field of view lines (dotted black lines). The locations of the aperture and bolometer are delineated.

E.4. Chapter 4 Figures

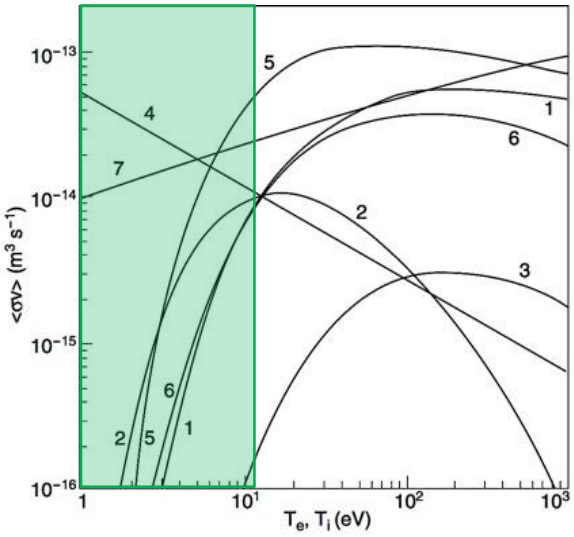

Figure 1.25. The rate coefficients for atomic and molecular hydrogen [1.23]. The numbered reactions are (1): $e + H_2 \rightarrow H_2^+ + 2e$, (2): $e + H_2 \rightarrow 2H^0 + e$, (3): $e + H_2 \rightarrow H^0 + H^+ + 2e$, (4): $e + H_2^+ \rightarrow 2H^0$, (5): $e + H_2^+ \rightarrow H^0 + H^+ + e$, (6): $e + H^0 \rightarrow H^+ + 2e$, and charge exchange (7): $H^0 + H^+ \rightarrow H^+ + H^0$.

Figure 4.1. Ionization rate coefficients for different electron-hydrogen reactions, listed in the source's figure description. The y-axis represents the average rate coefficient in cubic meters per second. The x-axis represents the particle temperature in eV. The effect of temperature on the rate coefficients is depicted by the various curves. Green box highlights temperature range observed in Proto-MPEX experiments.

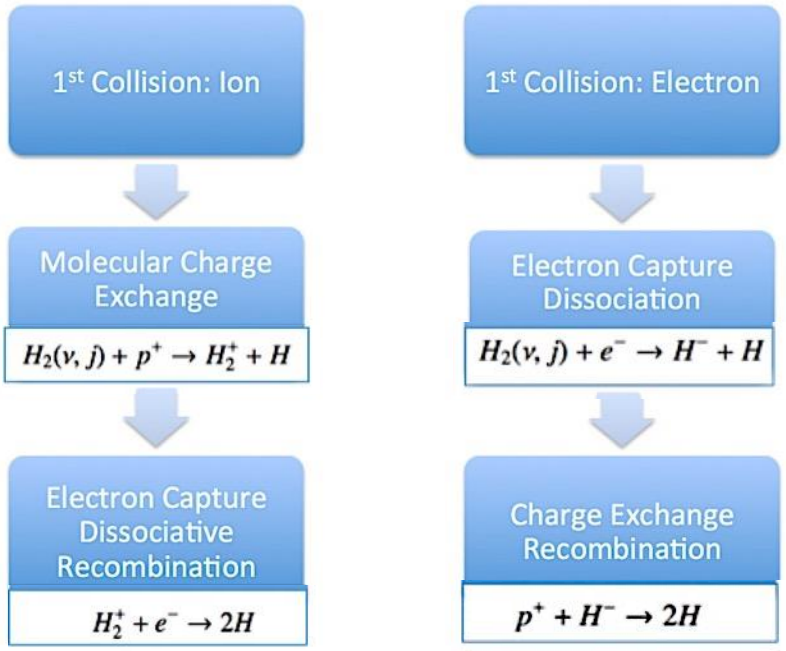

Figure 4.2. List of two possible MAR processes assuming vibrationally-excited molecular hydrogen (H2 (v, j)). p+ is the proton (ion), e- is the electron. The charge on the hydrogen particle is depicted across the processes.

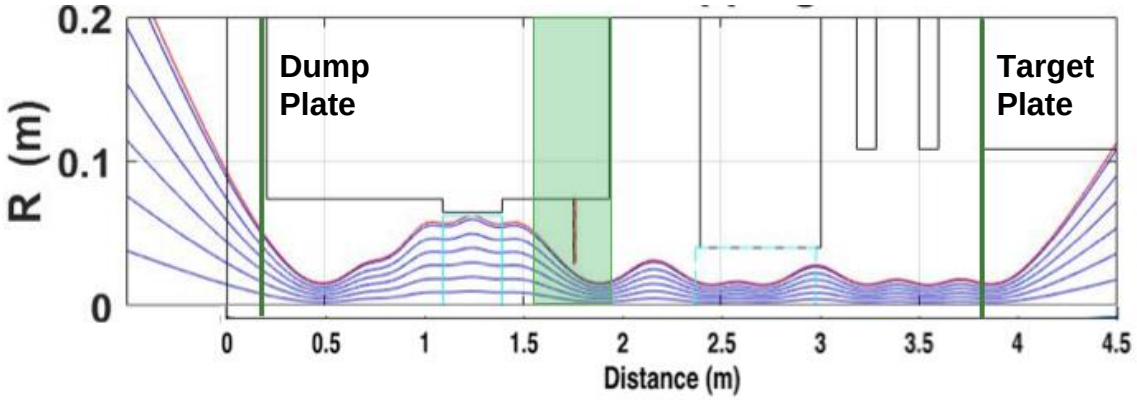

Figure 4.3. Schematic of magnetic field flux tube mapping along Proto-MPEX device for a modified flat field configuration. The blue lines represent the flux lines and the red line represents the last closed flux surface. The y-axis represents the radius of the machine in meters. The x-axis represents the axial length of the machine in meters. The changes in the inner diameter along the machine length are also shown. The green box highlights the region where the plasma limits on machine surfaces. Green lines depict the end plates.

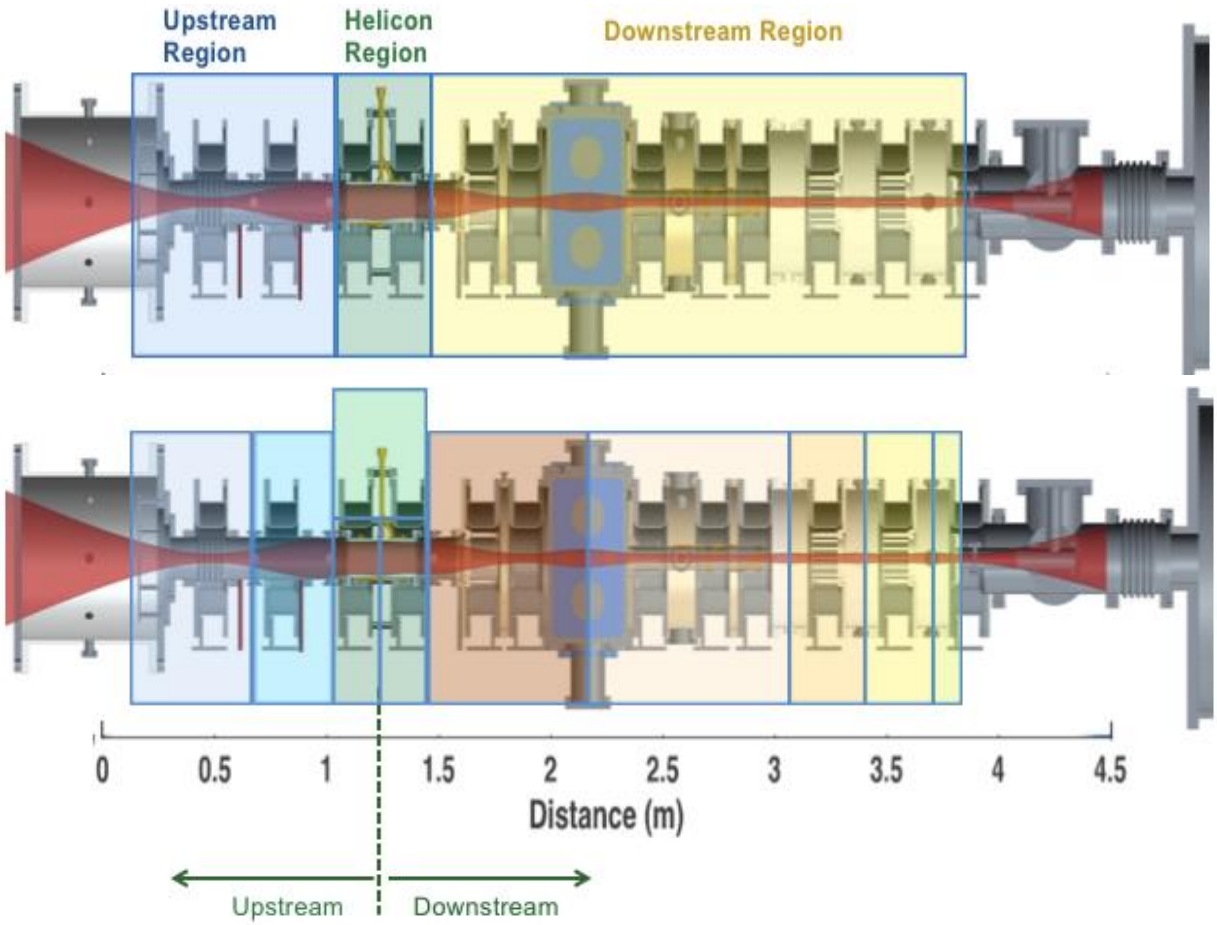

Figure 4.4. Diagrams of Proto-MPEX separated into its three main regions (top) and its sub-regions for improved efficiency analysis (bottom).

E.5. Chapter 5 Figures

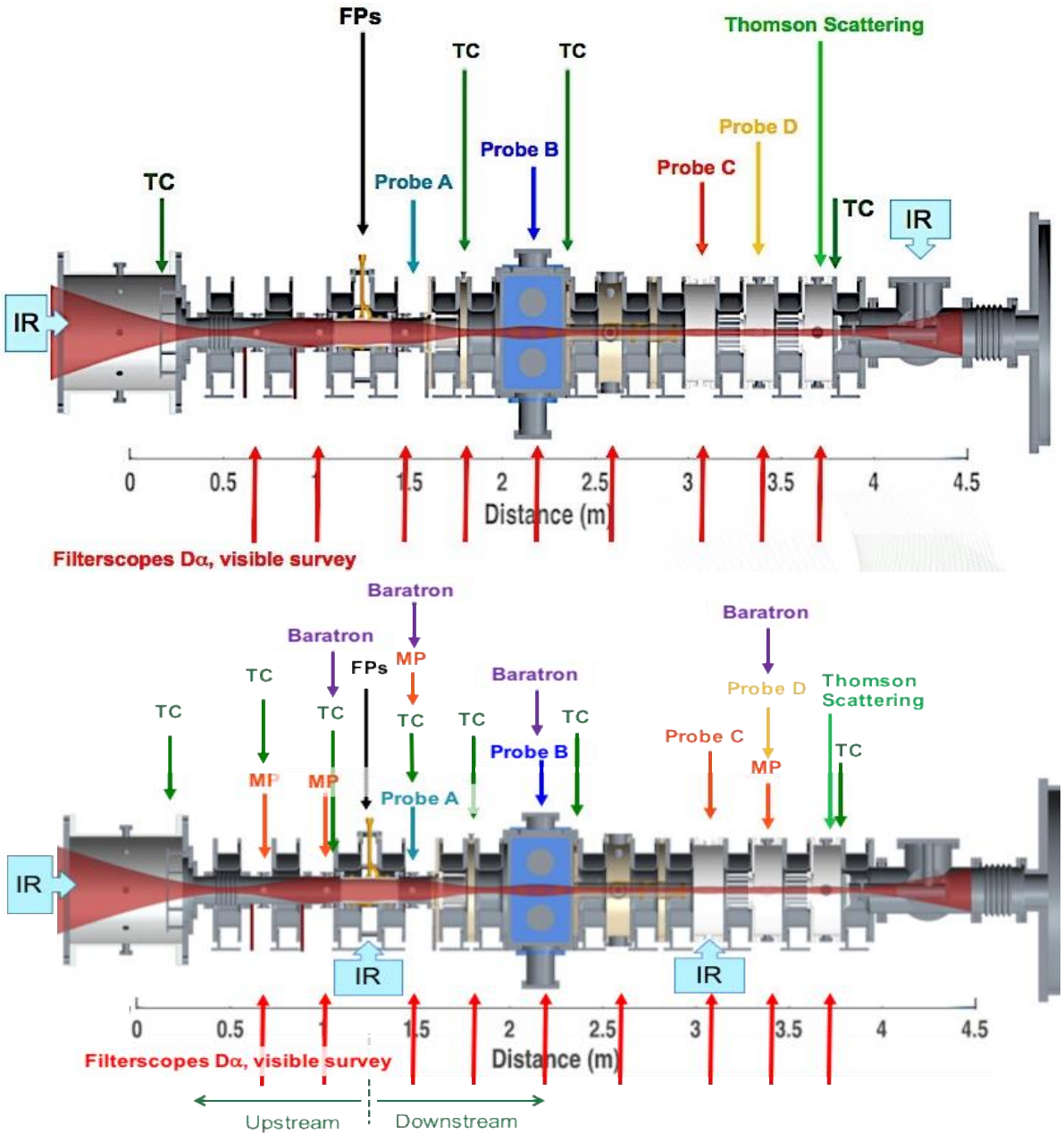

Figure 5.1. Diagrams of diagnostics installed on Proto-MPEX for first (top) and second (bottom) power accounting analysis. Machine length is approximately 4.5 m.

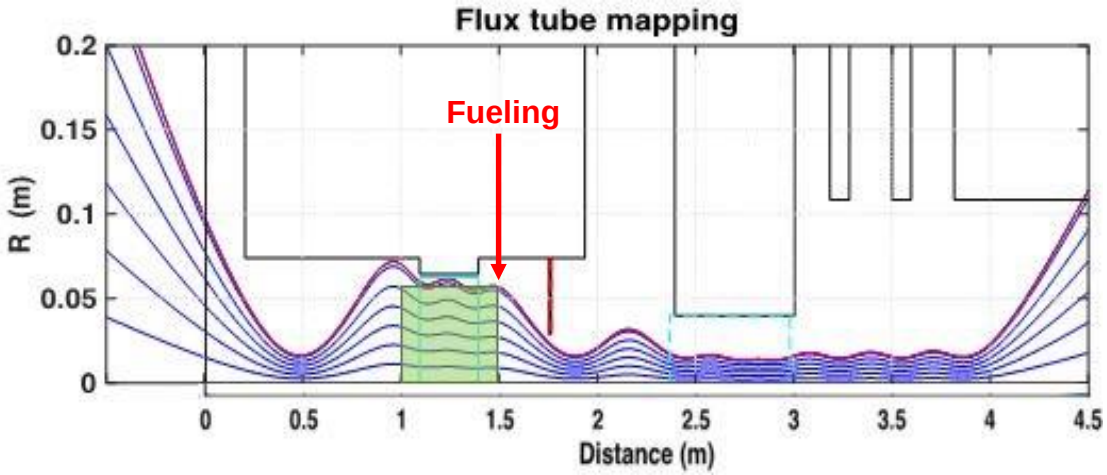

Figure 5.2. Schematic of magnetic field flux tube mapping along Proto-MPEX device for a modified flat field configuration. Blue lines represent flux lines and red line represents the outermost flux line. The y-axis represents radius of the machine (m). The x-axis represents axial length of the machine (m). Changes in the inner diameter along the machine length are shown. Helicon region is highlighted in green. Gas fueling location also shown.

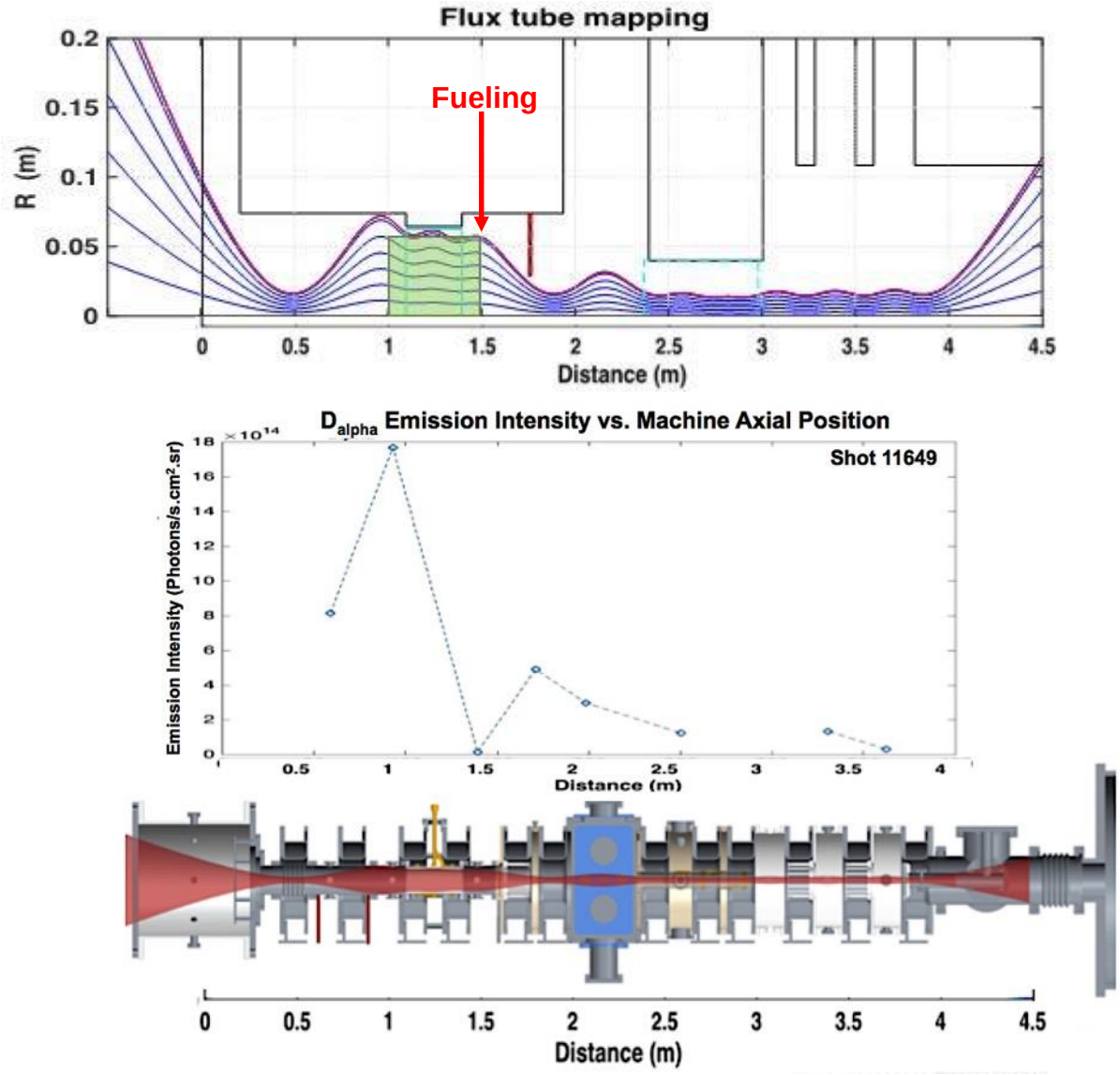

Figure 5.3. Intensities of Dα photons emitted from main plasma along length of Proto-MPEX. The y-axis represents the emission intensity in photons per second per square centimeter per steradian. The x-axis is the distance along the machine. The Proto-MPEX diagram and magnetic field configuration are provided for reference.

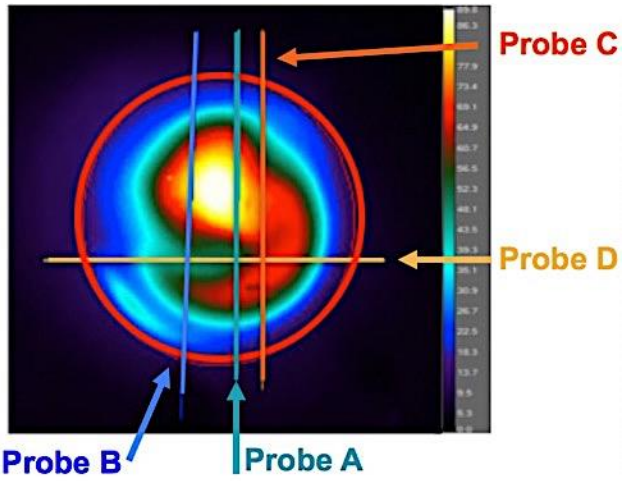

Figure 5.4. LP scanning locations for probes A-D through the plasma beam. Probes A-C scan vertically and probe D scans horizontally. The light blue line represents probe A, the dark blue line represents probe B, the orange line represents probe C, and the yellow line represents probe D.

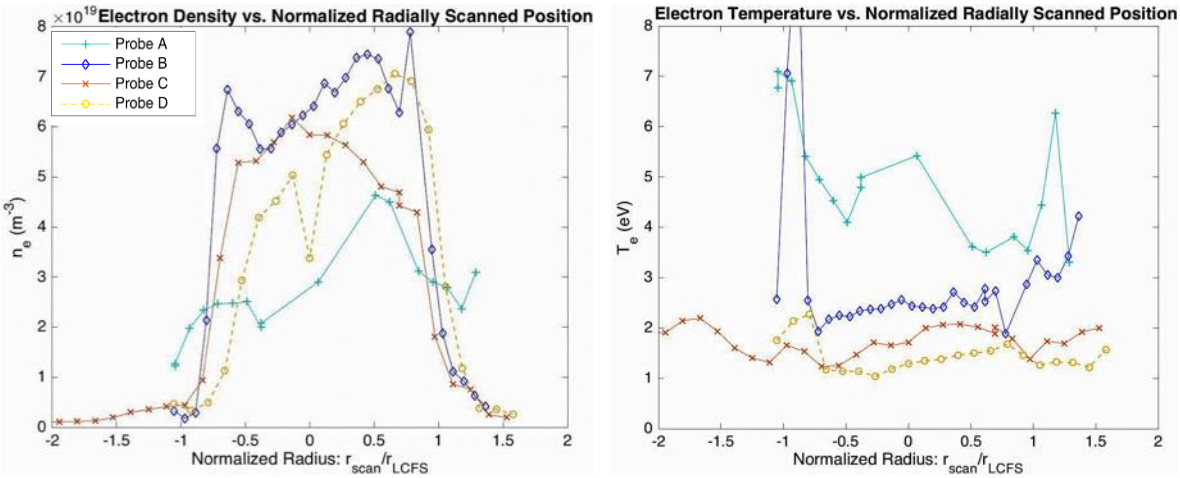

Figure 5.5. LP scans for probes A-D of electron density and temperature. Y-axes represent electron density (left) and temperature (right). X-axes represent the normalized radius. The light blue line represents probe A's scan, the dark blue line represents probe B's scan, the orange line represents probe C's scan, and the yellow line represents probe D's scan.

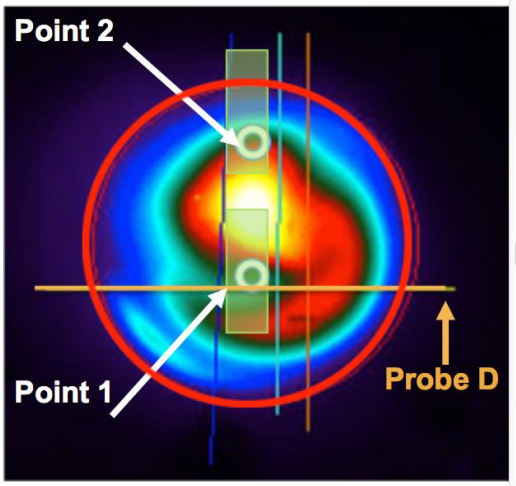

Figure 5.6. TS two-point scan. The yellow rectangles represent the swept sample area and the white circular disks represent the approximated points. The yellow line represents probe D's scanning location.

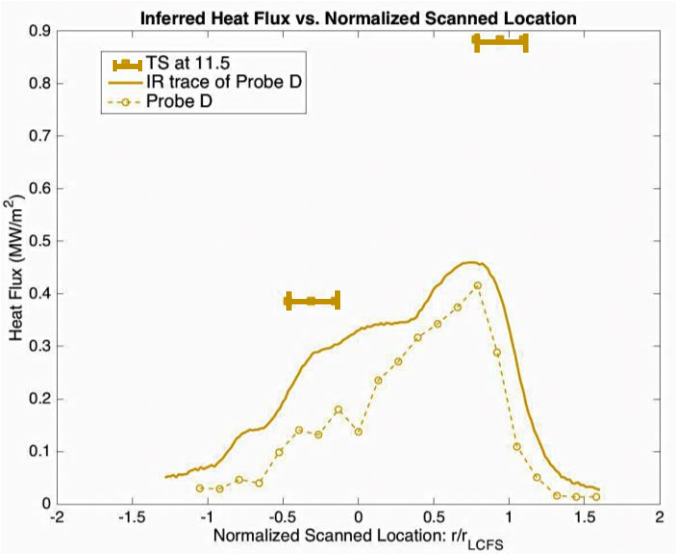

Figure 5.7. Heat flux profiles inferred by IR camera, probe D, and TS. The y-axis represents the heat flux in MW/m2. The x-axis represents the normalized scanned position. The dotted yellow line represents the probe D scan. The solid yellow line represents the IR-trace of probe D scan. The two trios of dots represent the TS scan.

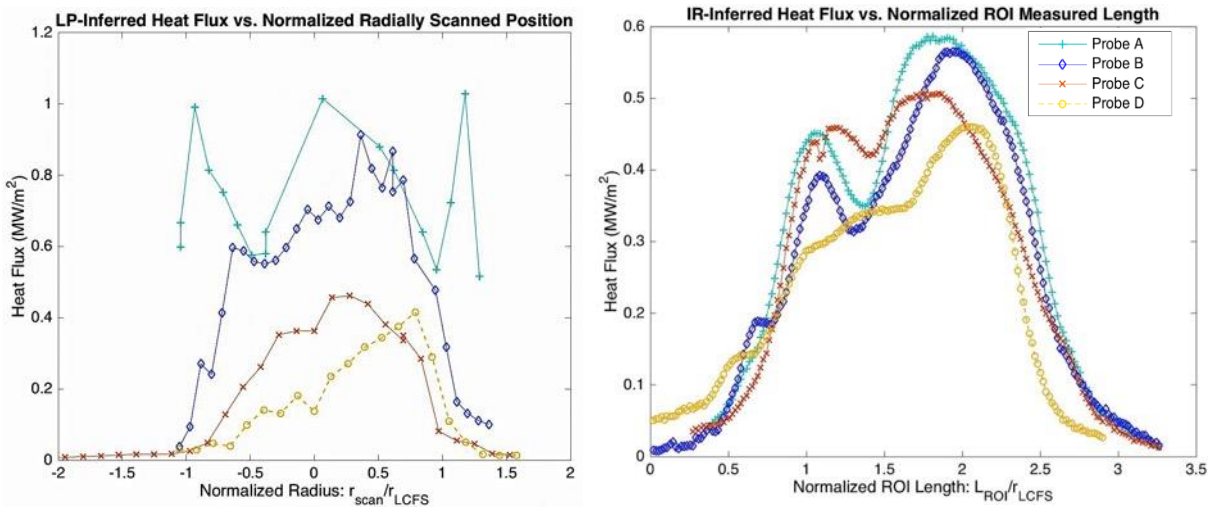

Figure 5.8. Heat flux profiles inferred by IR camera (right) and LPs A-D (left). The y-axis represents the heat flux in MW/m^2. The x-axis represents the normalized scanned position. For both graphs, the light blue line represents the probe A scan or trace, the dark blue line represents the probe B scan or trace, the orange line represents the probe C scan or trace, and the yellow line represents the probe D scan or trace.

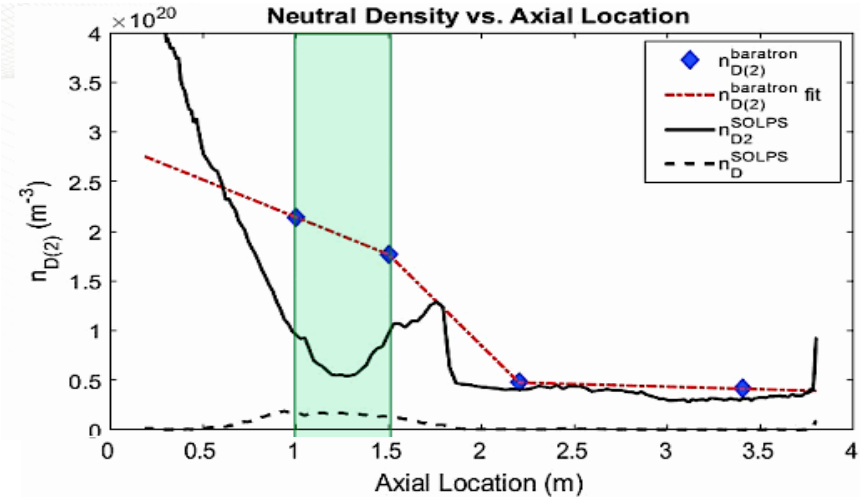

Figure 5.9. Plot depicting axial variation in neutral (n_{D2}, n_D) densities inferred by SOLPS modeling and experimental baratron data. The green box depicts the helicon region.

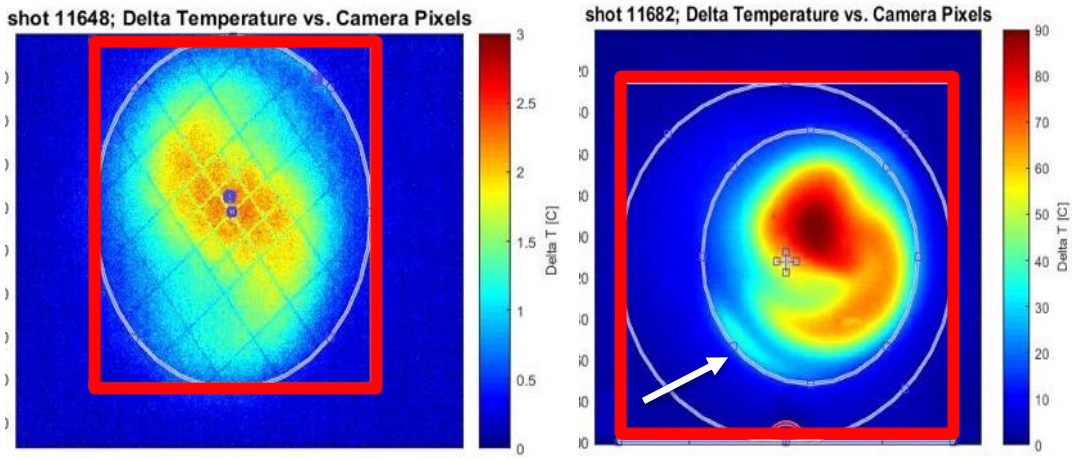

Figure 5.10. Profiles of plasma deposited on dump plate (left) and target plate (right). The ΔT scale for the target is 0-90°C. The ΔT scale for the dump is 0-3°C. The red rectangles delineate the area over which deposited power is accounted. The white arrow highlights the lower plasma lobe on the target plate.

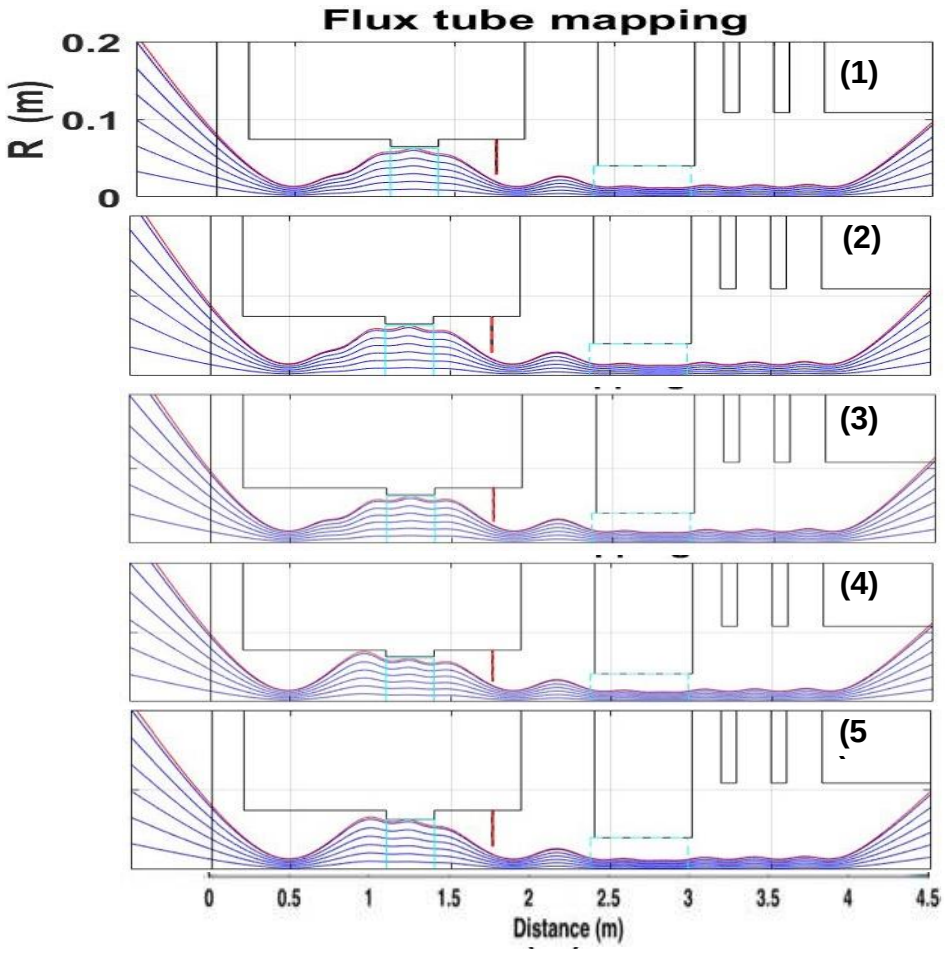

Figure 5.11. Schematic of magnetic field flux tube mapping along Proto-MPEX device for magnetic field configurations 1-5. The blue lines represent the flux lines and the red line represents the outermost flux line. The y-axis represents the radius of the machine in meters. The x-axis represents the axial length of the machine in meters.

E.6. Chapter 6 Figures

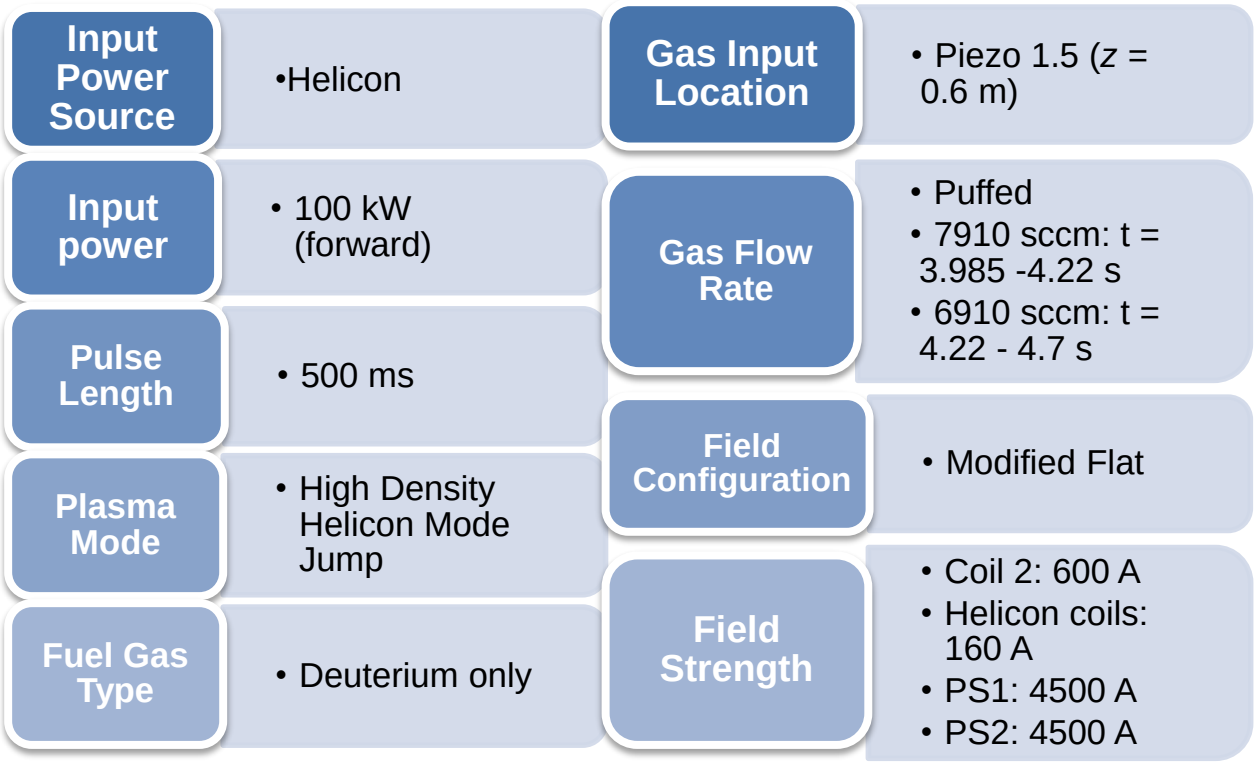

Figure 6.1. List of set machine operating parameters for power balance.

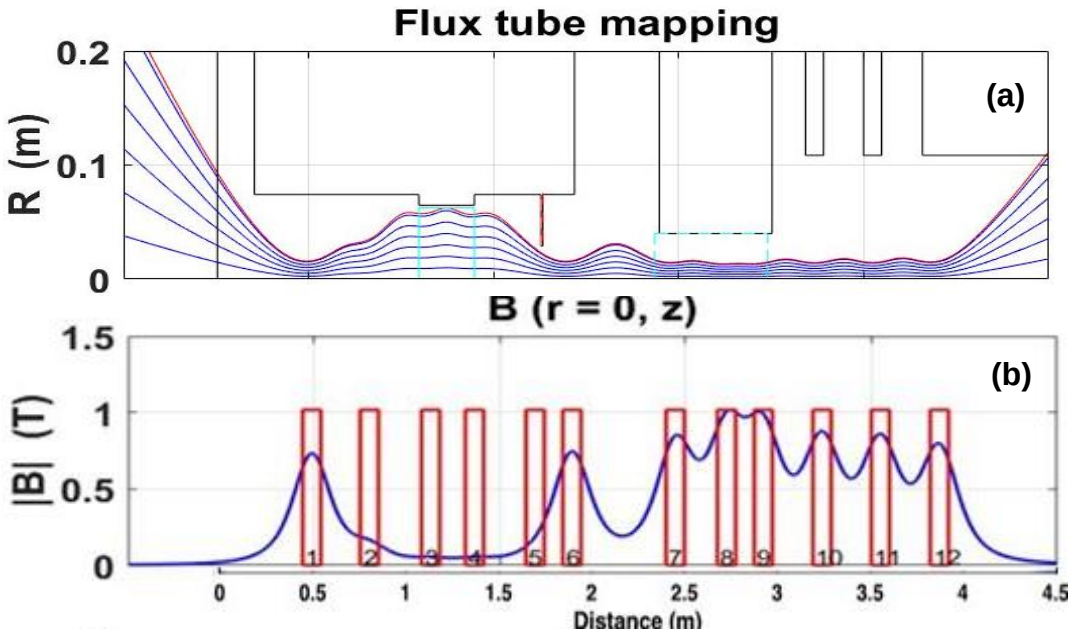

Figure 6.2. (a) Flux tube mapping along Proto-MPEX. Y-axis represents plasma radius. X-axis represents the distance along the machine axis. The blue lines represent the flux tube lines. The red line represents the outermost flux line (OFL). (b) On-axis magnetic field strength along Proto-MPEX. Y-axis represents magnetic field and x-axis represents distance along machine axis. Blue line represents the on-axis magnetic field.

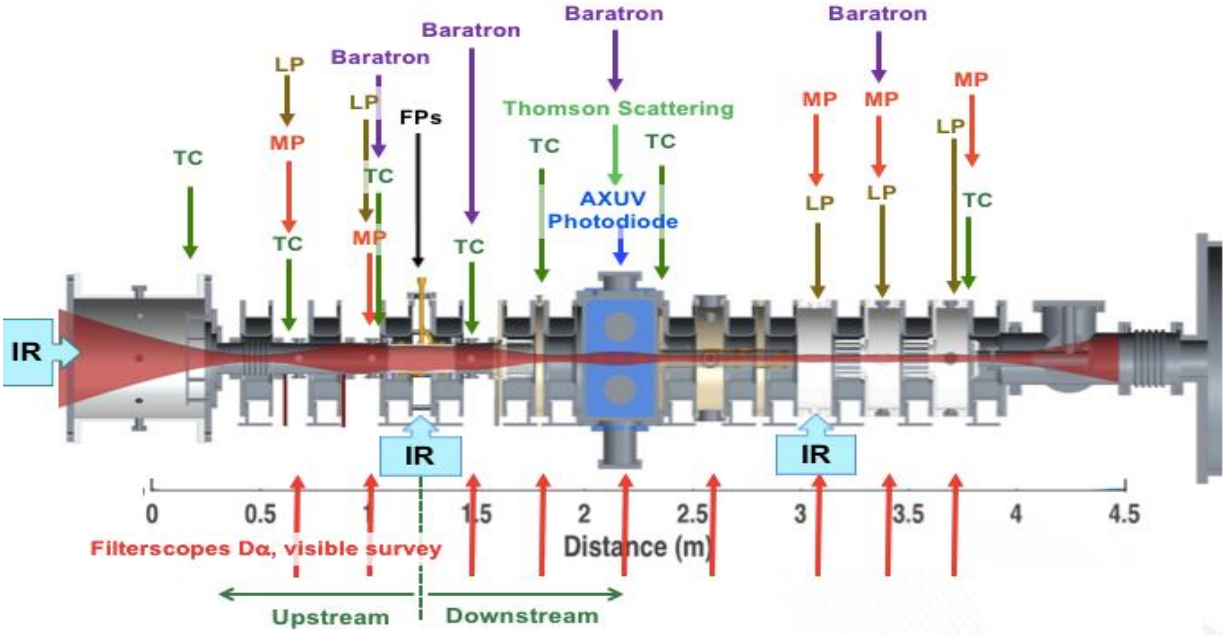

Figure 6.3. Diagram of diagnostics installed on Proto-MPEX for power accounting analysis. Machine length is approximately 4.5 m.

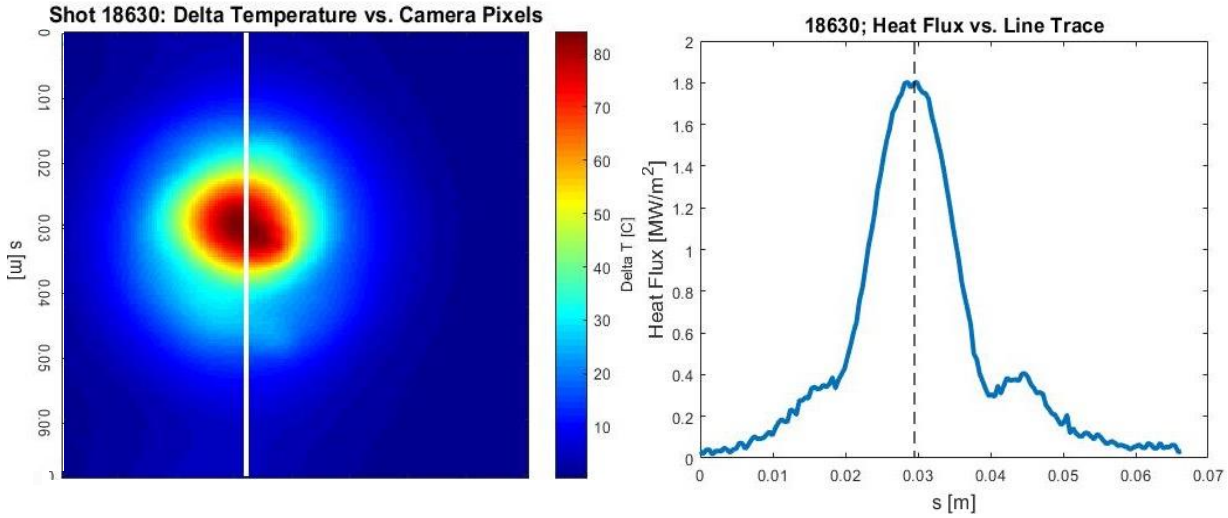

Figure 6.4. Left: Image of IR-obtained target plate temperature profile for shot 18630. White vertical line trace depicts the temperature profile slice to determine the heat flux. Right: Plot of heat flux versus the location on the white line trace, s. The left end of the x-axis (s = 0 m) corresponds to the top of the white line trace in the left image. Dotted black line depicts the approximate center peak of the heat flux profile.

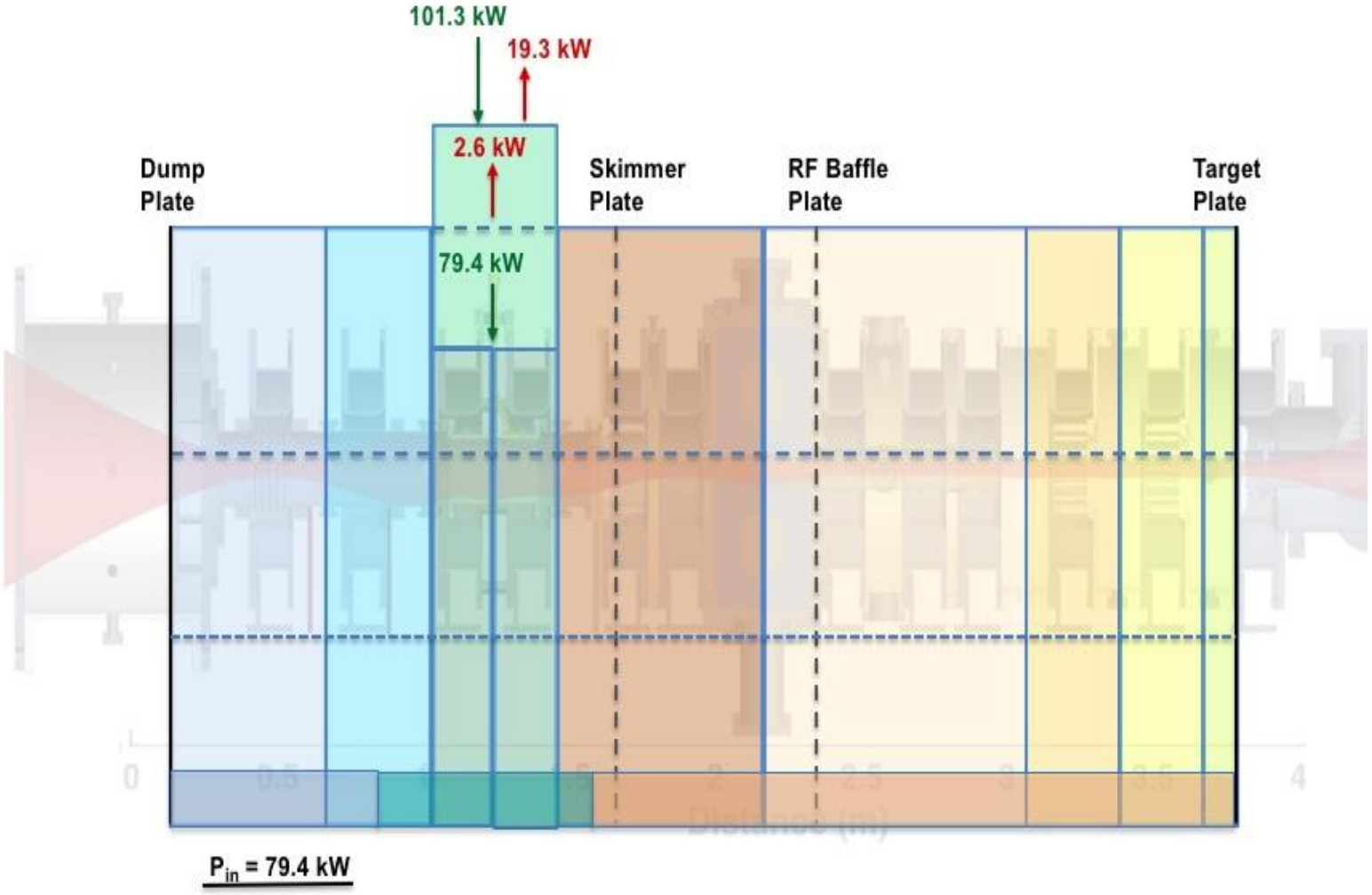

Figure 6.5. Diagram of Proto-MPEX device, broken down into sub-regions, showing the input power components of power balance. Green and red arrows represent power going into and leaving the plasma, respectively. Solid black lines represent the end plates. Dotted black lines represent the skimmer and RF baffle plate.

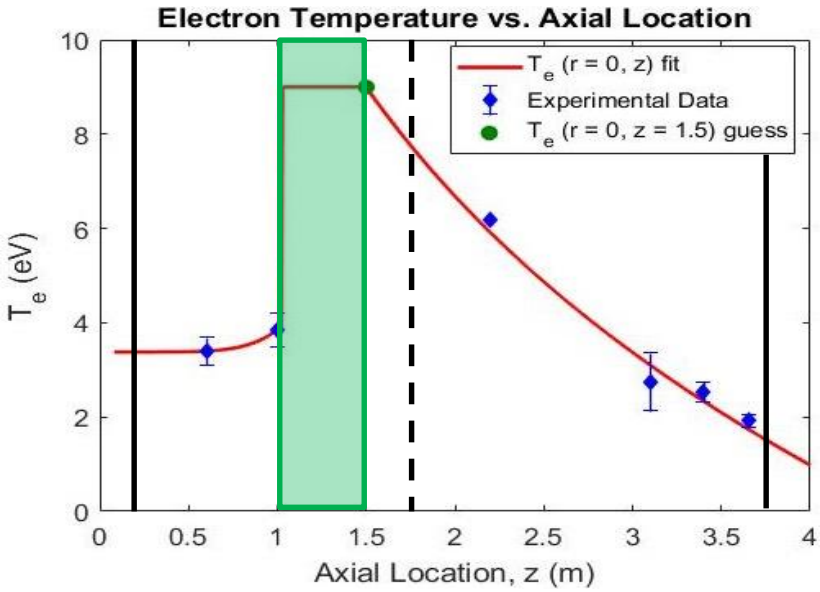

Figure 6.6. Plot depicting on-axis electron temperature measurements and MATLAB fit along the length of the Proto-MPEX machine. The green dot represents the electron temperature best-guess at z = 1.5 m. The helicon region is highlighted in light green. The solid black lines depict the approximate dump and target plate locations. The dotted black line depicts the approximate skimmer plate location.

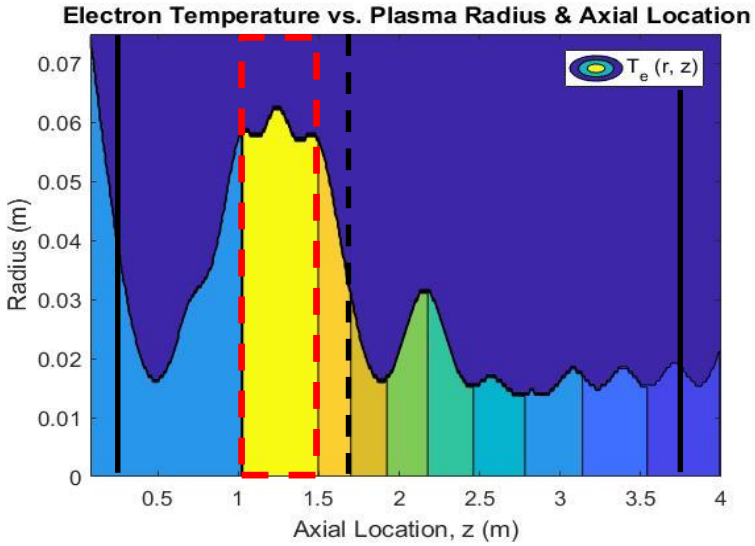

Figure 6.7. Contour plot depicting the radial and axial variation in electron temperatures based on MATLAB-inferred powerbase fits of on-axis experimental electron temperature data. The helicon region is highlighted in by the red dotted box. The solid black lines depict the approximate dump and target plate locations. The dotted black line depicts the approximate skimmer plate location.

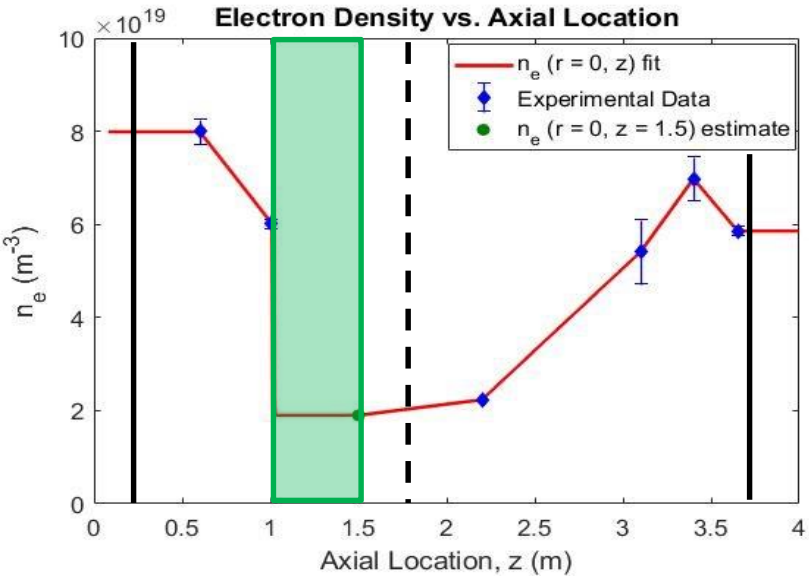

Figure 6.8. Plot depicting on-axis electron density measurements and MATLAB fit along the length of the Proto-MPEX machine. The green dot represents the electron density best-guess at z = 1.5 m. The helicon region is highlighted in light green. The solid black lines depict the approximate dump and target plate locations. The dotted black line depicts the approximate skimmer plate location.

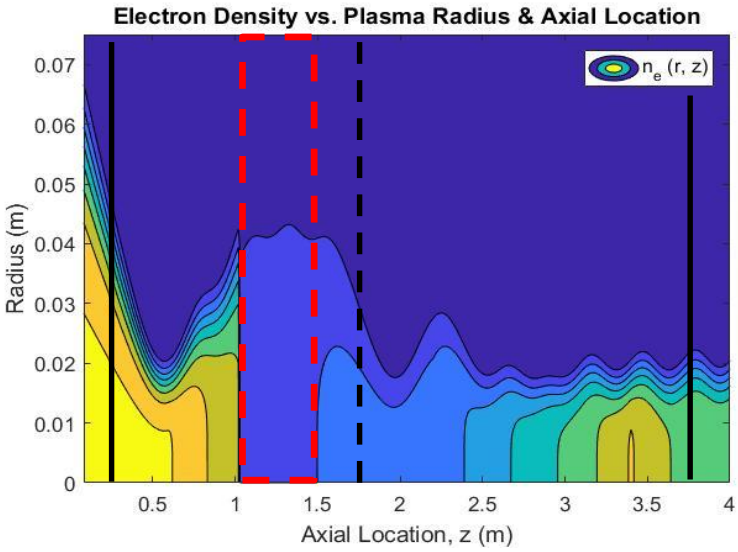

Figure 6.9. Contour plot depicting the radial and axial variation in electron density based on MATLAB-inferred powerbase fits of on-axis experimental electron density data. The helicon region is highlighted in by the red dotted box. The solid black lines depict the approximate dump and target plate locations. The dotted black line depicts the approximate skimmer plate location.

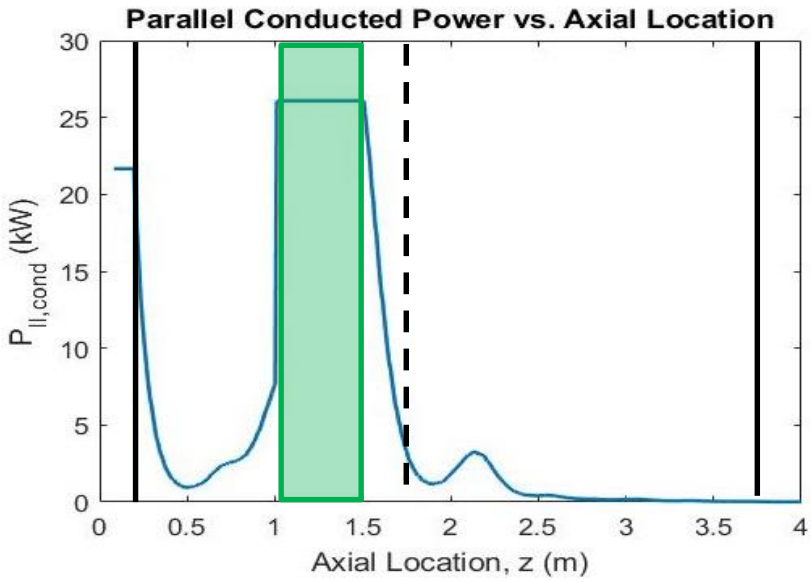

Figure 6.10. Parallel conducted power along machine length. The helicon region is highlighted in light green. The solid black lines depict the approximate dump and target plate locations. The dotted black line depicts the approximate skimmer plate location.

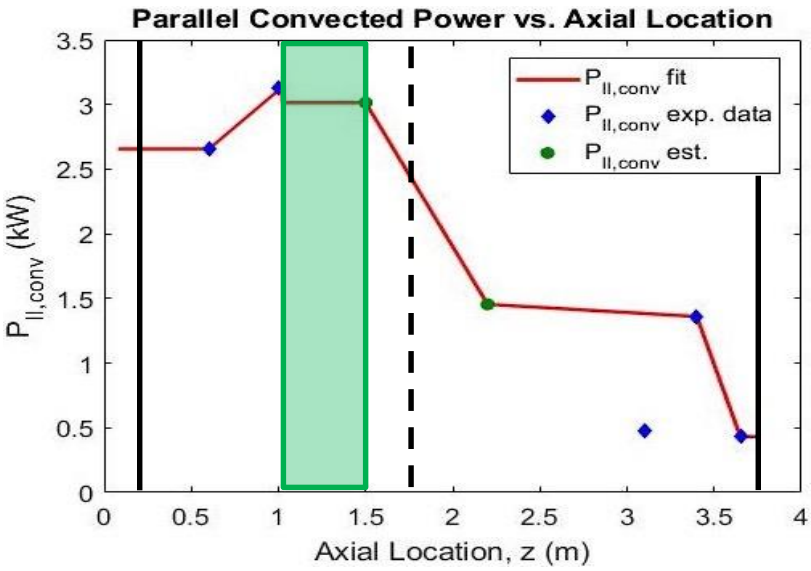

Figure 6.11. Parallel convective power along machine length. The helicon region is highlighted in light green. The solid black lines depict the approximate dump and target plate locations. The dotted black line depicts the approximate skimmer plate location.

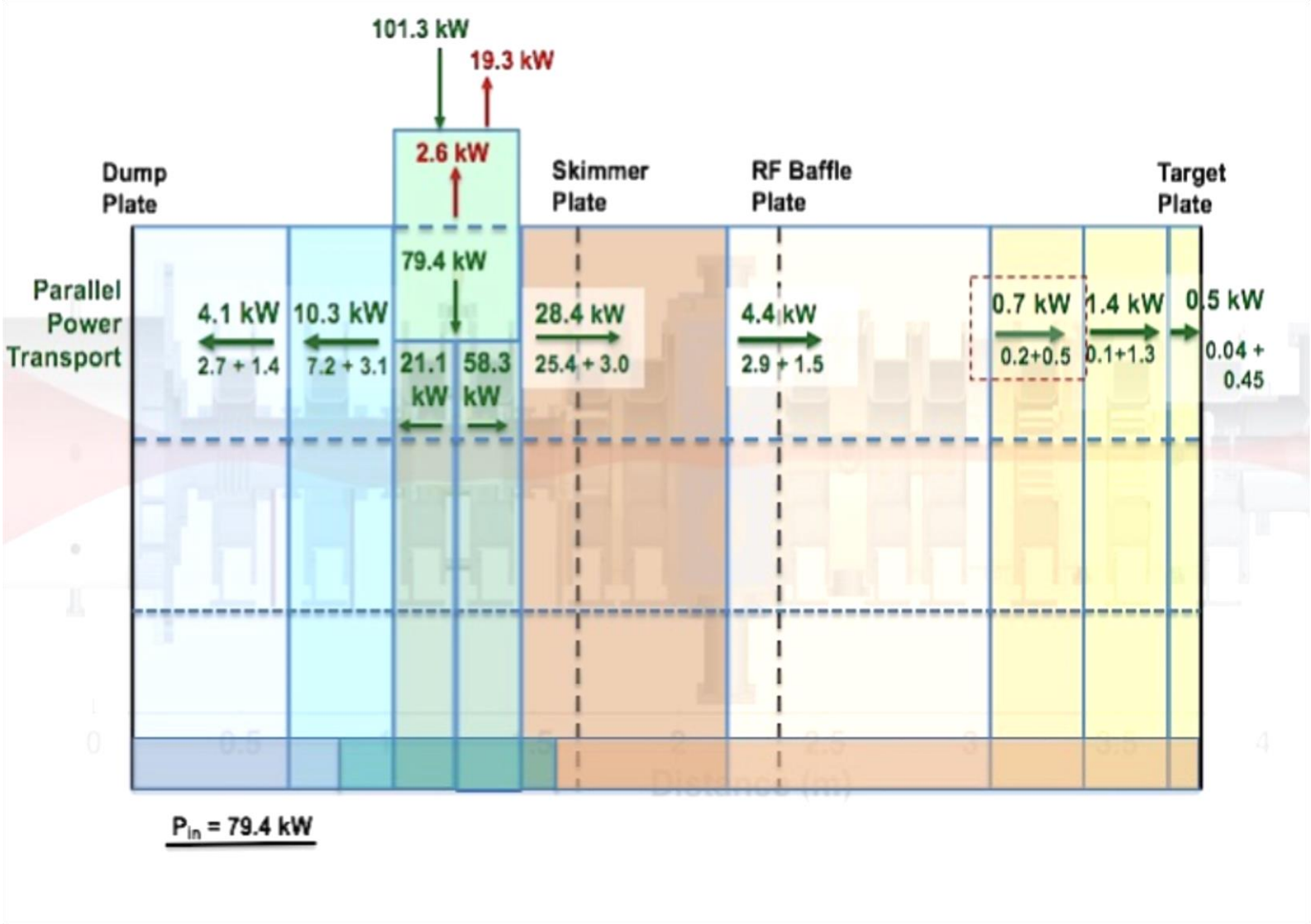

Figure 6.12. Diagram of Proto-MPEX device, broken down into sub-regions, showing parallel power transport & input power components of power balance. Green and red arrows represent power going into and leaving the plasma, respectively. Solid black lines represent the end plates. Dotted black lines represent the skimmer and RF baffle plate.

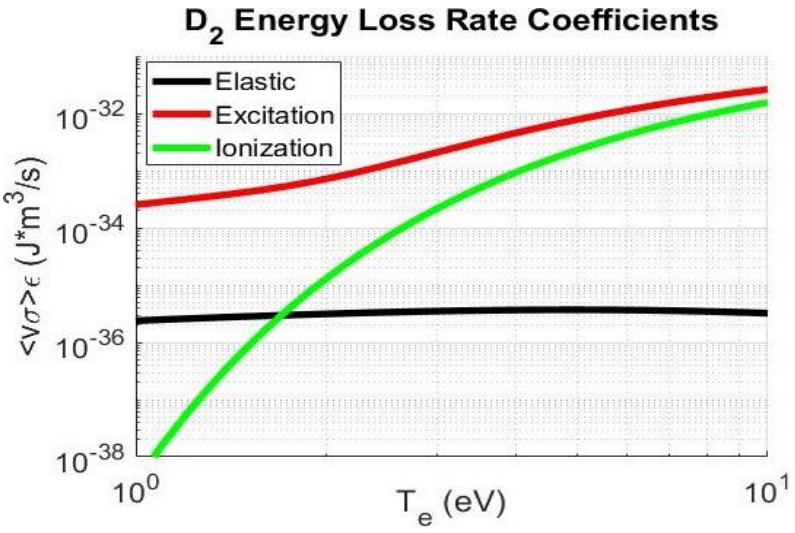

Figure 6.13. Graph of energy loss rate coefficients for molecular deuterium assuming a Maxwellian energy distribution function for a Te range of 0-10 eV. Larger values for molecular energy loss rate coefficients indicate atomic processes contribute more to power losses from the plasma.

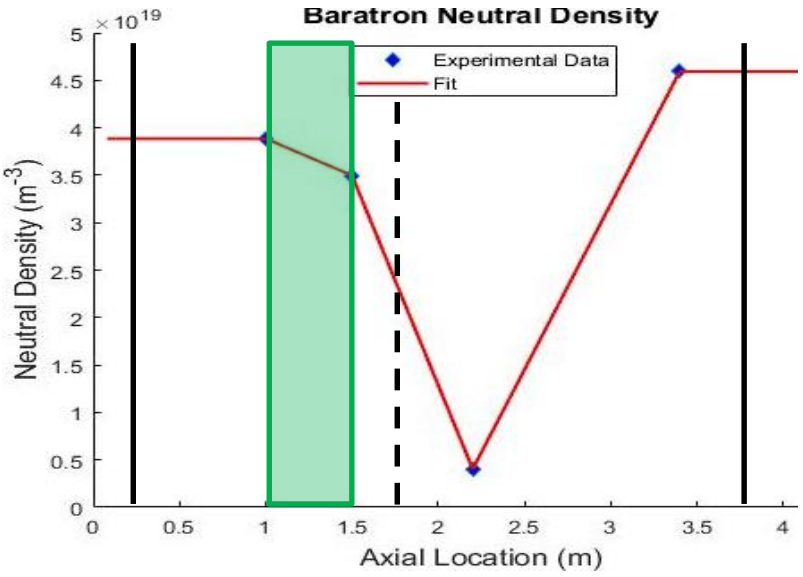

Figure 6.14. Plot depicting baratron-inferred neutral density measurements and MATLAB fit along the length of the Proto-MPEX machine. The helicon region is highlighted in light green. The solid black lines depict the approximate dump and target plate locations. The dotted black line depicts the approximate skimmer plate location.

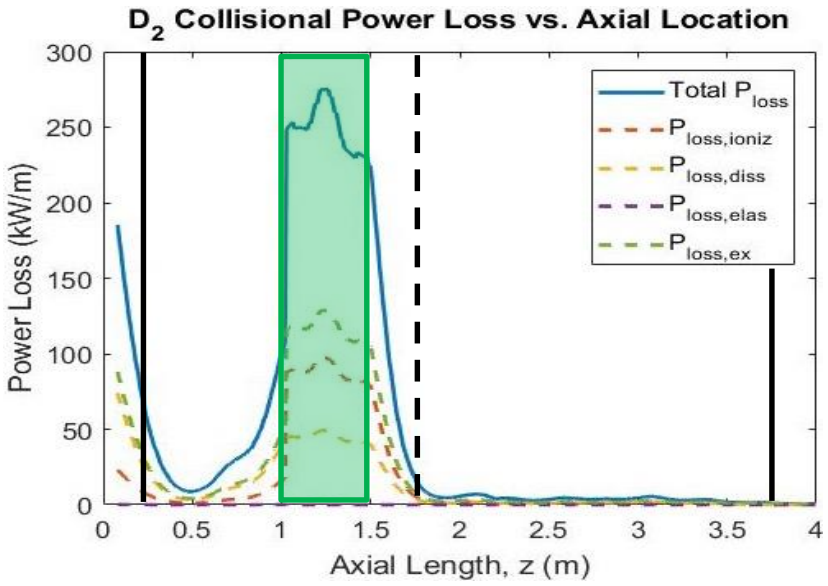

Figure 6.15. Plot depicting MATLAB-modeled power loss along the machine length due to molecular deuterium processes (ionization, dissociation, excitation, elastic) as well as the combined power loss due to their processes. The helicon region is highlighted in light green. The solid black lines depict the approximate dump and target plate locations. The dotted black line depicts the approximate skimmer plate location.

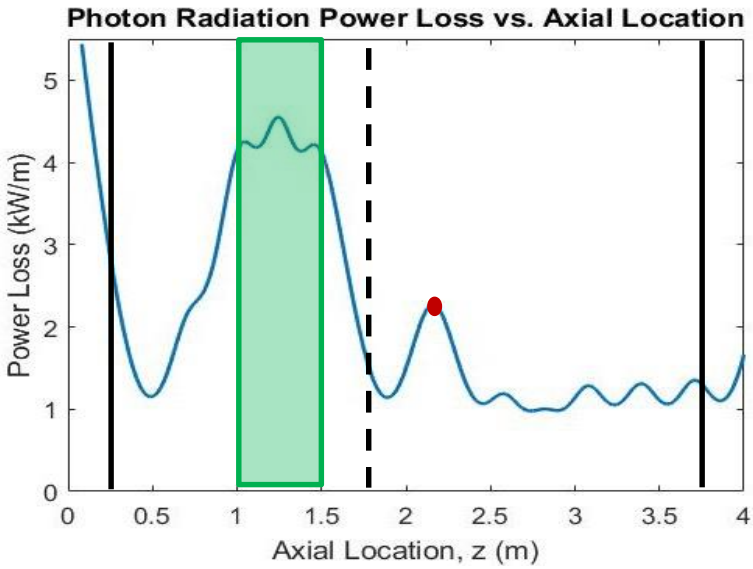

Figure 6.16. Plot depicting power loss along the machine length due to photon radiation as measured by the AXUV photodiode. The red dot depicts the location of the AXUV measurement location. The helicon region is highlighted in light green. The solid black lines depict the approximate dump and target plate locations. The dotted black line depicts the approximate skimmer plate location.

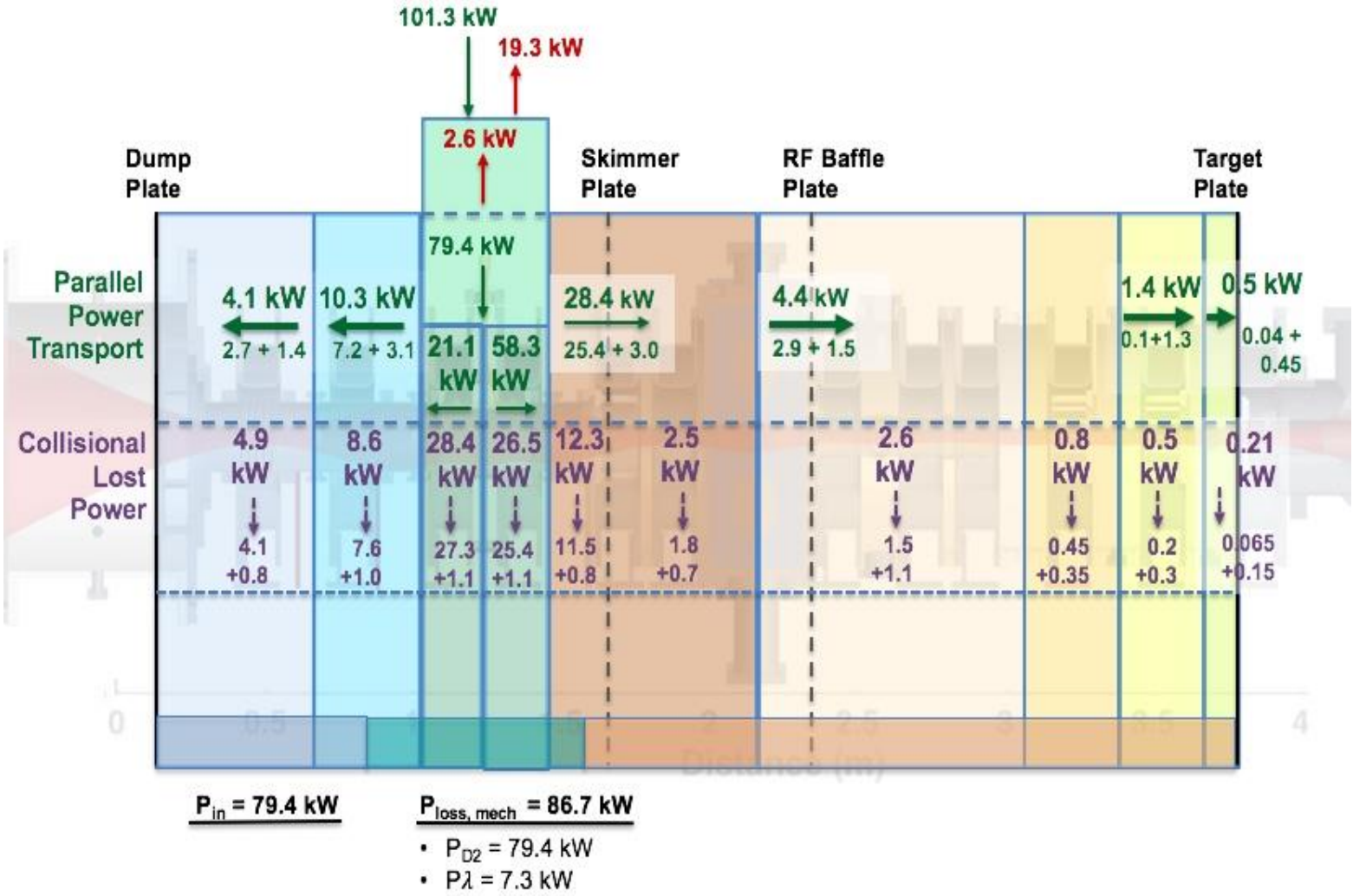

Figure 6.17. Diagram of power balance of Proto-MPEX device, updated to include collisional power losses from the plasma, depicted by purple arrows. Green arrows represent power going into the plasma. Red arrows represent power lost from plasma during input power injection. Solid black lines represent the end plates. Dotted black lines represent the skimmer and RF baffle plate.

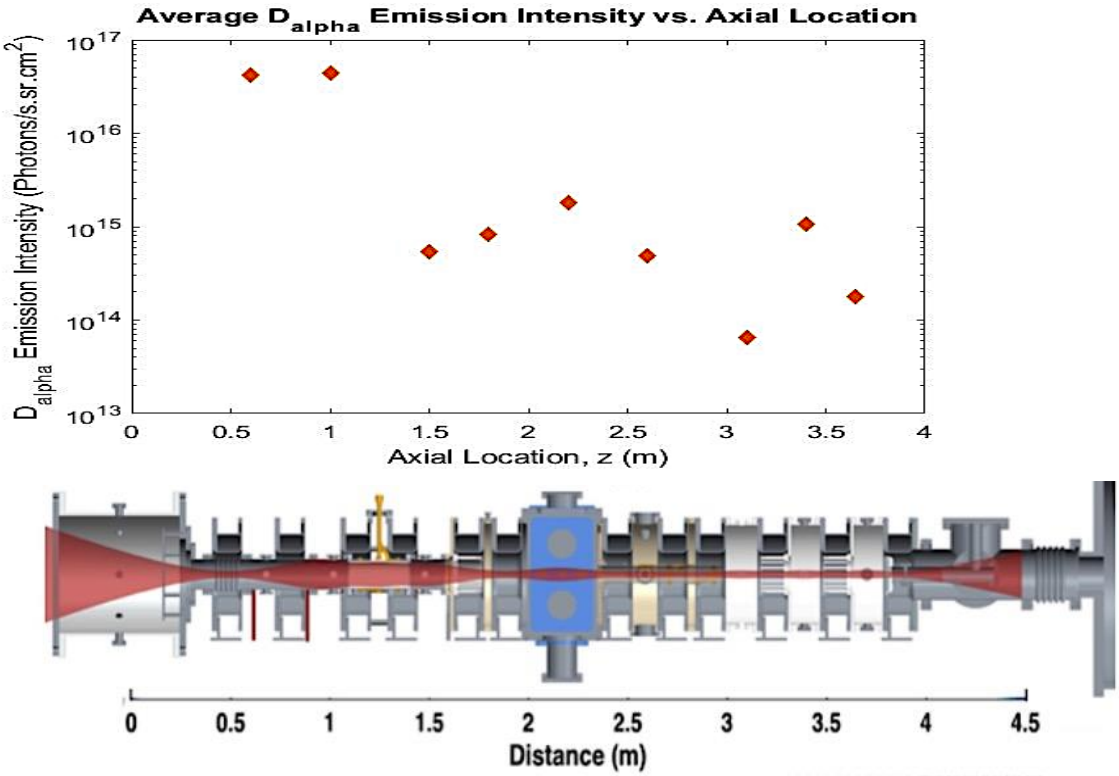

Figure 6.18. Intensities of Dα photons emitted from main plasma along length of Proto-MPEX, averaged from t = 4.4 – 4.5 s. The y-axis represents the emission intensity in photons per second per square centimeter per steradian. The y-axis is on a log10 scale. The x-axis is the distance along the machine. The Proto-MPEX diagram is provided for reference.

Figure 6.19.

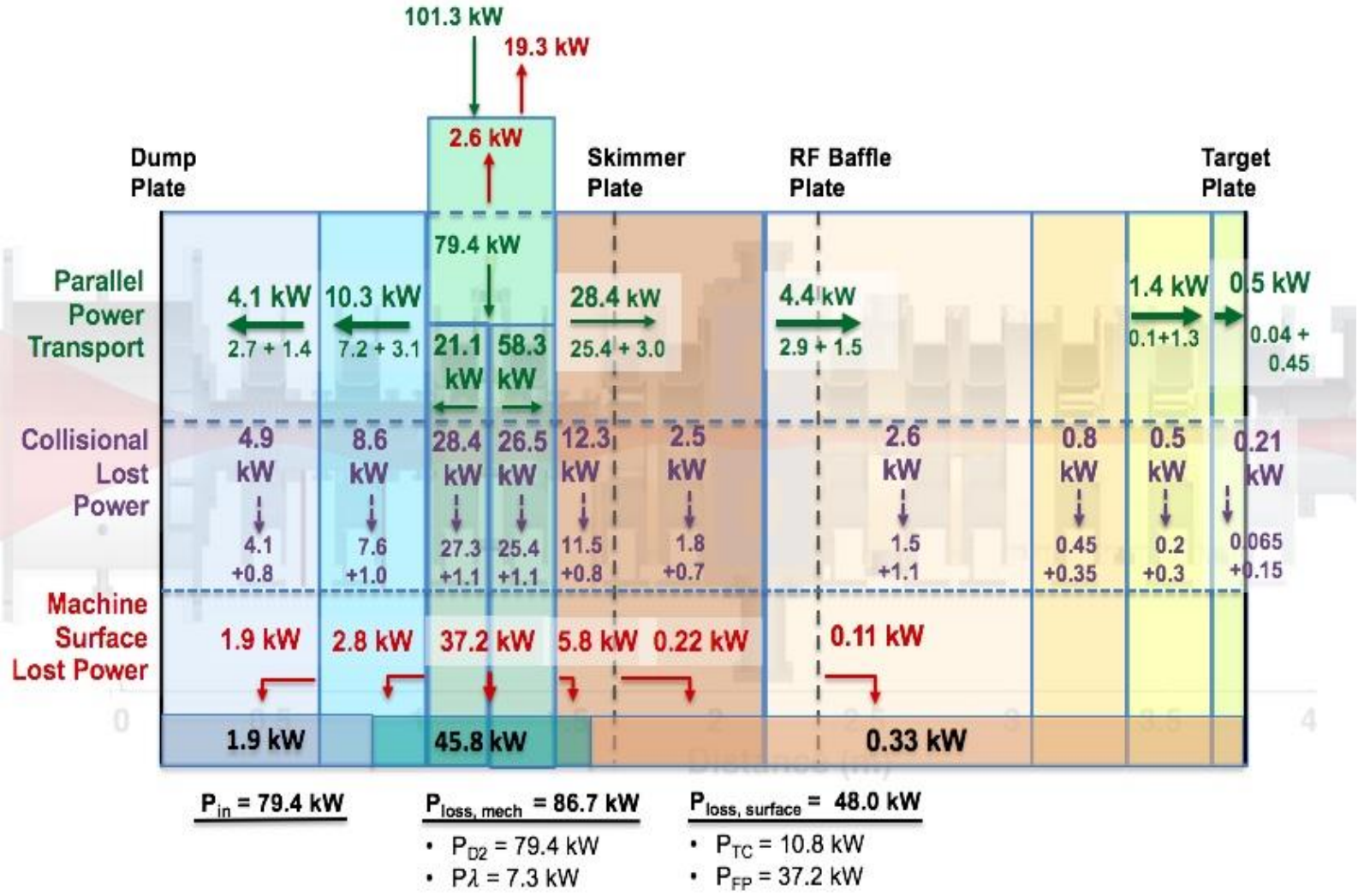

Diagram of power balance of Proto-MPEX device, updated to include power lost to machine surfaces, represented by additional red arrows. Green arrows represent power going into the plasma. Other red arrows represent power lost from plasma during input power injection. Solid black lines represent the end plates. Dotted black lines represent the skimmer and RF baffle plate.

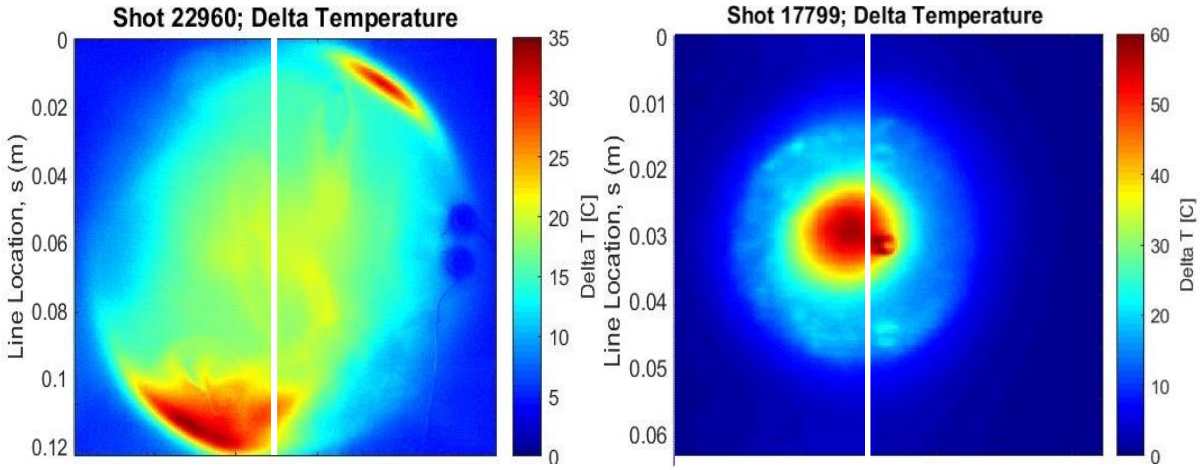

Figure 6.20. Plasma profiles of the dump plate (left) and target plate (right) for the IR frame with the largest temperature rise. The ΔT scale for the dump plate is 0°C - 35°C. The ΔT scale for the target plate is 0°C - 60°C. The white vertical lines depict the temperature profile slices to determine the heat flux along *s*.

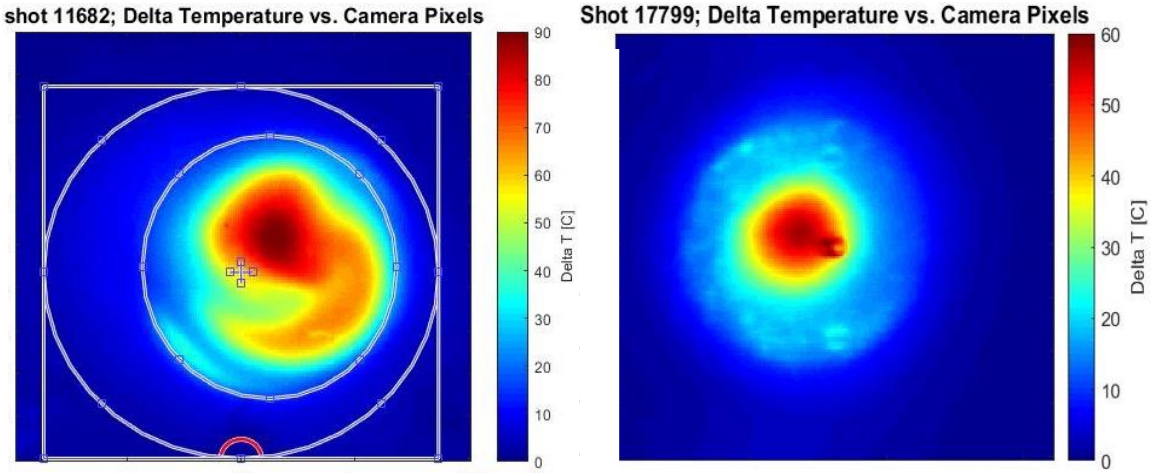

Figure 6.21. Plasma profiles of the target plates from previous power balance (left) and new power balance (right).

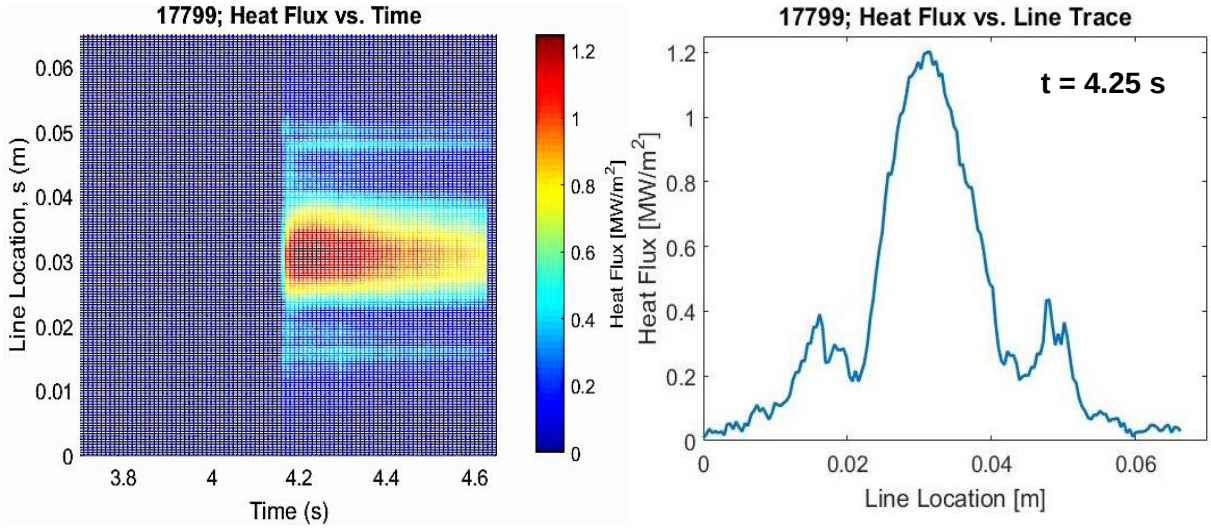

Figure 6.22. Target plate heat flux profiles derived from THEODOR analysis. Left: heat flux profile over the length of the pulse. Right: heat flux profile at time, t = 4.25 seconds.

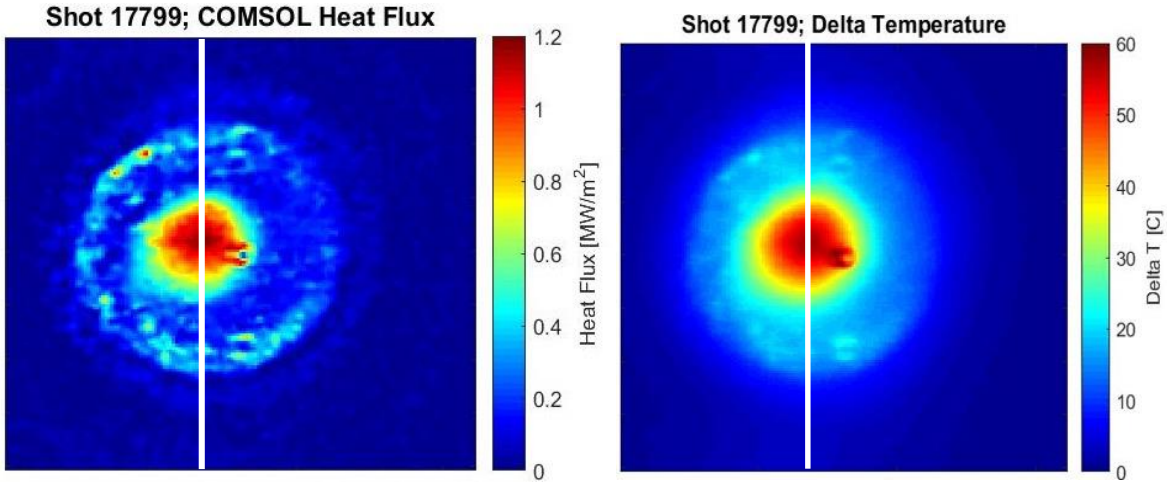

Figure 6.23. Plasma profiles of the target plate heat flux (left) and temperature change (right). The heat flux scale is 0 – 1.2 MW/m^2. The ΔT scale is 0°C - 60°C. The white vertical lines depict the heat flux and temperature profile slices to compare heat flux line profiles.

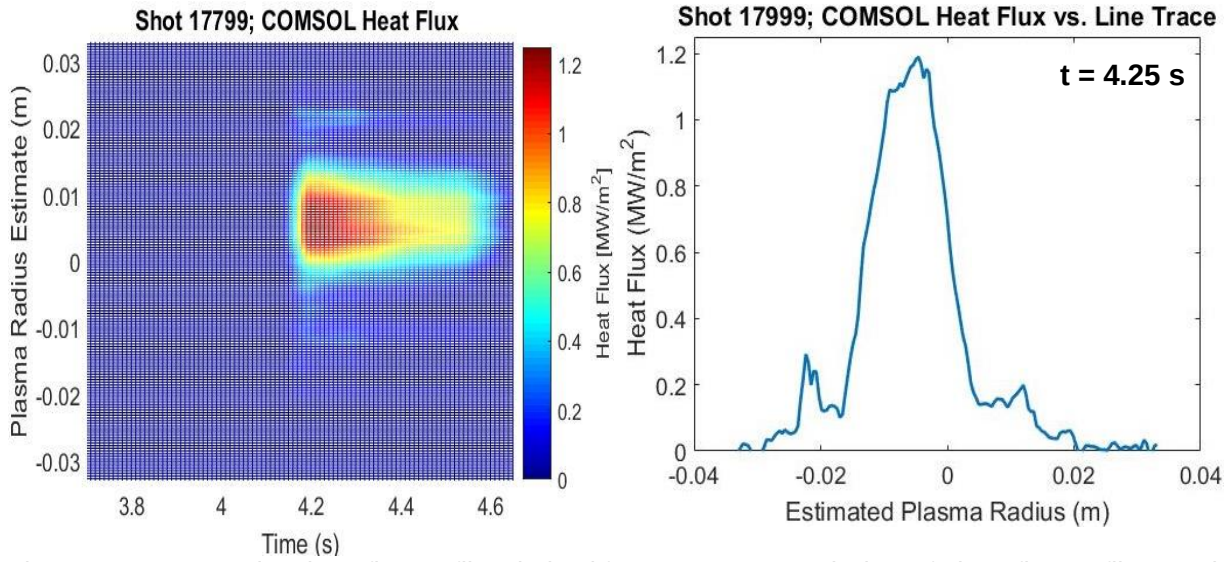

Figure 6.24. Target plate heat flux profiles derived from COMSOL analysis. Left: heat flux profile over the length of the pulse. Right: heat flux profile at time, t = 4.25 seconds.

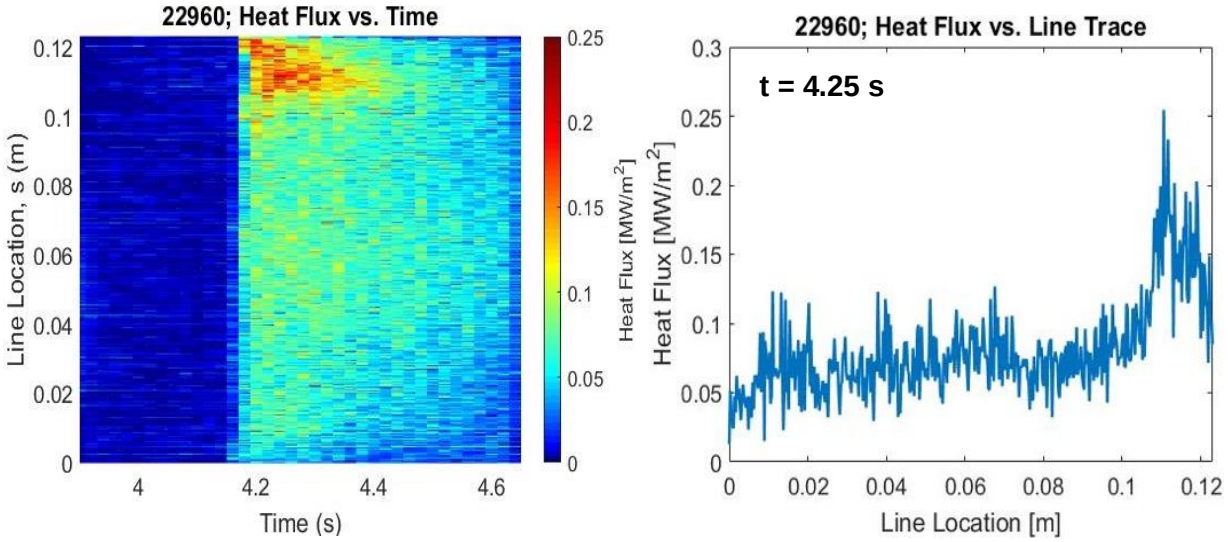

Figure 6.25. Dump plate heat flux profiles derived from THEODOR analysis. Left: heat flux profile over the length of the pulse. Right: heat flux profile at time, t = 4.25 seconds.

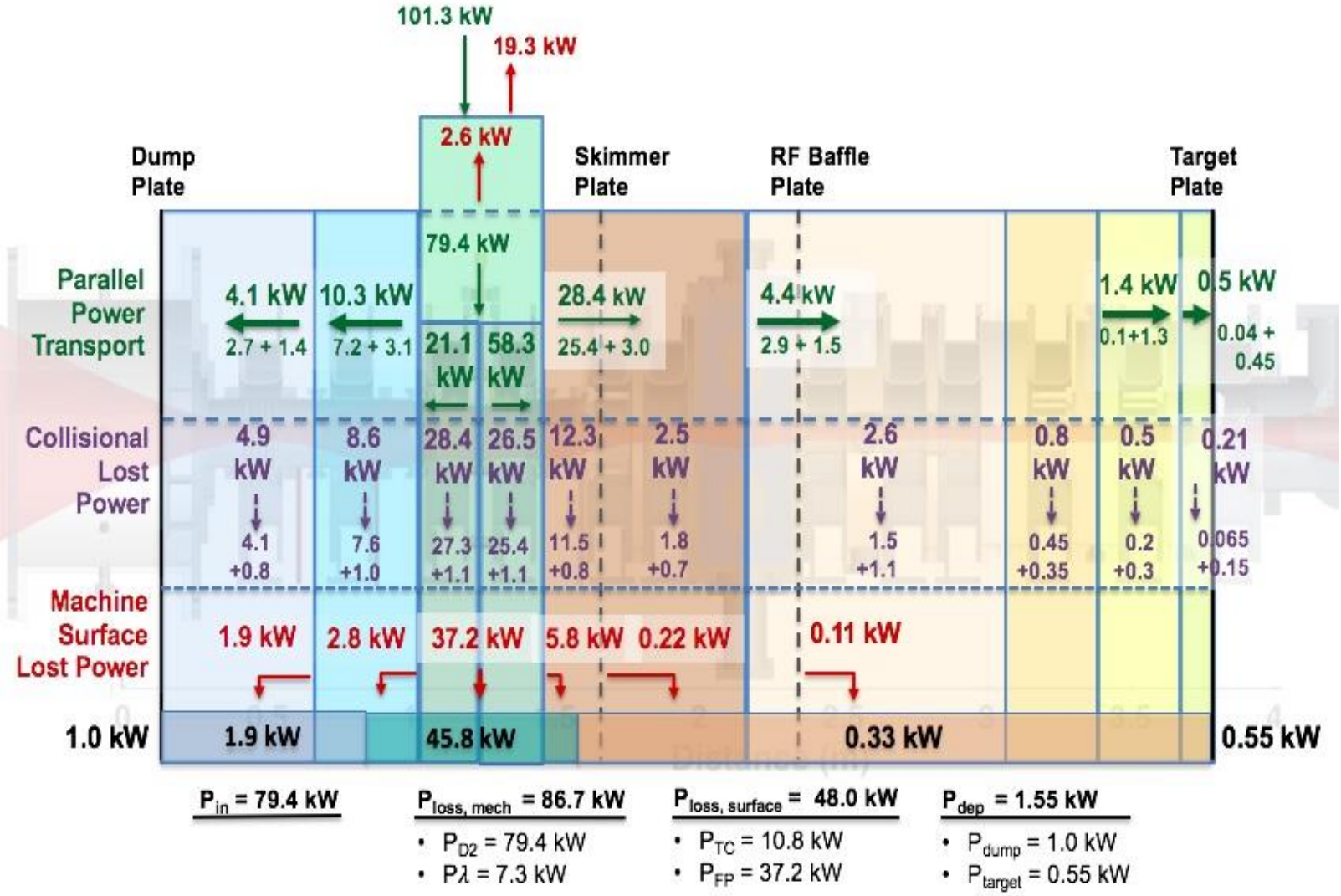

Figure 6.26. Diagram of power balance of Proto-MPEX device, updated to include the power deposited to end plates. Green arrows represent power going into the plasma. Red arrows represent power lost from plasma during input power injection and lost to machine surfaces. Solid black lines represent the end plates. Dotted black lines represent the skimmer and RF baffle plate.

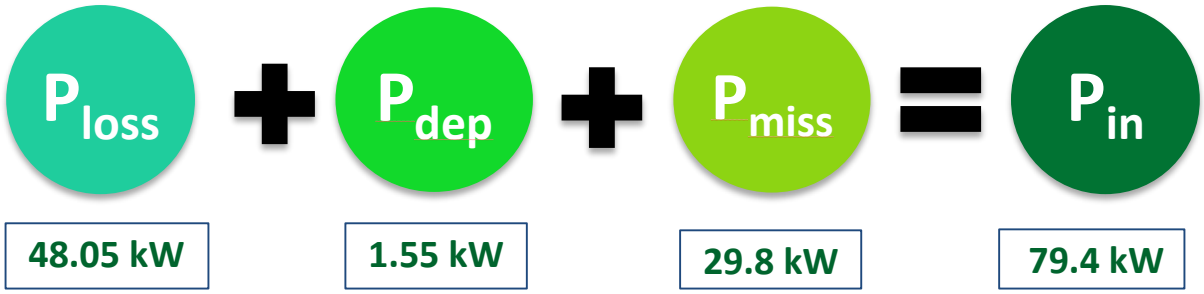

Figure 6.27. Summary of power balance in terms of three main sections. The total input power was 79.4 kW. Total accounted power lost was 48.05 kW. Total deposited power was 1.55 kW. Total missing (unverified) power was 29.8 kW.

E.7. Chapter 7 Figures

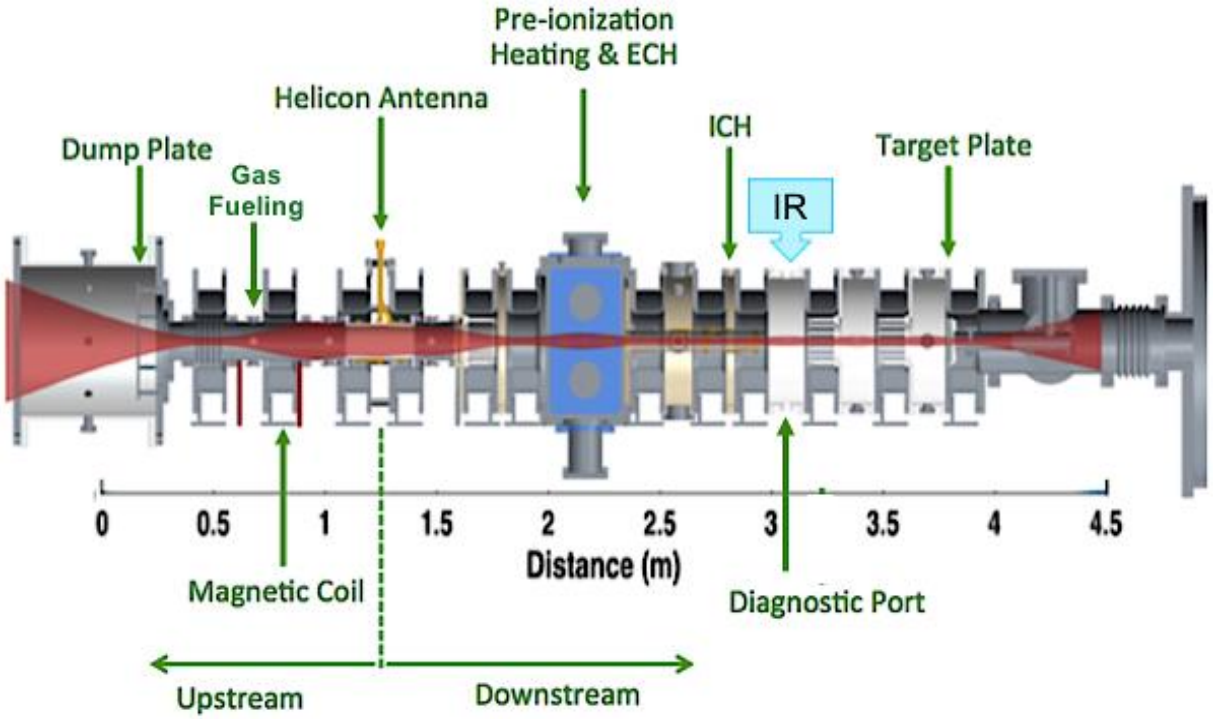

Figure 7.1. Diagrams of Proto-MPEX. Magnetic coils, diagnostic ports, installed power sources, IR camera and end plates are depicted. Machine length is approximately 4.5 m.

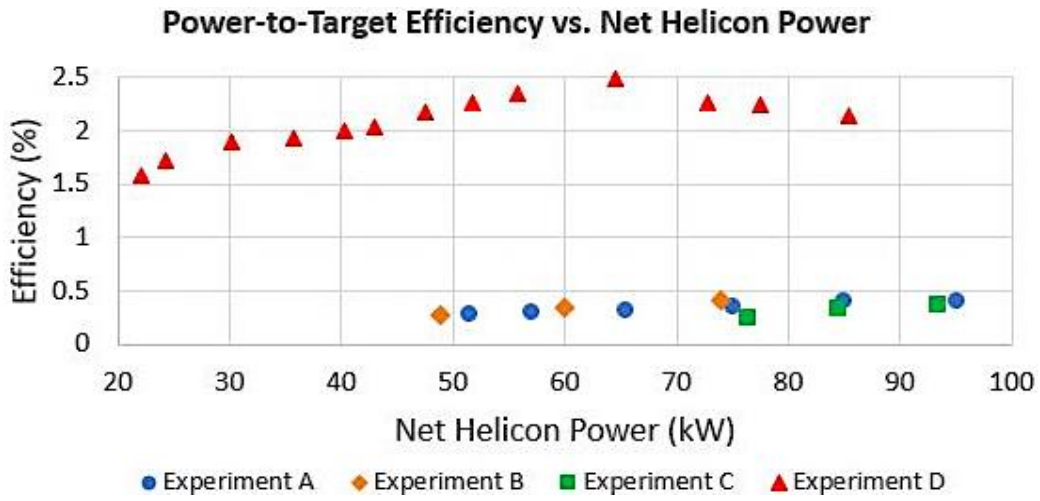

Figure 7.2. Results of power scan analysis. Power-to-target efficiencies remained constant or slightly increased as net helicon power increased.

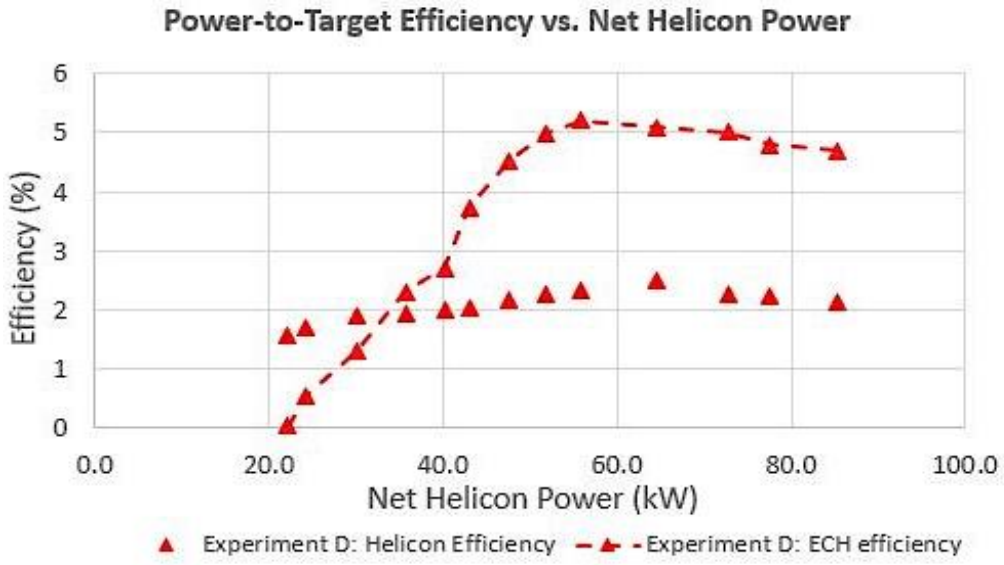

Figure 7.3. Results of power scan analysis for Experiment D, with and without ECH applied.

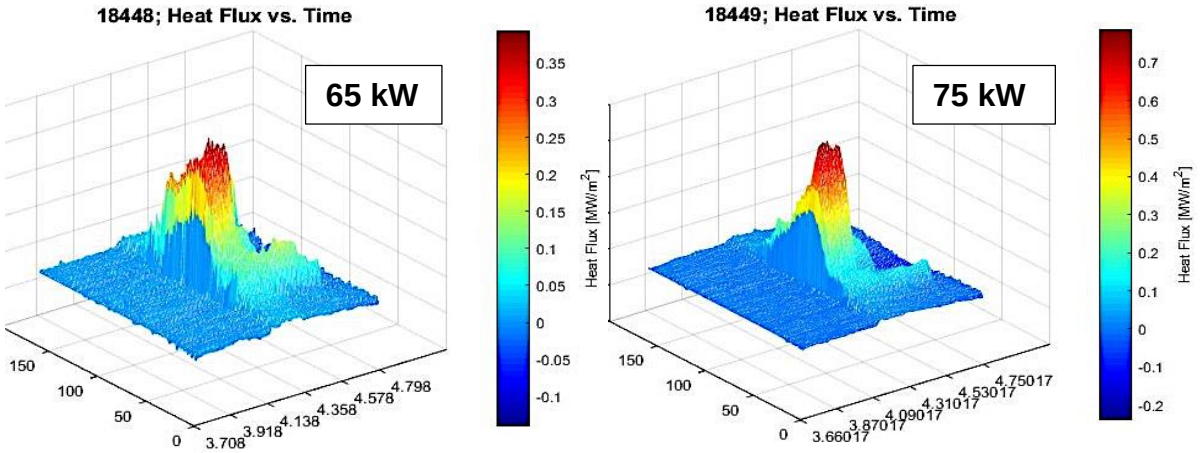

Figure 7.4. Heat flux contour plots of two consecutive plasma shots from experiment A power scan. The profile with 65 kW of net helicon power (left) is noisier than the profile with 75 kW of net helicon power (right).

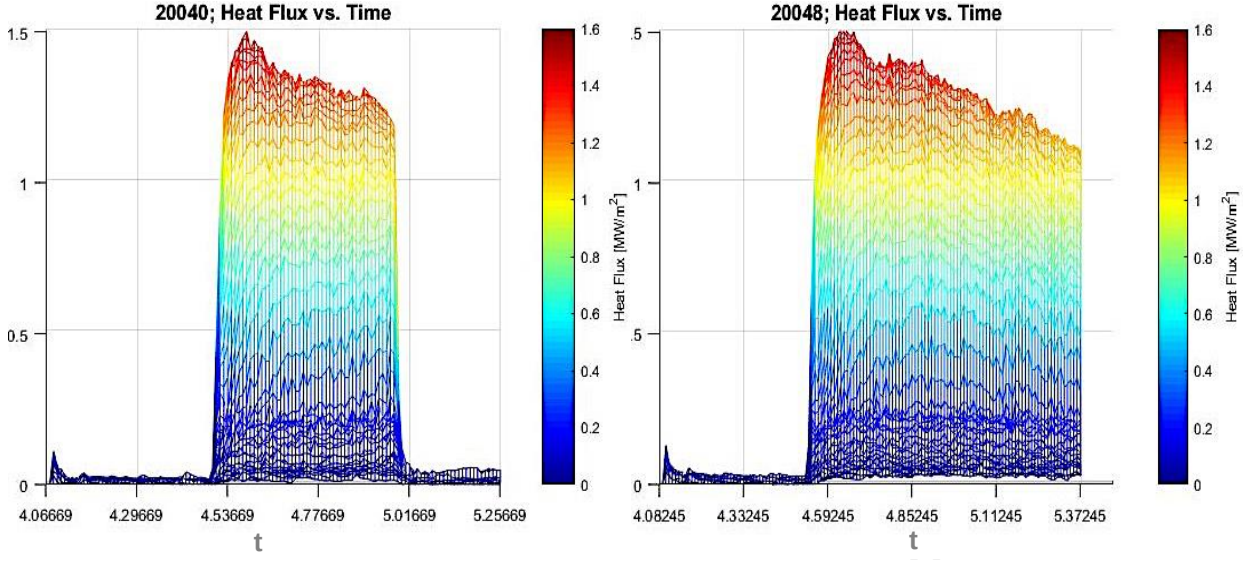

Figure 7.5. Heat flux contour plots of a 500 ms (right) and 1000 ms (left) plasma pulses. The highest heat fluxes and therefore power-to-target efficiencies occur towards the beginning of the plasma pulses. The IR data acquisition of the 1000 ms pulse cut a little short at about 800 ms, but the trend it clear.

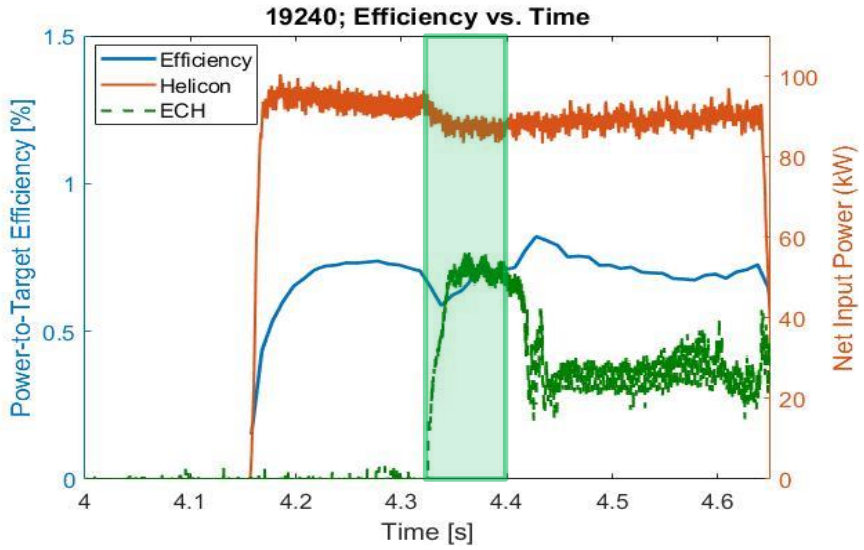

Figure 7.6. Power-to-target efficiency versus applied power sources during helicon + ECH pulse. The light green box highlights the approximate time range where the helicon efficiency and ECH efficiency were determined.

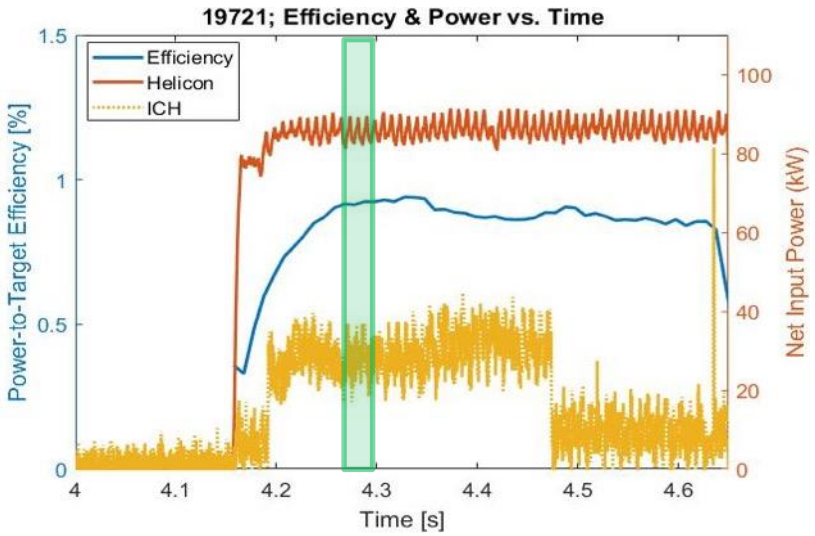

Figure 7.7. Power-to-target efficiency versus applied power sources during helicon + ICH pulse. The light green box highlights the approximate time range where the helicon efficiency and ICH efficiency were determined.

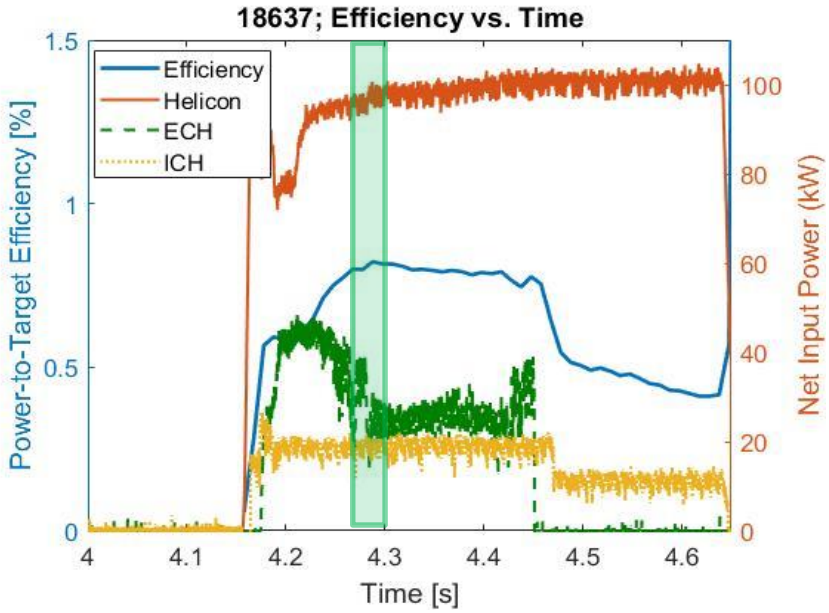

Figure 7.8. Power-to-target efficiency versus applied power sources during helicon + ECH + ICH pulse. The light green box highlights the approximate time range used to determine the helicon, ECH and ICH efficiencies.

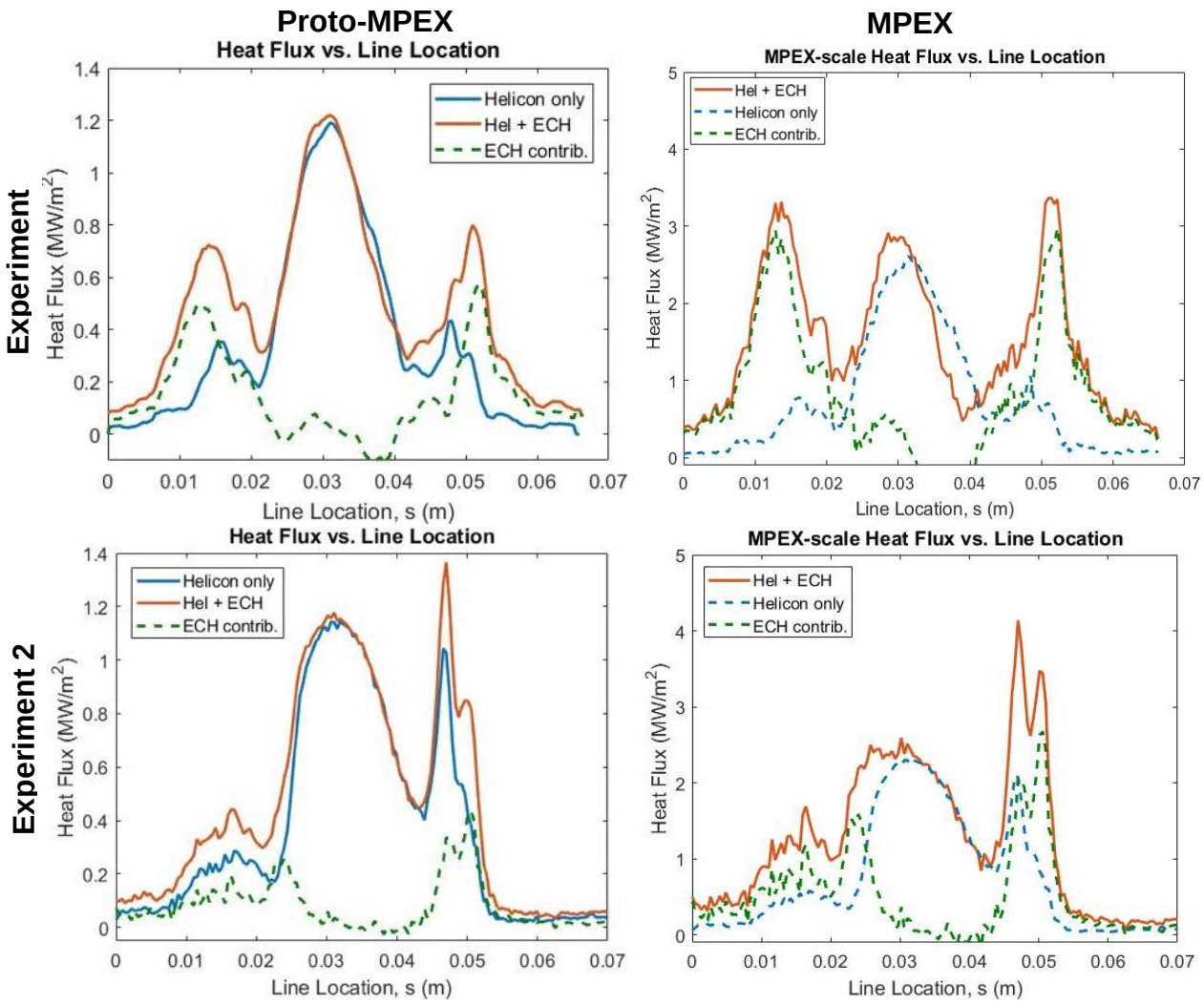

Figure 7.9. Comparison of heat flux profiles from experiments 1 and 2, taken at time ~ 50 ms after the application of ECH. The left column shows the Proto-MPEX-acquired heat flux profiles. The right column shows the expected MPEX-scale heat flux profiles. The top row shows the profiles of experiment 1. The bottom row shows the profiles of experiment 2.

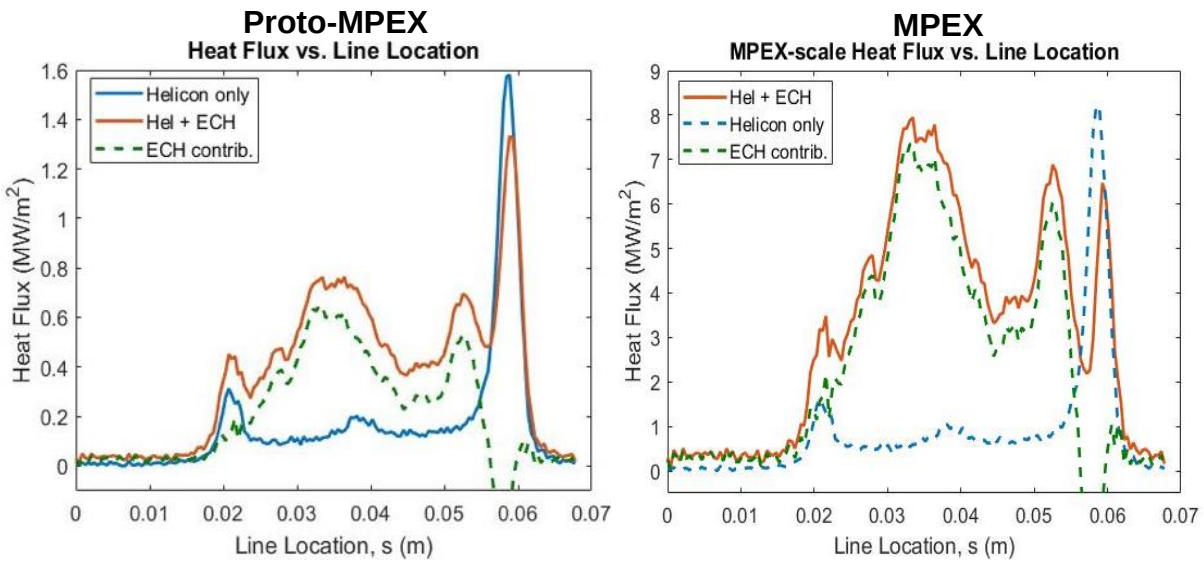

Figure 7.10. Comparison of heat flux profiles from experiments 3, taken at time ~ 50 ms after the application of ECH. The left column shows the Proto-MPEX-acquired heat flux profiles. The right column shows the expected MPEX-scale heat flux profiles.

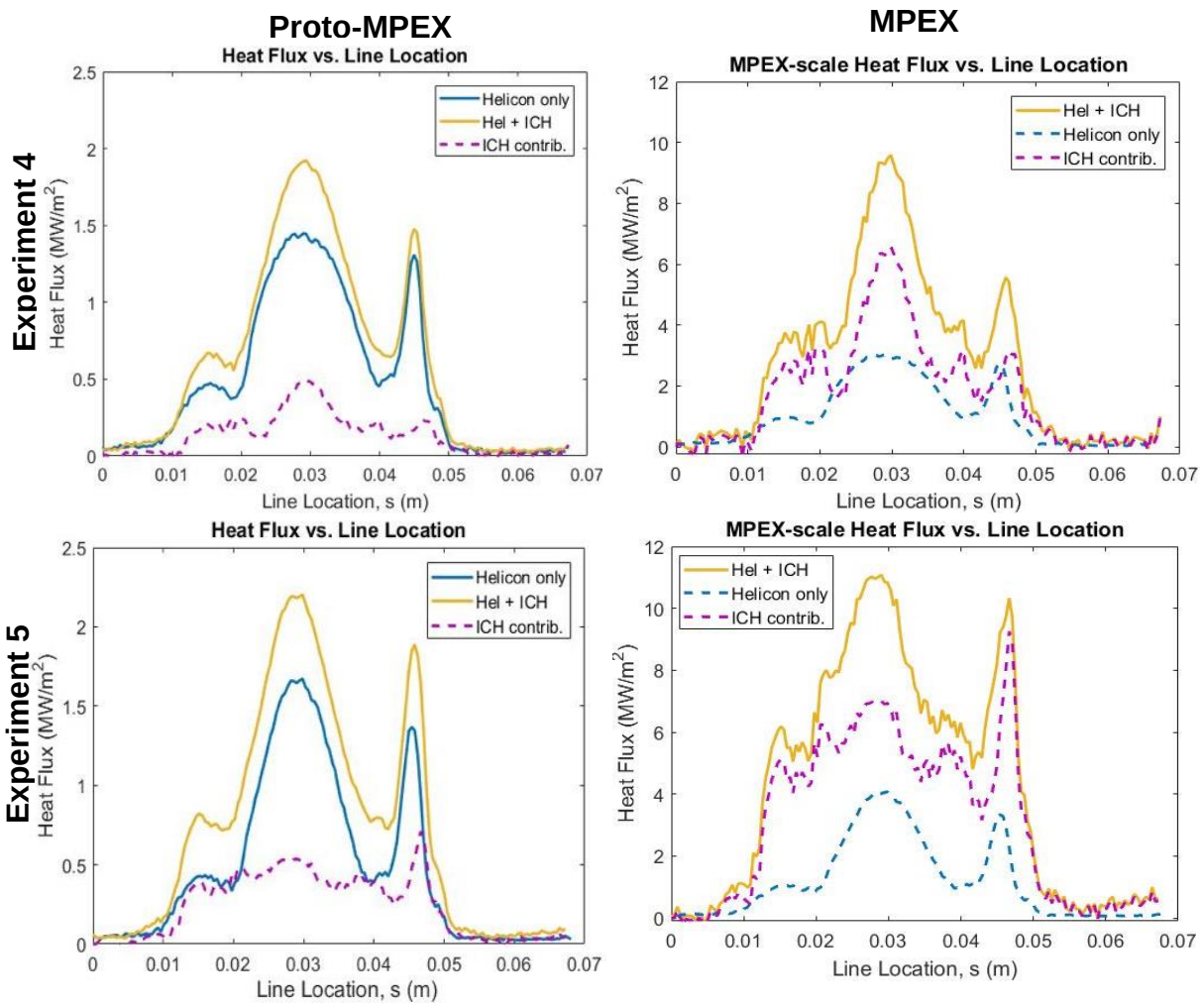

Figure 7.11. Comparison of heat flux profiles from experiments 4 and 5, taken at time ~ 100 ms after the application of ICH. The left column shows the Proto-MPEX-acquired heat flux profiles. The right column shows the expected MPEX-scale heat flux profiles. The top row shows the profiles of experiment 4. The bottom row shows the profiles of experiment 5.

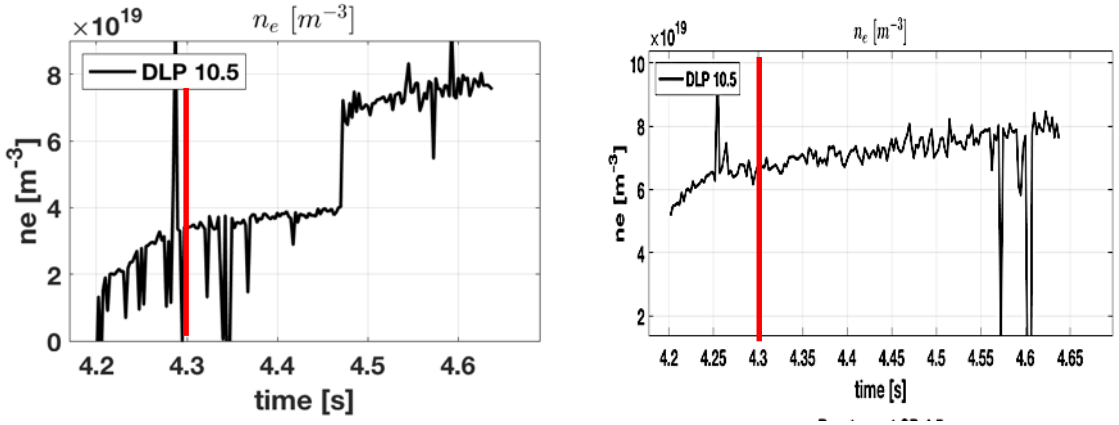

Figure 7.12. Comparison of electron densities measured by LPs at diagnostic port 10.5 (z = 3.4 m) during plasma pulse for experiments 4 (left) and 5 (right). Red lines depict time in pulse when extrapolation analysis is performed.

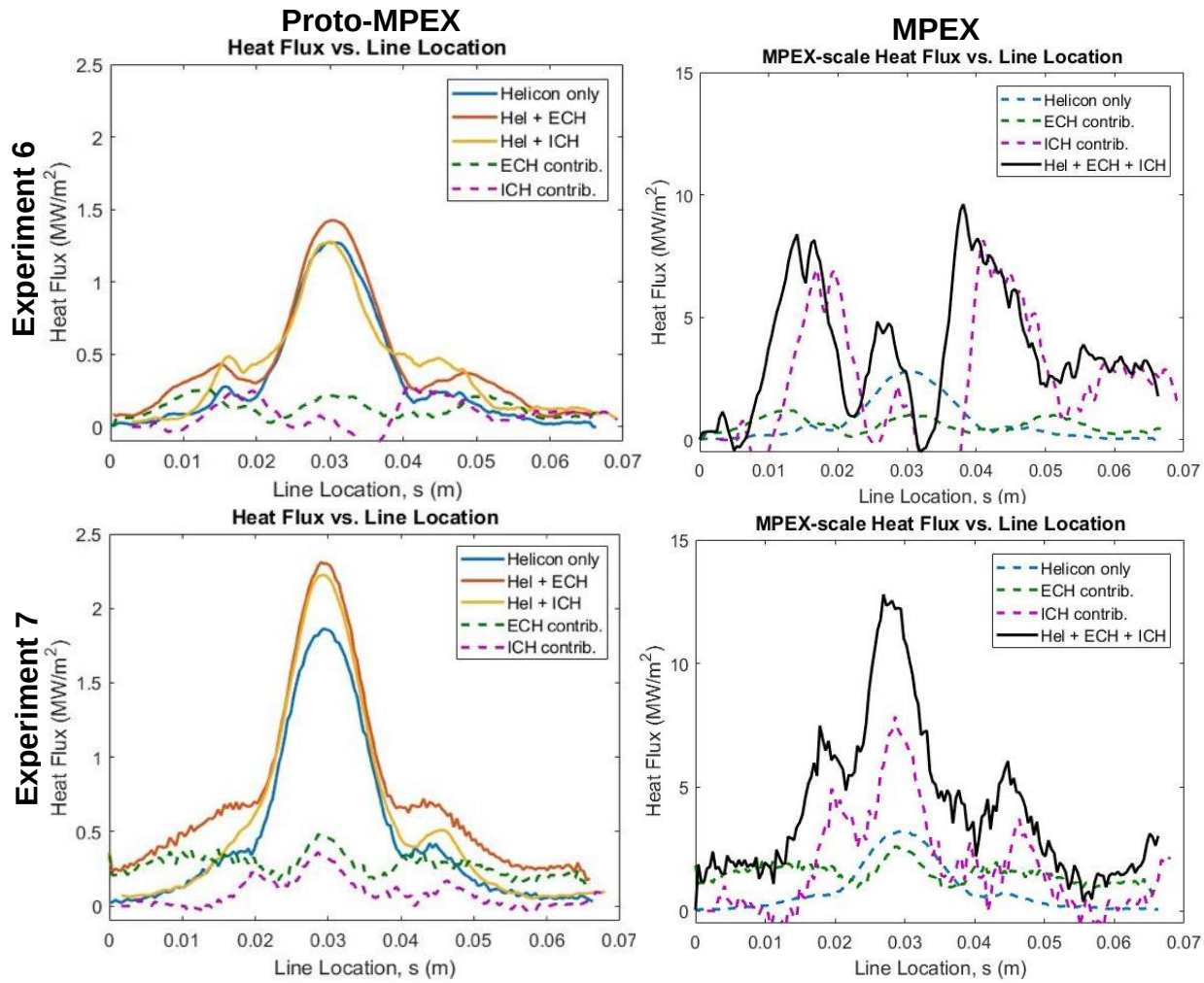

Figure 7.13. Comparison of heat flux profiles from experiments 6 and 7, taken at time ~ 70 ms after the application of ECH. The left column shows the Proto-MPEX-acquired heat flux profiles. The right column shows the expected MPEX-scale heat flux profiles. The top row shows the profiles of experiment 6. The bottom row shows the profiles of experiment 7.

VITA

Melissa “Missy” A. Showers was born in Camden, NJ to Anna and Drew Showers. Her mother is a retired speech therapist and a part-time swim coach. Her father is a software engineer in the process of starting his own company. Missy was raised in Cherry Hill, NJ, along with her three sisters. She spent her summers swimming at Kingston Estates Swim Club. She attended Cherry Hill High School East, where she graduated as valedictorian in 2009 with a total of twelve varsity letters from swimming, cross-country and track & field. Missy pursued a B.S. in Mechanical Engineering with a focus in Energy and Sustainability from Massachusetts Institute of Technology. She dual minored in Energy Studies and Applied International Studies. During her time at MIT, she was a member of the cross-country and track teams, the president of the Alpha Epsilon Phi sorority, the co-chair of the Undergraduate Association for Sustainability, a lifeguard, and a tour-guide. During her collegiate career, she gained research experience during her academic year and summer internships. One of her most memorable experiences was a summer internship in southern France where she helped a PhD student research demand response. Upon completing her bachelor’s degree, Missy took a gap year from academia and worked for a year as a research analyst at a consulting firm focusing on the electricity sector. She then began her graduate career at the University of Tennessee, pursing a PhD in Energy Science and Engineering through the Bredesen Center for Interdisciplinary Research and Graduate Education in August 2014. Her research focus was in nuclear fusion. She worked in the Fusion & Materials for Nuclear Systems Divison (FMNSD) at ORNL on a linear plasma device called the Proto-type Material Plasma Exposure eXperiment (Proto-MPEX), the precursor to MPEX. Her dissertation encompasses a power accounting of the Proto-MPEX machine and an extrapolation to future MPEX operations. While pursuing her PhD, Missy worked with her fellow graduate students to a white paper reviewing the EPA’s Clean Power Plan. She participated in the New York Academy of Sciences (NYAS) multi-day Science Alliance Leadership Training. She also volunteered as an MIT Educational Counselor and at the East Tennessee Children’s Hospital. Missy will complete her PhD degree in December 2018. Upon graduation, she will begin work as an Aeronautical Engineer at Lockheed Martin’s Skunk Works in Palmdale, CA, where she will continue working on nuclear fusion devices.